Effect of Substitution and Doping on Cathode Materials in Li- and Na-based Batteries: First-Principle Study

INAUGURAL DISSERTATION

to obtain the academic degree
Doctor rerum naturalium (Dr. rer. nat.)

submitted to

Department of Biology, Chemistry, Pharmacy

of Freie Universität Berlin

by

Liang-Yin Kuo

from Taipei, Taiwan

Berlin, 2021

This dissertation was prepared under the supervision of Dr. Payam Kaghazchi at Freie Universität Berlin from March 2016 until April 2021

The originality of this work is confirmed by the author

1st Reviewer: Dr. Payam Kaghazchi

2nd Reviewer: Prof. Dr. Beate Paulus

Date of the defense: 07.06.2021

I hereby declare that this dissertation was written independently by me. I used no other sources than the ones marked and acknowledged as such. This work has not yet been submitted or published as a dissertation to any other university.

To my parents

Abstract

Energy storage devices, *e.g.* lithium(Li)-ion and sodium(Na)-ion batteries (LIBs, SIBs) are becoming important due to the growing demands of electric vehicles (EVs) and large-scale power grids. LIBs are considered to be replacement for the fossil fuels in vehicles, while SIBs are expected to store the renewable energies in large-scale grids. However, the power densities, energy densities and cycle life of LIBs and SIBs are still low and insufficient to meet the needs. Thus, LIBs and SIBs are extensively studied, especially as cathode materials. $LiNiO_2$ (LNO) is one of the most popular cathode material for LIBs because it can deliver a higher energy density than commercialized $LiCoO_2$ (LCO) and consists of cheaper Ni element than that of LCO with Co. However, LNO suffers from large structural changes, resulting in the low energy density during charge/discharge processes. Substitution of Co and Mn with Ni cations to form the ternary (Ni-Co-Mn, NCM) oxide and lattice doping are practical strategies to improve the structural stability of LNO.

Hence, three (out of four) works are focusing on the $LiNi_aCo_bMn_{1-a-b}O_2$ (NCM*ab*1-*a*-*b*) materials in this dissertation for LIBs. The influence of increasing Ni contents on the structural stability of NCM was studied. Understanding of the origin of the structural changes (*i.e.* mechanical stability) in NCM111 and NCM811 during charging/discharging helps us to explain the reason behind the structural instability of NCM systems. Moreover, the effect of Al doping on vacancy formation energies of Li and O (*i.e.* chemical stability) in NCM materials was investigated. In the first work of this dissertation, an extensive set of electrostatic (Coulomb energy) and density functional theory (DFT) calculations were combined to determine the crystal, atomic and electronic structures of NCM111 as a function of Li concentration. A detailed analysis of the number of unpaired spins $N\uparrow - N\downarrow$ (NUS), spin density difference (SDD), density of state (DOS) and Bader charges (BCs) was applied to explain the reason behind the non-monotonic variation of lattice parameters and oxygen-stacking-induced phase transition. The influence of choosing the exchange-correlation (XC) functional on our results was also investigated. The SCAN functional provides reasonable predictions in agreement with experimental data. Our results indicate that the presence/absence of $Li-O$ attractions, charges on transition metals (TMs) and O anions, cooperative/collective Jahn$-$Teller ($J-T$) distortion and electrostatic interactions are key factors to control the lattice parameters change. The O-stacking-induced phase transition at the full delithiated structure, which has not been well understood, is shown to be driven by electrostatic forces. In

the second work of this dissertation, a similar approach (by combining extensive Coulomb energy and DFT calculations) to the study of NCM111 was used to determine the crystal, atomic and electronic structures of NCM811 at different levels of charging (delithiation). The electronic analysis of NUS, SDD, DOS, and BCs were analyzed to explain the reason behind the lattice parameters change and phase transitions. For the first time, the reason behind the hexagonal to monoclinic (H$-$M) phase transition at half Li concentration was explained. The O-stacking-induced phase transition at the full delithiated structure was also interpreted in details. It was found that the H$-$M phase transition is due to the collective J$-$T distortion, and the O-stacking-induced phase transition is driven by the electrostatic interaction. The third work of this dissertation was focusing on the effect of Al doping on vacancy formation energies of Li and O (*i.e.* chemical stability) in Ni-rich NCM90505. By analyzing the Li and O vacancy energies at lithiated and delithiated states, the reason for the higher structural stability of Al-doped NCM90505 (*i.e.* NCMA89) than that of undoped one was explained. It was found that the strong binding energy of Al$-$O bonds is beneficial for improving the structural stability of Ni-rich NCM.

SIBs are cost-efficient and thus are widely studied. One of the most interesting cathode materials in SIBs is $NaMnO_2$ (NMO). This is because NMO can deliver a higher energy density than other types of cathode materials in SIBs. Moreover, it consists of earth-abundant Mn element, which is beneficial to reduce the cost. However, NMO undergoes large structural changes, leading to the fast capacity loss (*i.e.* short battery lifetime) during cycling. To understand the reason behind the large structural changes in NMO, here, the effect of Fe doping with various concentration x of Fe contents on mechanical stability of $Na_{0.67}Fe_xMn_{1-x}O_2$ was studied. In the fourth work of this dissertation, a combination of extensive Coulomb energy and DFT calculations was also applied to find the most favorable arrangements of Na ions in $Na_{0.67}MnO_2$. Several possible configurations in which Mn sites are replaced by Fe dopants were explored to find the lowest total energy of the structures by using DFT calculations. The lattice parameters change with different $U-J$ values and the J$-$T distortion of $Na_{0.67}Fe_xMn_{1-x}O_2$ with various amount of Fe contents were simulated and analyzed. Our results indicate that Fe-doped $Na_{0.67}MnO_2$ can suppress the J$-$T distortion, where the difference in the length of axial and equatorial axis in Mn$-$O octahedra is reduced and thus improves the structural stability of $Na_{0.67}MnO_2$. These studies help us to gain insight into the influence of increasing amount of Ni contents on atomic and electronic structural changes in NCM as well as the cation doping on chemical and mechanical stability of NCM and NMO materials. Our results indicate that substitution or doping can alternate the charge states of TMs and thus suppress their J$-$T distortion effects.

Kurzfassung

Die Bedeutung von Energiespeichern wie zum Beispiel Lithium(Li)-Ionen- und Natrium(Na)-Ionen-Batterien (LIBs, NIBs) nimmt, aufgrund des wachsenden Bedarfs im Bereich der Elektromobilität und der Notwendigkeit von Zwischenspeichern in großen Stromnetzen, beständig zu. Während LIBs in Fahrzeugen die fossilen Kraftstoffe ersetzen sollen, sollen NIBs die Lücke zwischen der Erzeugung erneuerbarer Energie und dem Verbrauch in großen Stromnetzen schließen. Allerdings sind die Leistungsdichten, die Energiedichten und die Zykluszeiten von LIBs und NIBs noch gering und nicht ausreichend, um den Anforderungen gerecht zu werden. Daher sind insbesondere die Kathodenmaterialien von LIBs und NIBs Thema einer Vielzahl von Studien. $LiNiO_2$ (LNO) ist eines der populärsten Kathodenmaterialien für LIBs, da es eine höhere Energiedichte als das bereits kommerzialisierte $LiCoO_2$ (LCO) liefern kann und das im Vergleich zu Co kostengünstige Element Ni verwendet. Allerdings durchläuft LNO große strukturelle Veränderungen während des Lade-/Entladevorgangs, was zu einer geringen Energiedichte führt. Die Substitution von Ni-Kationen durch Co und Mn zur Bildung des ternären (Ni-Co-Mn, NCM) Oxids und die Gitterdotierung sind praktische Strategien zur Verbesserung der strukturellen Stabilität von LNO.

Drei (von vier) Arbeiten dieser Dissertation konzentrieren sich daher auf $LiNi_aCo_bMn_{1-a-b}O_2$ (NCM*ab*1-*a*-*b*) Materialien für LIBs. Hier wurde der Einfluss von steigenden Ni-Gehalten auf die strukturelle Stabilität von NCM untersucht. Das Verständnis des Ursprungs der strukturellen Veränderungen (d.h. der mechanischen Stabilität) in NCM111 und NCM811 während des Ladens/Entladens hilft uns, den Grund für die strukturelle Instabilität von NCM-Systemen zu erklären. Außerdem wurde der Effekt der Al-Dotierung auf die Leerstellenbildungsenergien von Li und O (d.h. die chemische Stabilität) in NCM-Materialien untersucht. Im ersten Teil dieser Dissertation wurde ein Umfangreicher Satz von elektrostatischen- (Coulomb Energie) und Dichtefunktionaltheorie Rechnungen (DFT) kombiniert, um die kristallinen, atomaren und elektronischen Strukturen von NCM111 als Funktion der Li-Konzentration zu bestimmen. Eine detaillierte Analyse der Gesamtzahl der ungepaarten Spins N↑–N↓ (NUS), der Spindichte-Differenz (SDD), Zustandsdichte (DOS) und Bader-Ladungen (BCs) wurde angewandt, um den Grund für nicht-monotone Variation der Gitterparameter und den durch Sauerstoffstapelung induzierten Phasenübergang zu erklären. Der Einfluss der Wahl des Austausch-Korrelations (XC)-Funktionals auf unsere

Ergebnisse wurde ebenfalls untersucht. Das SCAN-Funktional liefert vernünftige Vorhersagen in Über-einstimmung mit den experimentellen Daten. Wir fanden heraus, dass das Vorhandensein/Fe-hlen von Li-O-Attraktionen, Ladungen auf Übergangsmetalle (TMs) und O-Anionen, kooperative/kollektive Jahn-Teller (J–T)-Verzerrung und elektrostatische Wechselwirkungen Schlüsselfaktoren für die Steuerung der Gitterparameteränderung sind. Es konnte gezeigt werden, dass der durch O-Stapelung-induzierte Phasenübergang an der vollständig delithiierten Struktur, der bisher nicht gut verstanden wurde, durch elektrostatische Kräfte anget-rieben wird. Im zweiten Teil dieser Dissertation wurde ein ähnlicher Ansatz (durch Kombination von umfangreichen Coulomb Energie und DFT Rechnungen) wie bei der Untersuchung von NCM111 verwendet, um die kristallinen, atomaren und elektronischen Strukturen von NCM-811 bei verschiedenen Ladezuständen (Delithierung) zu bestimmen. Die elektronische Analyse von NUS, SDD, DOS und BCs wurde durchgeführt, um den Grund für die Änderung der Gitterparameter und die Phasenübergänge zu erklären. Zum ersten Mal konnte der Grund für den Phasenübergang von der hexagonalen zum monoklinen Struktur (H−M-Phasenüber-gang), bei halber Li-Konzentration erklärt werden. Der O-Stapel-induzierte Phasenübergang bei der vollständig delithiierten Struktur wurde hier ebenfalls im Detail interpretiert. Es wurde herausgefunden, dass der H−M-Phasenübergang auf die kollektive J−T-Verzerrung zurückzuführen ist, und dass der durch O-Stapelung-induzierte Phasenübergang durch die elektrostatische Wechselwirkung verursacht wird. Der dritte Teil dieser Dissertation befasste sich mit dem Effekt der Al-Dotierung auf die Leerstellenbildungsenergien von Li und O (d.h. die chemische Stabilität) in Ni-reichem NCM90505. Durch die Analyse der Li- und O-Leerstellen-Energien im lithiierten und delithiierten Zustand wurde der Grund für die im Vergleich zu undotiertem NCM höhere strukturelle Stabilität von Al-dotiertem NCM90505 (d.h. NCMA89) erklärt. Es wurde festgestellt, dass die starke Bindungsenergie der Al–O-Bindungen vorteilhaft für die strukturelle Stabilität von Ni-reichem NCM ist.

NIBs sind kosteneffizient und werden daher häufig untersucht. Eines der interessantesten Kathodenmaterialien für NIBs ist $NaMnO_2$ (NMO). Grund dafür ist die im Vergleich zu anderen Kathodenmaterialien höhere Energiedichte. Außerdem können durch Verwendung des reichlich vorhandenen Elements Mn die Kosten reduziert werden. Allerdings unterliegt NMO großen strukturellen Verän-derungen während des Zyklierens, was zu einem schnellen Kapazitätsverlust (d.h. einer kurzen Lebensdauer der Batterie) führt. Um den Grund für die großen strukturellen Veränderungen in NMO zu verstehen, wurde der Effekt der Fe-Dotierung auf die mechanische Stabilität von $Na_{0.67}Fe_xMn_{1-x}O_2$ durch Variation der Fe Anteile untersucht. Für verschiedene mögliche Konfigurationen mit Hilfe von DFT Berchnun-

gen untersucht, bei denen Mn-Plätze durch Fe-Dotierungen ersetzt werden, um die niedrigste Gesamtenergie zu finden. Auch im vierten Teil dieser Dissertation wurden Coulomb-Energie- und DFT-Berechnungen verwendet, um die günstigsten Anordnungen der Na-Ionen in $Na_{0.67}MnO_2$ zu finden. Die Änderung der Gitterparameter mit verschiedenen $U-J$-Werten die J–T-Verzerrung von $Na_{0,67}MnO_2$ bei verschiedenen Fe-Gehalten wurden simuliert und analysiert. Unsere Ergebnisse zeigen, dass Fe-dotiertes $Na_{0,67}MnO_2$ die J−T-Verzerrung unterdrücken kann, indem es die Längenunterschiede der axialen und äquatorialen Achse in MnO Oktaedern reduziert und somit die strukturelle Stabilität von $Na_{0,67}MnO_2$ verbessert. Diese Untersuchungen helfen uns, einen Einblick über die Auswirkungen eines steigenden Ni-Gehalts auf die atomaren und elektronischen Strukturveränderungen in NCM, sowie den Einfluss der Kationen-Dotierung auf die chemische und mechanische Stabilität von NCM- und NMO-Materialien zu erhalten. Unsere Ergebnisse weisen darauf hin, dass sich durch Substitution oder Dotierung die Ladungszustände der TMs verändern und dadurch die J−T-Verzerrungseffekte unterdrückt werden.

Contents

1 INTRODUCTION **1**

1.1 Lithium-ion Batteries . . . 3

1.1.1 Li_xCoO_2 . . . 5

1.1.2 Li_xNiO_2 . . . 7

1.1.3 Li_xMnO_2 . . . 9

1.1.4 Ternary oxides (Substitution of Co and Mn with Ni) . . . 11

1.1.4.1 $Li_xNi_{0.33}Co_{0.33}Mn_{0.33}O_2$ . . . 11

1.1.4.2 $Li_xNi_{0.8}Co_{0.1}Mn_{0.1}O_2$ . . . 14

1.1.4.3 Doping in NCM materials . . . 16

1.2 Sodium-ion Batteries . . . 17

1.2.1 Na_xMnO_2 . . . 19

1.2.1.1 Doping in $NaMnO_2$ . . . 20

2 OBJECTIVES **23**

3 THEORETICAL METHODS **25**

3.1 Quantum Mechanics based calculations . . . 25

3.1.1 Many-Body Problem . . . 25

3.1.1.1 Born-Oppenheimer Approximation . . . 26

3.1.1.2 Hartree-Fock Method . . . 28

3.1.1.3 Density-based Methods . . . 31

3.1.1.4 Thomas-Fermi-Dirac Model 31
3.1.2 Density functional Theory 32
3.1.2.1 Hohenberg-Kohn Theorems 32
3.1.2.2 Kohn-Sham Ansatz 34
3.1.2.3 Exchange-Correlation functional 36
3.1.2.3.1 Local Density Approximation 37
3.1.2.3.2 Generalized-gradient Approximation 38
3.1.2.3.3 Meta-Generalized-gradient Approximation . . . 39
3.1.2.4 Further Corrections on Exchange-Correlation functional . 40
3.1.2.4.1 Correlation Corrections 40
3.1.2.4.2 Dispersion Corrections 42
3.1.2.5 Periodic Systems 43
3.1.2.5.1 Bravais lattice 43
3.1.2.5.2 Boundary Conditions 44
3.1.2.5.3 Bloch's Theorem 44
3.1.2.6 Computational Approximations 45
3.1.2.6.1 **k**-Points Sampling 45
3.1.2.6.2 Plane waves 46
3.1.2.6.3 Pseudopotential Approximation 46
3.2 Electrostatic energy calculation 48
3.2.1 Ewald Summation 48

4 PUBLICATIONS **51**

4.1 Publication M1 52
4.2 Publication M2 70
4.3 Publication M3 94

4.4 Publication M4 119

5 SUMMARY **147**

ACKNOWLEDGEMENTS **155**

BIBLIOGRAPHY **169**

List of Figures

1.1 Schematic view of a typical commercialized LIB during charging. A SIB has similar a mechanism. Li, Co, O, and C are in green, blue, red, and black, respectively. 4

3.1 Illustration of all-electron (solid lines) and pseudo-electron (dashed lines) potentials and their wave functions. r_c is cutoff radius [134]. 47

4.1 Graphical Abstract [140]. 52

4.2 Graphical Abstract [141]. 70

4.3 Graphical Abstract [142]. 94

4.4 Graphical Abstract [143]. 119

5.1 Calculated variation of lattice parameters and unit cell volume of Li_xNCM111 with delithiation using different XC functionals [140]. 148

5.2 Top views of the Ni/Ni layer of NCM811 for different Li concentrations [141]. 149

5.3 Side views of atomic structures and calculated oxygen vacancy formation energy for the cathodes [142]. 150

5.4 Calculated axial and averaged equatorial bond lengths for the most favorable structures of $Na_{0.67}Fe_xMn_{1-x}O_2$ [143]. 151

List of Publications

M1 - L.-Y. Kuo, O. Guillon and P. Kaghazchi

"On the origin of non-monotonic variation of the lattice parameters of $LiNi_{1/3}Co_{1/3}Mn_{1/3}O_2$ with lithiation/delithiation: a first-principles study"

J. Mater. Chem. A, **8**, 13832 (2020)

DOI: 10.1039/D0TA02319A

M2 - L.-Y. Kuo, O. Guillon and P. Kaghazchi

"Origin of structural phase transitions in Ni-rich $LiNi_{0.8}Co_{0.1}Mn_{0.1}O_2$ with lithiation/delithiation: a first-principles study"

ACS Sustain. Chem. Eng., **9**, 7437 (2021)

DOI: 10.1021/acssuschemeng.0c07675

M3 - U.-H. Kim, L.-Y. Kuo, P. Kaghazchi, C. S. Yoon and Y.-K. Sun

"Quaternary Layered Ni-Rich NCMA Cathode for Lithium-Ion Batteries"

ACS Energy Lett., **4**, 576 (2019)

DOI: 10.1021/acsenergylett.8b02499

M4 - J. U. Choi, Y. J. Park, J. H. Jo, L.-Y. Kuo, P. Kaghazchi and S.-T. Myung

"Unraveling the Role of Earth-Abundant Fe in the Suppression of Jahn–Teller Distortion of P'2-Type $Na_{2/3}MnO_2$: Experimental and Theoretical Studies"

ACS Appl. Mater. Interfaces, **48**, 40978 (2018)

DOI: 10.1021/acsami.8b16522

Additional Publications

A1 - L. Yang, L.-Y. Kuo, J. M. López del Amo, P. K. Nayak, K. A. Mazzio, S. Maletti, D. Mikhailova, L. Giebeler, P. Kaghazchi, T. Rojo and P. Adelhelm
"Structural aspects of P2-type $Na_{0.66}Mn_{0.6}Ni_{0.2}Li_{0.2}O_2$ (MNL) stabilization by lithium defects as a cathode material for sodium-ion batteries"
accepted by *Adv. Funct. Mater.*

A2 - C.-J. Huang, J.-H. Cheng, W.-N. Su, P. Partovi-Azar, L.-Y. Kuo, M.-C. Tsai, M.-H. Lin, S. P. Jand, T.-S. Chang, N.-L. Wu, P. Kaghazchi, H. Dai, P. M. Bieker and B.-J. Hwang
"Origin of Shuttle-free Sulfurized Polyacrylonitrile in Lithium-sulfur Batteries"
J. Power Sources, **492**, 229508 (2021)
DOI: 10.1016/j.jpowsour.2021.229508

A3 - U.-H. Kim, G.-T. Park, B.-K. Son, G. W. Nam, J. Liu, L.-Y. Kuo, P. Kaghazchi, C. S. Yoon and Y.-K. Sun
"Heuristic solution for achieving long-term cycle stability for Ni-rich layered cathodes at full depth of discharge"
Nat. Energy, **5**, 860 (2020)
DOI: 10.1038/s41560-020-00693-6

A4 - A. Bakavets, Y. Aniskevich, O. Yakimenko, J. HyeonJo, E. Vernickaite, N. Tsyntsaru, H. Cesiulis, L.-Y. Kuo, P. Kaghazchi, G. Ragoisha, S.-T. Myung and E. Streltsov
"Pulse electrodeposited bismuth-tellurium superlattices with controllable bismuth content"
J. Power Sources, **450**, 227605 (2020)
DOI: 10.1016/j.jpowsour.2019.227605

A5 - X. Yang, X. Gao, Q. Sun, S. P. Jand, Y. Yu, Y. Zhao, X. Li, K. Adair, L.-Y. Kuo, J. Rohrer, J. Liang, X. Lin, M. N. Banis, Y. Hu, H. Zhang, X. Li, R. Li, H. Zhang, P. Kaghazchi, T.-K. Sham and X. Sun

"Promoting the Transformation of Li_2S_2 to Li_2S: Significantly Increasing Utilization of Active Materials for High-Sulfur- Loading Li-S Batteries"

Adv. Mater., **31**, 1901220 (2019)

DOI: 10.1002/adma.201901220

A6 - Y. Liu, Q. Sun, Y. Zhao, B. Wang, P. Kaghazchi, K. R. Adair, R. Li, C. Zhang, J. Liu, L.-Y. Kuo, Y. Hu, T.-K. Sham, L. Zhang, R. Yang, S. Lu, X. Song and X. Sun

"Stabilizing the Interface of NASICON Solid Electrolyte against Li Metal with Atomic Layer Deposition"

ACS Appl. Mater. Interfaces, **37**, 31240 (2018)

DOI: 10.1021/acsami.8b06366

A7 - K. J. Park, H. G. Jung, L.-Y. Kuo, P. Kaghazchi, C. S. Yoon, Y. K. Sun

"Improved Cycling Stability of Li[Ni0.90Co0.05Mn0.05]O2 Through Microstructure Modification by Boron Doping for Li-Ion Batteries"

Adv. Energy Mater., **8**, 1801202 (2018)

DOI: 10.1002/aenm.201801202

A8 - A. Heckmann, P. Meister, L.-Y. Kuo, M. Winter, P. Kaghazchi, T. Plackea

"A route towards understanding the kinetic processes of bis(trifluoromethanesulfonyl) imide anion intercalation into graphite for dual-ion batteries"

Electrochim. Acta, **284**, 669 (2018)

DOI: 10.1016/j.electacta.2018.07.181

A9 - Y. Zhao, X. Yang, L.-Y. Kuo, P. Kaghazchi, Q. Sun, J. Liang, B. Wang, A. Lushington,

R. Li, H. Zhang, X. Sun

"High Capacity, Dendrite-Free Growth, and Minimum Volume Change Na Metal Anode"

Small, **14**, 1703717 (2018)

DOI: 10.1002/smll.201703717

A10 - L.-Y. Kuo, A. Moradabadi, H.-F. Huang, B.-J. Hwang and P. Kaghazchi

"Structure and ionic conductivity of the solid electrolyte interphase layer on tin anodes in Na-ion batteries"

J. Power Sources, **341**, 107 (2017)

DOI: 10.1016/j.jpowsour.2016.11.077

A11 - J.-H. Cheng, Y.-H. Chen, Y.-S. Yeh, S. Hy, L.-Y. Kuo, B.-J. Hwang

"Enhancement of Electrochemical Properties by Freeze-dried Graphene Oxide via Glucose-assisted Reduction"

Electrochimica Acta, **197**, 146 (2016)

DOI: 10.1016/j.electacta.2015.12.116

Chapter 1

INTRODUCTION

Battery is one of the most important energy storage device, which can convert the chemical energy to electricity through electrochemical reactions and vice versa [1]. The main parts of a battery are two electrodes called positive and negative electrodes, and an electrolyte, which permits internal ions transport. During discharging (*i.e.* lithiation) electrons transfer from negative electrode (anode) to positive electrode (cathode) via external circuit along with the internal ions transport from anode to cathode through electrolyte to satisfy charge balancing. Thus, the active material of anode is oxidized and that of cathode is reduced upon the discharge process. The reverse reactions take place during charge process (*i.e.* delithiation).

Batteries are classified generally to primary (non-rechargeable) and secondary (rechargeable) [2]. Primary batteries, *e.g.* alkaline batteries are discarded after a single usage. They provide high internal resistances and low cell voltages, which lead to low current loadings. For this reason, they are only suitable for light load devices such as clock and flashlight. Secondary batteries, *e.g.* lithium (Li)-ion and sodium (Na)-ion batteries (LIBs and SIBs) can be recharged, which make them more economical and practical to use compared to primary batteries. Moreover, secondary batteries provide higher power densities with larger cell voltages and higher load currents compared to primary batteries. Because of these advantages, the rechargeable batteries, especially the LIBs are more interesting in large-scale mobile application such as electric vehicles (EVs). In LIBs, metallic Li possess higher elec-

trode potential (-3.04 V vs. standard hydrogen electrode, S.H.E) and lighter atomic weight, which lead to higher energy densities compared to other types of secondary batteries such as lead-acid and nickel-metal hydride (Ni-MH) batteries [3, 4]. Recently, the SIBs attract researchers' interests as well because of their relatively high electrode potential compared to S.H.E (-2.71 V) and lower cost of Na than Li element. Although the energy density of SIBs is generally lower than that of LIBs due to the large atomic weight of Na in SIBs, the cheaper price of Na is beneficial for cost efficiency and thus can be used in large-scale grid applications.

To make secondary batteries (*e.g.* LIBs) applicable for large-scale applications such as EVs, the following parameters should be improved: (i) power density, (ii) energy density, (iii) life time, (iv) safety, and (v) cost. However, to store renewable energies such as solar energy by secondary batteries (*e.g.* SIBs), the improvements on parameters (iv) and (v) should be achieved. To meet all the aforementioned demands, in particular the cathode materials in LIBs and SIBs should be improved in terms of their ionic/electronic conductivity, capacities and voltages as well as chemical stability and cost efficiency. One of the problem on the way for developing the high-performing cathode materials is their large structural changes, resulting in the capacity fading and low voltages during charge/discharge processes. Substitution and doping in the cathode materials are effective approaches to improve their structural stability. To understand the reason behind the large structural changes, *i.e.* non-monotonic variation of lattice parameters and phase transitions in cathode materials, in this dissertation, we studied the structural stability (*i.e.* mechanical stability) of ternary oxide cathode materials, namely $\mathrm{LiNi}_a\mathrm{Co}_b\mathrm{Mn}_{1-a-b}\mathrm{O}_2$ (NCM$ab1{-}a{-}b$) for LIBs. The influence of increasing amount of Ni contents on mechanical stability of NCM and cation doping in NCM's lattice on chemical stability were also investigated. Moreover, we studied the effect of lattice doping on mechanical stability of NaMnO_2 (NMO) for SIBs. In the next section, the LIBs and

SIBs will be discussed in details. The reason for studying these cathode materials and their electrochemical properties are also discussed in the following.

1.1 Lithium-ion Batteries

The concept of rechargeable LIBs originates from the "rocking chair" battery proposed by Armand *et al.* in the 1970s [5]. In this system, graphite intercalation compounds are used to replace the lithium metal as anode material for the safety reason. The Li ions are reversibly inserted into and extracted from host electrodes. Later, Goodenough *et al.* [6] used Li cobalt oxide ($LiCoO_2$), which is a layered transition-metal oxide (TMO_2) as a cathode material for LIBs. It was commercialized by Sony in 1991 [7]. Since then, LIBs have been widely applied in portable electronic devices. The electrochemical reactions in a LIB consisting of a layered TMO_2 as cathode material and graphite as anode material are

$$\begin{aligned}
&\mathrm{Cathode}: \mathrm{Li(TM)O_2} \underset{\text{discharge}}{\overset{\text{charge}}{\rightleftarrows}} \mathrm{Li_{1-x}(TM')O_2} + x\mathrm{Li^+} + x\mathrm{e^-} \\
&\mathrm{Anode}: n\mathrm{C} + x\mathrm{Li^+} + x\mathrm{e^-} \underset{\text{discharge}}{\overset{\text{charge}}{\rightleftarrows}} \mathrm{Li}_x\mathrm{C}_n \\
&\mathrm{Overall}: n\mathrm{C} + \mathrm{Li(TM)O_2} \underset{\text{discharge}}{\overset{\text{charge}}{\rightleftarrows}} \mathrm{Li}_x\mathrm{C}_n + \mathrm{Li_{1-x}(TM')O_2}.
\end{aligned} \tag{1.1}$$

In Eq. 1.1, TM′ denotes a change in the oxidation state of TM during charge process (*i.e.* delithiation). TM can be cobalt (Co), nickel (Ni) or manganese (Mn) etc. In addition to Eq. 1.1, the side chemical reactions can occur between the surface of electrode with electrolyte and form a new layer on the surface of cathode and/or anode. This is the so-called solid electrolyte interphase (SEI) layer. The mechanism of charging in LIBs is shown in Fig. 1.1.

In LIBs, cathode materials have lower Li-ion storage capacities than anode materials, for example $LiCoO_2$: 270 mAh/g $<$ LiC_6: 372 mAh/g or $Li_{4.4}Si$: 4299 mAh/g [8, 9]. This means that cathodes suppress the practical energy density of LIBs. Thus, a comprehensive understanding of charge/discharge process in cathode materials is crucial for developing

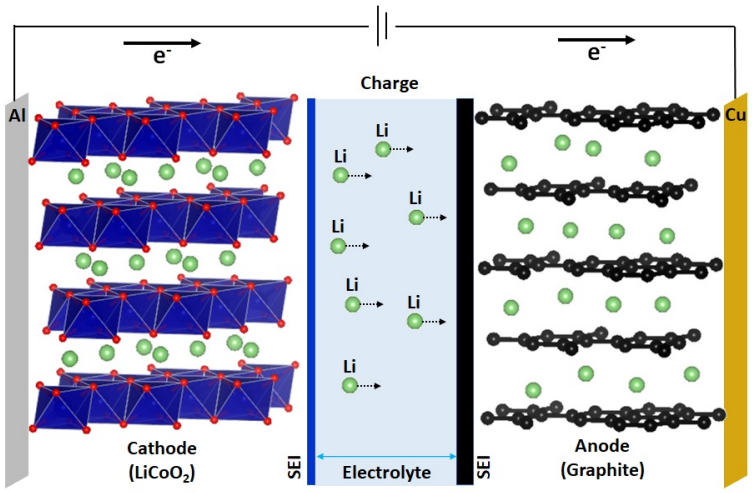

Figure 1.1: Schematic view of a typical commercialized LIB during charging. A SIB has similar a mechanism. Li, Co, O, and C are in green, blue, red, and black, respectively.

high-performing LIBs. Cathode materials in LIBs can be classified to layered (*e.g.* $LiCoO_2$), spinal (*e.g.* $LiMn_2O_4$), and polyanionic (*e.g.* $LiFePO_4$) materials based on their structures. Among them, layered materials are the most interesting ones because they possess higher theoretical capacities than spinal and polyanionic materials [10]. Conventional layered materials are mononary oxides such as $LiCoO_2$ (LCO), $LiNiO_2$ (LNO), and $LiMnO_2$ (LMO). However, they suffer from large volume changes, phase transitions, and thermal instability during delithiation/lithiation, which result in a large capacity fading and safety problem. Due to the drawbacks of the mononary oxides, combining two or three TMs to form the binary or ternary oxides have been extensively studied. Ternary oxides, *e.g.* $LiNi_aCo_bMn_{1-a-b}$, NCM$ab(1-a-b)$ have especially shown the improvement in their electrochemical performances [11, 12]. With various amounts of Ni, Co, and Mn contents, NCM$ab(1-a-b)$ show different electrochemical properties due to the contribution of each element and the synergistic effect among them. NCM materials with high Ni contents have been proved to increase capacity [13]. Thus, Ni-rich NCM materials, for example NCM811 are highly interesting for EVs [14]. However, the poor structural stability of Ni-rich NCM at high charge states causes large capacity fading. To achieve high capacity upon cycling, it is important to understand the reason behind the structural changes in NCM materials during charge/discharge

processes. Thus, in this dissertation, the origin of the structural changes (*i.e.* mechanical stability) in NCM111 and NCM811 were studied. Moreover, we studied the influence of lattice doping on chemical stability of Ni-rich NCM. The next section will discuss the electrochemical properties and structural changes (*i.e.* lattice parameters change and phase transitions) of LCO, LNO, and LMO followed by the NCM111, NCM811 and the effect of lattice doping on structural stability of NCM materials.

1.1.1 $\mathbf{Li}_x\mathbf{CoO}_2$

$LiCoO_2$ (LCO) is considered as a prototype of layered cathode materials for LIBs, because it was the first one that has been widely used as a Li-ion intercalated electrode in the market. Layered LCO (rhombohedral, space group $R\bar{3}m$) has a O3 phase where the oxygen layers stack in an $(ABC)_n$ sequence with Li and TM ions occupying the octahedral sites alternately between the oxygen planes [15]. Due to the hexagonal (H) unit cell of LCO, the O3 phase is also labeled to H1 phase as an initial phase during charge process (*i.e.* delithiation) [16, 17]. LCO has a theoretical capacity of 270 mAh/g with an average cell voltage of 4.0 V vs. Li electrode (Li/Li^+), which can provide an energy density higher than 800 Wh/kg [18]. However, in practice, LCO provides 140 mAh/g capacity as charging voltage is limited to 4.1 V, because only half of Li ions can be reversible cycled without losing capacity [19]. Structural damage on the surface has been observed by using transimission electron microscopy (TEM) when LCO is charged beyond its practical voltage [20]. This can be attributed to large volume changes and phase transitions upon delithiation/lithiation. The X-ray diffractometry (XRD) [21] and cyclic voltamogram (CV) [22, 23] have been used to analyze the lattice parameters and phase transitions during cycling. Ménétrier *et al.* [24] reported that the lattice parameter *a* decreases and the lattice parameter *c* increases when $1.0 \geq x \geq 0.70$ for Li_xCoO_2 by using XRD measurement. They proposed that the contraction of *a* is due

to the oxidation of Co cations. However, the expansion of c is because of the weakening of interlayer cohesion. Amatucci *et al.* [25] and Laubach *et al.* [26] observed by XRD that the lattice parameter c increases to a maximum value at $x \approx 0.50$ and then it decreases, being more significant at very low Li contents. By investigating CV curves with *in-situ* XRD, Reimers *et al.* [27] reported hexagonal to monolicnic (H $\rightarrow$ M) phase transition at $x = 0.50$. When $x \rightarrow 0$, Li_xCoO_2 undergoes another transition from O3 to O1 phase [28]. In the O1 phase, the oxygen layers stack in an $(AB)_n$ sequence, where the repeated unit is only one TMO_2 sheet rather than 3 in the O3 phase [29]. To analyze the TM$-$O bond lengths, oxidation state of Co and electron transfer, extended X-ray absorption fine structure (EXAFS) [30] and X-ray photoelectron spectroscopy (XPS) [22] are performed in experiment. However, without the help of first-principles studies, the origin of the atomic and electronic structures change of the materials is difficult to be fully understood through experiments.

Density functional theory (DFT) method is one of the most popular first principles approaches to investigate the variation of atomic and electronic structures of cathode materials. For example, Koyama *et al.* [31] applied DFT method with local density approximation (LDA) [32] to simulate the lattice parameters change of layered cathode materials during charging (*i.e.* delithiation). For Li_xCoO_2, they found that the lattice parameter a decreases and the lattice parameter c increases when $1.0 \geq x \geq 0.33$, however the value of a increases and c decreases when $0.33 > x$. Chakraborty *et al.* [33] used different exchange-correlation (XC) functionals, namely Perdew-Burke-Ernzerhof (PBE) [34], PBE with U parameters in Dudarev́'s method (PBE+U) [35], and strongly constrained and appropriately normed (SCAN) [34] functionals for DFT calculations to predict the properties of LCO, LNO, and LMO. They also considered dispersion corrections using Grimme's D3 method [36] for PBE+U and SCAN functionals. Their results show the importance of choosing the XC functionals for different materials. They indicated that SCAN and SCAN+D3 functionals

can predict the variation of *a* and *c* better than PBE and PBE+*U* functionals. The band gap, magnetic moment and voltage profiles for LCO, LNO, and LMO are also predicted in their report. By using DFT-LDA calculations, Van der Ven *et al.* [29] indicated that O1 phase is more favorable than O3 phase in CoO_2 structure. However, instead of H $\rightarrow$ M phase transition, they proposed an intermediate H1-3 (O3/O1) phase that consists of alternating O3 and O1 stacking during partial delithiation/lithiation. To understand the electronic configurations, oxidation states of TMs, and charge transfer, the density of states (DOS), spin density differences (SDD) and Bader charges (BCs) are analyzed by theoreticians [31, 33]. LCO has been used and studied for many years, however, its low capacity and the high cost of Co metal in LCO hinder its large-scale application in EVs. $LiNiO_2$ (LNO) is considered to replace LCO due to the fact that Ni element can provide high capacity and it is inexpensive. However, LNO undergoes chemical reactions with electrolyte on its surface and large volume changes at high states of charge that cause safety problem and large capacity lose with cycling. Substitution of Mn and/or Co for Ni is one of the most practical approach to improve its thermal stability and structural changes during delithiation/lithiation. Thus, the aim of this dissertation was to study the origin of the structural changes (*i.e.* mechanical stability) in ternary oxides (*i.e.* Ni-Co-Mn, NCM) as well as the effect of lattice doping on chemical stability of NCM. In the next section, the electrochemical properties and structural stability of LNO will be discussed in details.

1.1.2 $\mathbf{Li}_x\mathbf{NiO}_2$

$LiNiO_2$ (LNO) consists of the cheaper Ni element than that of LCO with Co. This can reduce the cost of LIBs for large-scale manufacturing. Layered LNO has the same crystal structure as LCO (*i.e.* $R\bar{3}m$) with the O3 stacking. It has a theoretical capacity of 275 mAh/g [37] with an average cell voltage of 3.8 V vs. Li/Li^+, which is similar to LCO [38]. However, unlike

LCO, the non-stoichiometric $Li_{1-x}Ni_{1+x}O_2$ is formed because partial Ni cations possess 2+ instead of 3+, showing that Ni is a mixed-valence state during synthesis. Since Ni^{2+} (0.69 Å) have similar size to Li^+ (0.76 Å), Ni^{2+} prefer to occupy Li^+ sites, resulting in the decrease in the theoretical capacity [39, 40]. LNO can practically deliver a reversible capacity of 200 mAh/g with operating voltage at 4.15 V vs. Li/Li^+ as more Li ions can be extracted from LNO than those from LCO [14]. The reason why a large amount of Li ions can be extracted from LNO is because Ni cations involve redox reactions at e_g orbitals rather than t_{2g} orbitals. This phenomenon leads to lower deintercalation voltage of Ni than Co cations [39]. LNO is thus considered as an alternative cathode material for LIBs. However, the chemical reactions on the surface of LNO with electrolyte cause severe safety issue [38]. Substitution of Mn for Ni has been discovered to suppress this problem [41]. In addition to safety problem, LNO suffers from larger volume changes compared to LCO, which causes extensive capacity fading during cycling [42]. Partial Ni replaced by Co [39] or Al [43] have been found to improve the structural stability. Cho *et al.* [44] observed by XRD that the lattice parameter a monotonically decreases when $1.0 \geq x \geq 0.20$ for Li_xNiO_2. However, the lattice parameter c increases for $1.0 \geq x \geq 0.50$, and then it dramatically decreases for $0.50 > x \geq 0.20$. A number of phase transitions have also been investigated by them using XRD and CV measurements. In their observations, LNO experiences H1 $\rightarrow$ M $\rightarrow$ H2 $\rightarrow$ H3 (O1) phase transitions. Li *et al.* [45] also showed multiple phase transitions during charge/discharge processes by using *in-situ* XRD. The TM$-$O bond lengths and the Jahn-Teller (J$-$T) distortion of Ni cations in LNO have been investigated with (E)XAFS experiments by Nakai *et al.* [46] and Rougier *et al.* [47].

Computations of atomic and electronic configurations of LNO have been investigated as well. Koyama *et al.* [31] used DFT-LDA calculations to explore the structural changes of LNO. They showed continuously decreases in the lattice parameter a when $1.0 \geq x \geq 0$

for Li_xNiO_2. However, the lattice parameter *c* increases for $1.0 \geq x \geq 0.33$ and decreases for $0.33 > x \geq 0$. The larger contraction of *c* in LNO compared to that in LCO is shown in their results, which agrees to the experimental data [44]. The changes in *a* and *c* have been reported by Chakraborty *et al.* [33] with SCAN and SCAN+D3 functionals as well. The DOS plots and magnetic moment of LCO, LNO and LMO before cycling have been shown in their results. Radin *et al.* [48] used DFT to study the J−T effect and phase transitions in LNO. They indicated that the ordering of the J−T active Ni cations determines the long-range collective/non-collective distortion in LNO. However, they could not explain the reason for LNO with hexagonal symmetry at the full lithiated structure, where no collective J−T distortion has been observed by experiments [47, 49]. This question is unanswered so far. Since substitution of Co and Mn with Ni (to form ternary NCM materials) and lattice doping in NCM can improve the electrochemical performances of LNO, in this dissertation, we calculated and analyzed the crystal, atomic and electronic structures of NCM materials during delithiation/lithiation to explain the reason behind their structural changes, in particular the structural phase transitions. We studied the structural stability of NCM111 and NCM811 as well as the Al-doped NCM90505 (*i.e.* NCMA89). The next section is focusing on the electrochemical properties and structural stability of $LiMnO_2$ (LMO). Later, the ternary NCM materials *i.e.* NCM111 and NCM811, which combine the advantages of LCO, LNO, and LMO will be discussed in details.

1.1.3 Li_xMnO_2

$LiMnO_2$ (LMO) costs even less than LNO due to abundance of Mn element, and it is less toxic compared to LCO and LNO [50]. LMO is considered to be an interesting layered cathode material. Layered LMO with monoclinic (space group *C*2/*m*) or orthorhombic (space group $Pmnm$) symmetry have been investigated [51, 52]. Monoclinic LMO (*m*-LMO) has

been found to have second and third phases, namely spinel and orthorhombic phases co-exist in the crystal structure. The presence of multi-phases causes *m*-LMO to have low theoretical capacity [53]. Orthorhombic LMO (*o*-LMO) can in principle provide a high theoretical capacity of 285 mAh/g with an average cell voltage of 3.3 V vs. Li/Li^+. Its practical capacity is, however 150 mAh/g with a voltage of 4.8 V vs. Li/Li^+ [14, 38]. The large irreversible capacity of *o*-LMO is due to a transition from the layered to spinal phase, where Mn cations tend to migrate into the Li layer upon cycling. The spinel crystal structure has been observed through TEM by Shao-Horn *et al.* [53]. They also investigated the layered $\rightarrow$ spinel phase transition by XRD and CV measurements. Hwang *et al.* [51] have analyzed the electronic configurations and J$-$T distortion of Mn cations during charging/discharging by EXAFS and X-ray absorption spectroscopy (XAS) experiments. Experimental studies on phase transition have been explored, however, the lattice parameters change of layered LMO is unclear in experiments. To investigate the structural stability of LMO, it is important to understand its volume change.

Computation of lattice parameters change by Koyama *et al.* [31] (using DFT-LDA) showed that the lattice parameter *a* decreases when $1.0 \geq x \geq 0$ for *m*-Li_xMnO_2. However, the lattice parameter *c* decreases for $1.0 \geq x \geq 0.67$ and increases for $0.67 > x \geq 0.33$. It further decreases for $0.33 > x$. The contraction of *c* at high-delithiated states in *m*-LMO is smaller than that in LCO and LNO. Chakraborty *et al.* [33] applied different XC functionals (*i.e.* PBE, PBE+U, and SCAN functionals) for DFT calculations and reported the lattice parameters change of *o*-LMO structure. In their results, the lattice parameter *a* monotonically increases for $1.0 \geq x \geq 0.0$, while the lattice parameter *c* initially increases for $1.0 \geq x \geq 0.5$ and decreases for $0.5 > x$ with all XC functionals. The volume change of LNO has been found greater than LCO and LMO when large amount of Li are extracted. However, LMO is unavailable in practical application due to its poor reversibility during cycling [54]. The

reason for the short calendar life is because Mn cations in LMO tend to react with electrolyte materials. This problem can be alleviated through a substitution of Mn by Co [55] or Ni [39] to change the oxidation state of Mn cations. The oxidation of Mn from 3+ to 4+ in $LiNi_{0.5}Mn_{0.5}O_2$ have been reported by Koyama *et al.* [14] using local spin density approximation (LSDA). The effect of cationic substitution will be discussed in details in the section of Ni-Co-Mn (NCM) ternary oxides. Layered LMO's electronic structures have been investigated by Chakraborty *et al.* [33] and Wang *et al.* [52] using DOS, SDD, magnetic moments and BCs analysis.

1.1.4 Ternary oxides (Substitution of Co and Mn with Ni)

To combine the advantages of LCO, LNO, and LMO to achieve a reasonable rate capability, energy density, and thermal stability, NCM$ab(1-a-b)$ materials have been proposed and synthesized. The synergistic effect of these three TMs with different molar ratio of Ni, Co, and Mn causes NCM systems to show superior electrochemical performances compared to LCO, LNO and LMO.

1.1.4.1 $\mathbf{Li}_x\mathbf{Ni}_{0.33}\mathbf{Co}_{0.33}\mathbf{Mn}_{0.33}\mathbf{O}_2$

Among various NCM materials, NCM111 (or NCM333) is one of the most common form of NCM, and has been commercialized in the battery market in recent years [11]. NCM111 and other NCM materials have the hexagonal ($R\bar{3}m$) symmetry with O3 stacking similar to LCO and LNO. Layered NCM111 has a theoretical capacity of 280 mAh/g with an average voltage of $\sim$4.2 V. It shows higher structural stability than the commercialized LCO. This is because the cracking of NCM111 microstructures, which leads to their voltage and capacity fading occurs at higher levels of delithiation/lithiation compared to LCO [13, 38, 56, 57]. However, Ohzuku *et al.* [58] observed that practical reversible capacity of NCM111 is 150 mAh/g

with an operating voltage at 4.2 V vs. Li/Li^+, which is still insufficient to be adopted in EVs application. The reason behind the microstructure fracture of NCM111 is attributed to an anisotropic lattice parameters change and O3 $\rightarrow$ O1 phase transition at high level of delithiation/lithiation. By using XRD measurement, Li *et al.* [59] and Choi *et al.* [60] reported that the lattice parameter a decreases when $1.0 \geq x \geq 0.30$ for $Li_xNi_{0.33}Co_{0.33}Mn_{0.33}O_2$ (Li_xNCM111). However, the lattice parameter c increases when $1.0 \geq x \geq 0.50$ and decreases when $0.50 > x \geq 0.30$. Moreover, Choi *et al.* [60] showed that the lattice parameter a increases and the lattice parameter c dramatically decreases when $0.30 > x$. The O3 $\rightarrow$ O1 phase transition has been reported by them through XRD [60]. The variation of a and c cause unit cell volume to contract slightly for $1.0 \geq x \geq 0.30$ and strongly for $0.30 > x$. Koerver *et al.* [61] have studied the volume change of LCO and NCM systems upon cycling. They found that Li_xCoO_2 shows larger volume change at $x \approx 0.50$ in comparison to other NCM materials such as Li_xNCM111. However, when further Li ions are extracted, the contraction of unit cell volume for Li_xNCM111 are observed, which causes structure cracking. To understand the mechanism of lattice parameters change in NCM111, Li *et al.* [59] analyzed the TM$-$TM distance and oxidation state of TMs with cycling by performing EXAFS and XANES. They indicated that the contraction of a is because of the delithiation-induced oxidation of TMs, which reduces their ionic radii. However, the expansion of a for $0.30 > x$ has not been understood. The expansion of c is usually interpreted as a result of increasing electrostatic O$-$O repulsion with Li ions extraction, which results from the weakening of screening of O charge by Li ions during delithiation [29,57,62]. However, the contraction of c for $0.50 > x$ has not been fully explained. The most common belief is the charge changes on O anions together with TMs for charge-balancing at low Li contents that weakens O$-$O repulsion, leading to the contraction of c [63]. The variation of charges for O anions and the stronger TM$-$O bonds (*i.e.* larger hybridization of TM$-$O orbitals) [64] during delithiation

have been proposed by theoreticians.

DFT calculations have also been applied to simulate the lattice parameters change in NCM111. For example, Koyama *et al.* [14] using DFT-LDA calculations found that the lattice parameter a decreases when $1.0 \geq x \geq 0.33$ and increases when $0.33 > x \geq 0$ for Li_xNCM111. However, c increases for $1.0 \geq x \geq 0.33$ and decreases for $0.33 > x \geq 0$. Hwang *et al.* [64] used DFT-PBE calculations and found that the lattice parameter a decreases when $1.0 \geq x \geq 0.50$, then it increases when $0.50 > x > 0$. The size of c increases for $1.0 \geq x \geq 0.33$ and decreases when $0.33 > x$. Min *et al.* [65] used DFT-PBE calculations to study NCM materials with different Ni contents. They showed that the value of a decreases for $1.0 \geq x \geq 0.35$ and then it increases for $0.35 > x \geq 0$. Moreover, they proposed that the experimental results can be reproduced only by considering a layer-by-layer Li extraction. This theory, however, has not been confirmed so far. To further understand the electronic structures of NCM111, DOS, magnetic moment and BCs are analyzed with delithiation/lithiation [64, 66]. By DOS plots, Hwang *et al.* [64] indicated that Li ions extraction leads to the increasing in the hybridization of the TM$-$O orbitals (more covalency). However, the reason for the lattice parameters change and phase transitions of NCM111 during cycling have not been explained so far. In this dissertation, we combined an extensive set of electrostatic (Coulomb energy) and DFT calculations to predict the non-monotonic lattice parameters change of LixNCM111 at various levels of delithiation x. By analyzing crystal, atomic and electronic structures, we explained the reason behind the variation of lattice parameters of NCM111 with delithiation/lithiation. The O3 $\rightarrow$ O1 phase transition at low Li concentration was also explained in this dissertation. In addition to NCM111 material, we studied Ni-rich NCM811 because Ni-rich NCM systems can provide a higher capacity than the one with low Ni contents. However, NCM811 suffers from larger structural changes than NCM111 at low Li concentration, which leads to capacity fading during cycling. Un-

derstanding of the origin of the structural changes (*i.e.* mechanical stability) in NCM811 is helpful for improving the reversible capacity of it upon delithiation/lithiation. In the next section, we will discuss the electrochemical properties and structural changes in NCM811 in details.

1.1.4.2 $\mathbf{Li}_x\mathbf{Ni}_{0.8}\mathbf{Co}_{0.1}\mathbf{Mn}_{0.1}\mathbf{O}_2$

To improve the energy density, Ni-rich NCM (*i.e.* $a > 0.5$) materials, *e.g.* NCM811 have been explored and developed due to the fact that NCM materials' capacity grows when Ni contents increases. Layered NCM811 ($R\bar{3}m$) has a theoretical capacity of higher than 200 mAh/g at operating voltage of 4.6 V vs. Li/Li$^+$ [12, 67]. However, its practical capacity is $\sim$200 mAh/g with an average voltage of $\sim$4.3 V vs. Li/Li$^+$ [15]. The reason for the significant capacity fading of NCM811 is due to the structural instability at high charge voltage. Microcracks in NCM811 after initial charging at 4.3 V have been observed using scanning electron microscopy (SEM) by Kim *et al.* [68]. Larger lattice parameters change of NCM811 compared to that of NCM111 upon delithiation/lithiation has been reported by Noh *et al.* [13] and Biasi *et al.* [57] using XRD measurement. Moreover, Noh *er al.* [13] analyzed CV and found several redox peaks of NCM811 during cycling. These peaks are related to H1 $\rightarrow$ M $\rightarrow$ H2 $\rightarrow$ H3 phase transitions, which are similar to those in LNO. To gain more insight into the mechanism of the variation of *c* during charging/discharging, Kondrakov *et al.* [12] analyzed the intralayer (O$-$TM$-$O layer) and interlayer (O$-$Li$-$O layer) distances through XRD. Using XAS instrument, they indicated that the O$-$TM$-$O layers shrink monotonically due to continuous TMs oxidation. However, the non-monotonic variation of O$-$Li$-$O layers is because of the charge changes on Ni and O ions. To further confirm their experimental results, they applied DFT-PBE calculations to simulate the Bader charges (BCs) for Ni and O. In their results, the oxidation of O anions is found with delithiation. They indicated that this leads to the contraction of O$-$Li$-$O layers as well as of the value of *c* at high level of

delithiation.

DFT calculations were applied by Min *et al.* [65] and Liang *et al.* [69] to simulate the change in lattice parameters of NCM with Ni contents using PBE and PBE+U functional, respectively. Min *et al.* [65] indicated that the lattice parameter a decreases for $1.0 \geq x \geq 0.20$, while it slightly increases for $0.20 > x \geq 0$. Both of them reported that the lattice parameter c increases for $1.0 \geq x \geq 0.25$, and then it decreases for $0.25 > x$. However, Dixit *et al.* [15] reported that the non-monotonic behavior of c in Ni-rich NCM with delithiation can be only reproduced with PBE+D3 functional for DFT calculations. In their results, the lattice parameter c expands until $x \approx 0.50$ for Li_xNCM811. Intra(inter)layer distances, DOS plots, BCs have been calculated and analyzed by Dixit *et al.* [15] to understand the structural changes of NCM811. Moreover, they analyzed the crystal orbital Hamilton populations (COHP) and indicated that the TM$-$O covalency increases with the increasing oxidation state of Ni cations [15]. Although, many experimental and theoretical studies on lattice changes have been reported, the atomic and electronic structures of NCM811 with delithiation/lithiation have not been fully explained. The reason for the phase transitions in NCM811 has not been interpreted in details so far. In this dissertation, we also used an extensive set of Coulomb energy and DFT calculations to study the non-monotonic lattice parameters change and phase transitions in LixNCM811 during delithiation/lihtiation. The reason for the lattice parameters change and phase transitions (*i.e.* H$-$M and O3 $\rightarrow$ O1 phase transitions) in NCM811 were explained by analyzing the crystal, atomic and electronic structures during charging (delithiation). In addition to substitution, lattice doping is another practical approach to improve the structural stability. The effect of cations doping on structural stability of NCM are discussed in the next section.

1.1.4.3 Doping in NCM materials

A small amount of cation substitutions, *i.e.* lattice doping is an effective strategy to enhance the electrochemical properties and structural stability of NCM materials. Cation dopants such as Fe [70], Al [71], Mo [72], W [73], and Zr [74] have been investigated for NCM materials. For example, Liu *et al.* [75] have studied the effect of Mg, Cr, and Al doping on NCM111. They found that the cycling performance of NCM111 at high voltage (4.6 V) has been improved by Cr doping. They proposed that this improvement is due to the larger particle size of Cr-doped material (analyzed by SEM), and higher structural stability of it (XRD measurement) compared to Mg- and Al-doped as well as undoped NCM111. Wang *et al.* [76] investigated various amount x of Mo doping in NCM111 ($x = 0$, 0.005, 0.01, and 0.02). In their results, the lattice parameter a and the lattice parameter c as well as the unit cell volume increase with increasing Mo contents. By analyzing XRD, XPS, and CV curves, they found that Mo doping enhances the structural stability of NCM111 due to the sliding of O−TM−O layer is reduced, and Mo can contribute the redox reactions during cycling. Thus, the Mo-doped NCM111 can deliver a higher specific discharge capacity than undoped one. Moreover, they found that NCM111 with an optimal amount of Mo contents improves reversible capacity upon charging/discharging. Susai *et al.* [72] combined the experiments and theory to study the electrochemical properties and electronic structures of NCM811 by doping with Mo cations. The expansion of a and c are observed by XRD when increasing the doping level of Mo contents in NCM811. By DFT calculations with PBE+U functional, they found that Mo preferably substitutes Ni sites. The oxidation state of Ni cations with various amount of Mo in NCM811 is explored by analyzing magnetic moment. The number of Ni^{2+} increases for all Mo-doped NCM811, showing their higher discharge capacity than the undoped one. The optimal ratio of Mo dopant in NCM811 has high reversible capacity and rate capability. Schipper *et al.* [74] have also combined experiments and DFT calculations

to study the influence of Zr doping on structural stability of NCM622. Their XRD patterns show that Zr-doped NCM622 can preserve the structure ordering after cycling. By using the PBE functional, they found that both *a* and *c* lattice parameters increase for Zr-doped NCM622. However, a smaller change in the lattice parameter *c* for Zr-doped NCM622 has been calculated by PBE+D3 functional compared to the undoped one. They indicated that Zr has some interlayer interaction with the oxygen atoms, which can reduce the structural changes of Zr-doped NCM622 during cycling. The electronic configurations of Zr-doped and undoped NCM622 were analyzed by DOS plots. To investigate the doping effect on the structural stability of NCM materials, we calculated and analyzed the Li and O vacancy formation energies of NCM90505 with and without Al dopant in this dissertation. Since Al dopant is one of the most widely used and studied dopant that can stabilize the NCM structures during cycling [71]. By computing the average values of Li (and O) vacancy energies for different Li (and O) sites at high (and low) Li concentrations, the reason for the high structural stability of Al-doped NCM90505 (*i.e.* NCMA89) was explained.

1.2 Sodium-ion Batteries

SIB is also a ”rocking chair” system with a similar (de)intercalcation mechanism to LIBs. The energy density of SIBs is lower than that of LIBs, due to the higher weight of Na metal and lower standard cell voltage. However, the use of Na element is beneficial to reduce the cost. SIBs could be applied when the cost efficiency is more important than the energy density. Moreover, some TMs have been found that they are electrochemically inactive in LIBs but can contribute into the redox reactions in SIBs. This behavior provides opportunities to use the new cathode materials such as $NaFeO_2$ and $NaCrO_2$ for SIBs [77]. Layered materials such as $NaCoO_2$ (NCO), $NaNiO_2$ (NNO) and $NaMnO_2$ (NMO) have also been explored and investigated [78]. Among them, NCO has attracted much attention due to the commer-

cialized LCO in LIBs. However, unlike LCO, NCO ($R\bar{3}m$) has both O3 and P2 stacking and suffers from more complex phase transitions than that for LCO during cycling. Oxygen layers in P2 phase have an $(ABBA)_n$ stacking sequence, where the Na ions occupy the prismatic sites, and the TMs are in octahedral sites alternately between the oxygen planes [79]. The prismatic phase is not observed in Li-based compounds because Li ions are smaller than Na ions, and they are electrostatically more favorable to occupy in the octahedral sites between oxygen layers. Delmas *et al.* [80] analyzed XRD patterns and indicated that NCO with O3 stacking undergoes O3 $\rightarrow$ M $\rightarrow$ P3 ($(ABC)_n$) phase transitions when Na ions are extracted. However, NCO with P2 stacking can transform to O2 ($(ABAC)_n$) phase due to gliding of some TMO_6 octahedra sheets at high level of desodiation. The P2 $\rightarrow$ O2 phase transition leads to the contraction of interlayer distance and reduces the structural stability. However, the structural stability of P2-NCO is higher than that of O3-NCO [80, 81]. Reddy *et al.* [82] reported that reversible capacity of P2-NCO is 121 mAh/g at an operating voltage of 4.2 V vs. Na/Na^+ after 50 times cycling. NCO can thus be hardly used in practical application. The expense of Co element is another problem since the use of SIBs aims for the cost efficiency. NNO and NMO consist of cheaper Ni and Mn element, in particular NMO, due to Mn cation is abundant on the earth. NMO is more interesting than NNO material. Moreover, NMO can deliver a larger reversible capacity ($>$ 140 mAh/g) compared to NNO (123 mAh/g) during charging/discharging, because it undergoes less phase transitions than NNO [79]. Han *et al.* [83] have studied the phase transitions in NNO by XRD. They reported that its multi-phase transitions lead to capacity fading during cycling. Although NMO shows better electrochemical performances than NNO, it suffers from structural changes during cycling, which causes poor calendar life. To improve the structural stability of NMO, doping in its lattice has been extensively studied. In this dissertation, we investigated the influence of Fe doping on the structural changes (*i.e.* mechanical stability) in $Na_{0.67}MnO_2$. Fe

dopant is an ideal candidate for SIBs because it is an abundant element on the earth and inexpensive. We used a similar approach (by combing extensive Coulomb energy and DFT calculations) to determine the most favorable arrangements of Na ions in $Na_{0.67}MnO_2$. By analyzing the change in lattice parameters and O−Mn−O as well as O−Fe−O bond lengths of $Na_{0.67}MnO_2$ with various amount of Fe contents, we explained the reason behind the structural changes in $Na_{0.67}MnO_2$. The next section will be focusing on the electrochemical properties and structural stability of NMO, followed by the introduction of the experimental and theoretical studies on lattice doping in NMO.

1.2.1 Na_xMnO_2

$NaMnO_2$ (NMO) has the advantages of cheaper and higher practical capacity compared to other types of layered cathode materials, thus it has been widely investigated for SIBs [79]. Unlike LMO, NMO can preserve layered structure without transition to spinel phase during cycling [38, 84]. Layered NMO has more number of crystal structures compared to LMO such as monoclinic (α-NMO, *C*2/*m*) and orthorhombic (β-NMO, *Pmmn*) structures as well as P3 ($R\bar{3}m$), P2 (*P*6_3*/mmc)*), and P′2 (*Cmcm*) phases. They are different in the concentration and distribution of Na ions as well as stacking sequence of TMO_6 sheets and synthesis temperatures [85, 86]. Among these phases, P2 and P′2-Na_xMnO_2 ($0.70 > x > 0.56$) can deliver a higher reversible capacity of more than 140 mA/g at an operating voltage of $\sim$3.8 V vs. Na/Na^+ than other structures [87–89]. Thus, P2 and P′2-Na_xMnO_2 are one of the most interesting cathode materials for SIBs. However, they have low initial capacity because Na contents are low in their structures (theoretical capacity of NMO is 242 mAh/g) [90]. Moreover, a strong J−T distortion of Mn^{3+} and phase transitions cause large irreversible capacity during cycling. Kumakura *et al.* [88] have investigated the structural stability of P2- and P′2-$Na_{0.67}MnO_2$ during charging/discharging. By XRD measurement, they found that

P2 structure has strong J−T distortion in Mn−O octahrdra, *i.e.* the ratio of lattice parameter b/a is large, while the J−T distortion in P′2 phase is reduced. Their CV profiles show that P′2 phase has less redox peaks than P2 one, indicating the suppression of phase transitions during cycling. By applying DFT calculations, Kim *et al.* [91] (using PBE+U functional) studied the lattice parameters change of Na_xMnO_2 with sodiation/desodiation. They found that the distribution of Na ions and existence/absence of Mn^{3+} play an important role to control the lattice parameters. Since the presence of J−T active Mn^{3+} causes poor structural stability of NMO, finding an approach to decrease the J−T distortion of Mn cations in NMO is important. Many strategies such as doping have been proposed to improve the structural stability of NMO. In the next section, we will discuss the effect of lattice doping on the structural stability of NMO.

1.2.1.1 Doping in $NaMnO_2$

Lattice doping in NMO can alter the oxidation state of Mn cations and reduce their J−T distortion to improve the structural stability of NMO. Thus, many experimental and theoretical studies carry in this topic. For example, Billaud *et al.* [92] studied the electrochemical properties of P2-$Na_{0.67}MnO_2$ with various ratio x of Mg dopants, ($0 \leq x \leq 0.2$). Their CV measurements show that Mg-doped $Na_{0.67}MnO_2$ have smoother voltage profiles than the undoped one. $Na_{0.67}MnO_2$ with optimal amount of Mg contents shows a high capacity retention during cycling. This improvement is due to the presence of Mg in the lattice that increases the oxidation state of Mn to close to 4+. Llave *et al.* [93] combined experiments and DFT-PBE+U calculations to investigate the effect of Li doping on the structural stability of P2-$Na_{0.6}MnO_2$. By XRD and CV curves, they found that $Na_{0.6}Li_{0.2}Mn_{0.8}O_2$ undergoes less phase transitions compared to $Na_{0.6}MnO_2$. The oxidation state of Mn^{4+} was found by XPS measurement for $Na_{0.6}Li_{0.2}Mn_{0.8}O_2$, showing the suppression of J−T distortion. Their DOS plots also confirm the charge state of 4+ for Mn cations. $Na_{0.6}Li_{0.2}Mn_{0.8}O_2$ thus shows a rea-

sonable reversible capacity during charging/discharging. Double dopants in NMO has also been explored for SIBs. For example, Yang *et al.* [94] have studied the effect of Li and Fe co-doping on the cycling stability of $Na_{0.66}MnO_2$. They found that $Na_{0.66}MnO_2$ with Li and Fe dopants, P2 $\rightarrow$ O2 phase transition for $Na_{0.66}MnO_2$ is eliminated. This is because of the presence of Li in the TM sites, which stabilize the P2 structure. In this dissertation, we studied the effect of Fe doping on structural changes (*i.e.* mechanical stability) in $Na_{0.67}MnO_2$ with various amount of Fe contents. A similar approach (by combining extensive Coulomb energy and DFT calculations) has been applied to find the most favorable arrangements of Na ions in Na sites. We simulated and analyzed the O$-$Mn$-$O and O$-$Fe$-$O bond lengths, and explained the reason behind the reduction of J$-$T distortion for Fe-doped $Na_{0.67}MnO_2$. These findings help us to develop high-performing SIBs.

Chapter 2

OBJECTIVES

Among various NCM materials with different Ni, Co, and Mn ratios, NCM111 is one of the most commonly used and investigated system. Ni-rich NCM materials such as NCM811 are becoming popular due to the fact that the energy density of NCM increases with high Ni contents. However, the energy density of NCM is still low and insufficient for LIBs in electric vehicles. One of the main reason for their low energy density is due to their large volume changes and phase transitions during charging/discharging. The non-monotonic variation of lattice parameters (*a*, *b*, and *c*) and phase transitions in NCM such as NCM111 and NCM811 have been studied in experiment. The computations of lattice parameters change with delithiation have also been investigated by theoreticians. However, the atomic and electronic structures changes in NCM111 and NCM811 during charge/discharge processes have not been fully explained. The reason behind their lattice parameters change, symmetry and oxygen-stacking-induced phase transition with delithiation/lithiation are still unclear. Choosing an appropriate method to find the arrangements of Li ions in Li sites is important to compute the lattice parameters change and electronic structures but has not been studied in details. Lattice doping is a practical strategy to improve the structural stability of cathode materials. Al doping in NCM is especially popular because of its stabilizing role in the layered structures. The effect of Al doping on the chemical stability of Li and O in NCM has not been investigated in details. $NaMnO_2$ (NMO) is one of the most interesting cathode materials for SIBs because of its higher energy density and lower cost compared to other types of cathode

materials in SIBs. The poor structural stability of NMO, however, causes low energy density during charging/discharging. This can be attributed to the large structural changes in NMO upon cycling. Fe doping in NMO has been widely used and studied to improve the structural stability of NMO. This is because Fe is an earth-abundant element that is beneficial for cost efficiency. Experimental and theoretical studies show that Fe-doped NMO has higher structural stability than undoped one. The reason behind this improvements should be explained in details in terms of its lattice parameters change and J−T distortion.

To gain insight into the crystal and atomic structures changes in NCM systems during delithiation/lithiation, an extensive set of electrostatic (Coulomb energy) and density functional theory (DFT) calculations were applied to find the most favorable arrangements of Li ions in Li sites as function of the state of charge. The influence of choosing the exchange-correlation (XC) functional by comparing the calculated lattice parameters change with experimental data was examined. The electronic analysis of the number of unpaired spins N↑ −N↓ (NUS), spin density difference (SDD), density of state (DOS) and Bader charges (BCs) [95] were applied to find the correlation of structural stability of NCM111 and NCM811 with their lattice parameters change and structural phase transitions during charging/discharging. Moreover, to understand the effect of Al doping on the chemical stability of NCM systems, the vacancy formation energies of Li and O at high and low Li concentrations in NCM90505 were computed. To explain the reason for higher structural stability of Fe-doped NMO compared to the undoped material, a similar approach (by combining the extensive Coulomb energy and DFT calculations) to the NCM systems was used to find the most favorable arrangements of Na ions in Na sites. The influence of choosing the value of Hubbard parameter U on the lattice parameters change and the J−T distortion was studied.

Chapter 3

THEORETICAL METHODS

3.1 Quantum Mechanics based calculations

3.1.1 Many-Body Problem

Most of the interesting electronic properties of materials can be computed by solving non-relativistic time-independent Schrödinger equation, which can be written as follows

$$\hat{H}\psi(\mathbf{r},\sigma;\mathbf{R}) = E\psi(\mathbf{r},\sigma;\mathbf{R}). \tag{3.1.1.1}$$

Here, $\hat{H}$ is the Hamiltonian operator, and $\psi(\mathbf{r},\sigma;\mathbf{R})$ is the wave function, which is a solution or eigenstate of the Hamiltonian of the spatial ($\mathbf{r}$) and spin (σ) coordinates of electrons as well as the spatial coordinates of nuclei ($\mathbf{R}$). E is the eigenvalue of Schrödinger equation, representing the total energy of the system.

Unlike a single-particle wave function, for example a hydrogen atom, the Hamiltonian operator of a many-body system consists of many particles, composing by *n* electrons and *M* nuclei that have complex interactions. Thus, numerous number of spatial variables, *i.e.* (3*n*+3*M*) have to be solved for many-body wave function. Finding an exact total energy of many-body Schrödinger equation is in practice an impossible task. Hence, certain approximation approaches, which can simplify the theory, should be developed to make possible for solving many-body Schrödinger equation.

Considering a system containing *N* interacting particles with a total number of *n* electrons

and *M* nuclei. Each of them is assumed as a point mass moving in the space. Their kinetic energies and potentials in many-body Hamiltonian operator can be expressed as follows

$$\hat{H} = -\frac{1}{2}\sum_{i=1}^{n}\nabla_i^2 - \frac{1}{2m_{\mathrm{N}}}\sum_{I=1}^{M}\nabla_I^2 - \sum_{i=1}^{n}\sum_{I=1}^{M}\frac{Z_I}{|\mathbf{r}_i - \mathbf{R}_I|} + \sum_{i=1}^{n}\sum_{j>i}^{n}\frac{1}{|\mathbf{r}_i - \mathbf{r}_j|} + \sum_{I=1}^{M}\sum_{J>I}^{M}\frac{Z_I Z_J}{|\mathbf{R}_I - \mathbf{R}_J|}, \tag{3.1.1.2}$$

where i and j refer to electrons, and I and J stand for nuclei. m_{N} represents the mass of nuclei and Z denotes the atomic number of nuclei. The atomic units were used for the Eq. 3.1.1.2 as well as other equations throughout this dissertation: $\hbar$ = m_{e} = e = $4\pi\varepsilon_0$ = 1. The Hamiltonian operator can be written as

$$\hat{H} = \hat{T}_{\mathrm{e}} + \hat{T}_{\mathrm{N}} + \hat{V}_{\mathrm{eN}} + \hat{V}_{\mathrm{ee}} + \hat{V}_{\mathrm{NN}}. \tag{3.1.1.3}$$

The five terms of $\hat{H}$ for interacting particles as well as their abbreviate notations are explained below:

(1) $\hat{T}_{\mathrm{e}}$: kinetic energy operator of electrons,

(2) $\hat{T}_{\mathrm{N}}$: kinetic energy operator of nuclei,

(3) $\hat{V}_{\mathrm{eN}}$: electron-nuclei attraction operator,

(4) $\hat{V}_{\mathrm{ee}}$: electron-electron interaction operator,

(5) $\hat{V}_{\mathrm{NN}}$: nuclei-nuclei repulsion operator.

Since the exact solution of Schrödinger equation is only possible for one-electron system such as an hydrogen atom, additional approximations to solve many-body wave function are required to obtain the eigenstates and eigenvalues of the Hamiltonians.

3.1.1.1 Born-Oppenheimer Approximation

One of the most important assumption for solving many-body wave function is the Born-Oppenheimer approximation (BOA) proposed by Born and Oppenheimer [96]. This as-

sumption allows to separate a wave function of a system consisting of *N* particles into an electronic (ψ_{e}) and nuclear (ψ_{N}) part

$$\psi_i(\mathbf{r}_i, \sigma_i; \mathbf{R}_I) = \psi_{\mathrm{e}}(\mathbf{r}_i, \sigma_i; \{\mathbf{R}_I\})\psi_{\mathrm{N}}(\mathbf{R}_I). \tag{3.1.1.1.1}$$

The BOA is a feasible approach because the mass of nuclei is much heavier than that of electron. This means that electron can almost respond the motion of nuclei instantaneously. Thus, to simplify the many-body problem, the positions of nuclei can be treated as parameters (static), while the electrons have their motions in the potential field generated by nuclei. Within this approximation, the quantity $\hat{T}_{\mathrm{N}}$ in the Eq. 3.1.1.3 is zero, and $\hat{V}_{\mathrm{NN}}$ becomes a constant depending on the arrangement of nuclei. Moreover, since the electrons experience an external potential from nuclei, the notation of $\hat{V}_{\mathrm{eN}}$ renamed as $\hat{V}_{\mathrm{ext}}$. Thus, the Hamiltonian operator (in Eq. 3.1.1.3) is written in only the electronic part

$$\hat{H} \equiv \hat{H}_{\mathrm{e}} = \hat{T}_{\mathrm{e}} + \hat{V}_{\mathrm{ext}} + \hat{V}_{\mathrm{ee}}, \tag{3.1.1.1.2}$$

and the Schrödinger equation as

$$\hat{H}_{\mathrm{e}}\psi_{\mathrm{e}}(\mathbf{r}, \sigma) = E_{\mathrm{e}}\psi_{\mathrm{e}}(\mathbf{r}, \sigma). \tag{3.1.1.1.3}$$

Then, the total energy including the electronic energy and the nuclei-nuclei repulsion can be written as follows

$$E \equiv E_{\mathrm{tot}} = E_{\mathrm{e}} + \sum_{I=1}^{M}\sum_{J>I}^{M} \frac{Z_I Z_J}{|\mathbf{R}_I - \mathbf{R}_J|}. \tag{3.1.1.1.4}$$

Although BOA reduces the number of spatial variables from $(3n + 3M)$ to $3n$ spatial coordinates in three dimensions for a n-electrons system, it is still difficult to solve the many-electrons wave function in practice. This is because computing the non classical part of the electron-electron interactions ($\hat{V}_{\mathrm{ee}}$) is a challenge. These correlations consist of two contributions: exchange correlation which has implemented the Pauli exclusion principle, and Coulomb correlation that shows the pairwise interactions of electrons. Further approximations have been proposed to simplify the non-classical interactions, which can be divided into

two main categories: (1) wave-function-based methods, where the eingenvalue of the system is computed by using the wave function such as Hartree-Fock (HF) method; (2) density-based methods, where the total energy of the system is determined by using electron density, for example density functional theory (DFT). In this dissertation, all the results are obtained by using DFT calculations, and thus more discussions on this theory will be given.

3.1.1.2 Hartree-Fock Method

Among the wave-function-based methods, the HF approach is regarded as a fundamental theory for solving the electronic Schrödinger equation. Hartree [97] initially proposed this theory by using a simple product to describe the wave functions. Later, Fock [98] improved it by introducing the Slater determinant [99]. In this approach, electrons are assumed to be affected only through the mean field electrostatic (Coulomb) potential, which are created by all other electrons. This potential is called the Hartree potential ($\hat{V}_{\mathrm{H}}$). Thus, the electronic Hamiltonian can be described by the sum of each single-electron operator ($\hat{h}_i$), namely $\hat{H}_{\mathrm{e}} = \sum_{i=1}^{n} \hat{h}_i$. According to this, the electronic wave function is simply a product of orthogonal single-electron orbitals, which is written as follows

$$\psi_{\mathrm{e}}(\mathbf{x}) \equiv \psi_{\mathrm{HP}}(\mathbf{x}_1, \mathbf{x}_2, \cdots, \mathbf{x}_n) = \varphi_1(\mathbf{x}_1)\varphi_2(\mathbf{x}_2)...\varphi_n(\mathbf{x}_n), \tag{3.1.1.2.1}$$

where $\mathbf{x} = \{\mathbf{r}, \sigma\}$, and $\varphi_i(\mathbf{x})$ is the individual single-electron orbital. This is known as the Hartree product (HP). However, HP fails to describe the antisymmetric property of electronic wave functions originating from the fact that electrons are fermions, which should obey the Pauli exclusion principle. That is, electrons in the same spin state cannot be found at the same location in space. Thus, the electronic wave function should change when interchange their positions. To satisfy this property, the Slater determinant can be introduced instead of

using a simple product wave function as shown below

$$\psi_{\mathrm{e}}(\mathbf{x}) \equiv \psi_{\mathrm{HF}}(\mathbf{x}_1, \mathbf{x}_2, \cdots, \mathbf{x}_n) = \frac{1}{\sqrt{n!}} \begin{vmatrix} \varphi_1(\mathbf{x}_1) & \varphi_2(\mathbf{x}_1) & \ldots & \varphi_n(\mathbf{x}_1) \\ \varphi_1(\mathbf{x}_2) & \varphi_2(\mathbf{x}_2) & \ldots & \varphi_n(\mathbf{x}_2) \\ \vdots & \vdots & \ddots & \vdots \\ \varphi_1(\mathbf{x}_n) & \varphi_2(\mathbf{x}_n) & \ldots & \varphi_n(\mathbf{x}_n) \end{vmatrix}, \quad (3.1.1.2.2)$$

where two electrons are interchangeable in each column and row between wave functions. For a two-electrons system, for example, the electronic wave function is

$$\psi_{\mathrm{HF}}(\mathbf{x}_1, \mathbf{x}_2) = \frac{1}{\sqrt{2!}}[\varphi_1(\mathbf{x}_1)\varphi_2(\mathbf{x}_2) - \varphi_2(\mathbf{x}_1)\varphi_1(\mathbf{x}_2)] = -\psi_{\mathrm{HF}}(\mathbf{x}_2, \mathbf{x}_1). \quad (3.1.1.2.3)$$

To find the lowest total energy for ψ_{HF}, the variational method is applied. The concept of variational method is that the expectation value of a Hamiltonian operator ($\hat{H}$) for a trial wave function (ψ_{trial}) is always equal or larger than the ground-state energy (E_0)

$$\int \psi^*_{\mathrm{trial}} \hat{H} \psi_{\mathrm{trial}} d\mathbf{x} \geq E_0. \quad (3.1.1.2.4)$$

By minimizing the expectation value of the electronic Hamiltonian ($\hat{H}_{\mathrm{e}}$) with respect to the HF wave function (ψ_{HF}), the energy of E_{HF} can be obtained by

$$E_{\mathrm{e}} = \mathrm{Min} \left\langle \psi_{\mathrm{HF}} \middle| \hat{H}_{\mathrm{e}} \middle| \psi_{\mathrm{HF}} \right\rangle \equiv \int \psi^*_{\mathrm{HF}} \hat{H}_{\mathrm{e}} \psi_{\mathrm{HF}} d\mathbf{x} = E_{\mathrm{HF}} \geq E_0. \quad (3.1.1.2.5)$$

Here, $\hat{H}_{\mathrm{e}} = \hat{T}_{\mathrm{e}} + \hat{V}_{\mathrm{ext}} + \hat{V}_{\mathrm{H}} + \hat{V}_{\mathrm{X}}$, where $\hat{V}_{\mathrm{ee}}$ is replaced by $\hat{V}_{\mathrm{H}}$ since the electrons are assumed to move in the Hartree potential field, and the exchange potential term ($\hat{V}_{\mathrm{X}}$) is considered to obey the Pauli exclusion. Thus, the electronic energy for the HF wave function can be written as follows

$$E_{\mathrm{HF}} \equiv \sum_{i=1}^{n} \int \varphi^*_i(\mathbf{x}) \left[-\frac{1}{2}\nabla^2_i - \sum_{I=1}^{M} \frac{Z_I}{|\mathbf{r}_i - \mathbf{R}_I|} \right] \varphi_i(\mathbf{x}) d\mathbf{x} + \frac{1}{2} \sum_{i=1}^{n} \sum_{j=1}^{n} (J_{ij} - K_{ij}), \quad (3.1.1.2.6)$$

in which J_{ij} is the Coulomb energy representing the Coulomb repulsion between one electron in orbital i (at $\mathbf{x}$) and the mean field charge distribution of all other electrons in orbital

j (at $\mathbf{x}'$)

$$J_{ij} = \int\int \varphi_i^*(\mathbf{x})\varphi_j^*(\mathbf{x}')\frac{1}{|\mathbf{r}_i - \mathbf{r}_j|}\varphi_j(\mathbf{x}')\varphi_i(\mathbf{x})d\mathbf{x}d\mathbf{x}'. \quad (3.1.1.2.7)$$

Here, K_{ij} is exchange energy that switches the positions of single-electron orbitals of φ_i and φ_j, which is written as follows

$$K_{ij} = \int\int \varphi_i^*(\mathbf{x})\varphi_j^*(\mathbf{x}')\frac{1}{|\mathbf{r}_i - \mathbf{r}_j|}\varphi_j(\mathbf{x})\varphi_i(\mathbf{x}')d\mathbf{x}d\mathbf{x}'. \quad (3.1.1.2.8)$$

Therefore, the n-electrons Schrödinger equation is simplified to n single-electron orbitals of HF equation, which is given by

$$\hat{F}_i\varphi_i = \epsilon_i\varphi_i, \quad (3.1.1.2.9)$$

where $\hat{F}$ is called Fock operator and the form is

$$\hat{F}_i = -\frac{1}{2}\nabla_i^2 - \sum_{I=1}^{M}\frac{Z_I}{|\mathbf{r}_i - \mathbf{R}_I|} + \sum_{j\neq i}^{n}(\hat{J}_j - \hat{K}_j). \quad (3.1.1.2.10)$$

To solve the Eq. 3.1.1.2.9, one can either use numerical calculations to achieve the eigenvalues of HF equation or a set of basis functions, where the Roothaan equations are introduced into the HF equation. In either case, the important task is to guess some initial orbitals (φ_i) for calculating $\hat{J}_j$, $\hat{K}_j$, and $\hat{F}_i$ in the Eq. 3.1.1.2.10. And then, we solve the Eq. 3.1.1.2.9 to obtain ϵ_i for these orbitals and achieve a set of new orbitals. This process is then repeated several times until the converge criteria is reached. This is known as self-consistent procedure.

Although the HF method simplifies the electronic Schrödinger equation, the total energy is generally overestimated due to the absence of electron correlation, which comes from the electron-electron interactions. The correlation interaction can be approximated by using post-HF methods such as Mϕller-Plesset perturbation theory (MP2) [100], configuration interaction (CI) [101], and coupled cluster theory (CC) [102]. However, wave-function-based methods are computationally demanding for large systems due to the number of $3n$ spatial

variables. An alternative method to speed up the computation of electronic properties of a large system should be considered.

3.1.1.3 Density-based Methods

In comparison to wave-function-based methods, density-based methods can decrease the computing cost. Since density is only a function of 3 coordinates (if spin is not considered) for a *n*-electrons system, applying density-based methods significantly speeds up the calculation of large systems. The electron density with spin coordinates is expressed as follows

$$\rho(\mathbf{r}) = n \int \cdots \int |\psi(\mathbf{r}, \sigma, \mathbf{x}_2, \cdots, \mathbf{x}_n)|^2 d\sigma d\mathbf{x}_2 \cdots d\mathbf{x}_n, \tag{3.1.1.3.1}$$

which indicates the probability of finding each of n electrons at position $\mathbf{r}$ with spin orbital σ along with the other $n-1$ electrons at arbitrary positions and spins ($\mathbf{x} = \{\mathbf{r}, \sigma\}$). Within this approach, the total energy of *n*-electrons wave function can be obtained. By combining with various approximations, density-based method becomes a more accurate approach.

3.1.1.4 Thomas-Fermi-Dirac Model

Using electron density of a system as the variable to calculate the total energy of many-body wave function originates from the Thomas-Fermi (TF) model proposed by Thomas and Fermi [103, 104]. In their model, the kinetic energy of electrons is an approximation of the homogeneous electron gas. Moreover, they assumed electron-nuclei and electron-electron interactions are classically, where the total energy functional of non-interacting electrons can be written as follows

$$\begin{aligned} E_{\mathrm{TF}}[\rho(\mathbf{r})] &= T_{\mathrm{e,TF}}[\rho(\mathbf{r})] + V_{\mathrm{ext}}[\rho(\mathbf{r})] + J[\rho(\mathbf{r})], \\ &= \frac{3}{10}(3\pi^2)^{2/3} \int \rho(\mathbf{r})^{5/3} d\mathbf{r} - Z \int \frac{\rho(\mathbf{r})}{\mathbf{r}} d\mathbf{r} + \frac{1}{2} \int \int \frac{\rho(\mathbf{r}_i)\rho(\mathbf{r}_j)}{|\mathbf{r}_i - \mathbf{r}_j|} d\mathbf{r}_i d\mathbf{r}_j. \end{aligned} \tag{3.1.1.4.1}$$

Since the exchange energy has no classical analogue, it is excluded in TF model, leading to an inaccurate total energy of the system. Dirac [105] further improved the model by adding

the following exchange energy term ($E_{\mathrm{X}}[\rho]$) to the Eq. 3.1.1.4.1

$$E_{\mathrm{X}}^{\mathrm{Dirac}}[\rho(\mathbf{r})] = -\frac{3}{4}\left(\frac{3}{\pi}\right)^{1/3}\int \rho(\mathbf{r})^{4/3} d\mathbf{r}. \tag{3.1.1.4.2}$$

Even though, the total energies of the systems are not accurate with Thomas-Fermi-Dirac (TFD) model. This is because the kinetic energy is poorly described, and the electron correlation is neglected in their model. Although TFD model was not successful in quantum chemistry and solid-state physics, it was the starting point for the density-based methods such as DFT method.

3.1.2 Density functional Theory

A well-known density-based method is the density functional theory (DFT). This theory was introduced by Hohenberg and Kohn [106], and then it was developed by Kohn and Sham [32]. Since then, DFT has been applied in many fields for calculating the chemical and physical properties of materials.

3.1.2.1 Hohenberg-Kohn Theorems

The basis of density functional theory (DFT) comes from two theorems proposed by Hohenberg and Kohn [106]. Within the Hohenberg-Kohn (HK) Theorems, the formulas of electron density and total energy for non-degenerate ground states have been defined and mathematically proved.

Theorem I The electron density uniquely determines the external potential (υ_{ext}) to a constant. According to this Theorem, the total energy is a unique functional of the electron density, which can be written as follows

$$E_{\mathrm{e}}[\rho(\mathbf{r})] = T_{\mathrm{e}}[\rho(\mathbf{r})] + \int \upsilon_{\mathrm{ext}}(\mathbf{r})\rho(\mathbf{r})d\mathbf{r} + V_{\mathrm{ee}}[\rho(\mathbf{r})], \tag{3.1.2.1.1}$$

where $T_{\mathrm{e}}[\rho]$ denotes kinetic energy functional and $V_{\mathrm{ee}}[\rho]$ represents electron-electron interaction energy functional. They are defined as HK functional, given by

$$F_{\mathrm{HK}}[\rho(\mathbf{r})] = T_{\mathrm{e}}[\rho(\mathbf{r})] + V_{\mathrm{ee}}[\rho(\mathbf{r})]. \tag{3.1.2.1.2}$$

As such, we have

$$E_{\mathrm{e}}[\rho(\mathbf{r})] = E_{\mathrm{HK}}[\rho(\mathbf{r})] = F_{\mathrm{HK}}[\rho(\mathbf{r})] + \int \upsilon_{\mathrm{ext}}(\mathbf{r})\rho(\mathbf{r})d\mathbf{r}. \tag{3.1.2.1.3}$$

However, the exact total energy is still unknown due to the lack of an explicit expression of $F_{\mathrm{HK}}[\rho]$. Since $F_{\mathrm{HK}}[\rho]$ is a universal functional, its mathematical form will be the same for any system. The electron-electron interaction energy functional ($V_{\mathrm{ee}}[\rho]$) can be written as follows

$$V_{\mathrm{ee}}[\rho(\mathbf{r})] = V_{\mathrm{H}}[\rho(\mathbf{r})] + V_{\mathrm{ncl}}[\rho(\mathbf{r})], \tag{3.1.2.1.4}$$

in which $V_{\mathrm{H}}[\rho]$ is the classical Coulomb repulsion energy and $V_{\mathrm{ncl}}[\rho]$ denotes the non-classical energy, including self-interaction correction, exchange, and Coulomb correlation energy.

Theorem II This functional achieves its minimum value if and only if the electron density is the true ground-state density. Hence, the total energy with a trial density (ρ_{trial}) is described by

$$E_{\mathrm{HK}}[\rho_{\mathrm{trial}}(\mathbf{r})] \geq E_{\mathrm{HK}}[\rho_0(\mathbf{r})] = E_0, \tag{3.1.2.1.5}$$

in which the electron (trial) density satisfies

$$\rho(\mathbf{r}) \geq 0, \text{and} \int \rho(\mathbf{r})d\mathbf{r} - n = 0. \tag{3.1.2.1.6}$$

Minimizing Eq. 3.1.2.1.5 by using Euler-Lagrange equation with respect to the constraint (Eq. 3.1.2.1.6). The second constraint in Eq. 3.1.2.1.6 assures that the system contains a fixed number of electrons (*n*), which is given by

$$\frac{\delta\left\{E_{\mathrm{HK}}[\rho(\mathbf{r})] - \mu\int\rho(\mathbf{r})d\mathbf{r}\right\}}{\delta\rho(\mathbf{r})} = 0. \tag{3.1.2.1.7}$$

Then,

$$\mu = \frac{\delta E_{\mathrm{HK}}[\rho(\mathbf{r})]}{\delta \rho(\mathbf{r})} = \frac{\delta F_{\mathrm{HK}}[\rho(\mathbf{r})]}{\delta \rho(\mathbf{r})} + V_{\mathrm{ext}}(\mathbf{r}), \tag{3.1.2.1.8}$$

where the Lagrange multiplier μ is called the $chemical\ potential$ of the electrons as defined in the Euler-Lagrange equation. Therefore, the ground-state properties of the system can be obtained by finding a $\rho(\mathbf{r})$ function that minimizes the total energy. However, the exact formulation of $F_{\mathrm{HK}}[\rho]$ is not defined in the HK Theorems. Later, as will be discussed in the following section, Kohn and Sham proposed a practical way to approximate the universal functional of $F_{\mathrm{HK}}[\rho]$.

3.1.2.2 Kohn-Sham Ansatz

To find the form of $F_{\mathrm{HK}}[\rho]$, Kohn and Sham [32] proposed a fictitious non-interacting system, which exhibits the same electron density as the ground-state density of a real interacting system. Within the Kohn-Sham (KS) approach, the exact kinetic energy functional ($T_{\mathrm{e}}[\rho]$) is then separated into two parts

$$T_{\mathrm{e}}[\rho(\mathbf{r})] = T_{\mathrm{e,s}}[\rho(\mathbf{r})] + T_{\mathrm{e,r}}[\rho(\mathbf{r})]. \tag{3.1.2.2.1}$$

The first part ($T_{\mathrm{e,s}}[\rho]$) describes the kinetic energy of fictitious non-interacting electrons that is given by

$$T_{\mathrm{e,s}}[\rho(\mathbf{r})] = -\frac{1}{2}\sum_{i=1}^{n} \left\langle \varphi_i(\mathbf{r}) \left| \nabla^2 \right| \varphi_i(\mathbf{r}) \right\rangle, \tag{3.1.2.2.2}$$

where $\varphi_i(\mathbf{r})$ is a set of independent one-electron wave functions. Whereas, the second part ($T_{\mathrm{e,r}}[\rho]$) describes the rest of kinetic energy that contribution is neglected in the fictitious non-interacting one

$$T_{\mathrm{e,r}}[\rho(\mathbf{r})] = T_{\mathrm{e}}[\rho(\mathbf{r})] - T_{\mathrm{e,s}}[\rho(\mathbf{r})]. \tag{3.1.2.2.3}$$

By combining $T_{\mathrm{e,r}}[\rho]$ with the non-classical part of electron-electron interaction ($V_{\mathrm{ncl}}[\rho]$), the so-called exchange-correlation (XC) energy functional is defined, which can be expressed as

$$E_{\mathrm{XC}}[\rho(\mathbf{r})] = T_{\mathrm{e,r}}[\rho(\mathbf{r})] + V_{\mathrm{ncl}}[\rho(\mathbf{r})]. \tag{3.1.2.2.4}$$

Thus, the form of $F_{\mathrm{HK}}[\rho]$ can be written as follows

$$F_{\mathrm{HK}}[\rho] = T_{\mathrm{e,s}}[\rho(\mathbf{r})] + V_{\mathrm{H}}[\rho(\mathbf{r})] + E_{\mathrm{XC}}[\rho(\mathbf{r})], \tag{3.1.2.2.5}$$

and then the total energy functional in Eq. 3.1.2.1.1 is expressed by KS equations which normally are called the determining equations for the KS orbitals

$$E_{\mathrm{e}}[\rho(\mathbf{r})] \equiv E_{\mathrm{KS}}[\rho(\mathbf{r})] = T_{\mathrm{e,s}}[\rho(\mathbf{r})] + V_{\mathrm{ext}}[\rho(\mathbf{r})] + V_{\mathrm{H}}[\rho(\mathbf{r})] + E_{\mathrm{XC}}[\rho(\mathbf{r})]. \tag{3.1.2.2.6}$$

The $T_{\mathrm{e,s}}[\rho]$, $V_{\mathrm{ext}}[\rho]$ and $V_{\mathrm{H}}[\rho]$ are the exact energy functionals for a single electron. Note that in an extended system, the $V_{\mathrm{ext}}[\rho]$, $V_{\mathrm{H}}[\rho]$, and $V_{\mathrm{NN}}[\rho]$ interactions are calculated by the Ewald summation. This will be discussed in details in the section 3.2.1. The $E_{\mathrm{XC}}[\rho]$ term is still the unknown quantity that should be further approximated for solving the KS equation.

The Eq. 3.1.2.1.8 can now be expressed as follows

$$\mu = \frac{\delta E_{\mathrm{KS}}[\rho(\mathbf{r})]}{\delta\rho(\mathbf{r})} = \frac{\delta T_{\mathrm{e,s}}[\rho(\mathbf{r})]}{\delta\rho(\mathbf{r})} + V_{\mathrm{eff}}^{\mathrm{KS}}(\mathbf{r}) \tag{3.1.2.2.7}$$

with

$$V_{\mathrm{eff}}^{\mathrm{KS}}(\mathbf{r}) = V_{\mathrm{ext}}(\mathbf{r}) + \int \frac{\rho(\mathbf{r}_j)}{|\mathbf{r}_i - \mathbf{r}_j|} d\mathbf{r}_j + V_{\mathrm{XC}}(\mathbf{r}), \tag{3.1.2.2.8}$$

in which $V_{\mathrm{eff}}^{\mathrm{KS}}(\mathbf{r})$ refers to the KS effective potential and $V_{\mathrm{XC}}(\mathbf{r})$ is the exchange-correlation potential

$$V_{\mathrm{XC}}(\mathbf{r}) = \frac{\delta E_{\mathrm{XC}}[\rho(\mathbf{r})]}{\delta\rho(\mathbf{r})}. \tag{3.1.2.2.9}$$

The solution of Eq. 3.1.2.2.7 is obtained by solving the following set of KS orbital equations

$$\left[-\frac{1}{2}\nabla^2 + V_{\mathrm{eff}}^{\mathrm{KS}}(\mathbf{r})\right]\varphi_i(\mathbf{r}) = \epsilon_i^{\mathrm{KS}}\varphi_i(\mathbf{r}), \tag{3.1.2.2.10}$$

where $\varphi_i(\mathbf{r})$ denotes the KS orbital and ϵ_i^{KS} is the energy of orbital. The electron density of the real system can be constructed from the KS orbitals over all occupied orbitals

$$\rho(\mathbf{r}) = \sum_{i=1}^{N_{\mathrm{occ}}} |\varphi_i(\mathbf{r})|^2 . \tag{3.1.2.2.11}$$

To find the solution of KS equation self-consistent procedure is adopted. Since $V_{\mathrm{eff}}^{\mathrm{KS}}[\rho]$ depends on $\rho(\mathbf{r})$ that we are searching for, an initial guessed electron density from the fictitious system is considered. With an initial guessed $\rho(\mathbf{r})$, the $V_{\mathrm{eff}}^{\mathrm{KS}}[\rho]$ from Eq. 3.1.2.2.8 is calculated, and then the ϵ_i^{KS} as well as a new $\varphi_i(\mathbf{r})$ is obtained from Eq. 3.1.2.2.10. We then use this new $\varphi_i(\mathbf{r})$ to solve the Eq. 3.1.2.2.11 and obtain a new $\rho(\mathbf{r})$. This process is repeated until $\rho(\mathbf{r})$ is converged with an expected tolerance. If the correct $V_{\mathrm{XC}}(\mathbf{r})$ is known in the Eq. 3.1.2.2.8, the exact total electronic energy can be obtained. However, it is practically impossible and different approximations should be applied to approximate the XC energy of the system, which is a challenge for DFT method.

3.1.2.3 Exchange-Correlation functional

The contribution of the exchange-correlation (XC) functional is relatively small compared to the total energy of the system. However, the role of the XC functional in determining the energy and density of materials cannot be ignored. A well-described XC functional is therefore essential to bring DFT into a real calculation. Many approximations of $E_{\mathrm{XC}}[\rho]$ have been proposed so far. Different levels of XC approximations have been categorized by Perdew *et al.* [107]. Among them, the first three levels are the most popular approximations of the XC functionals, which can be summarized in the following expression

$$E_{\mathrm{XC}}[\rho] = \int \rho(\mathbf{r}) \varepsilon_{\mathrm{XC}}[\rho, \nabla\rho, \tau] d\mathbf{r}, \tag{3.1.2.3.1}$$

in which $\rho(\mathbf{r})$, $\nabla\rho(\mathbf{r})$, and $\tau(\mathbf{r})$ represents the density, the density gradient, and the kinetic energy density, respectively.

3.1.2.3.1 Local Density Approximation The oldest and simplest model of the XC functional is called the local density approximation (LDA) [32]. Within this approximation, the electron density of an inhomogeneous system is treated locally as an uniform electron gas ($\rho(\mathbf{r})$ = constant). The XC energy functional of LDA ($E_{\mathrm{XC}}^{\mathrm{LDA}}$) is given by

$$E_{\mathrm{XC}}^{\mathrm{LDA}}[\rho] = \int \rho(\mathbf{r}) \varepsilon_{\mathrm{XC}}^{\mathrm{LDA}}[\rho] \, d\mathbf{r}. \tag{3.1.2.3.1.1}$$

The $\varepsilon_{\mathrm{XC}}^{\mathrm{LDA}}[\rho]$ is the exchange-correlation energy per particle of a homogeneous electron gas that can be divided into two contributions: exchange (correlation) energy ($\varepsilon_{\mathrm{X}}^{\mathrm{LDA}}[\rho]$) which obeys Pauli exclusion principle, and (Coulomb) correlation energy ($\varepsilon_{\mathrm{C}}^{\mathrm{LDA}}[\rho]$) that shows the pairwise interactions of electrons

$$\varepsilon_{\mathrm{XC}}^{\mathrm{LDA}}[\rho] = \varepsilon_{\mathrm{X}}^{\mathrm{LDA}}[\rho] + \varepsilon_{\mathrm{C}}^{\mathrm{LDA}}[\rho]. \tag{3.1.2.3.1.2}$$

The $\varepsilon_{\mathrm{X}}^{\mathrm{LDA}}[\rho]$ term has an exact expression originally derived by $E_{\mathrm{X}}^{\mathrm{Dirac}}$ in the Eq. 3.1.1.4.2, which can be written as follows

$$\varepsilon_{\mathrm{X}}^{\mathrm{LDA}}[\rho] = -\frac{3}{4}\left(\frac{3}{\pi}\right)^{1/3} \rho(\mathbf{r})^{1/3}. \tag{3.1.2.3.1.3}$$

The $\varepsilon_{\mathrm{C}}^{\mathrm{LDA}}[\rho]$ has been determined by an empirical fitting of quantum Monte Carlo (QMC) calculations for an uniform electron gas with a number of different densities [108]. However, various analytic forms were proposed in LDA to model the contribution of $\varepsilon_{\mathrm{C}}^{\mathrm{LDA}}[\rho]$ such as the Vosko-Wilk-Nusair (VWN) [109], the Perdew-Zunger (PZ) [110], and the Perdew-Wang (PW) [111] correlation functional.

In principle, LDA is accurate only for slowly varying density that can locally be treated as an uniform electron gas. However, it has been found to give success in some inhomogeneous situations. The reason behind this accuracy is due to the fact that only the spherical symmetry part of the XC hole of LDA determines the energy, which satisfies the sum rule showing the cancellation of the errors between $E_{\mathrm{X}}^{\mathrm{LDA}}[\rho]$ and $E_{\mathrm{C}}^{\mathrm{LDA}}[\rho]$ [112, 113]. The error cancellation is usually accurate for lattice parameter and bulk modulus, but not the cases for calculating

binding and cohesive energies of inhomogeneous systems. LDA poorly predicts the systems with highly inhomogeneous electron densities. Moreover, LDA fails to predict the weakly-bonded systems such as van der Waals (vdW) attractions and hydrogen-bonded systems.

3.1.2.3.2 Generalized-gradient Approximation To achieve accurate XC functional for inhomogeneous systems, the density gradient is taken into account (not only the density) to approximate the XC functional. This approach is called the generalized-gradient approximation (GGA) [107, 114]

$$E_{\mathrm{XC}}^{\mathrm{GGA}}[\rho] = \int \rho(\mathbf{r})\varepsilon_{\mathrm{XC}}^{\mathrm{GGA}}[\rho(\mathbf{r}), \nabla\rho(\mathbf{r})]\, d\mathbf{r}. \tag{3.1.2.3.2.1}$$

The exchange term of GGA is written as follows

$$E_{\mathrm{X}}^{\mathrm{GGA}}[\rho] = \int \rho(\mathbf{r})\varepsilon_{\mathrm{X}}^{\mathrm{unif}}[\rho]F_{\mathrm{X}}(s)\, d\mathbf{r}, \tag{3.1.2.3.2.2}$$

where $\varepsilon_{\mathrm{X}}^{\mathrm{unif}}[\rho]$ is the exchange energy per particle of an uniform electron gas as written in Eq. 3.1.2.3.1.3. $F_{\mathrm{X}}(s)$ refers to an exchange enhancement factor, which is a function of one dimensionless inhomogeneous parameter of s given below

$$s = \frac{|\nabla\rho|}{2(3\pi^2\rho)^{1/3}\rho}. \tag{3.1.2.3.2.3}$$

The quantity $F_{\mathrm{X}}(s)$ improves the deficiency of the exchange energy of LDA. Using different $F_{\mathrm{X}}(s)$ will alter the exchange functional of GGA such as Becke's 1988 (B88) [115] and the Perdew, Burke and Ernzerhof's (PBE) [34] exchange functional. The PBE exchange functional has been widely used in determining the energies of the materials, where $F_{\mathrm{X}}(s)$ is written by

$$F_{\mathrm{X}}(s) = 1 + \kappa - \frac{\kappa}{1 + \frac{\mu s^2}{\kappa}}, \kappa \approx 0.804, \mu \approx 0.2195. \tag{3.1.2.3.2.4}$$

In addition to exchange functional, many analytic forms of correlation functional ($E_{\mathrm{C}}^{\mathrm{GGA}}[\rho]$) have been proposed as well, *e.g.* Lee, Yang and Parr's (LYP) [116], the Perdew and Wang's

1991 (PW91) [117], and the Perdew, Burke and Ernzerhof's (PBE) [34] correlation functional. Among them, the PBE correlation functional is the most popular one for GGA

$$E_{\mathrm{C}}^{\mathrm{GGA}}[\rho(\mathbf{r})] = \int \rho(\mathbf{r})\Big\{\varepsilon_{\mathrm{C}}^{\mathrm{unif}}[\rho(\mathbf{r})] + H[\rho(\mathbf{r}),\omega]\Big\}d\mathbf{r}, \tag{3.1.2.3.2.5}$$

where

$$H[\rho(\mathbf{r}),\omega] = \gamma \ln\left[1 + \frac{\beta w^2}{\gamma}\Big(\frac{1+Aw^2}{1+Aw^2+A^2w^4}\Big)\right] \tag{3.1.2.3.2.6}$$

with

$$\gamma \approx 0.031; \beta \approx 0.067; A = \frac{\beta}{\gamma}\frac{1}{e^{-\varepsilon_{\mathrm{C}}^{\mathrm{unif}}/\gamma}-1}; \omega = \frac{|\nabla\rho|}{2\Big[\sqrt{\frac{4(3\pi^2\rho)^{1/3}}{\pi}}\Big]\rho}. \tag{3.1.2.3.2.7}$$

Here, ω is a dimensionless inhomogeneous parameter. Further improvements for PBE functional have been proposed to increase the accuracy, *e.g.* revPBE and RPBE [118]. However, there exists no single perfect functional to predict the properties of materials for all systems. Choosing an appropriate XC functional of GGA for solving KS equation in a desired system is important.

3.1.2.3.3 Meta-Generalized-gradient Approximation The meta-generalized-gradient approximation (meta-GGA) includes kinetic energy density ($\tau(\mathbf{r})$) as shown below [119]

$$E_{\mathrm{XC}}^{\mathrm{mGGA}}[\rho] = \int \rho(\mathbf{r})\varepsilon_{\mathrm{XC}}^{\mathrm{mGGA}}[\rho(\mathbf{r}),\nabla\rho(\mathbf{r}),\tau(\mathbf{r})]\,d\mathbf{r}, \tag{3.1.2.3.3.1}$$

where

$$\tau(\mathbf{r}) = \frac{1}{2}\sum_{i=1}^{N_{\mathrm{occ}}}|\nabla\varphi_i(\mathbf{r})|^2 \tag{3.1.2.3.3.2}$$

is the kinetic energy density of non-interacting electrons over all occupied orbitals. The exchange energy of meta-GGA is written as follows

$$E_{\mathrm{X}}^{\mathrm{mGGA}}[\rho(\mathbf{r})] = \int \rho(\mathbf{r})\varepsilon_{\mathrm{X}}^{\mathrm{unif}}[\rho(\mathbf{r})]F_{\mathrm{X}}(s,\alpha)\,d\mathbf{r}, \tag{3.1.2.3.3.3}$$

in which the enhancement factor (F_X) is a function of two dimensionless inhomogeneous parameters. The parameter s is same as the formula written in the Eq. 3.1.2.3.2.3, while α is given by

$$\alpha = \frac{(\tau - \tau^W)}{\tau^{\text{unif}}} > 0 \tag{3.1.2.3.3.4}$$

with

$$\tau^W = \frac{1}{8}\frac{|\nabla\rho|^2}{\rho}, \tag{3.1.2.3.3.5}$$

and

$$\tau^{\text{unif}} = \frac{3}{10}(3\pi^2)^{2/3}\rho^{5/3}. \tag{3.1.2.3.3.6}$$

The quantity τ^W refers to the kinetic energy density of a KS orbital, and the quantity τ^{unif} indicates uniform gas. The analytic forms of the exchange energy and the correlation energy have been proposed by Perdew *et al.* [120] and Tao *et al.* [121]. Based on these functionals, Sun *et al.* [122] proposed a new XC functional called strongly constrained and appropriately normed (SCAN) for meta-GGA [34]. It has been reported that the results predicted by using SCAN functional are more accurate than PBE functional in some cases, for example $3d$ transition-metal layered structures and the weakly-bonded systems [33].

3.1.2.4 Further Corrections on Exchange-Correlation functional

In comparison to the newly developed meta-GGA-SCAN functional, LDA and GGA-PBE functionals are established for a while and more commonly to be used for DFT calculations. However, they suffer from the poor predictions of $E_{\text{XC}}[\rho]$ on strongly-correlated or weakly-bonded systems. The next section will discuss the approaches to improve their accuracies.

3.1.2.4.1 Correlation Corrections In LDA or GGA-PBE functional and in particular LDA, the electrons experience an average Coulomb repulsion over the space due to the mean field approximation. This causes the electronic properties of rare earth elements such as

transition metals (TMs), which have open d-shell or open f-shell elements have been poorly predicted [123]. In addition, some materials that are predicted to be electronically conductive by LDA (GGA) simulation are insulators in reality. These materials are known as Mott insulators, where electrons are well-localized [124]. The band gap and magnetic properties of TMs and Mott insulators are thus poorly predicted by using LDA or GGA due to this on-site Coulomb repulsion.

A method to solve this problem was proposed by Hubbard [125, 126], who introduced a Hamiltonian including two major terms: (1) a kinetic energy operator described by using a tight-binding approximation, and (2) a potential operator consisting of the on-site Coulomb interaction. In addition, to evaluate the energy changes in terms of the number of particles in the system, the chemical potential (μ) is included. Thus, the Hubbard Hamiltonian operator can be written as follows

$$\hat{H}_{\mathrm{Hub}} = -t \sum_{\langle i,j\rangle,\sigma} (\hat{c}^{\dagger}_{i,\sigma}\hat{c}_{j,\sigma} + \hat{c}^{\dagger}_{j,\sigma}\hat{c}_{i,\sigma}) + U \sum_{i=1}^{N} \hat{n}_{i\uparrow}\hat{n}_{i\downarrow} - \mu \sum_{i,\sigma} \hat{n}_{i,\sigma}. \qquad (3.1.2.4.1.1)$$

Here, t is a hopping integral, and $\langle i, j\rangle$ refers to the nearest neighboring site indicating that the hopping occurs only between two adjacent sites, while $\sigma =\uparrow$ or $\downarrow$ represents the spin of electron. The first quantity $\hat{c}^{\dagger}_{i,\sigma}\hat{c}_{j,\sigma}$ in the parentheses denotes the creation $\hat{c}^{\dagger}_{i,\sigma}$ of an electron on site i and its annihilation $\hat{c}_{j,\sigma}$ on site j with spin (σ), while the second quantity $\hat{c}^{\dagger}_{j,\sigma}\hat{c}_{i,\sigma}$ in the parentheses switches the sites. The *U* value or so-called the Hubbard *U* represents the strength of the correlations, where the Coulomb repulsion is described by the electrons with spin (σ) doubly occupied at the same site. $\hat{n}_{i\uparrow}$ and $\hat{n}_{i\downarrow}$ denotes the number of spin up or down electrons on site *i*, respectively. N is the total number of electrons. The final term with chemical potential (μ) controls electrons filling of the orbitals due to the fact that μ reflects the energy changes when the electron density is changed in the system ($\mu = \delta E/\delta\rho$). According to the Eq. 3.1.2.4.1.1, for example, the XC energy functional of LDA

with Hubbard *U* can be expressed as follows

$$E_{\mathrm{XC}}^{\mathrm{LDA}+U}[\rho,\hat{n}] = E_{\mathrm{XC}}^{\mathrm{LDA}}[\rho] + E_{\mathrm{Hub}}(\hat{n}) - E_{\mathrm{dc}}^{\mathrm{LDA}}(\hat{n}). \quad (3.1.2.4.1.2)$$

The last energy term of Eq. 3.1.2.4.1.2 is called the double-counting term, which is considered to avoid the double counting of the Coulomb correlation energy for strongly-localized electrons that has been partially included in the energy of LDA.

Two major schemes of Hubbard corrections are used in DFT calculations. One is proposed by Liechtenstein *et al.* [127], who considered the *U* and exchange (*J*) parameters separately for $E_{\mathrm{Hub}}(\hat{n}) - E_{\mathrm{dc}}^{\mathrm{LDA}}(\hat{n})$. The other one is developed by Dudarev *et al.* [35], who introduced the effective *U* parameter ($U_{\mathrm{eff}} = U - J$) for the Eq. 3.1.2.4.1.2. In this dissertation, the effective *U* parameter is considered for the PBE functional.

3.1.2.4.2 Dispersion Corrections Dispersion interaction, *i.e.* long-range van der Waals (vdW) attraction is a force due to charge distribution of the atoms or molecules causing instantaneous dipole moment. Although vdW interaction is much weaker than the strength of metal, ionic and covalent bonds, it significantly controls the electronic properties of materials such as layered structures [128]. DFT with LDA or GGA functional cannot very well describe this long-range dispersion force. To include this weak interaction into DFT, many approaches have been proposed [129]. A simple idea has been proposed by Grimme *et al.* [130]. They proposed to add an empirical potential of $-C_{6,IJ}/R_{IJ}^6$ into DFT calculation, where $C_{6,IJ}$ is the pairwise atomic coefficient and R_{IJ} is the distance between atoms I and J. This approach is known as the dispersion-corrected DFT (DFT-D) [130]. Further improvements of the DFT-D approach, for example, DFT-D3 [131] method has also been proposed. They are all based on the sum over the pairwise atoms. The general form for the dispersion contribution to the total energy of the system between each pair of atoms in the

materials is [129]

$$E_{\mathrm{tot}} \equiv E_{\mathrm{DFT+D}} = E_{\mathrm{DFT}} + E_{\mathrm{Disp}} \tag{3.1.2.4.2.1}$$

with

$$E_{\mathrm{Disp}} = -\sum_{J>I}^{M}\sum_{n} s_n \frac{C_{n,IJ}}{R_{IJ}^{n}} f_{n,\mathrm{damp}}(R_{IJ}). \tag{3.1.2.4.2.2}$$

Here, I and J indexes refer to the interacting atom pairs and s_n is a scaling factor. n (n = 6, 8, 10,...) is the order of dispersion contributions, and $f_{n,\mathrm{damp}}$ is a damping function of order n at the atom-atom distance (R_{IJ}), which is included to avoid a double counting of DFT for the dispersion at short-range distances [128].

3.1.2.5 Periodic Systems

Although many-body problem has been simplified by DFT, a remaining challenge is how to deal with the extended systems such as crystals consisting of an infinite number of atoms and electrons. These crystalline solids are used almost everywhere and thus are interesting to be modelled and studied in the atomic and electronic scales. However, solving KS equation for crystalline solids is practically intractable in DFT calculations. To tackle this problem, we assume the boundary conditions and apply Bloch theorem due to the fact that their atomic arrangement have periodicity and symmetry through the space.

3.1.2.5.1 Bravais lattice To model a periodic system, the smallest possible unit cell that can represent an infinite repeated system over the space is chosen. Any point in a crystal can be mapped into the primitive unit cell by using a translational vector ($\mathbf{R}$) in a real space

$$\mathbf{R} = u\mathbf{a}_1 + v\mathbf{a}_2 + w\mathbf{a}_3. \tag{3.1.2.5.1.1}$$

Here, u, v, and w are set of integers, while $\mathbf{a}_1$, $\mathbf{a}_2$, and $\mathbf{a}_3$ are primitive vectors in the unit cell. These primitive vectors are not all on the same plane. This kind of lattice is called the Bravais lattice, where the primitive unit cell is referred to the Wigner-Seitz cell. Thus,

the position of atoms in the real space is depicted by the Bravais lattice. By introducing a basis at each lattice point with the Bravais lattice, a crystal structure can be obtained. To calculate the electronic structure of a periodic system, its Bravais lattice needs to be converted to its reciprocal lattice in the reciprocal space or the so-called k-space by using Fourier transformation. In the reciprocal lattice, any vector ($\mathbf{G}$) can be written as a linear combination of the primitive vectors ($\mathbf{b}_1$, $\mathbf{b}_2$, and $\mathbf{b}_3$) as shown below

$$\mathbf{G} = h\mathbf{b}_1 + k\mathbf{b}_2 + l\mathbf{b}_3, \tag{3.1.2.5.1.2}$$

h, k, and l are called Miller indices where the notation of $\{hkl\}$, $[\,hkl]$, and $(\,hkl)$ represents a family of planes, a direction, and a plane, respectively for a crystal. The primitive vectors satisfy $\mathbf{b}_i \cdot \mathbf{a}_j = \mathbf{2}\pi\delta_{ij}$ and their primitive unit cell in k-space is known as the (first) Brillouin zone (BZ), which represents the Wigner-Seitz cell of the reciprocal lattice.

3.1.2.5.2 Boundary Conditions An infinite periodic system can in principle be modelled by defining a primitive unit cell and then assuming the boundary conditions. Thus, to simulate the electronic properties in a crystal, the wave function under the boundary conditions can be expressed as

$$\varphi(\mathbf{r}) = \varphi(\mathbf{r} + \mathbf{R}), \tag{3.1.2.5.2.1}$$

This periodic boundary conditions is also known as Born-von Karman boundary conditions [132, 133].

3.1.2.5.3 Bloch's Theorem Bloch's theorem states that an electronic wave function in a periodic solid can be written as a product of a periodic function ($u_{n,\mathbf{k}}(\mathbf{r})$) and a plane wave

$$\varphi_{n,\mathbf{k}}(\mathbf{r}) = u_{n,\mathbf{k}}(\mathbf{r})e^{i\mathbf{k}\cdot\mathbf{r}}, \tag{3.1.2.5.3.1}$$

where n refers to a band index representing each KS orbital in a crystal. $\mathbf{k}$ denotes the wave vector within the BZ. The periodic function can be expended to a linear combination

of plane-wave basis sets within the reciprocal lattice vectors shows

$$u_{n,\mathbf{k}}(\mathbf{r}) = \sum_{\mathbf{G}}^{N_{\text{cell}}} c_{n,\mathbf{G}}\, e^{i\mathbf{G}\cdot\mathbf{r}}, \tag{3.1.2.5.3.2}$$

in which N_{cell} denotes total number of atoms in a unit cell. $\mathbf{G}$ are reciprocal lattice vectors, and $c_{n,\mathbf{G}}$ refer to the plane wave coefficients. Thus, the one-particle wave function of KS equations can be written as follows

$$\varphi_{n,\mathbf{k}}(\mathbf{r}) = \frac{1}{\sqrt{\Omega}_{\text{BZ}}} \sum_{\mathbf{G}}^{N_{\text{cell}}} c_{n,\mathbf{k}+\mathbf{G}}\, e^{i(\mathbf{k}+\mathbf{G})\cdot\mathbf{r}}, \tag{3.1.2.5.3.3}$$

where Ω_{BZ} denotes the cell volume in the BZ. Within the Bloch's theorem, the computation of electronic structures of solids is simplified in DFT calculations. However, due to plenty of $\mathbf{k}$-points in the BZ, it is necessary to give some restrictions for choosing a proper grid of $\mathbf{k}$-points in a crystal. The method for finding the $\mathbf{k}$-points will be discussed in the next section.

3.1.2.6 Computational Approximations

To reduce the complexity of periodic wave functions and increase the computational speed without losing the accuracy, certain approximate methods were developed. Since, in this dissertation, the Vienna $Ab\ initio$ Simulation package (VASP) code is used for the DFT calculations, the approach in this code will be discussed in the following.

3.1.2.6.1 k-Points Sampling Electron densities and total energies are calculated by integration of electronic wave functions over the BZ in k-space

$$\rho(\mathbf{r}) = \sum_{n=1}^{N\text{occ}} \frac{1}{\Omega_{\text{BZ}}} \int_{\mathbf{k}\in\mathbf{\Omega}_{\text{BZ}}} |\varphi_{n,\mathbf{k}}(\mathbf{r})|^2 d\mathbf{k}, \tag{3.1.2.6.1.1}$$

where n denotes each band of the KS orbitals, while Ω_{BZ} refers to the cell volume of the BZ, and $\varphi_{n,\mathbf{k}}(\mathbf{r})$ indicates the KS orbitals (Bloch wave). Since it is computationally intractable to integrate over a continuous $\mathbf{k}$-point space, numerical integration, *i.e.* weighted sum is

therefore introduced

$$\rho(\mathbf{r}) \approx \sum_{n=1}^{N_{\mathrm{occ}}} \sum_{\mathbf{k}\in \mathrm{BZ}}^{N_{\mathrm{kpt}}} \omega_{\mathbf{k}} |\varphi_{n,\mathbf{k}}(\mathbf{r})|^2. \tag{3.1.2.6.1.2}$$

Here, N_{occ} and N_{kpt} determines the number of occupied orbitals and $\mathbf{k}$-points, respectively, and $\omega_{\mathbf{k}}$ is the weighting factor as a function of $\mathbf{k}$. Different methods have been proposed to find appropriate sets of $\mathbf{k}$-points. Among them, the Monkhorst-Pack (MP) grid is one of the popular method. Within the MP method, a grid of $\mathbf{k}$-points is homogeneously generated in the BZ in the reciprocal space. Moreover, by making use of lattice symmetry, the number of necessary $\mathbf{k}$-points over entire BZ is reduced to the ones in the irreducible BZ (IBZ). In certain cell geometries, *e.g.* hexagonal cells, the even meshes can break the symmetry. Thus Γ-centered grids are applied to preserve the symmetry.

3.1.2.6.2 Plane waves To fully describe the wave function in the Eq. 3.1.2.5.3.3, an infinite number of plane waves over $\mathbf{G}$ vectors should be considered, which is computationally intractable. To save the computing cost, only the plane waves that have kinetic energies less than a particular energy cutoff, E_{cut} is included in the basis sets

$$\frac{1}{2}|\mathbf{k}+\mathbf{G}|^2 \leq E_{\mathrm{cut}}. \tag{3.1.2.6.2.1}$$

However, it is still difficult to compute the electronic structures of a crystal near the nuclei by the plane-wave basis sets and choose the right E_{cut} of an orbital, due to the strong potential and oscillatory behavior of the wave functions. One way to solve this problem is applying pseudopotential. The next section will discuss this approach in details.

3.1.2.6.3 Pseudopotential Approximation Description of core electrons needs more computational efforts than valence ones. This is because in core region strong electron-nuclei interaction leads to a strong ionic potential, which causes large oscillations of valence wave functions due to the necessity of orthogonality to core wave functions. Core orbitals thus require a very fine grid of BZ integration or huge number of plane-wave basis sets to describe.

Fortunately, most of interesting electronic properties in the materials are determined by the valence electrons rather than the core electrons. Hence, to reduce the computational cost, an effective potential is introduced to replace the strong ionic potential in core region. This weak potential is called pseudopotential. Smooth pseudo wave functions can, therefore, be used instead of valence electron wave functions in this region. The pseudo wave functions, however, should be the same as the full single-electron KS wave functions outside the core region (defined by a radius cutoff, r_{c}). The ionic and pseudo potentials as well as the valence and pseudo wave functions that depicted by Payne *et al.* are shown in Fig. 3.1 [134]. Many approaches have been proposed to develop pseudopotential such as norm-conserving [135], ultrasoft [136], and projector augmented-wave (PAW) method [137]. The last one that has been implemented in the VASP code has been used to perform all DFT calculations of this dissertation, and thus it will be discussed in the following.

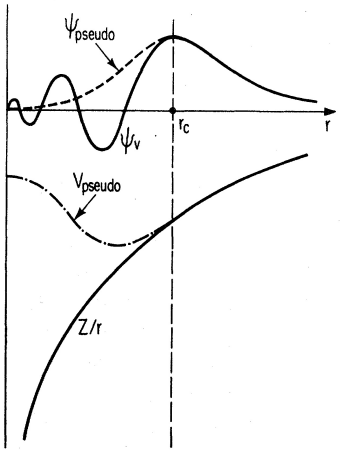

Figure 3.1: Illustration of all-electron (solid lines) and pseudo-electron (dashed lines) potentials and their wave functions. r_{c} is cutoff radius [134].

Projector augmented-wave Method The PAW method was first proposed by Blöchl in 1994 [137]. The concept of the PAW method is that it works directly with the full single-electron KS wave functions (all electron (AE) wave functions) and AE potentials. Within the PAW method, the AE wave functions ($\varphi_{n,\mathbf{k}}(\mathbf{r})$) are mapped onto the pseudo wave functions

$$|\varphi_{n,\mathbf{k}}\rangle = |\tilde{\varphi}_{n,\mathbf{k}}\rangle + \sum_i (|\phi_i\rangle - |\tilde{\phi}_i\rangle)\langle\tilde{p}_i|\tilde{\varphi}_{n,\mathbf{k}}\rangle. \qquad (3.1.2.6.3.1)$$

Here, $\tilde{\varphi}_{n,\mathbf{k}}(\mathbf{r})$ are pseudo wave functions that satisfy $|\tilde{\varphi}_{n,\mathbf{k}}\rangle = \sum_i |\tilde{\phi}_i\rangle c_i$, where c_i denotes the expansion coefficient. *n* and $\mathbf{k}$ refers to band index of KS orbital and wave vector in the BZ, respectively. The index *i* represents the atomic position ($\mathbf{R}$) and the angular momentum quantum numbers (*l, m, ...*). $|\phi_i\rangle$ and $|\tilde{\phi}_i\rangle$ are AE partial waves and pseudo partial waves.

$\langle \tilde{p}_i|$ are projector functions, which obey

$$\langle \tilde{p}_i|\tilde{\phi}_j\rangle = \delta_{ij}. \tag{3.1.2.6.3.2}$$

Since the AE partial waves are solutions of the radial Schrodinger equation

$$\left[-\frac{1}{2}\nabla^2 + V_{\text{eff}}^{\text{KS}}\right]|\phi_i\rangle = \epsilon_i^{\text{KS}}|\phi_i\rangle, \tag{3.1.2.6.3.3}$$

the pseudo partial waves can be written as follows

$$\left(-\frac{1}{2}\nabla^2 + \tilde{V}_{\text{eff}}^{\text{KS}} + \sum_{ij}|\tilde{p}_i\rangle D_{ij}\langle\tilde{p}_j|\right)|\tilde{\phi}_k\rangle = \epsilon_i^{\text{KS}}\left(1 + \sum_{ij}|\tilde{p}_i\rangle Q_{ij}\langle\tilde{p}_j|\right)|\tilde{\phi}_k\rangle, \tag{3.1.2.6.3.4}$$

where D_{ij} is the PAW strength parameters and Q_{ij} denotes augmentation charges

$$D_{ij} = \langle\phi_i| - \frac{1}{2}\nabla^2 + V_{\text{eff}}^{\text{KS}}|\phi_j\rangle - \langle\tilde{\phi}_i| - \frac{1}{2}\nabla^2 + V_{\text{eff}}^{\text{KS}}|\tilde{\phi}_j\rangle, \tag{3.1.2.6.3.5}$$

$$Q_{ij} = \langle\phi_i|\phi_j\rangle - \langle\tilde{\phi}_i|\tilde{\phi}_j\rangle.$$

The use of PAW method transforms AE wave functions into the computationally convenient pseudo wave functions that make the electronic properties of the materials can be computed by a coarse grid of BZ integration or few number of plane-wave basis sets for DFT calculations.

3.2 Electrostatic energy calculation

3.2.1 Ewald Summation

Finding the arrangement of substitution atoms or vacant Li or Na sites is a challenging task. To obtain all possible atomic configurations, the *supercell* program was used in this dissertation. The idea is to find the atomic structures by evaluating their electrostatic interactions. The Ewald summation has been implemented in this program since it is a fast and absolute

method for computing the Coulomb energy in a crystal. A detailed explanation of Ewald summation is in the following.

In a periodic system, the total Coulomb (electrostatic) energy for N particles possessing a set of point charges under boundary conditions is

$$E_{\mathrm{Coul}} = \frac{1}{2} \sum_{\mathbf{R}\in \mathrm{Z}^3}^{\dagger} \sum_{i=1}^{N} \sum_{j=1}^{N} \frac{q_i q_j}{|\mathbf{r}_{ij} + \mathbf{R}|}. \tag{3.2.1.1}$$

The factor $1/2$ is applied to cancel the double-counting of pair particles. $\mathbf{R}$ are translational vectors in the real space, implying interactions between atoms of periodic images. The dagger symbol indicates that for $\mathbf{R} = 0$ the self-interaction terms, $i = j$, are neglected. The quantity q_i and q_j denote charges of atoms, while $\mathbf{r}_{ij}$ refers to the distance between q_i and q_j charges. However, the sum in Eq. 3.2.1.1 not only converges very slowly in a crystal but also its convergence depends on the order of the summation. The Ewald sum method [138, 139] is thus introduced to evaluate E_{Coul} by rearranging Eq. 3.2.1.1 into rapidly convergent and nearly exact sums. The expression of Ewald method satisfying charge neutrality ($\sum_{i=1}^{N} q_i = 0$) with an energy of E^{R} in the real space and E^{G} in the reciprocal space can be written as follows

$$E_{\mathrm{Coul}} \equiv E_{\mathrm{Ewald}} = E^{\mathrm{R}} + E^{\mathrm{G}} - E^{\mathrm{self}}, \tag{3.2.1.2}$$

where

$$\begin{aligned} E^{\mathrm{R}} &= \frac{1}{2} \sum_{\mathbf{R}}^{\dagger} \sum_{i=1}^{N} \sum_{j=1}^{N} q_i q_j \frac{\mathrm{erfc}(\alpha |\mathbf{r}_{ij} + \mathbf{R}|)}{|\mathbf{r}_{ij} + \mathbf{R}|}, \\ E^{\mathrm{G}} &= \frac{1}{2\Omega} \sum_{\mathbf{G}\neq\mathbf{0}} \frac{4\pi}{\mathbf{G}^2} \exp(-\frac{\mathbf{G}^2}{4\alpha^2}) \sum_{i=1}^{N} \sum_{j=1}^{N} q_i q_j \exp(-i\mathbf{G}\cdot\mathbf{r}_{ij}), \\ E^{\mathrm{self}} &= \frac{\alpha}{\sqrt{\pi}} \sum_{i=1}^{N} q_i^2. \end{aligned} \tag{3.2.1.3}$$

E^{self} is the self-interaction term. The $\mathrm{erfc}(z) = 1 - \mathrm{erf}(z)$ is known as the complementary error function. α is the arbitrary Ewald constant that can alternate the width of Gaussian functions. Ω is the volume of the system. The E^{R} term can converge quickly in the real

space. This is due to the fact that when $\mathbf{R} \to \infty$, the function of $\mathrm{erfc}(\alpha \|\mathbf{r}_{ij} + \mathbf{R}\|)$ decays rapidly. The E^{G} term shows fast decay in the reciprocal space. When the system is affected by the dipole moment, the summation for E^{dipole} should be added in E_{Ewald}. Thus, Eq. 3.2.1.2 is given by

$$E_{\mathrm{Coul}} \equiv E_{\mathrm{Ewald}} = E^{\mathrm{R}} + E^{\mathrm{G}} - E^{\mathrm{self}} + E^{\mathrm{dipole}}, \tag{3.2.1.4}$$

with

$$E^{\mathrm{dipole}} = \frac{2\pi}{(1+2\epsilon')\Omega}(\sum_{i=1}^{N} q_i r_i)^2, \tag{3.2.1.5}$$

where ϵ' is the dielectric constant. The Ewald method is also implemented in VASP code for calculating all the electrostatic interactions of ions in an extended system.

Chapter 4

PUBLICATIONS

In this chapter, four publications, which are the main studies in this dissertation are illustrated. Two of them are completely computational works, and another two works are the joint projects with experimental groups form Prof. Yang-Kook Sun in Hanyang University Seoul and Prof. Seung-Taek Myung in Sejong University Seoul. In these studies, the origin of the structural changes (*i.e.* mechanical stability) in NCM and NMO as well as the effect of lattice doping on the chemical and mechanical stability of NCM and NMO were investigated and analyzed in details.

4.1 Publication M1

"On the origin of non-monotonic variation of the lattice parameters of $LiNi_{1/3}Co_{1/3}Mn_{1/3}O_2$ with delithiation/lithiation: a first-principles study"

L.-Y. Kuo, O. Guillon and P. Kaghazchi

J. Mater. Chem. A, **8**, 13832 (2020)

DOI: 10.1039/D0TA02319A

URL: http://dx.doi.org/10.1039/D0TA02319A

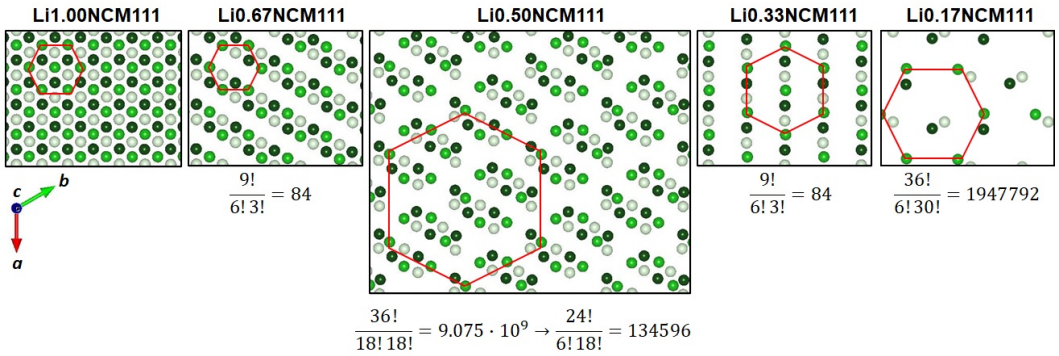

Figure 4.1: Graphical Abstract [140].

Author contributions

The first publication (**M1**) was a computational work proposed by Dr. Payam Kaghazchi. Most of the computational results were analyzed by him and partly by me. I performed the electrostatic (Coulomb energy) and DFT calculations as well as prepared the figures. The manuscript was mainly written by Dr. Payam Kaghazchi. Dr. Payam Kaghazchi, Prof. Olivier Guillon and I discussed the final results and finished the manuscript.

Journal of Materials Chemistry A

ROYAL SOCIETY OF CHEMISTRY

PAPER

View Article Online
View Journal | View Issue

Cite this: *J. Mater. Chem. A*, 2020, **8**, 13832

On the origin of non-monotonic variation of the lattice parameters of $LiNi_{1/3}Co_{1/3}Mn_{1/3}O_2$ with lithiation/delithiation: a first-principles study†

Liang-Yin Kuo, [ab] Olivier Guillon[b] and Payam Kaghazchi *[b]

Received 27th February 2020
Accepted 1st June 2020

DOI: 10.1039/d0ta02319a

rsc.li/materials-a

Here, we show that the non-monotonic variation of lattice parameters of $Li_xNi_{1/3}Co_{1/3}Mn_{1/3}O_2$ during delithiation/lithiation can be predicted in good agreement with experimental results by applying an approach combining an extensive set of Coulomb energy and density functional theory calculations. Moreover, the influence of choosing an exchange-correlation functional on our results is discussed. By analyzing the local spin polarization, spin density plot, density of states, and Bader charges, the reason behind this behavior is explained. It is found that the presence/absence of electrostatic Li–O interactions and Jahn–Teller distortion and oxidation of O anions are key parameters to control the lattice parameter changes. In particular, the contraction of c for $0.5 > x$, which has not been fully explained so far, is found to be due to the vanishing of the Jahn–Teller distortion in NiO_6 octahedra. The O3 → O1 phase transition for low concentrations of Li, which has also not been justified until now, is shown to be driven by strengthening of ionic bonds and electrostatic interaction in the latter phase.

Introduction

Although $LiCoO_2$ (LCO) is the most widely used cathode material for lithium-ion batteries (LIBs) in small-scale devices,[1,2] it is not a suitable candidate for LIBs in electric vehicles because of its low energy density and the high cost of Co metal.[3] The major reason for the low energy density is its structural instability (due to a large volume change and/or phase transition) upon more than half delithiation. Thus, the charge process should be restricted below this level resulting in a low practical voltage of LCO.[4] $LiNiO_2$ (LNO) has the same space group and atomic structure as LCO, while it consists of low-cost Ni metal and provides higher energy density than LCO as more Li ions can be safely (from the structural stability point of view) extracted from LNO during charging. The structural instability occurs only after removing ~0.75 Li ions.[5] However, the thermal instability (due to the high reactivity with the electrolyte) of LNO is more severe than in LCO.[6,7] $LiMnO_2$ (LMO) contains Mn which is cheaper and less toxic than Co and Ni metals.[8] Moreover, it provides higher safety (thermal stability) than LCO and LNO. However, LMO possesses a lower energy density (due to a lower structural stability) than LCO and LNO.[9,10] To combine advantages of LCO, LNO, and LMO, $LiNi_xCo_yMn_{1-x-y}O_2$ cathodes were proposed, synthesized, and even commercialized.[11] Among various possible NCM systems with different Ni, Co, and Mn ratios, $LiNi_{1/3}Co_{1/3}Mn_{1/3}O_2$ (hereafter called NCM111) is one of the most commonly used and studied systems.[12–14] The structural stability of NCM111 is higher than that of LCO, as the cracking of NCM111 microstructures that leads to their voltage and capacity fading[15–22] occurs at higher levels of lithiation/delithiation in comparison to LCO. The main reason behind the microstructure cracking of cathode materials such as NCM111 is an anisotropic change in their lattice parameters during charging/discharging. Understanding the mechanism of this phenomenon is therefore important to improve the performance of NCM cathode materials.

During charging (*i.e.* delithiation), the lattice parameter a ($a = b$) of $Li_xNi_{1/3}Co_{1/3}Mn_{1/3}O_2$ (hereafter called LixNCM111) contracts for $1.00 > x > 0.35$, while it expands for $0.35 > x$.[23] However, the lattice parameter c expands for $1.00 > x > 0.51$ and then it contracts for $0.51 > x > 0.29$.[24] These changes in a and c cause the unit cell volume to contract slightly for $1.00 > x > 0.35$ and then strongly for $0.35 > x$.[23] Experimental measurements by Li *et al.*[25] showed that the contraction of a is because of the delithiation-induced oxidation of transition metal (TM) cations which reduces their ionic radii. The expansion of c in NCM111 was mainly explained to be because of the increase in the electrostatic O–O repulsive force resulting from the weakening of screening of O charge by Li ions during delithiation.[26,27] However, the contraction of the c-axis in NCM cathodes for $x <$ 0.50 has not been fully explained. The most common belief is that oxidation of O anions (together with TM cations) at high

[a]*Physikalische und Theoretische Chemie, Freie Universität Berlin, Arnimallee 22, D-14195 Berlin, Germany. E-mail: kuoliangyin@zedat.fu-berlin.de*

[b]*Forschungszentrum Jülich GmbH, Institute of Energy and Climate Research, Materials Synthesis and Processing (IEK-1), D-52425, Jülich, Germany. E-mail: o.guillon@fz-juelich.de; p.kaghazchi@fz-juelich.de*

† Electronic supplementary information (ESI) available. See DOI: 10.1039/d0ta02319a

delithiation levels weakens interlayer O–O repulsions leading to the contraction of c.[16] The delithiation-induced decrease in the negative charge of O[28] and/or stronger TM–O bonds (due to more hybridization of TM–O orbitals)[29] had been proposed before by theoreticians.

Density functional theory (DFT) has been applied to simulate lattice parameters (*i.e.* unit cell volume) changes through delithiation. For example, DFT calculations (using the local density approximation (LDA) functional) by Koyama *et al.*[30] found that the parameter a decreases from $x = 1.00$ to $x = 0.33$, while it increases from $x = 0.33$ to $x = 0.00$. However, it is known that NCM111 undergoes a phase transition from O3 to O1 for very deep delithiation levels, *i.e.* $x < 0.23$.[23] Moreover, they found that the c value increases monotonically from $x = 1.00$ to $x = 0.33$, while it decreases from $x = 0.33$ to $x = 0.00$.[30] However, experimental results show that the contraction of c starts for $x < 0.51$. Hwang *et al.*[29] used the more accurate generalized gradient approximation (GGA) of the Perdew–Burke–Ernzerhof (PBE)[31] functional compared to LDA for their DFT calculation to study this system. They found that the size of a decreases from $x = 1.00$ to $x = 0.50$, while it increases from $x = 0.50$ to $x = 0.00$. However, according to the experimental data, increase in a should occur after removing 0.67 Li.[23] Furthermore, their results show that the c value increases from $x = 1.00$ to $x = 0.33$ and decreases from $x = 0.33$ to $x = 0.00$. The decrease in the c value from $x = 0.33$ to $x = 0.17$ was calculated to be only 0.018 Å. In addition, they found that the value of c for $x = 0.17$ is 0.71 Å higher than the value of c for $x = 1.00$. Experimental measurements, however, reported that the c value for $x < 0.30$ is 0.39 Å shorter than that for $x = 1.00$.[26] Min *et al.*[32] carried out GGA-PBE calculation to study NCM with different Ni contents. They showed that the value of a decreases from $x = 1.00$ to $x \approx 0.35$ and then increases from the $x \approx 0.35$ to $x = 0.00$ state. However, the c value increases from $x = 1.00$ to $x \approx 0.35$ and then decreases for $x \approx 0.35$ to $x = 0.00$. They proposed that the experimental results can be reproduced only by considering a layer-by-layer delithiation mechanism, which has not been reported so far by any experimental or other theoretical studies. A comparison between the aforementioned theoretical studies shows that the model structure (arrangement of TMs and Li ions), type of exchange-correlation (XC) functional, and computational setup (*e.g.* spin polarization) are key points in modelling and understanding lattice parameter changes with delithiation. In these studies, in order to find the arrangement of Li ions for various Li concentrations, a series of DFT calculations[29,30] or cluster expansion (CE) has been applied.[32] Both approaches have advantages and disadvantages. Sampling of configurations by DFT calculation is limited by the computational cost and time. Applying the CE method can misguide us to find minimum-energy structures for systems where magnetization of TM cations is very sensitive to the concentration and arrangement of Li ions. The other more promising types of XC functionals for studying metal-oxide systems such as PBE + U[33] have been used to simulate Ni-rich NCM,[34] while the Heyd–Scuseria–Ernzerhof (HSE)[35] and recently developed SCAN (Strongly Constrained and Appropriately Normed)[36–39] functionals have not been so far applied to study lattice changes in NCMxy1-x-y cathodes. Recently, Chakraborty *et al.*[40] calculated the lattice parameters, magnetic moments, density of states, and voltage profiles of LCO, LNO and LMO in different lithiated/delithiated states by using PBE, PBE + U, and SCAN. Their results showed that the SCAN functional performs better than the PBE functional for the prediction of band-gaps, while better than the PBE + U functional for calculation of DOS, and better than both PBE and PBE + U functionals for computation of lattice parameters.[37]

In this work, by combining an extensive Coulomb energy analysis and DFT calculations, we obtain the Li arrangement in LixNCM111 as a function of Li concentration x. The influence of exchange-correlation functionals, in particular SCAN, on the calculated lattice parameters is discussed. By analyzing electronic and atomic structures, the reason for the non-monotonic change of lattice parameters in NCM111 will be explained.

Results and discussion

Our DFT-PBE calculations, in agreement with a previous DFT-HSE06 study,[45] showed that a homogeneous distribution of TM cations in fully lithiated NCM111 (Li1.00NCM111) is the most favourable structure (see Fig. 1 and S1 in the ESI†). Focusing on this structure, we explored the most favourable arrangement of Li ions in Li sites for various Li concentrations x in LixNCM111. To achieve this aim, we first calculated the total Coulomb energies (E_C) of a large number of possible configurations for each Li concentration as follows. For Li0.67NCM111 and Li0.33NCM111, which were modelled with $1 \times 1 \times 1$ unit cells (only for Coulomb energy analysis), we considered all possible arrangements of Li ions in Li sites, namely $\frac{9!}{6!3!} = 84$ configurations. However, for Li0.50NCM111, which we had to model with a $2 \times 2 \times 1$ supercell, there exists a large number of possible configurations of $\frac{36!}{18!18!} = 9.075 \times 10^9$, which is computationally intractable. In this case, the most favorable structure of Li0.67NCM111 with a $2 \times 2 \times 1$ supercell was considered and all possible arrangements of 18 Li ions in 24 occupied Li sites, namely $\frac{24!}{6!18!} = 134\,596$ configurations, were modelled. For Li0.17NCM111, we considered all possible Li arrangements in Li sites in a $2 \times 2 \times 1$ supercell and modelled $\frac{36!}{30!6!} = 1\,947\,792$ structures. Two sets of charge values, *i.e.* two charge-balancing mechanisms, were considered for computing the total Coulomb energies: (I) charge values of 3.00+, 3.33+, 3.50+, 3.67+, and 3.83 + for each TM (Ni, Co and Mn) cation at $x = 1.00$, $x = 0.67$, $x = 0.50$, $x = 0.33$, and $x = 0.17$, respectively and (II) charge values of 2+, 3+, 4+ for Ni, 3+ and 4+ for Co depending on the Li concentration, and 4+ for Mn. For both mechanisms we considered charges of 1+ for Li and 2− for O, respectively.

The calculated E_C values for configurations 1–50 with charge balancing mechanism I and II are illustrated in Fig. S2.† For Li0.67NCM111 and Li0.33NCM111, we performed DFT-PBE calculation for 6 and 10 distinguishable structures with the

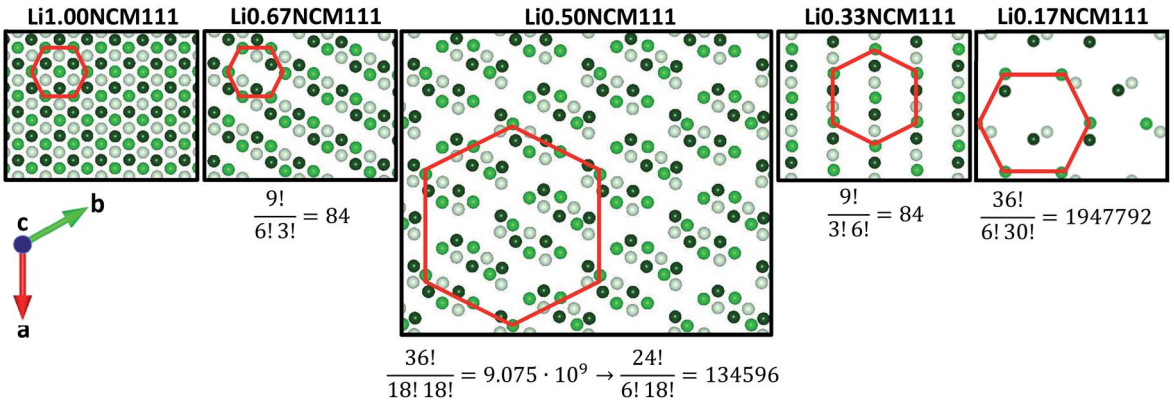

Fig. 1 Top views of Li layers in the most favourable structures and the considered number of configurations for the Coulomb-energy analysis for Li*x*NCM111 with various Li concentrations *x*.

lowest E_C values. The DFT-PBE-calculated most favourable structures for $x = 0.67$ (configuration vi) and $x = 0.33$ (configuration i) possess well-ordered hexagonal arrangements of Li ions at each layer. Since the lowest (DFT-PBE) total-energy structure was among the determined structures from Coulomb energy analysis with mechanism I for Li0.33NCM111 and Li0.67NCM111, we further considered only mechanism I to determine the electrostatically most favourable structures for Li0.50NCM111. Afterward, we performed DFT-PBE calculations for 7 distinguishable Li arrangements with the lowest E_C values for Li0.50NCM111. The configuration v was then found to be the minimum-total-energy structure. Furthermore, 3 well-ordered arrangements of Li ions (Fig. S2:† viii, ix, x) were modelled from the configuration v. These 3 configurations were investigated because for Li0.50NCM111 we had to start with the structure of Li0.67NCM111 and, therefore, we might have missed some important (symmetric) structures. Comparing the total energies of all 10 (7 + 3) DFT-PBE calculations showed that the most favourable structure is configuration x. Finally, for Li0.17NCM111, we carried out 50 DFT-PBE calculations for topmost favourable structures determined after performing 1 947 792 total Coulomb-energy calculations. The minimum total-energy structure according to DFT-PBE, namely configuration v, was found to have a well-ordered hexagonal arrangement of Li ions at each layer (see Fig. S2†).

The computed lattice parameters ($a = b$ and c) and corresponding volume changes for Li*x*NCM111 using DFT-PBE, PBE + *U*, and SCAN are illustrated in Fig. 2. All three XC functionals indicate that the value of a decreases with delithiation from $x = 1.00$ to $x = 0.33$ and increases from $x = 0.33$ to $x = 0.17$. However, the value of c expands from $x = 1.00$ to $x = 0.50$, then it shrinks slightly for $x = 0.50 \rightarrow 0.33$, and finally it decreases significantly for $x = 0.33 \rightarrow 0.17$. The maximum value of c is found for $x = 0.50$. Nevertheless, the volume always decreases from $x = 1.00$ to $x = 0.17$, being more significant for $x = 0.33$ to $x = 0.17$. Although the DFT-PBE and SCAN results are similar, generally, the calculated absolute values and changes in a, c, and volume with the latter functional are more comparable to the experimental data. For example, the volume decrease ΔV for $x = 1.00 \rightarrow x = 0.33$ is −1.83% and −3.32%, respectively, with DFT-PBE and SCAN functionals. The latter functional predicts that (using a linear interpolation) $c = 13.877$ Å, $a = 2.841$ Å, and $\Delta V = -4.61\%$ for $x = 0.30$. In comparison to DFT-PBE and PBE + *U* results, the DFT-SCAN data are closer to the experimental values $c = 13.876(1)$ Å, $a = 2.829(1)$ Å, and $\Delta V = -5.14\%$ (see Fig. 2) by Hua *et al.*[26] reported for Li*x*NCM111 with $x < \sim 0.30$ Li. The variation of a and volume with x is found to be larger with DFT-PBE + *U* than the other two functionals and the experimental data by Petersburg *et al.*[24] and Hua *et al.*[26] The DFT-PBE + *U*-overestimated decrease in volume is because of overestimation of the decrease in the a value. Comparing calculated

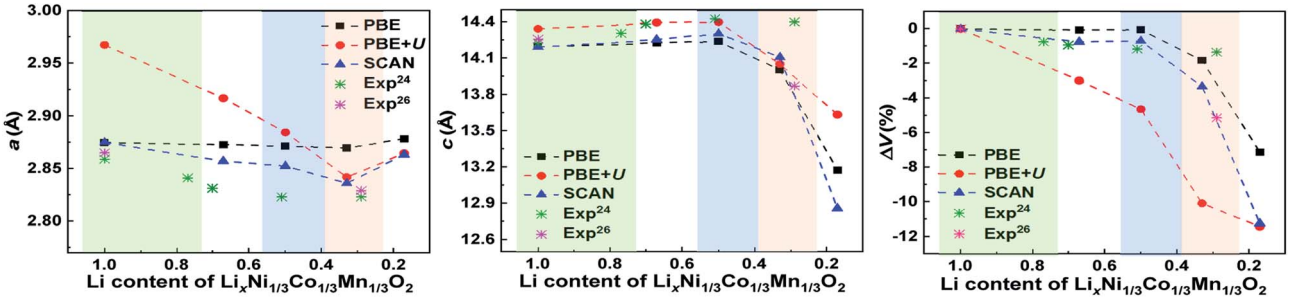

Fig. 2 Calculated variation of lattice parameters and unit cell volume of Li*x*NCM111 with delithiation using DFT-PBE, PBE + *U* ($U_{Ni} = 6.8$ eV, $U_{Co} = 5.9$ eV, and $U_{Mn} = 5.2$ eV), and SCAN functionals. Experimental results are also given for comparison.

a, c, and volume with various U values for Ni (see Fig. S3 in ESI†), we find no significant changes for $0.33 < x < 1.00$, where only oxidation of Ni cations occurs, as will be discussed later in this article. However, for $x < 0.33$, where oxidation of Co cations occurs, the important role of charge localization on Ni cations to determine the lattice sizes appears. As will be discussed later, the increase in the value of a for $x < 0.33$ is due to the strengthening of electrostatic repulsion between the TM cations. Non-realistic delocalization of holes on Ni cations which arises by considering smaller U values cannot reproduce the experimental data showing the increase of the a parameter.

To find the reason behind lattice parameter and volume changes, we further calculated the local number of unpaired spin N↑–N↓ (NUS), spin density difference (SDD), and density of states (DOS) illustrated in Fig. 3 and Bader charges and bond lengths shown in Fig. 4. Our results show that SCAN predicts more reasonable NUS values than the other two functionals. For example, calculated total NUS values of 58.5, 46.5, and 35.6 with SCAN for Li1.00NCM111, Li0.67NCM111, and Li0.33NCM111, respectively, are in good agreement with the NUS values 60 (NUS for Ni: 12×2 and NUS for Mn: 12×3), 48 (NUS for Ni: 12×1 and NUS for Mn: 12×3), and 36 (NUS for Mn: 12×3) which are expected for $Li_xNi_{12}Co_{12}Mn_{12}O_{72}$ supercells with pure ionic bonds when considering the formal charge states of ions. The calculated NUS values with different XC functionals and those which are expected for pure ionic crystals of LixNCM111 are listed in Table S1 of the ESI.† In addition, as mentioned before, the lattice parameters calculated with SCAN are more comparable to measurements. We therefore continued our analyzis by using DFT-SCAN calculation. We focused on the following Li concentrations: $x = 1.00$, 0.67, and 0.33, since for these cases a similar electronic configuration is expected for each type of TM cation. It is worth mentioning that the DOS of the d orbitals of Ni, Co, and Mn is clearly different (see Fig. 3) from that of a simple t_{2g}–e_g splitting model. For example, from the classical picture, the electronic configuration of Ni cations is expected to be $t_{2g}^6e_g^2$. However, besides occupations of up-spin and down-spin of t_{2g} and up-spin of e_g orbitals for the Ni cations, a partial occupation of down-spin of e_g and a depletion of down-spin of t_{2g} are also observed in the DOS plot. This is because of a large overlap between t_{2g} and e_g orbitals for all the TM cations at all the Li concentrations. The overlap and broadening of t_{2g} and e_g orbitals lead to uncertainty in determining electronic configuration of the TM cations. Thus, as will be shown in the following a detailed analysis of the NUS, SDD, and Bader charge together with the DOS is indispensable.

Li1.00NCM111

The SDD plot shows unpaired up-spin on all the O anions indicating that the O atoms are not completely reduced. The SDD feature on Mn is larger than that on Ni confirming that the oxidation state of the former is larger. However, in both cases, the charge state is lower than that expected: 1.64+ for Ni and 3.87+ for Mn. For the sake of simplicity, in the following, we discuss our SDD results with respect to a complete ionic system. The up-spin electrons (yellow isosurface) on p(O) are directed toward Ni confirming back donation of down-spin electrons to e_g(Ni) orbitals. The existence of down-spin states at -0.80 eV $\leq \varepsilon - \varepsilon_F \leq -0.15$ eV in the DOS of e_g(Ni), *i.e.* d_{z^2}(Ni) and $d_{x^2-y^2}$(Ni), confirms this hypothesis. The non-zero NUS (-0.03) together with DOS peaks in -0.86 eV $\leq \varepsilon - \varepsilon_F \leq -0.20$ eV for Co cations shows partial up-spin and down-spin occupation of e_g states, the latter being slightly larger in particular for $d_{x^2-y^2}$(Co). These results indicate that Co cations have charge states slightly lower than 3+ charge. The SDD on Co cations, however, is so small that it is not observed with a 0.004 isosurface. The down-spin electrons (blue isosurface) on p(O) orbitals towards d(Mn) orbitals arise from an up-spin electron transfer from p(O) to e_g(Mn). The corresponding DOS plot shows the presence of e_g(Mn) features (more up-spin states) in -1.58 eV $\leq \varepsilon - \varepsilon_F \leq -0.18$ eV. Moreover, a back-donation of down-spin electrons from p(O) to t_{2g}(Mn) with pre-existing three up-spin electrons can also be observed in -7.10 eV $\leq \varepsilon - \varepsilon_F \leq -4.91$ eV. Back donation of electrons from O to TMs can be an indication of the existence of partial covalent bonding between TMs and O in fully lithiated NCM111. It is hard to conclude such bonding from our DOS data. TM–O covalency has also been reported for fully lithiated LMO by experimentalists[46] and fully lithiated NCM811 by theoreticians.[47] From the DOS data, we find a band gap of 0.56 eV confirming the semiconducting nature of Li1.00NCM111. The DOS plots also demonstrate that the e_g states of Ni and the t_{2g} states of Co are close to the Fermi level and are likely to be depleted with delithiation. The Bader charge analysis (Fig. 4a) will be discussed for the lower lithium concentration cases since only the relative values can help us to analyse oxidation or reduction of ions.

Li0.67NCM111

Oxidation of Ni cations with respect to the full lithiation state can be recognized by comparing the DOS plots for Li1.00NCM111 and Li0.67NCM11 where up-spin features close to ε_F, *i.e.* e_g(Ni) states, become narrower and lower in the latter case. The SDD plots also show oxidation of all the Ni cations as their SDDs become smaller after extracting 0.33 Li. This can also be qualitatively concluded from the Bader charge analysis where an oxidation of 0.14 $|e|$ was observed. Since the up-spin d_{z^2}(Ni) states are larger than the $d_{x^2-y^2}$(Ni) ones at -0.61 eV $\leq \varepsilon - \varepsilon_F \leq -0.19$ eV and the SDD features are d_{z^2} like we propose that the electron is removed from the $d_{x^2-y^2}$(Ni) orbital. The delithiation-induced electron removal from the $d_{x^2-y^2}$ orbital of Ni^{2+} has also been proposed by Radin *et al.*[48] for Ni-based cathodes. A similar oxidation mechanism has also been reported by Dompablo *et al.*[49] based on DFT-PBE calculated Ni–O bond lengths. From the average NUS value of 0.80 for Ni we estimated the charge state of Ni to be 2.48+ for $x = 0.67$ as Ni is oxidized by 0.84 $|e|$. Hoang *et al.* calculated the NUS for Ni^{2+} to be 0.91.[45] One important result of the formation of $Ni^{(3-\Delta)+}$ is the creation of Jahn–Teller (J–T) distortion upon which the average axial Ni–O bond lengths ($\bar{d}^{Ni}_{axial} = 2.04$ Å) are longer than the average equatorial Ni–O bond lengths ($\bar{d}^{Ni}_{equatorial} = 1.93$ Å). A similar result to our calculation has been reported by Hoang *et al.* using DFT-HSE calculation: two

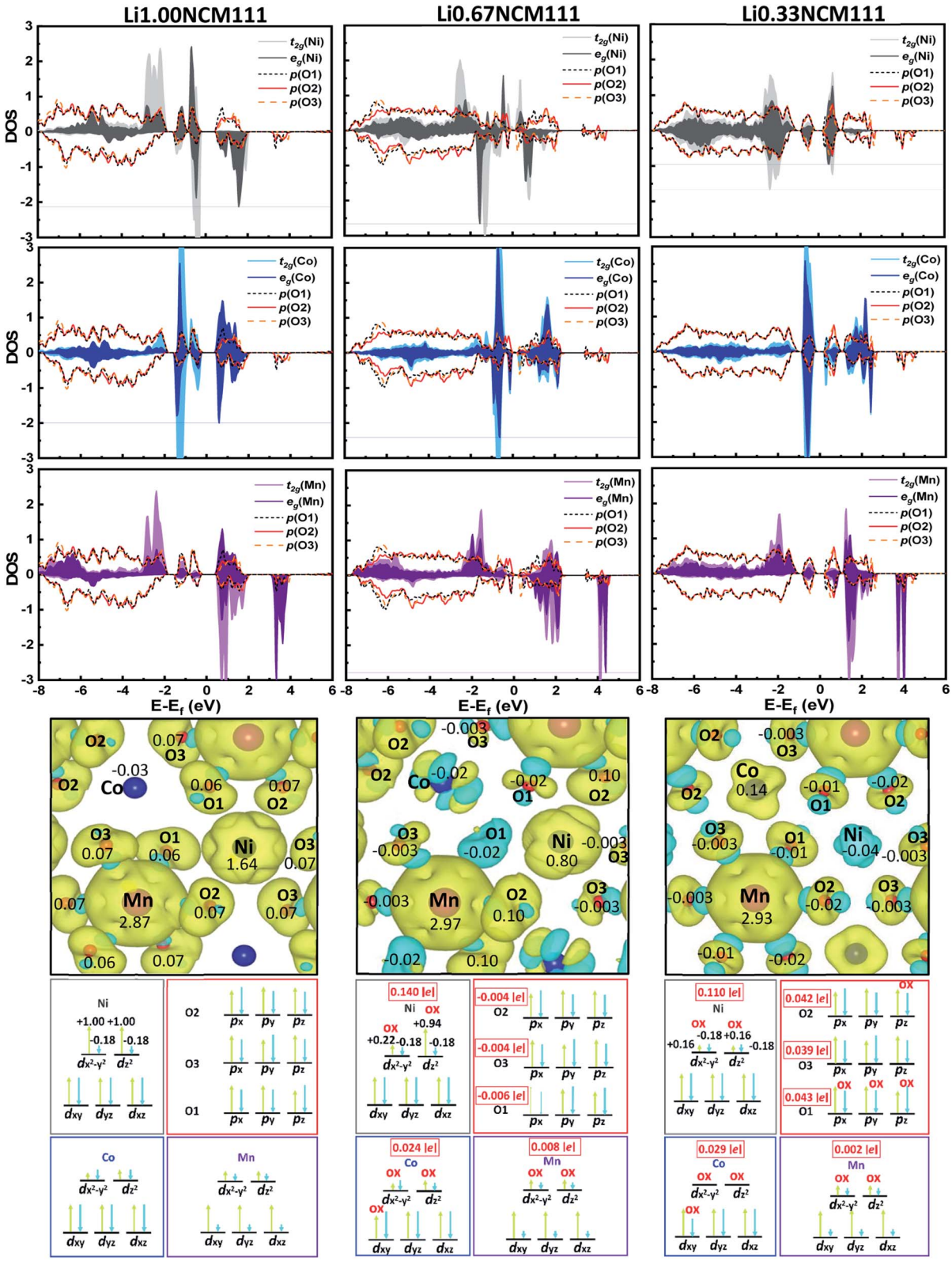

Fig. 3 Density of states (DOS), spatial spin density difference (SDD) with average local numbers of unpaired spin (NUS) on each ion, and proposed electronic configurations with average Bader charges (in |e|) in the most favourable LixNCM111 structures based on DFT-SCAN calculation. Ni, Co, Mn, and O are in gray, blue, purple, and red, respectively. The atomic coordinates were rotated about the b_y-axis to align axial TM–O bonds (in TMO_6 octahedra) along the global c_z-axis of the unit cell to assign e_g and t_{2g} states. Up-and down-spins in SDD are in yellow and blue, respectively. Projected DOSs are shown in Fig. S6–S8.†

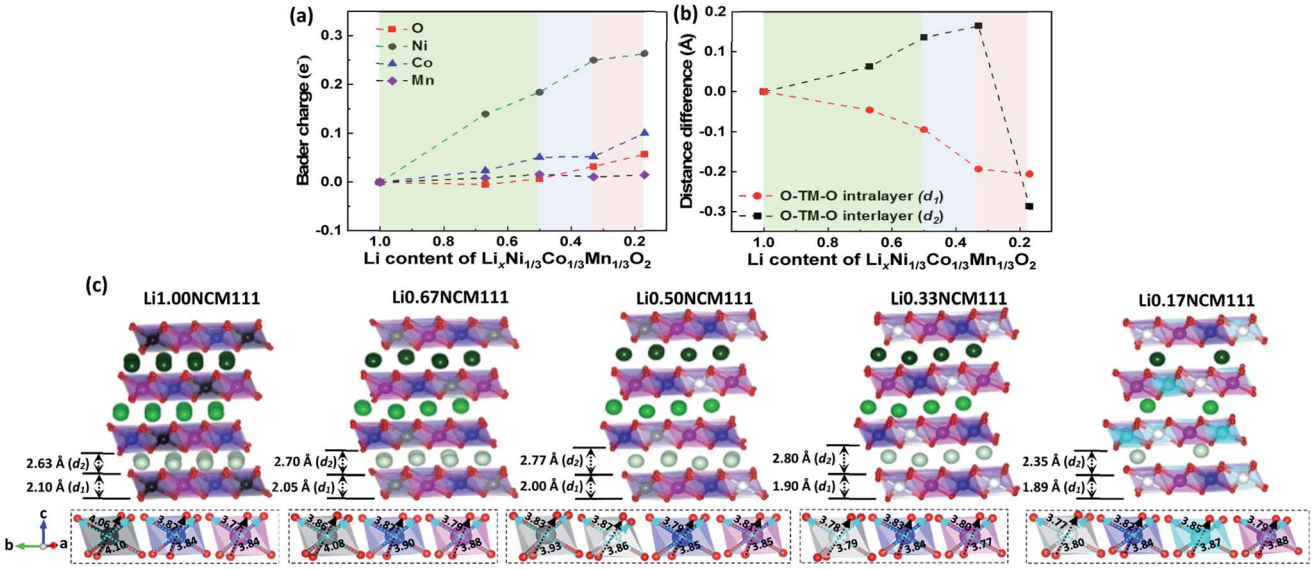

Fig. 4 Calculated (a) Bader charges and (b) projected intralayer O–TM–O (d_1) and interlayer O–TM–O (d_2) lengths along the *c* axis. (c) Details of bond lengths in TM–O octahedra. Ni, Co, Mn, O, and Li are in grey (dark: $Ni^{(2-\Delta)+}$, light: $Ni^{(3-\Delta)+}$, white: $Ni^{(4-\Delta)+}$), blue (dark: $Co^{(3-\Delta)+}$, light: $Co^{(4-\Delta)+}$), purple, red, and green (lighter at deeper layers), respectively.

long Ni–O bonds of 2.07 Å and four short Ni–O bonds of 1.91 Å.[45] The J–T effect for Ni^{3+} has also been observed by experimental measurements.[24,50] The corresponding SDD plot clearly shows an enlargement of up-spin electrons on the p orbitals of each O anion overlapping with the d_{z^2} orbitals of the Ni cations, hereafter called p(O2). This is accompanied by the contraction of axial O2–Ni–O2 bond lengths. Small parts of the topmost e_g states of Co and Mn disappear as well. This means that Co and Mn are also partially oxidized. The Bader charge values, also, confirm that, in comparison to that for $x = 1.00$, Co and Mn are slightly oxidized. The oxidation state of Co cannot be estimated from the change in the NUS value. This is because there are both up-spin and down-spin electron transfers from Co to O. Thus, the local NUS value on Co changes slightly from −0.03 ($x = 1.00$) to −0.02 ($x = 0.67$). In this case, the Bader charge values help to conclude that oxidation of Co (0.024 $|e|$) is higher than that of Mn (0.008 $|e|$). A comparison between the SDD for $x = 1.00$ and $x = 0.67$ confirms a slight internal down-spin electron transfer from e_g(Co) to p(O3) and probably a slight delithiation-induced oxidation. The DOS plots show a large overlap between e_g(Ni) and e_g(Co) with p(O) at -0.27 eV $\leq \varepsilon - \varepsilon_F \leq -0.01$ eV, but a very small overlap between e_g(Mn) and p(O). This indicates that the internal electron transfers are mainly between Ni and Co with O. Considering the changes in the SDD and Bader charge variation (−0.005 $|e|$) on O anions and the increase of the NUS by 0.10 and Bader charge by 0.008 $|e|$ on Mn for $x = 1.00 \rightarrow x = 0.67$, we conclude a partial down-spin electron transfer from d(Mn), probably from e_g, to p(O1) and p(O3). Moreover, there should be a delithiation-induced oxidation of Mn since the amount of O reduction is much smaller than the oxidation of Mn. Note that the oxidation of Mn cannot be observed by comparing the SDD plots for $x = 1.00$ and $x = 0.67$ cases since the spin density variation is considerably smaller than the original spin density of the Mn cations. No clear J–T distortion is observed for $Co^{(3-\Delta)+}$ and $Mn^{(4-\Delta)+}$, which is in line with previous experimental[24] and theoretical[20] studies. The small difference between $\bar{d}_{axial}$ = 1.95 Å and $\bar{d}_{equatorial}$ = 1.94 Å in Co–O octahedra and that between $\bar{d}_{axial}$ = 1.94 Å and $\bar{d}_{equatorial}$ = 1.90 Å in Mn–O octahedra, respectively, are induced due to J–T distortion in Ni–O and symmetry breaking due to the partial oxidation of Co and Mn. The Bader charge analysis indicates that in average all O anions are slightly reduced when $x = 1.00 \rightarrow x = 0.67$. The local NUS and SDD of O and TM cations help us to find the mechanism of O anions reduction, which is governed by the transfer of up- and down-spin electrons from TMs to O anions. The SDD figures indicate an up-spin electron transfer from e_g(Ni) to p(O2), while down-spin from e_g(Co) and e_g(Mn) to p(O3) and p(O1). Appearance of up-spin (yellow-colour) on Co is an indication of down-spin electron transfer from Co to O. However, the overall reduction of O anions is very small, which might be an indication of partial oxidation of O anions, besides the electron transfers from TMs to O. Oxidation of O has been also reported experimentally[51] and theoretically.[28,47] Similar to the case of Li1.00NCM111, we cannot comment on the formation of TM–O covalent bonds from our DOS data, but partial electron pairing in TM orbitals might be an indication of such bonds in Li0.67NCM111.

Li0.33NCM111

Upon delithiation ($x = 0.67 \rightarrow x = 0.33$) the topmost features of the d orbitals of Ni below ε_F, namely shallow d_{z^2}(Ni) states, disappear indicating a further oxidation of Ni ions. The SDD plots clearly show the oxidation of Ni cations as well. The Bader charge analysis also qualitatively confirms the oxidation of Ni (by 0.11 $|e|$). The delithiation-induced oxidation of d_{z^2}(Ni) for $x = 0.67 \rightarrow x = 0.33$ agrees with previous experimental[50] and theoretical[29] studies. From the average NUS value of −0.04 on Ni, we

estimate a removal of 0.84 up-spin electrons from e_g(Ni) and a charge state of 3.32+ at $x = 0.33$. Calculated average NUS values of −0.11,[52] 0.00,[53] and 0.10,[47] (absolute NUS) have been reported for Ni^{4+} in NCM systems by performing DFT-PBE + U and DFT-PBE calculation. The coexistence of both spin states in e_g(Ni) can be seen from the DOS plot showing down-spin and up-spin features at $-0.87\ \text{eV} \leq \varepsilon - \varepsilon_F \leq -0.17\ \text{eV}$, the downward peaks being larger. An overlap between e_g(Ni) and p(O) in the aforementioned energy range indicates that a small up-spin electron transfer from Ni to O is possible. The formation of $Ni^{(4-\Delta)+}$ leads to the suppression of Jahn–Teller (J–T) distortion where $\overline{d}^{Ni}_{axial} = 1.90$ Å becomes comparable to $\overline{d}^{Ni}_{equatorial} = 1.89$ Å. The absence of J–T distortion in Ni^{4+}–O has also been reported in previous experimental[24] and theoretical[30] studies. A comparison between NUS values for $x = 0.67$ and $x = 0.33$ does not provide a certain quantitative value for oxidation of Co. Nevertheless, the Bader charge analysis shows a larger oxidation of Co compared to Mn. An experimental study by Saadoune *et al.*[54] has also proposed that the oxidation of Co cations starts before all Ni cations are completely oxidized. The disappearance of down-spin states in the DOS plot of Co at $-0.32\ \text{eV} \leq \varepsilon - \varepsilon_F \leq -0.02\ \text{eV}$ when $x = 0.67 \rightarrow x = 0.33$ and a slightly larger density of up-spin states in the DOS plot of the latter case indicate that the yellow-colour of SDD on Co is due to the removal of down-spin electrons from Co. An electron transfer from O to Co is not observed in the DOS plots as no p(O) state exists below ε_F. The NUS data show a back-donation of 0.04 down-spin electrons from O anions to e_g(Mn), showing the reduction of Mn by ∼0.04 $|e|$. The electron transfer can be confirmed from an overlap between e_g(Mn) and p(O) states in the energy range of $-0.87\ \text{eV} \leq \varepsilon - \varepsilon_F \leq -0.17\ \text{eV}$ which can be seen in the corresponding DOS plot. In average, about 0.12 up-spin electron is removed from p(O1) anions. Moreover, there is a very small down-spin electron oxidation and/or transfer (to Mn) from p(O3) and p(O1) anions meaning a small oxidation of these O anions compared to that for $x = 0.67$. The average oxidation of all O anions is estimated to be 0.037 $|e|$ which is 0.008 $|e|$ larger than that of Co cations. Note that the majority of electron removal occurs from O1. Comparing DOSs shows a clear hybridization between d(Ni) and p(O) orbitals for $-7.84\ \text{eV} \leq \varepsilon - \varepsilon_F \leq -1.09\ \text{eV}$ in Li0.33NCM111 which is not observed in Li1.00NCM111 and Li0.67NCM111. This result is in line with previous experimental[25] and theoretical[29] studies reporting a stronger Ni–O covalency at low Li contents.

Bader charge and TM–O bond length results in Fig. 4 indicate oxidation of several $Ni^{(3-\Delta)+}$ cations and suppression of J–T distortion in the NiO_6 octahedra when 0.17 Li is removed from Li0.67NCM111. The O anions are slightly oxidized when $x = 0.67 \rightarrow 0.50$. Fig. 4 shows that a strong oxidation of O anions occurs for $x = 0.33 \rightarrow 0.17$, similar to the case of $x = 0.50 \rightarrow 0.33$. We also find that some of the Co cations start to oxidize strongly when $x = 0.33 \rightarrow 0.17$ (see Fig. S4 in the ESI†).

Fig. 4b shows the average projected O–O separation on the c axis for the O–TM–O intralayer (d_1) and that for the O–TM–O interlayer (d_2). Removing 0.33 Li from Li1.00NCM111 causes d_1 to shrink by 2.15%, which is due to the radius contraction of all the Ni cations that are oxidized (see the SDD plots and NUS values in Fig. 3 as well as Bader charge analysis in Fig. 4a) in Li0.67NCM111 with respect to Li1.00NCM111. Due to the J–T distortion for $Ni^{(3-\Delta)+}$, axial Ni–O bond lengths only slightly shrink (by 0.02 Å), while equatorial Ni–O bond lengths contract by 0.2 Å in the delithiated case compared to the fully lithiated one. However, d_2 expands by 2.40% when $x = 1.00 \rightarrow 0.67$. According to a previous explanation,[26] this is due to the weakening of screening of O charges by Li ions. Our Bader charge calculations in Fig. 4a, however, indicate that O anions are only slightly reduced and therefore their charge magnitudes probably play no significant role in controlling the O–O interaction. We therefore propose that the expansion of d_2 is mainly because of vanishing of the attractive electrostatic interactions of removed Li ions with O anions. As the expansion of d_2 is larger than the contraction of d_1, the c lattice parameter slightly increases. Further removing 0.17 Li from Li0.67NCM111 results in a contraction of d_1 by 2.40%, which is larger than the 2.15% contraction arising when $x = 1.00 \rightarrow 0.67$. This is because, due to the further oxidation, the J–T distortion of half of the Ni cations in the unit cell is released. In this case, the oxidation of O anions (see Fig. 4a) tends to shrink d_2. However, due to vanishing Li–O interactions, d_2 expands by 3.77%. Due to the larger expansion of d_2 than the contraction of d_1, the c lattice parameter still increases. However, removing 0.17 Li from Li0.50NCM111 causes d_1 to shrink strongly by 4.93% which is due to the fact that J–T distortion is lifted in all Ni cations. This contraction is larger than the expansion of 1.05% in d_2 which is not as large as that expected from $x = 1.00 \rightarrow 0.50$ as O anions are significantly oxidized. In this case, the impact of the disappearing (attractive) electrostatic interaction of the Li ions with O anions is weaker than that of oxidation of O anions on the O–O separation (d_2). The larger contraction of d_1 compared to the expansion of d_2 leads to the shortening of c with respect to not only Li0.67NCM111 but also Li1.00NCM111. Although previous studies proposed that the contraction of c is due to the oxidation of O, we show that this is mainly due to the vanishing of J–T distortion in NiO_6 octahedra. Upon removing 0.17 Li from Li0.33NCM111, d_1 shrinks only slightly by 0.68% and not as large as that from $x = 0.50$ to $x = 0.33$. This is because that all the Ni cations have been already oxidized to $(4 - \Delta)+$ at $x = 0.33$, and now half of the Co cations are oxidized to $(4 - \Delta)+$ at $x = 0.17$. The radius change of a Co cation upon oxidation from $(3 - \Delta)+$ to $(4 - \Delta)+$ was estimated by other groups to be only from 0.545 Å to 0.53 Å, which is much smaller than that of a Ni cation upon a similar oxidation (0.56 Å to 0.48 Å).[55–58] Therefore, contraction of d_1 is small. On the other hand, d_2 also shrinks significantly for $x = 0.33 \rightarrow 0.17$. This is because most of the attractive electrostatic Li–O interactions are absent for $x = 0.17$ letting O–TM–O layers to slide with respect to each other. Fig. 5 shows that the first and second O–TM–O layers (counted from the topmost layer) move in the in-plane direction so that their TM ions become closer to the TMs of the third O–TM–O layer. The sliding of the first layer is almost two times larger than that of the second layer. Moreover, O anions have a less negative charge (see Fig. 4a) leading to a weaker repulsive O–O interaction. Thus, the c lattice parameter decreases dramatically.

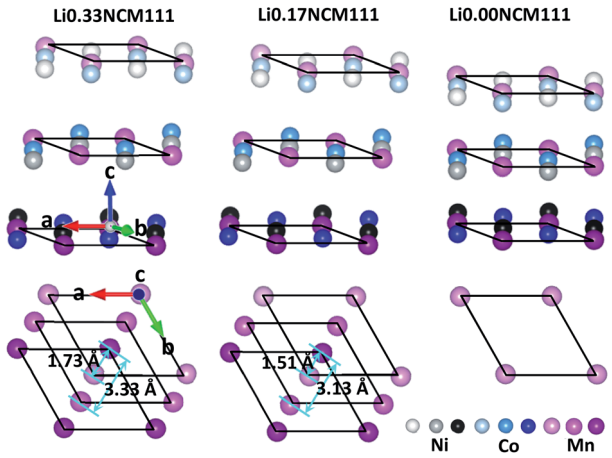

Fig. 5 Side views of TM layers (top) and top views of these layers with only Mn cations (bottom) in the O3 phase of Li0.33NCM111 and Li0.17NCM111 and the O1 phase of Li0.00NCM111. In-plane distances between arbitrary Mn ions of different layers are shown in the bottom.

To explain the changes in a with delithiation we used the average TM–O bond lengths in Fig. 4 to determine creation or suppression of J–T distortions in TM–O octahedra. When $x = 1.00 \rightarrow 0.67$, a decreases from 2.88 Å to 2.86 Å which is due to the oxidation of all the Ni cations from $(2-\Delta)$+ to $(3-\Delta)$+. Upon oxidation, $Ni^{(3-\Delta)+}$–O octahedra undergo Jahn–Teller (J–T) distortion in which the length of equatorial axis shrinks from 2.03 Å to 1.93 Å. However, no J–T distortion occurs for $Co^{(3-\Delta)+}$–O and $Mn^{(4-\Delta)+}$–O octahedra since there is no significant change in the oxidation states of Co and Mn. The projection of contraction of equatorial Ni–O bonds on the a axis leads to the decrease in the value of a. The reason for further contraction of a from $x = 0.67$ ($a = 2.86$ Å) to $x = 0.33$ ($a = 2.84$ Å) in Fig. 2 is the vanishing of J–T distortion in $Ni^{(4-\Delta)+}$–O leading to similar values of equatorial and axial Ni–O bond lengths. The reason for increase in a for $x = 0.33$ ($a = 2.84$ Å) $\rightarrow$ $x = 0.17$ ($a = 2.86$ Å) in Fig. 2 is because (i) the ionic radius of $Co^{(4-\Delta)+}$ in the latter case does not change much with respect to that of $Co^{(3-\Delta)+}$ in the former case,[57] while (ii) the in-plane electrostatic repulsion between $Co^{(4-\Delta)+}$ cations with each other and other cations enhances.

To check the possibility of the phase transition from O3 to O1 through a deep delithiation, we modelled Li0.17NCM111 and Li0.00NCM111 in O1 phases (see Fig. S8 in the ESI†). Our DFT-SCAN calculation shows that the O3 phase is more favourable than O1 for $x = 0.17$, which is in spite of a slight sliding of the O–TM–O layer-stacking in Li0.17NCM111 (Fig. 5). However, the O1 phase becomes more favorable than the O3 one for the fully delithiated case. This finding agrees with the experimental observations by Choi *et al.*[23] and Yin *et al.*[58] showing a O3 $\rightarrow$ O1 phase transition for deep delithiation levels. Furthermore, we computed the total Coulomb energies for the DFT-SCAN calculated structures of O1 and O3 phases using Bader charges. It is found that the latter structure is electrostatically more favorable for $x = 0.17$, while the former is more favorable for $x = 0.00$. The total Coulomb energy for Li0.00NCM111 is, however, calculated to be lower in O3 than the O1 phase when considering formal charge states of 4+ for TMs and 2− for O ions. Since the Bader charges on ions are larger in the O1 phase than the other phase of Li0.00NCM111 (Table S2 in ESI†), the O3 $\rightarrow$ O1 phase transition is expected to be driven by the strengthening of ionic bonds and electrostatic interactions.

Conclusions

Here, we showed a computational approach to simulate and understand the variation of lattice sizes of layered cathode materials with delithiation/lithiation. It was found that an extensive Coulomb energy analysis and DFT calculations are required to find the arrangement of Li ions in these materials at different levels of charging/discharging. Among PBE, PBE + U, and SCAN functionals, the last one can compute the lattice parameters (a, b, and c) of $Li_xNi_{1/3}Co_{1/3}Mn_{1/3}O_2$ (LixNCM111) as a function of Li concentration in better agreement with experimental data. A detailed analysis of the local spin polarization, spin density difference plot, density of states, and Bader charges was then applied to gain insight into the nature of delithiation-induced oxidation and lattice size change in this system. Delithiation of LixNCM111 from $x = 1.00$ to 0.67 leads to the $Ni^{(2-\Delta)+} \rightarrow Ni^{(3-\Delta)+}$ oxidation of all the Ni cations. Although this causes the intralayer O–TM–O length along c (d_1) to become slightly shorter, this contraction is smaller than the expansion of the interlayer O–TM–O length along c (d_2) leading to the increase in the c parameter. The expansion is due to the vanishing of the attractive electrostatic Li–O interaction. Although equatorial Ni–O bonds shrink significantly, the axial ones remain almost unchanged due to the J–T distortion. For this reason, the parameter a, which is influenced by the projection of equatorial $Ni^{(3-\Delta)+}$–O bond lengths on this axis, undergo a small contraction. From $x = 0.67$ to 0.50, the value of c increases slightly due to a further vanishing of the attractive electrostatic Li–O interaction. This is in spite of suppression of J–T distortion in half of the Ni cations which results in the contraction of intralayer O–TM–O bonds along the c and a directions. Therefore, the length of a which is controlled by the in-plane projection of O–TM–O bonds is shortened. From $x = 0.50$ to 0.33, all the Ni cations undergo a $Ni^{(3-\Delta)+} \rightarrow Ni^{(4-\Delta)+}$ oxidation. In this case, the J–T distortion in all the NiO_6 octahedra is relieved leading to a large contraction of d_1. For this reason, the size of a decreases further. Although the value of d_2 increases due to further vanishing of the attractive electrostatic Li–O interaction, this expansion is not large enough because of the decrease in the negative charge (*i.e.* oxidation) of the O anions. Therefore, the small expansion of d_2 cannot overcome the large shrinkage of d_1. For this reason, the value of c contracts. Finally, from $x = 0.33$ to $x = 0.17$, some Co cations undergo $Co^{(3-\Delta)+} \rightarrow Co^{(4-\Delta)+}$ oxidation. Since the radius of the oxidized Co cations does not reduce much, the increase in the electrostatic repulsion between $Co^{(4-\Delta)+}$ and other cations leads to an increase in a. However, the c value shrinks significantly, which is due to the in-plane displacements of O–TM–O layers with respect to each other to pack in the direction c. At higher concentrations of Li, the sliding of O–TM–O layers does not take

place because Li ions keep the O–TM–O layers together. Furthermore, our calculations show that at $x = 0.00$ for which O anions are oxidized more strongly than higher Li concentration cases a phase transition from O3 to O1 occurs in the absence of Li ions that act as glue between O–TM–O layers. Our total Coulomb energy calculation indicates that the O3 → O1 phase transition is driven by increased strength of ionic bonds and electrostatic interaction. A comparison between PBE, PBE + *U*, and SCAN functional results demonstrates that the last one is generally the best choice to predict the lattice parameters and magnetic properties. However, all three functionals can qualitatively predict the lattice parameters and volume change correctly.

Theoretical methods

Spin-polarized DFT calculations were carried out using the projector augmented wave (PAW)[41] method implemented in the Vienna *Ab Initio* Simulation Package (VASP).[42] To examine the effect of the XC functional on the results, PBE, PBE + *U*, and SCAN were used. The *U–J* (hereafter called *U*) values for Ni, Co, and Mn are 6.8 eV, 5.9 eV, and 5.2 eV respectively. We also further checked the influence of the *U* value on lattice parameters and volume by considering *U* values of 4 eV and 8 eV for Ni. We only studied the different *U* values for Ni because Ni is the active cation for a wide range of lithium concentrations of $1.00 > x > 0.33$. The $Li_xNi_{1/3}Co_{1/3}Mn_{1/3}O_2$ (Li*x*NCM111) bulk structure with a space group of $R\bar{3}m$ was modelled with a unit cell of $[\sqrt{3} \times \sqrt{3}]$R30-type symmetry ($1 \times 1 \times 1$ unit cell: $Li_9Ni_3Co_3Mn_3O_{18}$). A $1 \times 1 \times 1$ unit cell was considered to calculate total Coulomb energies for $x = 0.67$ and $x = 0.33$, while a $2 \times 2 \times 1$ supercell ($Li_{36}Ni_{12}Co_{12}Mn_{12}O_{72}$) was used to calculate total Coulomb energies for $x = 0.50$ and $x = 0.17$ and to perform all DFT calculations for $1.00 \geq x \geq 0.00$. A gamma-centered *k*-point mesh of $2 \times 2 \times 1$ and an energy cut off of 500 eV were applied for the $2 \times 2 \times 1$ supercell. An electronic and force convergence criterion of 10^{-4} eV and 10^{-3} eV Å^{-1}, respectively, was considered. Total Coulomb energy calculations were carried out using the so-called supercell code.[43] Atomic structures were visualized with the VESTA program.[44]

Author contributions

L.-Y. K. performed the calculations. L.-Y. K, O. G., and P. K. analysed the data and wrote the manuscript.

Conflicts of interest

There are no conflicts to declare.

Acknowledgements

The authors gratefully acknowledge support from the "Bundesministerium für Bildung und Forschung" (BMBF) and the computing time granted through JARA-HPC on the supercomputer JURECA at Forschungszentrum Jülich.

Notes and references

1 J.-M. Tarascon and M. Armand, *Nature*, 2001, **414**, 359–367.
2 M. Winter, B. Barnett and K. Xu, *Chem. Rev.*, 2018, **118**, 11433–11456.
3 N. Nitta, F. Wu, J. T. Lee and G. Yushin, *Mater. Today*, 2015, **18**, 252–264.
4 A. Yano, M. Shikano, A. Ueda, H. Sakaebe and Z. Ogumi, *J. Electrochem. Soc.*, 2017, **164**, A6116–A6122.
5 C. S. Yoon, D.-W. Jun, S.-T. Myung and Y.-K. Sun, *ACS Energy Lett.*, 2017, **2**, 1150–1155.
6 T. Ohzuku, A. Ueda and M. Nagayama, *J. Electrochem. Soc.*, 1993, **140**, 1862–1870.
7 A. Rougier, P. Gravereau and C. Delmas, *J. Electrochem. Soc.*, 1996, **143**, 1168–1175.
8 T. Uyama, K. Mukai and I. Yamada, *RSC Adv.*, 2018, **8**, 26325–26334.
9 M. S. Whittingham, *Chem. Rev.*, 2004, **104**, 4271–4302.
10 P. G. Bruce, A. R. Armstrong and R. L. Gitzendanner, *J. Mater. Chem.*, 1999, **9**, 193–198.
11 O. Tsutomu and M. Yoshinari, *Chem. Lett.*, 2001, **30**, 642–643.
12 A. M. Dreizler, N. Bohn, H. Geßwein, M. Müller, J. R. Binder, N. Wagner and K. A. Friedrich, *J. Electrochem. Soc.*, 2018, **165**, A273–A282.
13 W. Hua, Z. Wu, M. Chen, M. Knapp, X. Guo, S. Indris, J. R. Binder, N. N. Bramnik, B. Zhong, H. Guo, S. Chou, Y.-M. Kang and H. Ehrenberg, *J. Mater. Chem. A*, 2017, **5**, 25391–25400.
14 G.-L. Xu, Q. Liu, K. K. S. Lau, Y. Liu, X. Liu, H. Gao, X. Zhou, M. Zhuang, Y. Ren, J. Li, M. Shao, M. Ouyang, F. Pan, Z. Chen, K. Amine and G. Chen, *Nat. Energy*, 2019, **4**, 484–494.
15 K. Min and E. Cho, *Phys. Chem. Chem. Phys.*, 2018, **20**, 9045–9052.
16 A. O. Kondrakov, A. Schmidt, J. Xu, H. Geßwein, R. Mönig, P. Hartmann, H. Sommer, T. Brezesinski and J. Janek, *J. Phys. Chem. C*, 2017, **121**, 3286–3294.
17 J. Kasnatscheew, U. Rodehorst, B. Streipert, S. Wiemers-Meyer, R. Jakelski, R. Wagner, I. C. Laskovic and M. Winter, *J. Electrochem. Soc.*, 2016, **163**, A2943–A2950.
18 J. C. Garcia, J. Bareño, J. Yan, G. Chen, A. Hauser, J. R. Croy and H. Iddir, *J. Phys. Chem. C*, 2017, **121**, 8290–8299.
19 R. C. Longo, F. Kong, C. Liang, D.-H. Yeon, J. Yoon, J.-H. Park, S.-G. Doo and K. Cho, *J. Phys. Chem. C*, 2016, **120**, 8540–8549.
20 H. Sun and K. Zhao, *J. Phys. Chem. C*, 2017, **121**, 6002–6010.
21 G. Luo, J. Zhao, X. Ked, P. Zhang, H. Sun and B. Wang, *J. Electrochem. Soc.*, 2012, **159**, A1203–A1208.
22 J. Y. Lee, J. Y. Kim, H. I. Cho, C. H. Lee, H. S. Kim, S. U. Lee, T. J. Prosa, D. J. Larson, T. H. Yu and J.-P. Ahn, *J. Power Sources*, 2018, **379**, 160–166.
23 J. Choi and A. Manthiram, *J. Electrochem. Soc.*, 2005, **152**, A1714–A1718.
24 C. F. Petersburg, Z. Li, N. A. Chernova, S. M. Whittingham and F. M. Alamgir, *J. Mater. Chem.*, 2012, **22**, 19993–20000.

25 Z. Li, N. A. Chernova, M. Roppolo, S. Upreti, C. Petersburg, F. M. Alamgir and M. S. Whittingham, *J. Electrochem. Soc.*, 2011, **158**, A516–A522.
26 W. Hua, B. Schwarz, M. Knapp, A. Senyshyn, A. Missiul, X. Mu, S. Wang, C. Kubel, J. R. Binder, S. Indris and H. Ehrenberg, *J. Electrochem. Soc.*, 2019, **166**, A5025–A5032.
27 L. de Biasi, B. Schwarz, T. Brezesinski, P. Hartmann, J. Janek and H. Ehrenberg, *Adv. Mater.*, 2019, **31**, 1900985.
28 A. O. Kondrakov, H. Geßwein, K. Galdina, L. de Biasi, V. Meded, E. O. Filatova, G. Schumacher, W. Wenzel, P. Hartmann, T. Brezesinski and J. Janek, *J. Phys. Chem. C*, 2017, **44**, 24381–24388.
29 B. J. Hwang, Y. W. Tsai, D. Carlier and G. Ceder, *Chem. Mater.*, 2003, **15**, 3676–3682.
30 Y. Koyama, N. Yabuuchi, I. Tanaka, H. Adachi and T. Ohzuku, *J. Electrochem. Soc.*, 2004, **151**, A1545–A1551.
31 J. P. Perdew, K. Burke and M. Ernzerhof, *Phys. Rev. Lett.*, 1996, **77**, 3865–3868.
32 K. Min, K. Kim, C. Jung, S.-W. Seo, Y. Y. Song, H. S. Lee, J. Shin and E. Cho, *J. Power Sources*, 2016, **315**, 111–119.
33 J. Hubbard, *Phys. Eng. Sci.*, 1963, **276**, 238–257.
34 C. Liang, R. C. Longo, F. Kong, C. Zhang, Y. Nie, Y. Zheng, J.-S. Kim, S. Jeon, S. Choi and K. Cho, *J. Power Sources*, 2017, **340**, 217–228.
35 J. Heyd, G. E. Scuseria and M. Ernzerhof, *J. Chem. Phys.*, 2003, **118**, 8207–8215.
36 J. W. Sun, A. Ruzsinszky and J. P. Perdew, *Phys. Rev. Lett.*, 2015, **115**, 036402.
37 J. Sun, R. C. Remsing, Y. Zhang, Z. Sun, A. Ruzsinszky, H. Peng, Z. Yang, A. Paul, U. Waghmare, X. Wu, M. L. Klein and J. P. Perdew, *Nat. Chem.*, 2016, **8**, 831–836.
38 J. P. Perdew, J. Sun, R. M. Martin and B. Delley, *Int. J. Quantum Chem.*, 2016, **116**, 847–851.
39 Y. Zhang, D. A. Kitchaev, J. Yang, T. Chen, S. T. Dacek, R. A. Sarmiento-Pérez, M. A. L. Marques, H. Peng, G. Ceder, J. P. Perdew and J. Sun, *npj Comput. Mater.*, 2018, **4**, 9.
40 A. Chakraborty, M. Dixit, D. Aurbach and D. T. Major, *npj Comput. Mater.*, 2018, **4**, 60.
41 P. E. Blöchl, *Phys. Rev. B: Condens. Matter Mater. Phys.*, 1994, **50**, 17953–17979.
42 G. Kresse and J. Furthmüller, *Phys. Rev. B: Condens. Matter Mater. Phys.*, 1996, **54**, 11169–11186.
43 K. Okhotnikov, T. Charpentier and S. Cadars, *J. Cheminf.*, 2016, **8**, 17.
44 K. Momma and F. Izumi, *J. Appl. Crystallogr.*, 2011, **44**, 1272–1276.
45 K. Hoang and M. Johannes, *Chem. Mater.*, 2016, **28**, 1325–1334.
46 Y. Idemoto, T. Mochizuki, K. Ui and N. Koura, *J. Electrochem. Soc.*, 2006, **153**, A418–A424.
47 M. Dixit, B. Markovsky, F. Schipper, D. Aurbach and D. T. Major, *J. Phys. Chem. C*, 2017, **121**, 22628–22636.
48 M. D. Radin, S. Hy, M. Sina, C. Fang, H. Liu, J. Vinckeviciute, M. Zhang, M. S. Whittingham, Y. S. Meng and A. Van der Ven, *Adv. Energy Mater.*, 2017, **7**, 1602888.
49 M. E. Arroyo y de Dompablo, C. Marianetti, A. Van der Ven and G. Ceder, *Phys. Rev. B*, 2001, **63**, 144107.
50 Y. W. Tsai, B. J. Hwang, G. Ceder, H. S. Sheu, D. G. Liu and J. F. Lee, *Chem. Mater.*, 2005, **17**, 3191–3199.
51 W.-S. Yoon, M. Balasubramanian, K. Y. Chung, X.-Q. Yang, J. McBreen, C. P. Grey and D. A. Fischer, *J. Am. Chem. Soc.*, 2005, **127**, 17479–17487.
52 T. Ohnum and T. Kobayashi, *RSC Adv.*, 2019, **9**, 35655.
53 M. Dixit, M. Kosa, O. S. Lavi, B. Markovsky, D. Aurbach and D. T. Major, *Phys. Chem. Chem. Phys.*, 2016, **18**, 6799–6812.
54 I. Saadoune, M. Ménétrier and C. Delmas, *J. Mater. Chem.*, 1997, **7**, 2505–2511.
55 H. H. Li, *Chem. Mater.*, 2007, **19**, 2551–2565.
56 K.-S. Lee, S.-T. Myung, K. Amine, H. Yashiro and Y.-K. Sun, *J. Electrochem. Soc.*, 2007, **154**, A971–A977.
57 R. D. Shannon, *Acta Crystallogr., Sect. A: Cryst. Phys., Diffr., Theor. Gen. Crystallogr.*, 1976, **32**, 751–767.
58 S.-C. Yin, Y.-H. Rho, I. Swainson and L. F. Nazar, *Chem. Mater.*, 2006, **18**, 1901–1910.

Electronic Supplementary Material (ESI) for Journal of Materials Chemistry A.

Supporting Information

for

On the origin of non-monotonic variation of lattice parameters of $LiNi_{1/3}Co_{1/3}Mn_{1/3}O_2$ with lithiation/delithiation: a first-principles study

Liang-Yin Kuo,[a,b] Olivier Guillon,[b] and Payam Kaghazchi*[b]

[a]Physikalische und Theoretische Chemie, Freie Universität Berlin, Arnimallee 22, D-14195 Berlin, Germany

[b]Forschungszentrum Jülich GmbH, Institute of Energy and Climate Research, Materials Synthesis and Processing (IEK-1), D-52425, Jülich, Germany

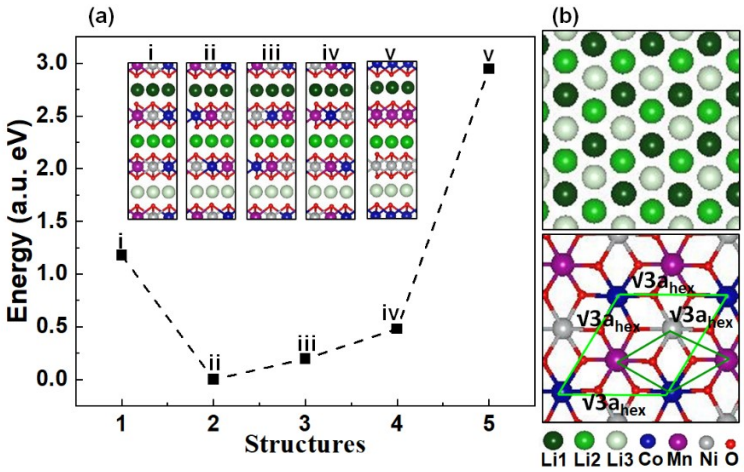

Figure S1. (a) Energy difference between NMC111 structures with various TM cations arrangements. (b) Top views of the Li and O–TM–O layers in the most favorable NMC111 structure (ii).

x	PBE	PBE+*U*	SCAN	Exp.
1.00	48.1	86.0	58.5	60
0.67	43.9	83.9	46.5	48
0.50	21.4	73.8	41.0	42
0.33	36.0	61.2	35.6	36
0.17	24.0	70.9	33.5	-

Table S1. Calculated total number of unpaired spins (NUS) for Li*x*NCM111 with *x*= 1.00, 0.67, 0.50, 0.33, and 0.17 using different types of XC functionals. Expected NUS values (based on previous experimental and theoretical studies) for a perfect ionic system are also listed.

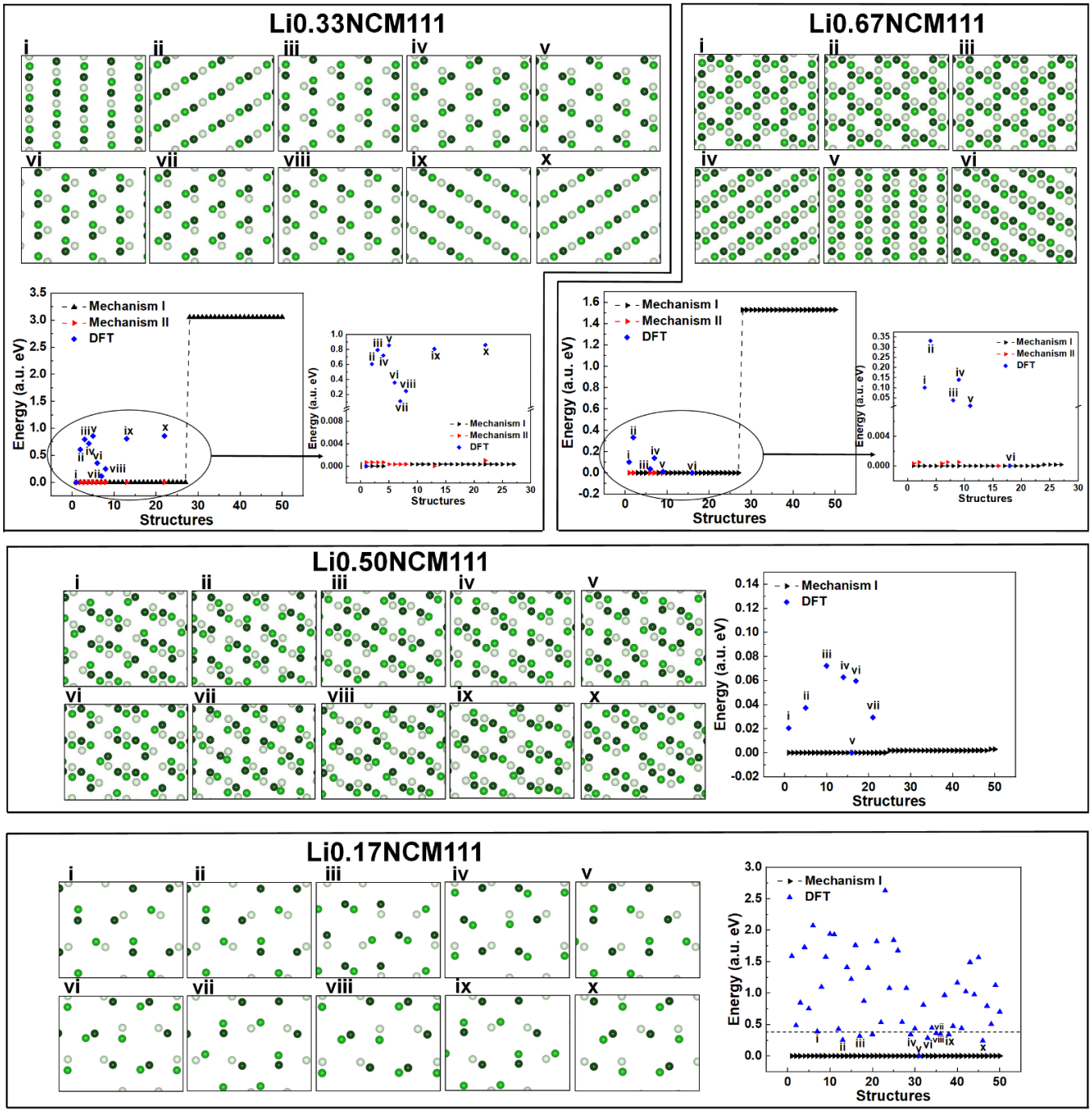

Figure S2. Calculated total Coulomb energies (referenced to the minimum energy) for Li*x*NCM111 (*x* = 0.67, 0.50, 0.33, and 0.17). Calculated DFT-PBE total energies of the most favorable structures based on the electrostatic analysis are also given. Arrangements of Li ions in several (DFT-PBE-calculated) lowest-energy structures are also presented.

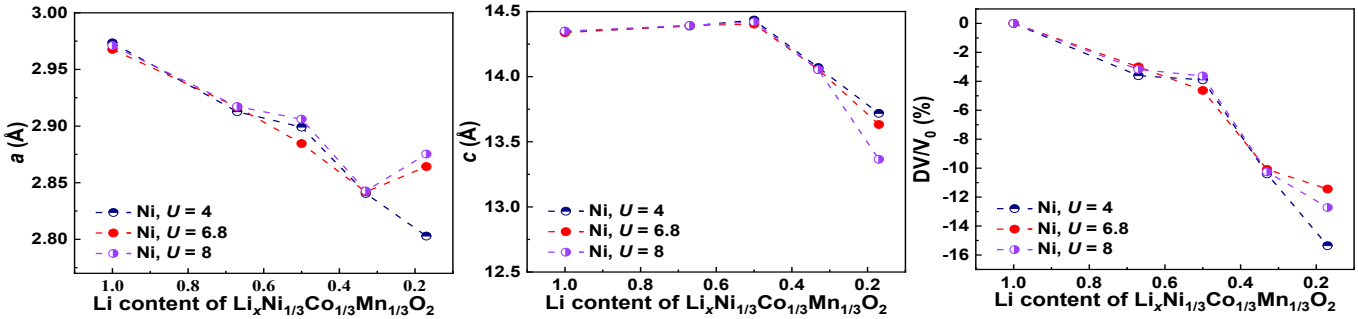

Figure S3. Calculated lattice parameters and volume change as function of *x* for Li*x*NCM111 using DFT-PBE+*U* with different *U* values for Ni.

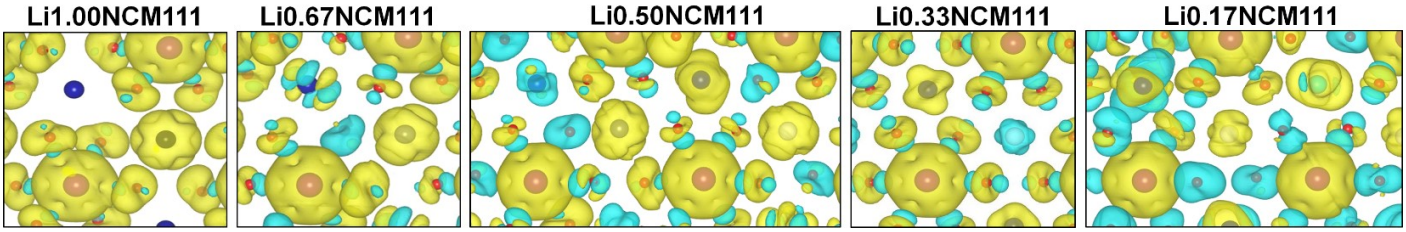

Figure S4. Calculated spin density difference (SDD) in the most favorable Li*x*NCM111 structures using the SCAN functional. Up-spin and down-spin electrons are in yellow and blue, respectively. An isosurface of 0.004 electrons/Å^3 was applied.

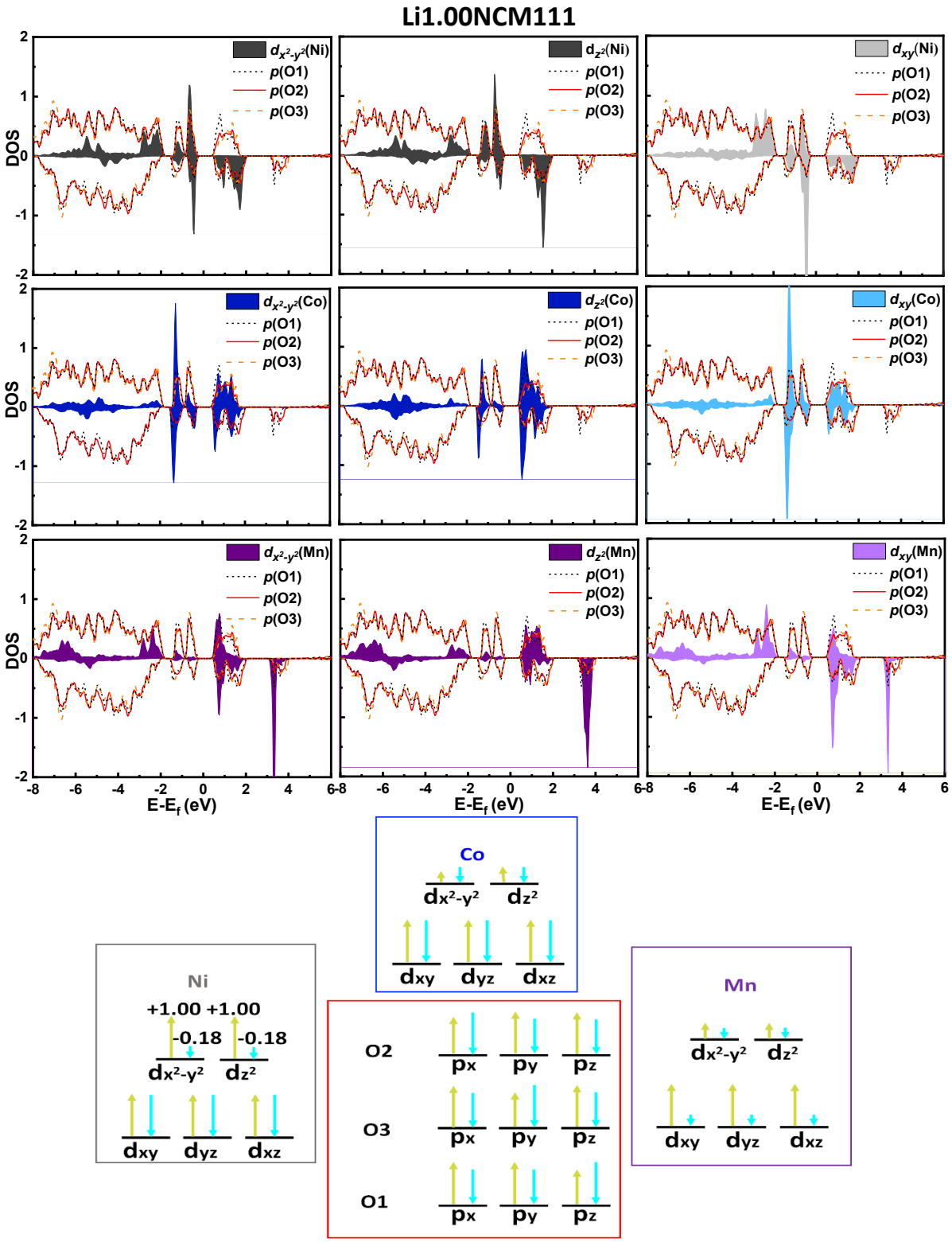

Fig. S5. Partial density of states (PDOSs) and proposed electronic configurations in the most favorable Li1.00NCM111 structures based on DFT-SCAN calculation. The atomic coordinates were rotated about the by-axis to align axial TM–O bonds (in TMO_6 octahedra) along the global *z*-axis of the unit cell to assign the e_g and representative t_{2g} states.

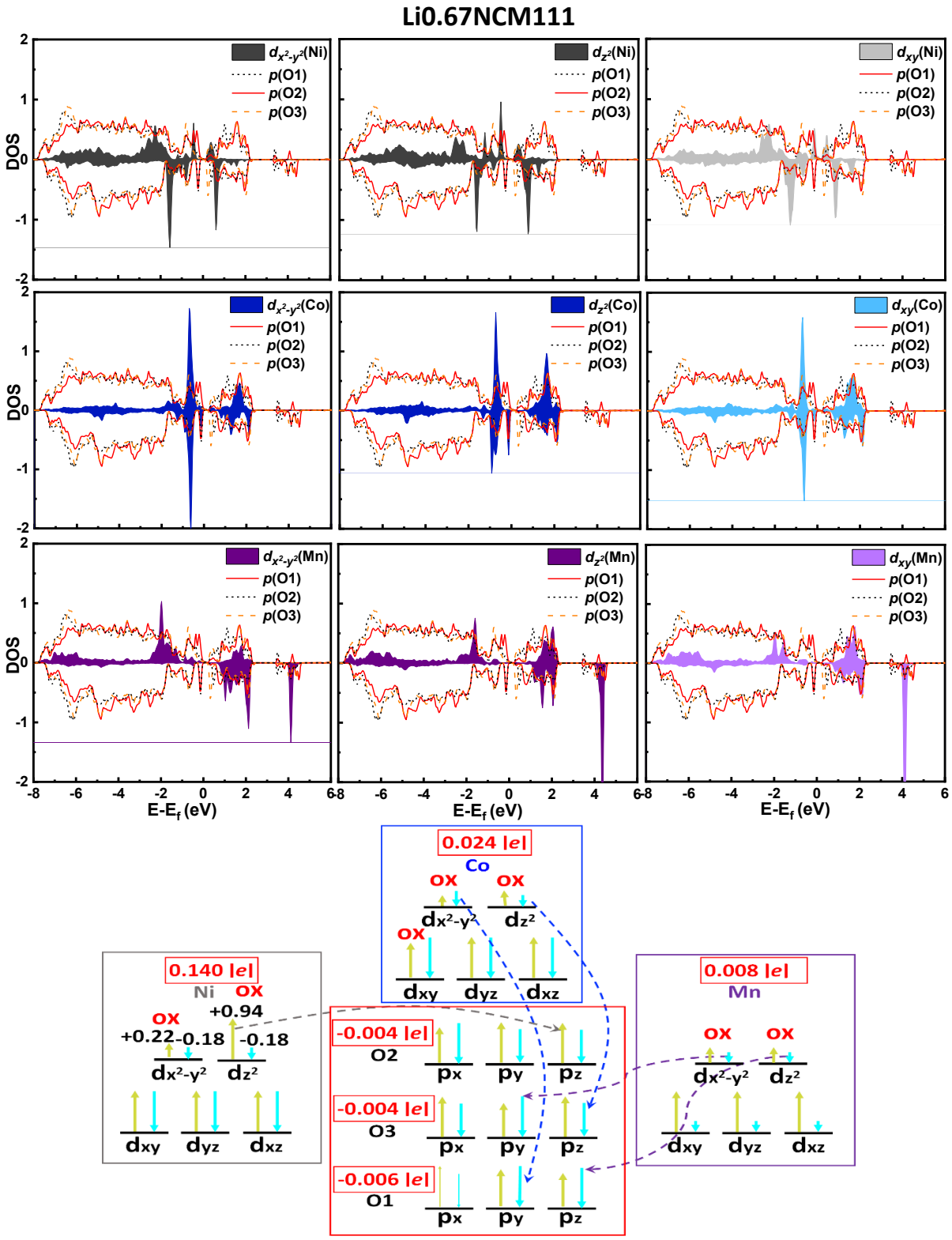

Fig. S6. Partial density of states (PDOSs) and proposed electronic configurations in the most favorable Li0.67NCM111 structures based on DFT-SCAN calculation. The atomic coordinates were rotated about the by-axis to align axial TM–O bonds (in TMO_6 octahedra) along the global *z*-axis of the unit cell to assign the e_g and representative t_{2g} states.

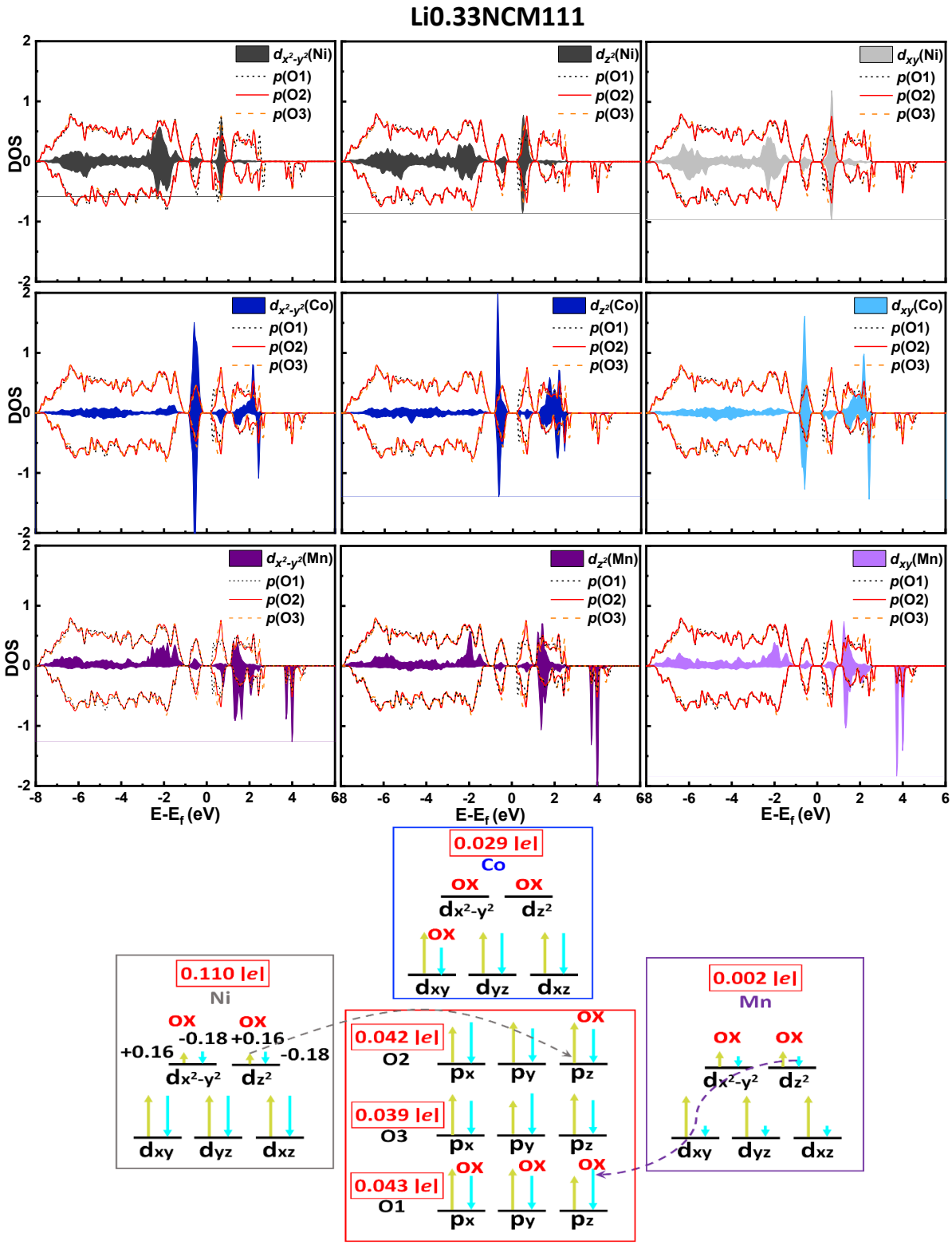

Fig. S7. Partial density of states (PDOSs) and proposed electronic configurations in the most favorable Li0.33NCM111 structures based on DFT-SCAN calculation. The atomic coordinates were rotated about the by-axis to align axial TM–O bonds (in TMO_6 octahedra) along the global *z*-axis of the unit cell to assign the e_g and representative t_{2g} states.

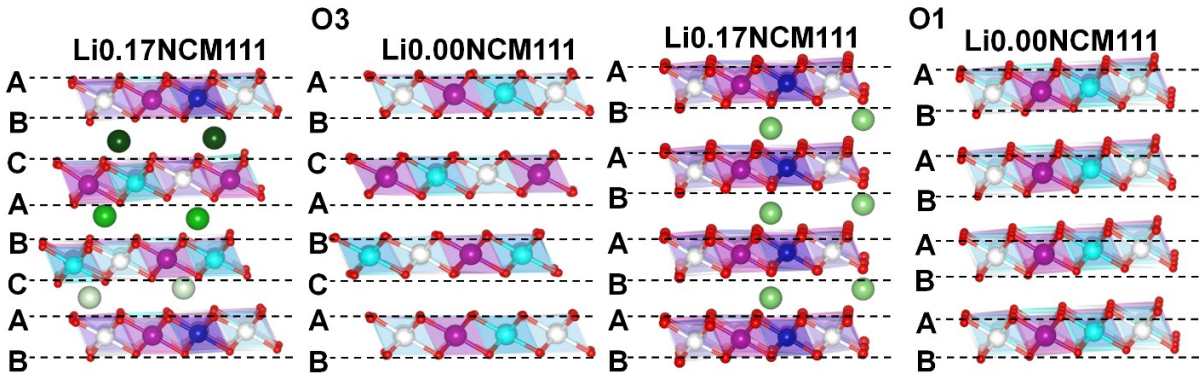

Figure S8. Calculated atomic structures and stacking of Li0.17NCM111 and Li0.00NCM111 structures in O3 and O1 phases using the SCAN functional.

	Bader charge [e^-]					E_C [eV]
	Li	Ni	Co	Mn	O	
O3	-	1.406	1.504	1.755	-0.778	-777.73
O1	-	1.494	1.617	2.017	-0.855	-931.28
	formal charge [e^-]					
O3	-	4	4	4	-2	-5126.13
O1	-	4	4	4	-2	-5064.89

Table S2. Calculated Coulomb energies (E_c) for O3 and O1 phases of Li0.00NCM111 using calculated averaged Bader charges (DFT-SCAN).

4.2 Publication M2

"Origin of structural phase transitions in Ni-rich $Li_xNi_{0.8}Co_{0.1}Mn_{0.1}O_2$ with delithiation/lithiation: a first-principles study"

L.-Y. Kuo, O. Guillon and P. Kaghazchi

ACS Sustain. Chem. Eng., **9**, 7437 (2021)

DOI: 10.1021/acssuschemeng.0c07675

URL: https://doi.org/10.1021/acssuschemeng.0c07675

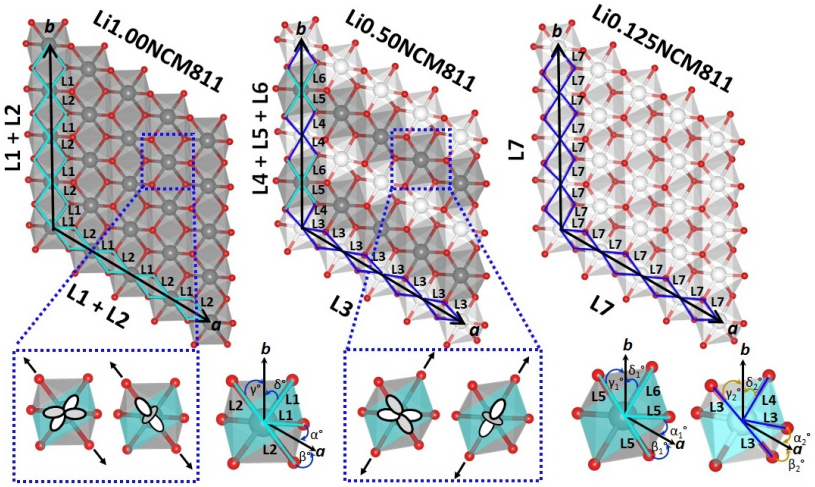

Figure 4.2: Graphical Abstract [141].

Author contributions

The idea of the second publication (**M2**) was proposed by Dr. Payam Kaghazchi. I performed the Coulomb energy and DFT calculations as well as prepared the figures. The computational results were analyzed by me and Dr. Payam Kaghazchi. I wrote the manuscript and Dr. Payam Kaghazchi commented on it. Prof. Olivier Guillon also gave the suggestions and commented on it. All co-authors discussed the final results and finished the manuscript.

4.3 Publication M3

"Quaternary Layered Ni-Rich NCMA Cathode for Lithium-Ion Batteries"

U.-H. Kim, L.-Y. Kuo, P. Kaghazchi, C. S. Yoon and Y.-K. Sun

ACS Energy Lett., **4**, 576 (2019)

DOI: 10.1021/acsenergylett.8b02499

URL: https://doi.org/10.1021/acsenergylett.8b02499

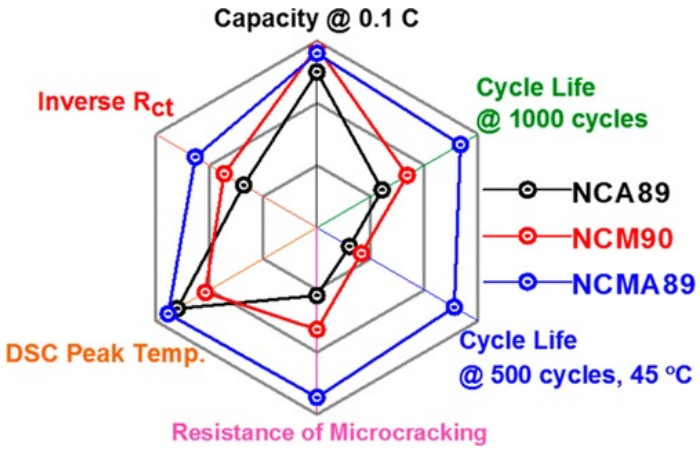

Figure 4.3: Graphical Abstract [142].

Author contributions

The third publication (**M3**) was a combination of experimental and theoretical studies. It was a joint project between Dr. Payam Kaghazchi at Freie Universität Berlin and Prof. Yang-Kook Sun in Hanyang University Seoul. The experimental results in the manuscript were analyzed and written by Prof. Yang-Kook Sun's group. I performed the DFT calculations and prepared the figures for computational section. Dr. Payam Kaghazchi and I analyzed the data and he wrote the theoretical part of the manuscript. All co-authors discussed the final results and finished the manuscript.

ACS Energy LETTERS

Cite This: ACS Energy Lett. 2019, 4, 576−582

http://pubs.acs.org/journal/aelccp

Quaternary Layered Ni-Rich NCMA Cathode for Lithium-Ion Batteries

Un-Hyuck Kim,[†] Liang-Yin Kuo,[‡] Payam Kaghazchi,[∥] Chong S. Yoon,[*,§] and Yang-Kook Sun[*,†]

[†]Department of Energy Engineering, Hanyang University, Seoul 04763, South Korea

[‡]Physikalische und Theoretische Chemie, Institut für Chemie und Biochemie, Freie Universität Berlin, Takustraße 3, 14195 Berlin, Germany

[∥]Forschungszentrum Jülich GmbH, Institute of Energy and Climate Research (IEK-1), Materials Synthesis and Processing, Wilhelm-Johnen-Straße, 52425 Jülich, Germany

[§]Department of Materials Science and Engineering, Hanyang University, Seoul 04763, South Korea

Supporting Information

ABSTRACT: $Li[Ni_{1-x-y}Co_xAl_y]O_2$ (NCA) and $Li[Ni_{1-x-y}Co_xMn_y]O_2$ (NCM) cathodes have been the archetypes of current high-energy-density cathodes for Li-ion batteries. A hybrid of NCA and NCM cathodes, a quaternary system consisting of $Li[Ni_{0.89}Co_{0.05}Mn_{0.05}Al_{0.01}]O_2$ (NCMA) was benchmarked against NCM and NCA with similar Ni contents. The quaternary NCMA cathode delivered a capacity of 228 mAh g^{-1} and outperformed the benchmarking cathodes in long-term cycling stability (85% after 1000 cycles). The reduction in the volume change during deintercalation and the enhanced intrinsic mechanical strength confirmed by the single-particle compression test suppressed the microcrack nucleation and propagation. Microcrack suppression was important because microcracks serve as channels for electrolyte infiltration and lead to subsequent surface degradation of internal surfaces. The proposed NCMA cathode provides extra cycling stability, which is essential for electric vehicles, which require a long battery life and improves the thermal stability of the cathode, which contributes to a safer battery.

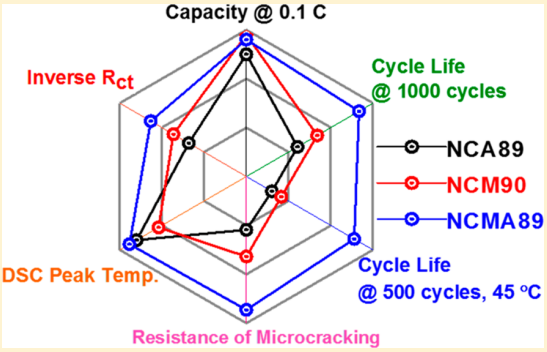

With the rapid development of electric vehicles (EVs) and large-scale energy storage systems, the demand for high-energy-density rechargeable batteries has grown dramatically, and the trend is expected to continue. Lithium-ion batteries (LIBs) have become the primary power source for EVs due to their high energy density, good rate capability, and long-term cycling performance. To satisfy the consumer-threshold driving range of 300 miles (480 km) per single charge,[1,2] extensive research for the development of high-capacity cathodes has been carried out in the past decades.[3−10] Among the cathodes developed to date, a series of layered Ni-rich lithium transition metal oxides, $Li[Ni_{1-x-y}Co_xAl_y]O_2$ (NCA) or $Li[Ni_{1-x-y}Co_xMn_y]O_2$ (NCM), are the most promising candidates because they provide high reversible capacity with a long cycle life and high operating potential of 3.6 V vs Li/Li^+. To further increase the capacity of current NCM and NCA cathodes, the fraction of Ni in the cathodes has been progressively increased;[11−13] however, this approach is limited by the deterioration of capacity retention and thermal stability resulting from excessive Ni enrichment (above x = 0.6 for NCM and 0.8 for NCA). One method for overcoming the obstacles posed by the Ni enrichment strategy is to dope alien metallic ions to pristine NCA or NCM cathodes to improve the structural stability and thus Li^+ intercalation stability.[14−22] Among the various doping metals, Al is the most widely used dopant because of its stabilizing role in the host layered structure. Moreover, it tends to improve the thermal stability owing to the stronger strength of Al−O bonds than those of Ni(Co, Mn)−O bonds.[17−19,23] However, the Al-doping content should be carefully considered because of its nonparticipation in the redox reaction. Therefore, the Al fraction has been limited to a relatively low concentration below 5 mol %. Recently, we demonstrated that Al-doping greatly extends battery life as the 2 mol % Al-doped gradient $Li[Ni_{0.76}Co_{0.09}Mn_{0.15}]O_2$ cathode retained 95% of its initial capacity after 1000 cycles.[23]

Al-doping clearly improves the cycling stability of a Ni-rich NCM cathode but is accompanied by a concurrent capacity

Received: December 20, 2018
Accepted: January 25, 2019
Published: January 25, 2019

DOI: 10.1021/acsenergylett.8b02499
ACS Energy Lett. 2019, 4, 576−582

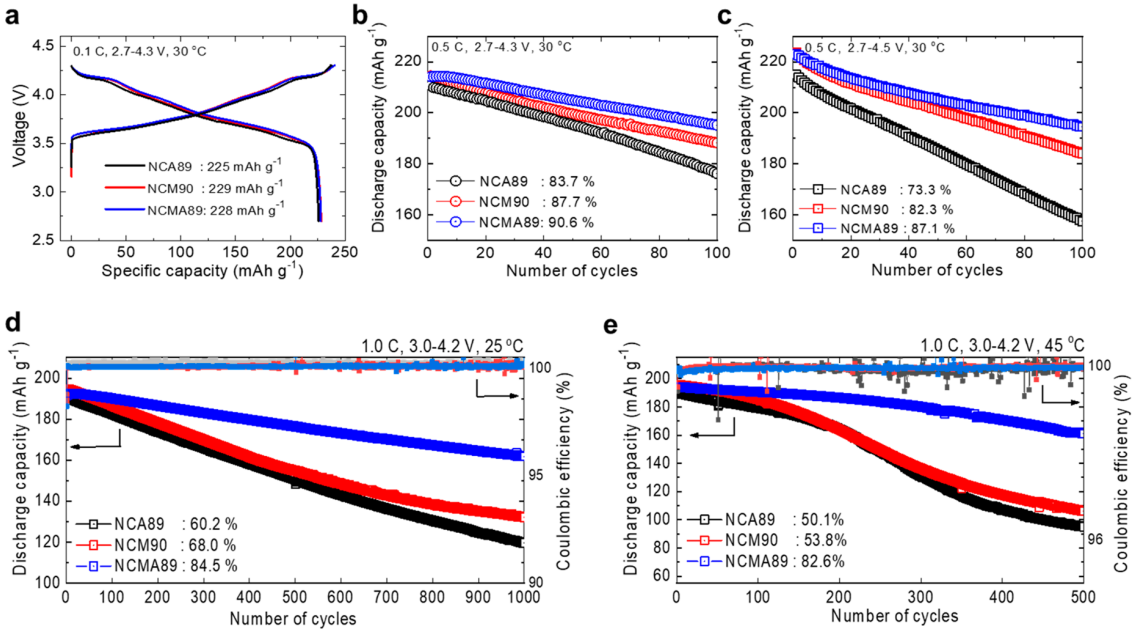

Figure 1. Comparison of electrochemical performance of the NCA89, NCM90, and NCMA89 cathodes: (a) first cycle voltage profiles for the three cathodes. All cells are cycled with a voltage range of 2.7−4.3 V at 0.1 C and 30 °C in a half-cell using Li metal as an anode. Cycling performance of the three cathodes tested with voltage ranges of (b) 2.7−4.3 and (c) 2.7−4.5 V at 0.5 C and 30 °C. Long-term cycling performance of the NCA89, NCM90, and NCMA89 cathodes using pouch full cells at 1.0 C and (d) 25 and (e) 45 °C with a voltage range of 3.0−4.2 V with mesocarbon microbead graphite as an anode.

loss when introduced in excess (Figure S1). Here, we report a hybrid NCM and NCA cathode $Li[Ni_{0.89}Co_{0.05}Mn_{0.05}Al_{0.01}]O_2$ (hereafter referred to as NCMA89) that provides an optimal combination of capacity and cycle life among cathodes with different Al content and whose performance surpasses that of the NCA and NCM cathodes with similar Ni contents. A comparative study of structural and electrochemical properties of $Li[Ni_{0.90}Co_{0.05}Mn_{0.05}]O_2$ (NCM90), $Li[Ni_{0.885}Co_{0.100}Al_{0.015}]O_2$ (NCA89), and NCMA89 is carried out by investigating bulk and surface structural degradation before and after long-term cycling.

Scanning electron microscopy (SEM) images of the NCA89, NCM90, and NCMA89 cathode particles show that the synthesized cathodes have spherical morphology with an average particle diameter of 10 μm (Figure S2a). There is no essential difference in the size and shape of particles among the three cathodes, implying that particle morphology is an unlikely factor affecting the electrochemical performance of the cathodes. X-ray diffraction (XRD) patterns of the NCA89, NCM90, and NCMA89 cathodes in Figure S2b are indexed to an α-$NaFeO_2$ structure with $R\bar{3}m$ space group, and no impurity phases were observed. Both *a*- and *c*-axis parameters for the tested cathodes in Table S1 were similar in magnitude.

Figure 1a shows the initial charge−discharge curves of the three cathodes cycled between 2.7 and 4.3 V at 0.1 C (18 mA g^{-1}) at 30 °C in 2032 coin-type half-cells. NCM90 delivers a high initial discharge capacity of 229 mAh g^{-1}. In comparison, the NCMA89 cathode exhibits a slightly reduced capacity of 228 mAh g^{-1} due to the addition of inactive Al, while the NCA89 cathode produces a yet lower capacity of 225 mAh g^{-1}. Interestingly, the NCMA89 cathode, as shown in Figure 1b, exhibits a substantial improvement in capacity retention at 90.6% after 100 cycles compared to the NCA and NCM cathodes, although the Al-doping level was limited to a mere 1 mol %. The NCM90 and NCA89 cathodes exhibit capacity retentions of 87.7 and 83.7%, respectively, during the same cycling period. Increasing the upper cutoff voltage to 4.5 V further substantiates enhancement of the cycling stability by the addition of Al to NCM90 as NCMA89, NCM90, and NCA89 maintain 87.1, 82.3, and 73.3% of their respective initial capacities after 100 cycles at 0.5 C (Figure 1c). Moreover, the NCM90 cathode apparently exhibits better Li intercalation stability than the NCA89 cathode when charged to 4.3 and 4.5 V. The improved cycling stability is emphasized during long-term cycling of the cathodes in aluminum pouch-type full cells using a graphite anode. As shown in Figure 1d, the full cell with the NCMA89 cathode exhibits outstanding capacity retention of 84.5% after 1000 cycles, while NCM90 and NCA89 cathodes retain only 68.0 and 60.2% of their respective initial capacities, respectively. The cycling stability of the NCMA89 cathode at an elevated temperature (45 °C) is much better than that of the NCM90 and NCA89 cathodes (Figure 1e). After 500 cycles, 82.6% of the initial capacity of NCMA89 is retained, while that of the NCM90 and NCA89 cathodes is limited to 53.8 and 50.1%, respectively.

To study the effect of the H2 ↔ H3 phase transition, dQ dV^{-1} profiles were obtained by numerically differentiating the charge−discharge curves (Figure S3a,b). All three Ni-rich cathodes undergo multiphase transitions during Li^+ removal and insertion. The intensity changes of the redox peaks at ∼4.2 V corresponding to the H2 ↔ H3 phase transition during cycling correlate well with the relative cycling stability of the three cathodes. For both NCA89 and NCM90 cathodes, the deteriorating reversibility of the redox peak is clearly observed as the H2 ↔ H3 peak intensity gradually decreases during cycling, whereas that of the NCMA89 cathode remains nearly unchanged during the same cycling period. The relative reversibility of the H2 → H3 phase transition can be better

DOI: 10.1021/acsenergylett.8b02499
ACS Energy Lett. 2019, 4, 576−582

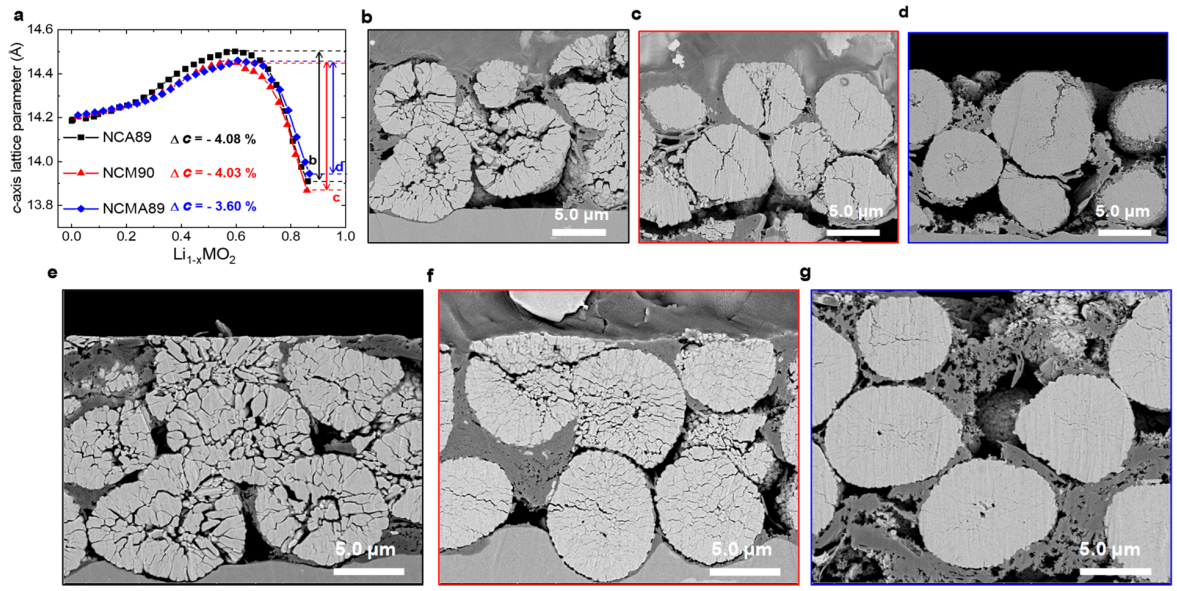

Figure 2. (a) *c*-axis lattice parameters of the NCA89, NCM90, and NCMA89 cathodes as a function of the extracted lithium. Cross-sectional SEM images of the fully charged cathodes at first cycle ($Li_{1-x}MO_2$ x = 0.88): (b) NCA89, (c) NCM90, and (d) NCMA89. Cross-sectional SEM images of the fully discharged cathodes after 1000 cycles: (e) NCA89, (f) NCM90, and (g) NCMA89.

seen in Figure S3c,d, which illustrates the normalized integrated peak intensity against the cycle number. The superior structural stability of the NCMA89 cathode is pronouncedly advertised when cycled at 4.5 V as the H2 → H3 peaks for NCA89 and NCM90 cathodes decay at a much faster rate in comparison to that for the NCMA89 cathode (Figure S3b,d). To explicitly demonstrate the deleterious effect of the H2 → H3 phase transition, which causes highly anisotropic strain in the deeply charged state, a series of in situ XRD experiments were performed while charging the three cathodes from 3.0 to 4.5 V at a constant current density of 36 mA g^{-1}. The lattice parameters estimated from the XRD data are plotted as a function of the state of charge in Figures 2a and S4. As equal amounts of Li ions are extracted from each cathode, the *a*-axis parameter continuously decreases. The magnitude of the overall lattice parameter reduction, Δa, is 2.1−2.2% for the three cathodes (Figure S4). However, in the *c*-direction, the lattice parameter gradually increases and then contracts sharply at the onset of the H2 → H3 phase transition. This abrupt contraction in the *c*-direction, which amounts to ∼4%, undermines the mechanical integrity of the secondary particle. The mechanical strain triggered by this phase transition is further aggravated by its anisotropy because the contraction in the *a*-direction is limited to ∼0.5% while the unit cell concurrently contracts by 4% in the *c*-direction during the phase transition. Hence, the extent of the *c*-axis contraction during the H2 → H3 phase transition critically determines the magnitude and the distribution of the local internal strain. Δc for the NCMA89 cathode was considerably lower than that of the NCA89 and NCM90 cathodes (Figure 2a). The effect of the reduced strain for the NCMA89 cathode is manifested by reduced or lack of microcracks in the secondary particles of the NCMA89 cathode in its deeply charged state (x = 0.88), whereas visible microcracks were observed in the cross-sectional images even in the first charge state for the other two cathodes (Figure 2b−d). In the case of the NCA89 cathode, the microcracks that nearly fractured the secondary particles were observed at x = 0.88, which is in agreement with the noticeably faster capacity fading observed when the cathode cycled at 4.5 V (Figure 2b). The cross-sectional images of both 1000 cycled NCA89 and NCM90 cathode particles fractured along the interparticle boundaries, exhibited almost pulverizing the cathode particles (Figure 2e,f), whereas the NCMA89 secondary particles remained mostly free of any microcracks (in the discharged state) even after performing 1000 cycles (Figure 2g). The cross-sectional SEM images of the cycled cathodes suggest that the introduction of a minute amount of Al together with Mn not only reduces the magnitude of the anisotropic strain of the NCMA89 cathode in the deeply charge state but also appears to increase the interparticle boundary strength, which is plausible because Al−O bonds provide strong bonding.[13,24,25] To directly verify the enhancement of the fracture toughness of the NCMA cathode, the fracture strength of a single particle from each cathode was measured using a microcompression tester. Shown in Figure S5, the NCMA89 particle withstood a force of 22.9 mN, which amounts to a particle strength of 185.7 MPa. In comparison, the failure load of the NCA89 particle was limited to only a 12.9 mN force (particle strength of 125.5 MPa), while the NCM90 particle had a slightly larger particle strength (force of 14.0 mN and particle strength of 137.2 MPa) than that of NCA89. It appears that the simultaneous presence of both Al and Mn ions in the NCMA89 cathode improves the mechanical stability, as evidenced by the microcompression test and the microcracking extent. The particle strength data also correlate well with the long-term cycling behavior of the three cathodes, and the Mn−Al-doping toughens the boundaries among primary particles to retard microcrack formation during the deleterious phase transition.[26,27]

The mechanical stability of the NCMA89 cathode (i.e., retardation of the microcrack nucleation and propagation) brings an additional benefit because the microcracks serve as channels for electrolyte infiltration into the particle interior. The infiltrated electrolyte attacks the internal exposed surface

DOI: 10.1021/acsenergylett.8b02499
ACS Energy Lett. 2019, 4, 576−582

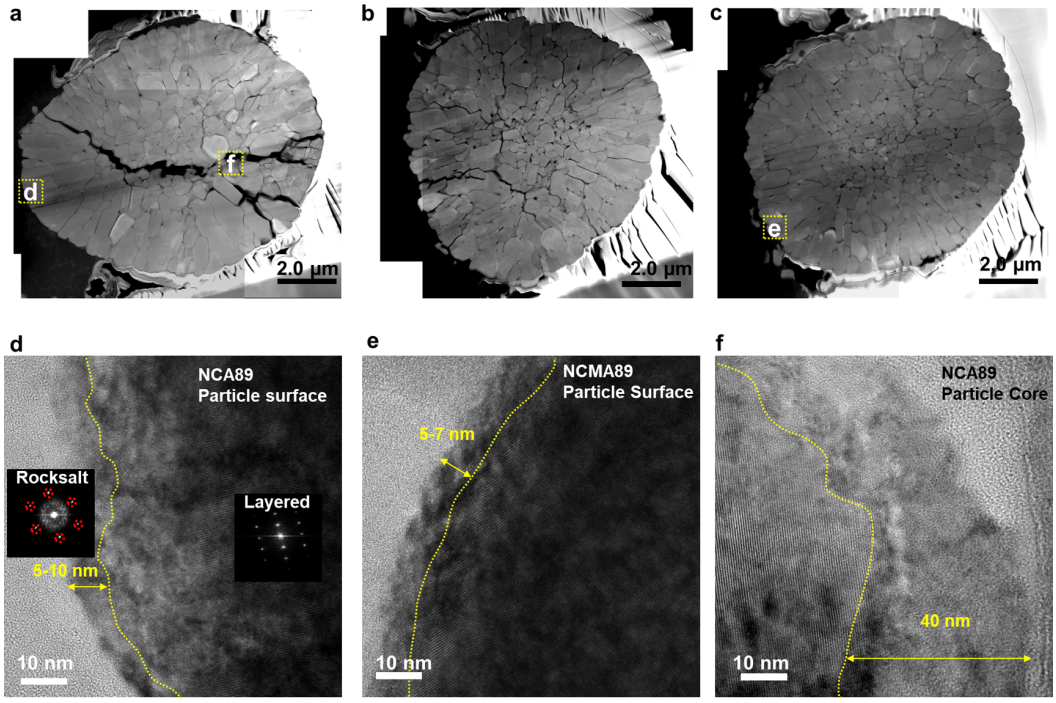

Figure 3. Mosaic scanning TEM images of the cycled cathodes after 100 cycles: (a) NCA89, (b) NCM90, and (c) NCMA89. High-resolution TEM images of surface primary particles: (d) NCA89 and (e) NCMA89 cathodes after 100 cycles. The high-resolution TEM images in (d,e) correspond to the regions marked by yellow boxes in (a,c). Fourier transforms of the marked regions by numerals are shown in (d) as insets. (f) High-resolution TEM image of a primary particle in the core region of the cycled NCA89 cathode marked by a yellow box in (a).

and increases the cathode's impedance through the continuous accumulation of a passivating NiO-like impurity layer on the particle surfaces.[28,29] Electrochemical impedance spectroscopy (EIS) was used to measure the impedance at the charged state. The impedance growth anticipated from the cycling data was clearly observed for the three cathodes (Figure S6a−c). The three cathodes exhibit a similar surface film resistance, which hardly changes during the entire cycling duration. Meanwhile the charge transfer resistance (R_{ct}) of the NCA89 cathode increases from 6.3 to 55 Ω after 100 cycles, whereas the NCMA89 cathode has a relatively stable R_{ct} value at 33 Ω after same cycling period (Figure S6d). The R_{ct} values from EIS data verify that the electrolyte infiltration into the particle interior is substantially reduced in the NCMA89 cathode because the three cathodes have a similar particle diameter and the damage of the external particle surface is likely identical in extent for the three cathodes. The relative electrolyte damage was also confirmed using TEM analysis of the cycled cathodes. The dark-field STEM image of the cycled NCA89 cathode shows a major crack traversing the entire particle and nearly fracturing the secondary particle into two halves (Figure 3a). Although several cracks in the cycled NCM90 cathode reached the particle surface and expedited the electrolyte infiltration (Figure 3b), the secondary particle remained mechanically intact. In turn, no visible cracks were observed in the NCMA89 cathode, attesting to its superior mechanical stability (Figure 3c). While assessing the surface structure degradation using high-resolution TEM (HR-TEM), a typical NiO-like surface layer that increases the charge transfer resistance was observed on the surface of the cycled NCA89 cathode, as shown in Figure 3d. Local Fourier transform images of the cycled cathode show that the surface rocksalt layer was confined to a thickness of 5−10 nm. Figure 3e shows the surface damaged layer of the cycled NCMA89 cathode whose thickness was 5−7 nm, demonstrating that the extent of the impedance-increasing surface damage was roughly the same for the three cathodes. However, the HR-TEM image of an interior grain along the microcrack in the NCA89 and NCM90 cathodes reveals that the rocksalt layer was substantially thicker (NCA89: ∼40 nm; NCM90: ∼25 nm) in Figures 3f and S7 compared to that found on the surface grain (5−10 nm). It appears that the exposed interior surfaces on the interior primary particles are relatively more susceptible to the electrolyte attack. Once the microcracks originating in the particle core extend to the external surface during charging (Li removal phase) and thereby allow electrolyte infiltration, crack faces are exposed to electrolyte attack. These internal surfaces are more vulnerable to electrolyte attack compared to the external surfaces as Li migration out of the particle core likely leaves the particle interior in a Li-deficient state, which is thermodynamically unstable and predisposed to phase transformation to the rocksalt state.[30] The TEM analysis in agreement with the EIS result, i.e., the R_{ct} buildup observed in the NCA89 cathode, mostly stems from the degradation of the interior surface exposed to the electrolyte through the microcracks. Thus, the retardation of microcrack formation in the NCMA89 cathode reinforces not only the mechanical integrity of the secondary particles in the Ni-rich layered cathodes but also the chemical stability against electrolyte attack by preventing infiltration of the electrolyte into the particle interior.

Recently, it was proposed that oxygen release from the lattice during deintercalation promotes transition metal dissolution and destabilizes the crystal structure of the layered

DOI: 10.1021/acsenergylett.8b02499
ACS Energy Lett. 2019, 4, 576−582

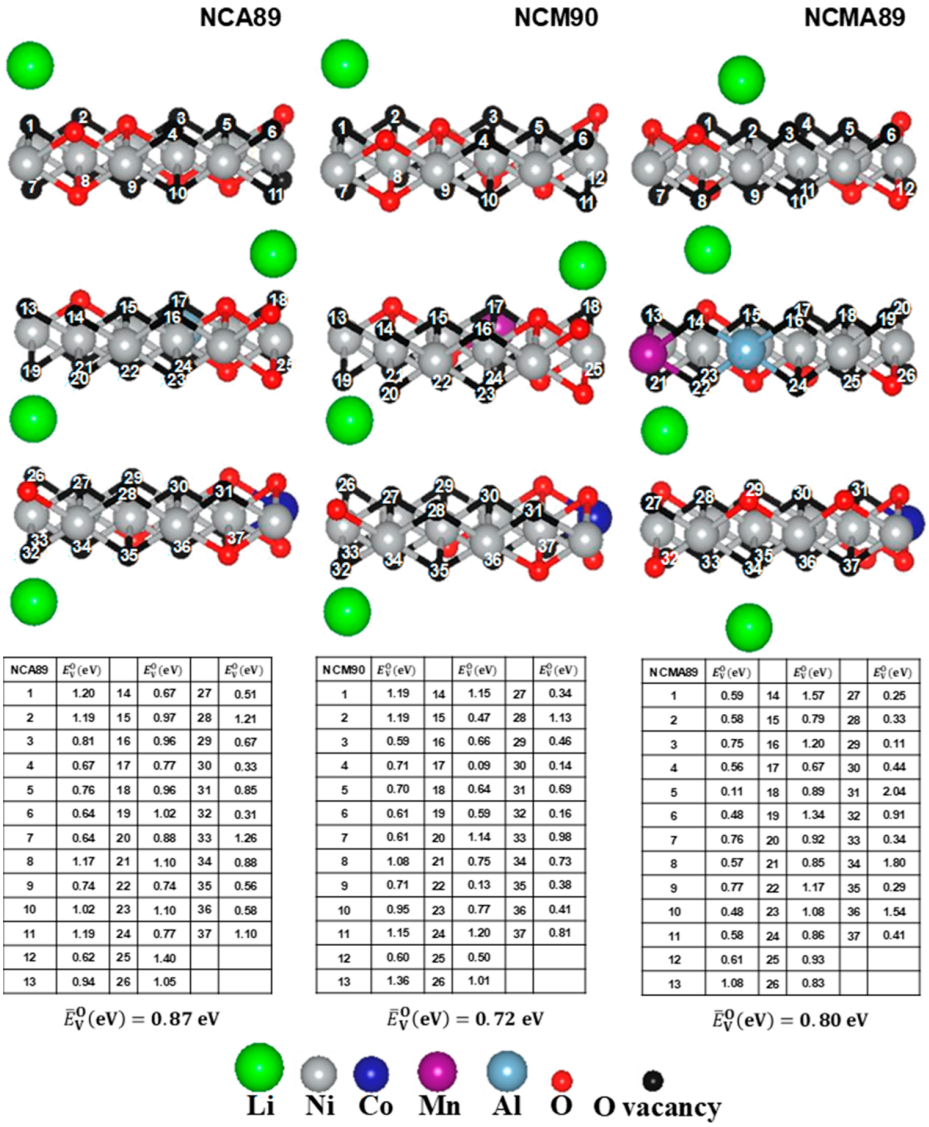

NCA89	E_V^O(eV)		E_V^O(eV)		E_V^O(eV)
1	1.20	14	0.67	27	0.51
2	1.19	15	0.97	28	1.21
3	0.81	16	0.96	29	0.67
4	0.67	17	0.77	30	0.33
5	0.76	18	0.96	31	0.85
6	0.64	19	1.02	32	0.31
7	0.64	20	0.88	33	1.26
8	1.17	21	1.10	34	0.88
9	0.74	22	0.74	35	0.56
10	1.02	23	1.10	36	0.58
11	1.19	24	0.77	37	1.10
12	0.62	25	1.40		
13	0.94	26	1.05		

$\bar{E}_V^O$(eV) = 0.87 eV

NCM90	E_V^O(eV)		E_V^O(eV)		E_V^O(eV)
1	1.19	14	1.15	27	0.34
2	1.19	15	0.47	28	1.13
3	0.59	16	0.66	29	0.46
4	0.71	17	0.09	30	0.14
5	0.70	18	0.64	31	0.69
6	0.61	19	0.59	32	0.16
7	0.61	20	1.14	33	0.98
8	1.08	21	0.75	34	0.73
9	0.71	22	0.13	35	0.38
10	0.95	23	0.77	36	0.41
11	1.15	24	1.20	37	0.81
12	0.60	25	0.50		
13	1.36	26	1.01		

$\bar{E}_V^O$(eV) = 0.72 eV

NCMA89	E_V^O(eV)		E_V^O(eV)		E_V^O(eV)
1	0.59	14	1.57	27	0.25
2	0.58	15	0.79	28	0.33
3	0.75	16	1.20	29	0.11
4	0.56	17	0.67	30	0.44
5	0.11	18	0.89	31	2.04
6	0.48	19	1.34	32	0.91
7	0.76	20	0.92	33	0.34
8	0.57	21	0.85	34	1.80
9	0.77	22	1.17	35	0.29
10	0.48	23	1.08	36	1.54
11	0.58	24	0.86	37	0.41
12	0.61	25	0.93		
13	1.08	26	0.83		

$\bar{E}_V^O$(eV) = 0.80 eV

Figure 4. Side views of atomic structures and calculated oxygen vacancy formation energy: E_V^O for the labeled oxygen sites and average vacancy formation energies and $\bar{E}_V^O$ for the NCA89, NCM90, and NCMA89 cathodes with 89% of Li ions removed from the lattice.

cathodes.[31,32] Density functional theory (DFT) calculations were employed to calculate the lithium and oxygen vacancy energies of the three cathodes in order to elucidate the Al-doping effect on the intrinsic structural stability of the three cathodes. To compute the average values of Li vacancy formation energies ($\bar{E}_V^{Li}$), we considered fully lithiated NCA89, NCM90, and NCMA89 cathodes. Li vacancy energies of the cathodes were calculated for 16 different vacancy sites (alphabet marking) shown in Figure S8 and Table S2. The respective average Li vacancy formation energies for the NCA89, NCM90, and NCMA89 cathodes were 3.96, 3.94, and 3.97 eV. These nearly identical Li vacancy energies suggest that the energy required for Li intercalation/deintercalation for the three cathodes is nearly equal for the three cathodes because of their similar compositions, which is in agreement with the fact that the initial discharge capacities delivered by the three cathodes were almost the same. The difference in the structural stability is, however, clearly observed in the O vacancy energy calculated with 89% of Li atoms removed from each lattice. The respective O vacancy energies for the three cathodes in the delithiated state were calculated for 37 different O sites, as shown in Figure 4, and the O vacancy energies are also listed in the accompanying tables. The average O vacancy energies were 0.87, 0.72, and 0.80 eV for the NCA89, NCM90, and NCMA89, respectively, indicating that the oxygen atoms are least likely released from the NCA89 cathode, as conjectured from the strong binding energy of Al−O bonds. The density functional calculation provides a strong basis for confirming the relative high structural stability of the NCA89 cathodes, in general, compared to the NCM90 cathodes. Incidentally, the O vacancy energy for the NCMA89 cathode is an average of the vacancy energies of the NCA89 and NCM90 cathodes so that the NCMA89 cathode partially benefits from the improved structural stability in the delithiated state by having Al ions in its lattice.

Thermal stability of a cathode is also important to battery safety. As seen in the differential scanning calorimetry (DSC) data in Figure 5, the peak temperature of the exothermic

DOI: 10.1021/acsenergylett.8b02499
ACS Energy Lett. 2019, 4, 576−582

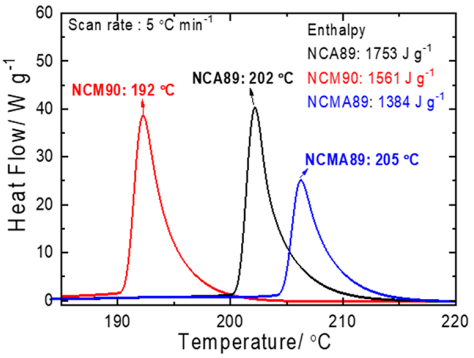

Figure 5. DSC profiles for the NCA89, NCM90, and NCMA89 cathodes measured in their second charged state ($Li_{0.3}MO_2$) in the presence of 1.2 M $LiPF_6$ EC:EMC = 3:7 by vol % with 2 wt % VC.

reaction for the NCA89 cathode was 202 °C, with heat generation of 1753 J g^{-1}, while the NCM90 cathode exhibited a peak temperature of 192 °C and heat generation of 1561 J g^{-1}. In comparison, NCMA89 demonstrates improved thermal stability with its exothermic peak temperature at 205 °C and heat generation of 1384 J g^{-1}. The improved thermal property of the NCMA89 cathode is ascribed to the decreased amount of microcracks, which reduces the amount of the infiltrated electrolyte. The DSC result confirms that the NCMA89 cathode is structurally stable due to the synergetic effect of Al and Mn ions stabilizing the layered structure and delaying the thermally induced phase transitions.

We have demonstrated that a hybrid of Ni-rich NCA and NCM cathodes, a quaternary system consisting of Li-$[Ni_{0.89}Co_{0.05}Mn_{0.05}Al_{0.01}]O_2$, is capable of outperforming both NCA89 and NCM90 with similar Ni contents in terms of cycling and thermal stabilities. In situ XRD analysis shows that the Al-doping effect is rather subtle as the volume contraction/expansion during the H2 ↔ H3 phase transition is slightly reduced by Al-doping of the NCM cathode. This reduction in volume change, however, together with the enhanced intrinsic mechanical strength directly confirmed by the single-particle compression test, is sufficient to suppress microcrack nucleation and propagation. It was shown that the microcrack suppression observed in the NCMA89 cathode was the key to ensure its long-term cycling stability as microcracks serve as channels for electrolyte infiltration and lead to subsequent surface degradation of internal surfaces. The proposed Ni-enriched NCMA cathode provides extra cycling stability, which is essential in the case of EVs that require a long battery life (>500 cycles). The structural stability gained by Al-doping also improved the thermal stability of the cathode, which contributes to a safer battery.

■ ASSOCIATED CONTENT

Supporting Information

The Supporting Information is available free of charge on the ACS Publications website at DOI: 10.1021/acsenergylett.8b02499.

Experimental methods, electrochemical performance data, lithiated oxide SEM image, XRD patterns, lattice parameters of cathodes, Nyquist plots as a function of cycles, microcompression tests, TEM image of the cycled cathode, and simulation data for the formation energy (PDF)

■ AUTHOR INFORMATION

Corresponding Authors

*E-mail: yksun@hanyang.ac.kr (Y.-K.S.).
*E-mail: csyoon@hanyang.ac.kr (C.S.Y.).

ORCID

Chong S. Yoon: 0000-0001-6164-3331
Yang-Kook Sun: 0000-0002-0117-0170

Notes

The authors declare no competing financial interest.

■ ACKNOWLEDGMENTS

This work was mainly supported by the Global Frontier R&D Programme (2013M3A6B1078875) on the Center for Hybrid Interface Materials (HIM), by the Ministry of Science and ICT, and by a Grant from the Human Resources Development program (No. 20154010200840) of the Korea Institute of Energy Technology Evaluation and Planning (KETEP), funded by the Ministry of Trade, Industry and Energy of the Korean government.

■ REFERENCES

(1) U.S. Department of Energy. Energy Efficiency & Renewable Energy. *Annual Merit Review Result Report - Energy Storage Technologies*; 2012.

(2) Myung, S.-T.; Maglia, F.; Park, K.-J.; Yoon, C. S.; Lamp, P.; Kim, S.-J.; Sun, Y.-K. Nickel-Rich Layered Cathode Materials for Automotive Lithium-Ion Batteries: Achievements and Perspectives. *ACS Energy Lett.* **2017**, *2*, 196−223.

(3) Saadoune, I.; Delmas, C. $LiNi_{1-y}Co_yO_2$ Positive Electrode Materials: Relationships between the Structure, Physical Properties and Electrochemical Behavior. *J. Mater. Chem.* **1996**, *6*, 193−199.

(4) Liu, Z.; Yu, A.; Lee, J. Y. Synthesis and Characterization of $LiNi_{1-x-y}Co_xMn_yO_2$ as the Cathode Materials of Secondary Lithium Batteries. *J. Power Sources* **1999**, *81*−*82*, 416−419.

(5) Ohzuku, T.; Makimura, Y. Layered Lithium Insertion Material of $LiNi_{1/2}Mn_{1/2}O_2$: A Possible Alternative to $LiCoO_2$ for Advanced Lithium-Ion Batteries. *Chem. Lett.* **2001**, *30*, 744−745.

(6) Kostecki, R.; McLarnon, F. Local-Probe Studies of Degradation of Composite $LiNi_{0.8}Co_{0.15}Al_{0.05}O_2$ Cathodes in High-Power Lithium-Ion Cells. *Electrochem. Solid-State Lett.* **2004**, *7*, A380−A383.

(7) Kondo, H.; Takeuchi, Y.; Sasaki, T.; Kawauchi, S.; Itou, Y.; Hiruta, O.; Okuda, C.; Yonemura, M.; Kamiyama, T.; Ukyo, Y. Effects of Mg-Substitution in $Li(Ni,Co,Al)O_2$ Positive Electrode Materials on the Crystal Structure and Battery Performance. *J. Power Sources* **2007**, *174*, 1131−1136.

(8) Sun, Y.-K.; Myung, S.-T.; Park, B.-C.; Prakash, J.; Belharouak, I.; Amine, K. High-Energy Cathode Material for Long-Life and Safe Lithium Batteries. *Nat. Mater.* **2009**, *8*, 320−324.

(9) Zhou, P.; Meng, H.; Zhang, Z.; Chen, C.; Lu, Y.; Cao, J.; Cheng, F.; Chen, J. Stable Layered Ni-rich $LiNi_{0.9}Co_{0.07}Al_{0.03}O_2$ Microspheres Assembled with Nanoparticles as High-Performance Cathode Materials for Lithium-Ion Batteries. *J. Mater. Chem. A* **2017**, *5*, 2724−2731.

(10) Kim, U.-H.; et al. Pushing the Limit of Layered Transition Metal Oxide Cathodes for High-Energy Density Rechargeable Li Ion Batteries. *Energy Environ. Sci.* **2018**, *11*, 1271−1279.

(11) Noh, H.-J.; Youn, S.; Yoon, C. S.; Sun, Y.-K. Comparison of the Structural and Electrochemical Properties of Layered $Li[Ni_xCo_yMn_z]O_2$ (x = 1/3, 0.5, 0.6, 0.7, 0.8 and 0.85) Cathode Material for Lithium-Ion Batteries. *J. Power Sources* **2013**, *233*, 121−130.

(12) Sun, H.-H.; Choi, W.; Lee, J. K.; Oh, I.-H.; Jung, H.-G. Control of Electrochemical Properties of Nickel-Rich Layered Cathode Materials for Lithium Ion Batteries by Variation of the Manganese to Cobalt Ratio. *J. Power Sources* **2015**, *275*, 877−883.

(13) Yoon, C. S.; Choi, M. H.; Lim, B.-B.; Lee, E.-J.; Sun, Y.-K. Review—High-Capacity $Li[Ni_{1-x}Co_{x/2}Mn_{x/2}]O_2$ (x = 0.1, 0.05, 0)

DOI: 10.1021/acsenergylett.8b02499
ACS Energy Lett. 2019, 4, 576−582

Cathodes for Next-Generation Li-Ion Battery. *J. Electrochem. Soc.* **2015**, *162*, A2483−A2489.
(14) Chowdari, B. V. R.; Subba Rao, G. V.; Chow, S. Y. Cathodic Behavior of (Co, Ti, Mg)-Doped $LiNiO_2$. *Solid State Ionics* **2001**, *140*, 55−62.
(15) Subramanian, V.; Fey, G. T.-K. Preparation and Characterization of $LiNi_{0.7}Co_{0.2}Ti_{0.05}M_{0.05}O_2$ (M = Mg, Al and Zn) Systems as Cathode Materials for Lithium Batteries. *Solid State Ionics* **2002**, *148*, 351−358.
(16) Croguennec, L.; Suard, E.; Willmann, P.; Delmas, C. Structural and Electrochemical Characterization of the $LiNi_{1-y}Ti_yO_2$ Electrode Materials Obtained by Direct Solid-State Reactions. *Chem. Mater.* **2002**, *14*, 2149−2157.
(17) Zhou, F.; Zhao, X.; Lu, Z.; Jiang, J.; Dahn, J. R. The Effect of Al Substitution on the Reactivity of Delithiated $Li-Ni_{1/3}Mn_{1/3}Co_{(1/3-z)}Al_zO_2$ with Non-Aqueous Electrolyte. *Electrochem. Commun.* **2008**, *10*, 1168−1171.
(18) Woo, S.-W.; Myung, S.-T.; Bang, H.; Kim, D.-W.; Sun, Y.-K. Improvement of Electrochemical and Thermal Properties of $Li[Ni_{0.8}Co_{0.1}Mn_{0.1}]O_2$ Positive Electrode Materials by Multiple Metal (Al, Mg) Substitution. *Electrochim. Acta* **2009**, *54*, 3851−3856.
(19) Wilcox, J.; Patoux, S.; Doeff, M. Structure and Electrochemistry of $LiNi_{1/3}Co_{1/3-y}M_yMn_{1/3}O_2$ (M = Ti, Al, Fe) Positive Electrode Materials. *J. Electrochem. Soc.* **2009**, *156*, A192−A198.
(20) Tang, H.; Zhao, F.; Chang, Z.-r.; Yuan, X.-Z.; Wang, H. Synthesis and Electrochemical Properties of High Density $Li-Ni_{0.8}Co_{0.2-x}Ti_xO_2$ for Lithium-Ion Batteries. *J. Electrochem. Soc.* **2009**, *156*, A478−A482.
(21) Conry, T. E.; Mehta, A.; Cabana, J.; Doeff, M. M. Structural Underpinnings of the Enhanced Cycling Stability upon Al-Substitution in $LiNi_{0.45}Mn_{0.45}Co_{0.1-y}Al_yO_2$ Positive Electrode Materials for Li-ion Batteries. *Chem. Mater.* **2012**, *24*, 3307−3317.
(22) Schipper, F.; et al. From Surface ZrO_2 Coating to Bulk Zr Doping by High Temperature Annealing of Nickel-Rich Lithiated Oxides and Their Enhanced Electrochemical Performance in Lithium Ion Batteries. *Adv. Energy Mater.* **2018**, *8*, 1701682.
(23) Kim, U.-K.; Myung, S.-T.; Yoon, C. S.; Sun, Y.-K. Extending the Battery Life Using an Al-Doped $Li[Ni_{0.76}Co_{0.09}Mn_{0.15}]O_2$ Cathode with Concentration Gradients for Lithium Ion Batteries. *ACS Energy Lett.* **2017**, *2*, 1848−1854.
(24) Zhou, F.; Zhao, X.; Lu, Z.; Jiang, J.; Dahn, J. R. The Effect of Al Substitution on the Reactivity of Delithiated $LiNi_{(0.5-z)}Mn_{(0.5-z)}-A1_{2z}O_2$ with Nonaqueous Electrolyte. *Electrochem. Solid-State Lett.* **2008**, *11*, A155−A157.
(25) Myung, S.-T.; Komaba, S.; Hirosaki, N.; Hosoya, K.; Kumagai, N. Improvement of Structural Integrity and Battery Performance of $LiNi_{0.5}Mn_{0.5}O_2$ by Al and Ti Doping. *J. Power Sources* **2005**, *146*, 645−649.
(26) Araki, K.; Taguchi, N.; Sakaebe, H.; Tatsumi, K.; Ogumi, Z. Electrochemical Properties of $LiNi_{1/3}Co_{1/3}Mn_{1/3}O_2$ Cathode Material Modified by Coating with Al_2O_3 Nanoparticles. *J. Power Sources* **2014**, *269*, 236−243.
(27) Kim, H.-R.; Woo, S.-G.; Kim, J.-H.; Cho, W.; Kim, Y.-J. Capacity Fading Behavior of Ni-Rich Layered Cathode Materials in Li-ion Full Cells. *J. Electroanal. Chem.* **2016**, *782*, 168−173.
(28) Yoon, C. S.; Park, K.-J.; Kim, U.-K.; Kang, K. H.; Ryu, H.-H.; Sun, Y.-K. High-Energy Ni-Rich $Li[Ni_xCo_yMn_{1-x-y}]O_2$ Cathodes via Compositional Partitioning for Next-Generation Electric Vehicles. *Chem. Mater.* **2017**, *29*, 10436−10445.
(29) Ryu, H.-H.; Park, K.-J.; Yoon, C. S.; Sun, Y.-K. Capacity Fading of Ni-Rich $Li[Ni_xCo_yMn_{1-x-y}]O_2$ ($0.6 \leq x \leq 0.95$) Cathodes for High-Energy-Density Lithium-Ion Batteries: Bulk or Surface Degradation? *Chem. Mater.* **2018**, *30*, 1155−1163.
(30) Xia, S.; et al. Chemomechanical Interplay of Layered Cathode Materials Undergoing Fast Charging in Lithium Batteries. *Nano Energy* **2018**, *53*, 753−762.
(31) Bak, S.-M.; et al. Structural Changes and Thermal Stability of Charged $LiNi_xMn_yCo_zO_2$ Cathode Materials Studied by Combined *in Situ* Time-Resolved XRD and Mass Spectroscopy. *ACS Appl. Mater. Interfaces* **2014**, *6*, 22594−22601.
(32) Hausbrand, R.; Cherkashinin, G.; Ehrenberg, H.; Gröting, M.; Albe, K.; Hess, C.; Jaegermann, W. Fundamental Degradation Mechanisms of Layered Oxide Li-Ion Battery Cathode Materials: Methodology, Insights and Novel Approaches. *Mater. Sci. Eng., B* **2015**, *192*, 3−25.

DOI: 10.1021/acsenergylett.8b02499
ACS Energy Lett. 2019, 4, 576−582

Supporting Information

Quaternary Layered Ni-Rich NCMA Cathode for Lithium-Ion Batteries

Un-Hyuck Kim,[†] Liang-Yin Kuo,[‡] Payam Kaghazchi,[‖] Chong S. Yoon[,§], and Yang-Kook Sun*[,†]*

[†]Department of Energy Engineering, Hanyang University, Seoul 04763, South Korea

[‡]Physikalische und Theoretische Chemie, Institut für Chemie und Biochemie, Freie Universität Berlin, Takustraße 3, 14195 Berlin, Germany

[‖]Forschungszentrum Jülich GmbH, Institute of Energy and Climate Research (IEK-1), Materials Synthesis and Processing, Wilhelm-Johnen-Straße, 52425 Jülich, Germany

[§]Department of Materials Science and Engineering, Hanyang University, Seoul 04763, South Korea

Corresponding Author

E–mail: C.S.Y: csyoon@hanyang.ac.kr, Y.K.S: yksun@hanyang.ac.kr

EXPERIMENTAL METHODS

Synthesis of NCA89 ($Li[Ni_{0.888}Co_{0.097}Al_{0.015}]O_2$): Spherical NC $[Ni_{0.90}Co_{0.10}](OH)_2$ precursor was synthesized via the co-precipitation method with 2.0 M of $NiSO_4 \cdot 6H_2O$ and $CoSO_4 \cdot 7H_2O$ (Samchun Chemical, Korea) aqueous solution (Ni:Co = 90:10 molar ratio) as a starting material. A homogeneously mixed solution was fed into a batch reactor (17 L) filled with a solution of deionized (D.I.) water, NH_4OH (aq.), and NaOH (aq.) (Junsei, Japan) under in N_2 atmosphere. Concurrently, 4 M NaOH (aq.) (Samchun Chemical, Korea) (molar ratio of NaOH to transition metal = 2.0) and an NH_4OH chelating agent (aq.) (molar ratio of NH_4OH to transition metal = 1.2) were pumped separately into the reactor. The final precursor powder was obtained through filtration, washing with DI water and vacuum drying at 110 °C for 12 h. To obtain $Li[Ni_{0.888}Co_{0.097}Al_{0.0015}]O_2$, the precursor, $[Ni_{0.90}Co_{0.10}](OH)_2$ was mixed with $LiOH \cdot H_2O$ and $Al(OH)_3 \cdot 3H_2O$ (Li:Al:(Ni+Co)=1.01:0.015:0.985 in molar ratio) and calcined at 730 °C with heating rate 2 °C min^{-1} for 10 h in oxygen atmosphere and then followed by cooling at 30 °C with same cooling rate.

Synthesis of NCM90 ($Li[Ni_{0.90}Co_{0.05}Mn_{0.05}]O_2$) and NCMA89 ($Li[Ni_{0.89}Co_{0.05}Mn_{0.05}Al_{0.01}]O_2$): Spherical NCM90 $[Ni_{0.90}Co_{0.05}Mn_{0.05}](OH)_2$ precursor was synthesized via the co-precipitation method with 2.0 M of $NiSO_4 \cdot 6H_2O$, $CoSO_4 \cdot 7H_2O$ and $MnSO_4 \cdot H_2O$ aqueous solution (Ni:Co:Mn = 90:5:5 in molar ratio) as a starting material. A homogeneously mixed solution was fed into a batch reactor (17 L) filled with a solution of D.I. water, NH_4OH (aq.), and NaOH in N_2 atmosphere. Concurrently, 4 M NaOH (aq.) (molar ratio of NaOH to transition metal = 2.0) and an NH_4OH chelating agent (aq.) (molar ratio of NH_4OH to transition metal = 1.2) were pumped separately into the reactor. The final precursor powder was obtained through filtration, washing with D.I. water and vacuum drying at 110 °C for 12 h. To obtain $Li[Ni_{0.90}Co_{0.05}Mn_{0.05}]O_2$ and $Li[Ni_{0.89}Co_{0.05}Mn_{0.05}Al_{0.01}]O_2$, the precursor, $[Ni_{0.90}Co_{0.05}Mn_{0.05}](OH)_2$ was mixed with $LiOH \cdot H_2O$ (Li:(Ni+Co+Mn)=1.01:1 molar ratio) and then mixed with $LiOH \cdot H_2O$ and

$Al(OH)_3 \cdot 3H_2O$ (Li:Al:(Ni+Co+Mn)=1.01:0.01:0.99 molar ratio). The mixed powder was calcined at 750 °C for 10 h in oxygen atmosphere.

Analytical Techniques: The chemical compositions of the prepared powders were determined by inductively coupled plasma (ICP, OPIMA 8300, Perkin Elmer). The morphologies and structures of the prepared particles were observed by SEM (Nova Nano SEM 450, FEI). To observe the cross-section of the charged cathode electrode (particles) by SEM, half-cells were charged at different end cut-off voltage (4.3 and 4.5 V) and subsequently disassembled in an Ar-filled glove box. The recovered cathode was rinsed immediately using dimethyl carbonate (DMC) and completely dried under vacuum. The electrode was cut using a cross-sectional polisher (CP, JEOL SM-09010). Powder X-ray diffraction (XRD, Empyrean, Panalytical) using Cu Kα radiation was employed to identify the crystalline phases of the prepared powders. XRD data were obtained between 10 and 110° 2θ with a step size of 0.02°, and the collected XRD data were analyzed by the Rietveld refinement program Fullprof. *in-situ* XRD experiments were performed at the 6D-UNIST beamline at PAL in Pohang, Korea. The wavelength (λ = 0.65303 Å) of the incident beam and the sample-to-detector distance were calibrated using the LaB_6 standard. A modified 2032 coin-type half-cell with a 3-mm-diameter hole at its center containing a Kapton window served as the X-ray beam path. While the cell was being charged by applying a constant current of 36 mA g^{-1}, the XRD patterns were continuously recorded every 4 min with a 2D charge-coupled device detector (Rayonix MX225-HS) in transmission mode. The particle morphologies and structures of all powders were observed by SEM (JSM 6400, JEOL Ltd) and TEM (JEOL 2010, JEOL Ltd). Transmission electron microscopy (TEM) samples were prepared by focused ion beam and element mapping was carried out using a JEOL, Model JEM 2100F instrument.

Density functional theory (DFT) calculations: Density functional theory (DFT) calculations were carried out using the projector-augmented plane-wave (PAW) method implemented in the Vienna *Ab Initio* Simulation Package (VASP).[1] The Perdew–Burke–Ernzerhof (PBE) functional[2] with on-site Coulomb interaction correction introduced by Dudarev *et al.*[3] (U-J=6.2 for Ni, U-J=3.9 for Mn, U-J=3.3 for Co) were applied. A Monkhorst–Pack *k*-point mesh of 2×2×1 and an energy cut off of 500 eV were used. To study NCM, NCA, and NCMA structures, we first modelled bulk $LiNiO_2$ with a $R\bar{3}m$ structure and a 3×3×1 unit cell. To find minimum-energy structures of the ternary systems, we considered 13 possible arrangements of Ni, Co, and Mn in NCM and 13 possible arrangements of Ni, Co, and Al in NCA. To find minimum-energy structure of the quaternary system, we considered 92 possible arrangements of Ni, Co, Mn, and Al. To find the minimum energy structure of NCM. NCA, and NCMA with 89% removed Li ions, we have checked 4 possible arrangements of Li ions in each case. The most favorable structures are presented in Figure 4. Please note that a NCMA structure with a similar Li arrangement to NCM and NCA is 0.18 eV (per unit cell) less favorable than that is presented in Figure 4. The formation energies of Li and O vacant sites were obtained by $E_{\mathrm{V}}^{\mathrm{Li}} = E_{\mathrm{V}}^{\mathrm{tot}} - E_{\mathrm{pr}}^{\mathrm{tot}} + E_{\mathrm{Li}}^{\mathrm{tot}}$ and $E_{\mathrm{V}}^{\mathrm{O}} = E_{\mathrm{V}}^{\mathrm{tot}} - E_{\mathrm{pr}}^{\mathrm{tot}} + \frac{1}{2}E_{\mathrm{O_2}}^{\mathrm{tot}}$, respectively. $E_{\mathrm{V}}^{\mathrm{tot}}$ and $E_{\mathrm{pr}}^{\mathrm{tot}}$ are total energies of the system with and without vacancy, respectively. $E_{\mathrm{Li}}^{\mathrm{tot}}$ and $\frac{1}{2}E_{\mathrm{O_2}}^{\mathrm{tot}}$ are total energy of Li and O atom in an O_2 molecule and bulk Li (bcc), respectively.

(1) Kresse, G.; Furthmuller J. Efficient iterative schemes for ab initio total-energy calculations using a plane-wave basis set. *Phys. Rev. B* **1996**, *54*, 11169-11186.

(2) Perdew, J. P.; Burke, K.; Ernzerhof M. Generalized Gradient Approximation Made Simple. *Phys. Rev. Lett.* **1996**, *77*, 3865-3868.

(3) Dudarev, S. L.; Botton, G. A.; Savrasov, S. Y.; Humphreys, C. J.; Sutton A. P. Electron-energy-loss spectra and the structural stability of nickel oxide: An LSDA+U study. *Phys. Rev.B* **1998**, *57*, 1505-1509.

Electrochemical Testing: In order to fabricate the cathodes, the synthesized powders were mixed with carbon black and poly-(vinylidene fluoride) (PVdF, Solvay) (90: 5.5: 4.5) in N-methyl-2-pyrrolidone (NMP, Daejungchem, Korea). The slurry was coated on Al foil (UACJ, Japan), vacuum dried and roll-pressed (4 kN pressure). The electrolyte solution was 1.2 M $LiPF_6$ in ethylene carbonate−ethyl methyl carbonate (EC:EMC=3:7 by vol%) with 2 wt% vinylene carbonate(VC) additive (Panaxetec, Korea). Initial cell tests were performed with 2032 coin-type half-cells (Hosen, Japan) using lithium metal as an anode. The cells were cycled (charge and discharge) by applying a constant current density of 90 mA g^{-1} (0.5 C-rate) at 30 °C. Long-term cycle life tests were performed in a laminated pouch-type full-cell (34 mAh). Mesocarbon microbead (MCMB, Osaka Gas) graphite was used as an anode. A full-cell capacity balance (N/P ratio) was in the range of 1.15-1.20. The cells were charged and discharged between 3.0 and 4.2 V by applying a constant 1 C current (200 mA g^{-1}) at 25 and 45 °C.

Differential Scanning Calorimetry (DSC): For differential scanning calorimetry (DSC) analysis, the coin-cells were charged at a constant voltage of 4.3 V versus Li/Li^+ (2^{nd} cycle) after 1^{st} charging and discharging, and disassembled in an Ar-filled dry box. After the remaining electrolyte solution was carefully removed from the surface of the electrode, the cathode materials were recovered from the current collector. A stainless steel sealed pan with a gold-plated copper seal was used to collect 7.0 mg samples with electrolyte. Measurements were performed using a DSC 200 PC (Netzsch, Germany) at a temperature scan rate of 5 °C min^{-1}.

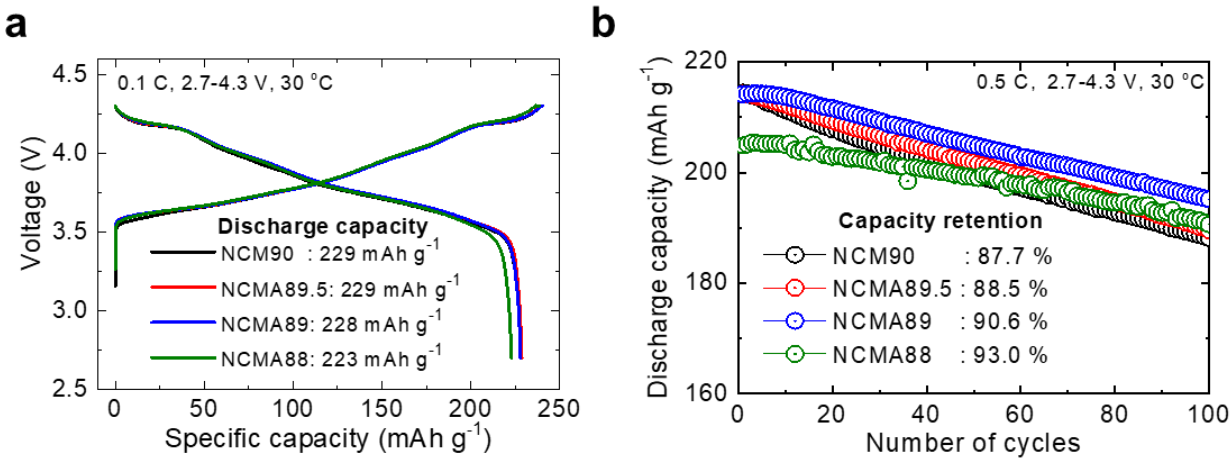

Figure S1. Electrochemical performance of $Li[Ni_{0.90}Co_{0.05}Mn_{0.05}]O_2$ (NCM90), $Li[Ni_{0.895}Co_{0.05}Mn_{0.05}Al_{0.005}]O_2$ (NCMA89.5), $Li[Ni_{0.89}Co_{0.05}Mn_{0.05}Al_{0.01}]O_2$ (NCMA89), and $Li[Ni_{0.88}Co_{0.05}Mn_{0.05}Al_{0.02}]O_2$ (NCMA88): (a) Initial charge and discharge curves of the four cathodes at 0.1 C and 30 °C cycled between 2.7 and 4.3 V with a 2032 coin-type half-cell using a Li metal anode and (b) cycling performances of the four cathodes at 0.5 C and 30 °C cycled between 2.7 and 4.3 V.

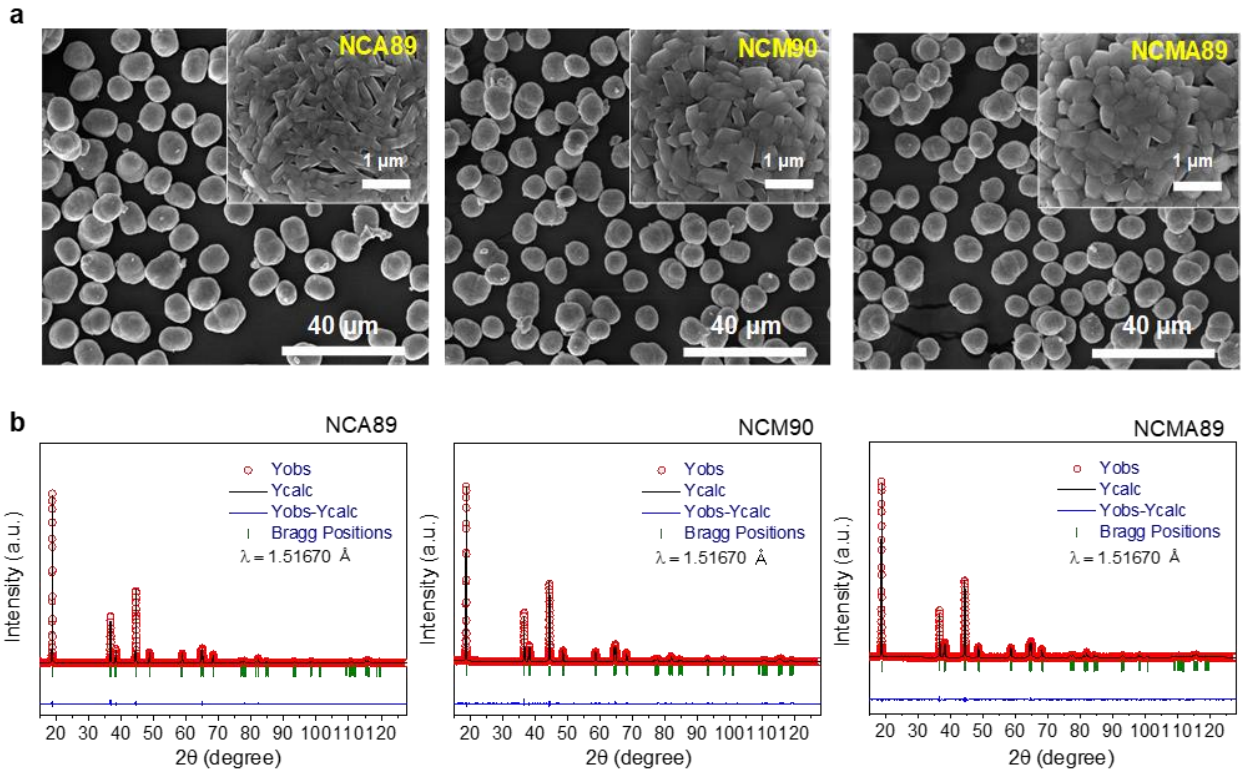

Figure S2. (a) SEM images of the as-prepared NCA89, NCM90, and NCMA89 cathodes at different magnifications displaying uniform spherical morphology. Each particle was composed of nano-sized primary particles. (b) XRD patterns and Rietveld refinement of the as-prepared NCA89, NCM90, and NCM89 cathodes.

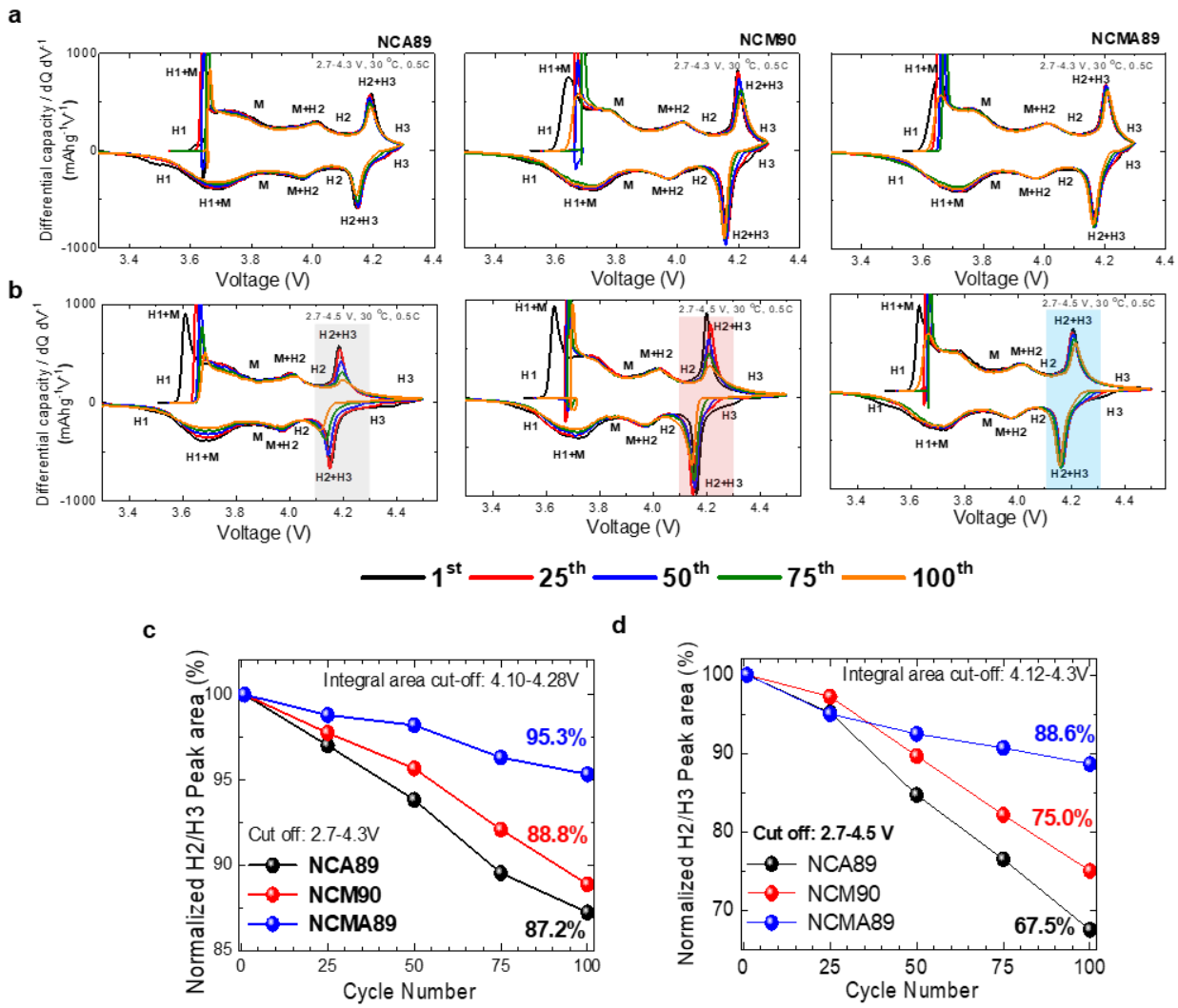

Figure S3. *dQ dV*$^{-1}$ vs. V curves for the NCA89, NCM90, and NCMA89 cathodes at 1st, 50th, 75th, and 100th cycles. All cells were tested with a voltage range of (a) 2.7–4.3 V and (b) 2.7–4.5 V at 0.5 C and 30 °C in a half cell using Li metal as an anode. Phase transition during charging and discharging are labeled (H = hexagonal and M = monoclinic). Normalized the integrated peak intensity plotted against the cycle number (c) 4.10 - 4.28 V and (d) 4.12 - 4.3 V.

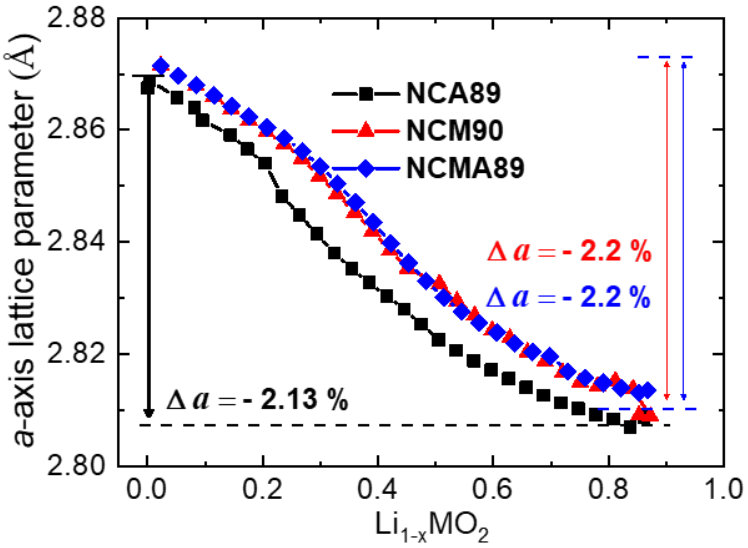

Figure S4. *a*-axis lattice parameters of the NCA89, NCM90, and NCMA89 cathodes as a function of the extracted lithium.

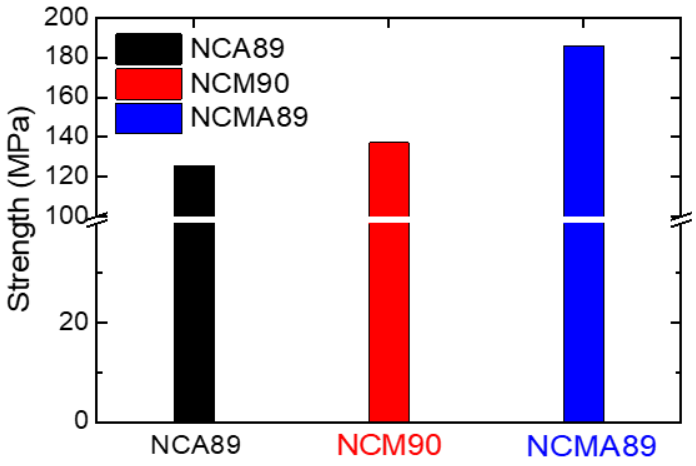

Figure S5. Micro compression test result of the NCA89, NCM90, and NCMA89 cathodes.

Particle strength = a x P / πd^2, where a = 2.8 (geometric factor), P: test force (N), and d: particle diameter (mm).

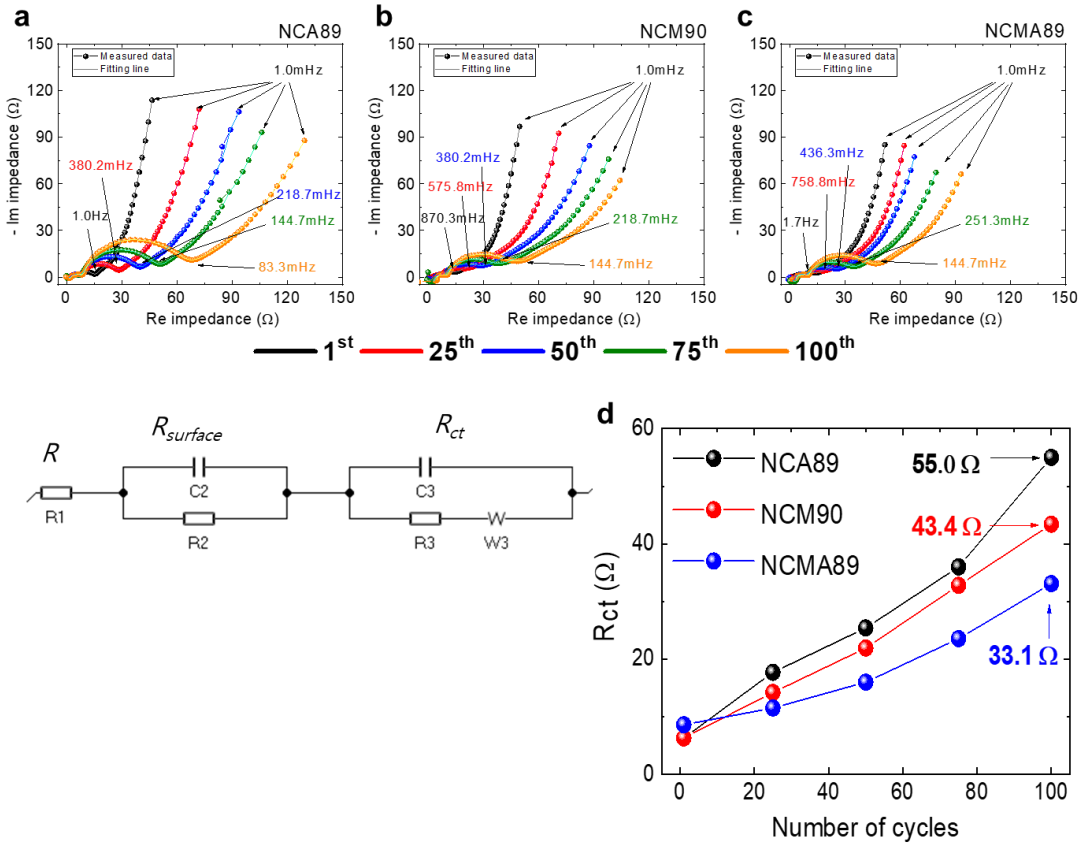

Figure S6. Nyquist plots of the impedance measured after every 25 cycle interval: (a) NCA89, (b) NCM90, and (c) NCMA89. (d) Comparison of the charge transfer resistance (R_{ct}) as a function of the number of cycles from Nyquist plots of (a-c).

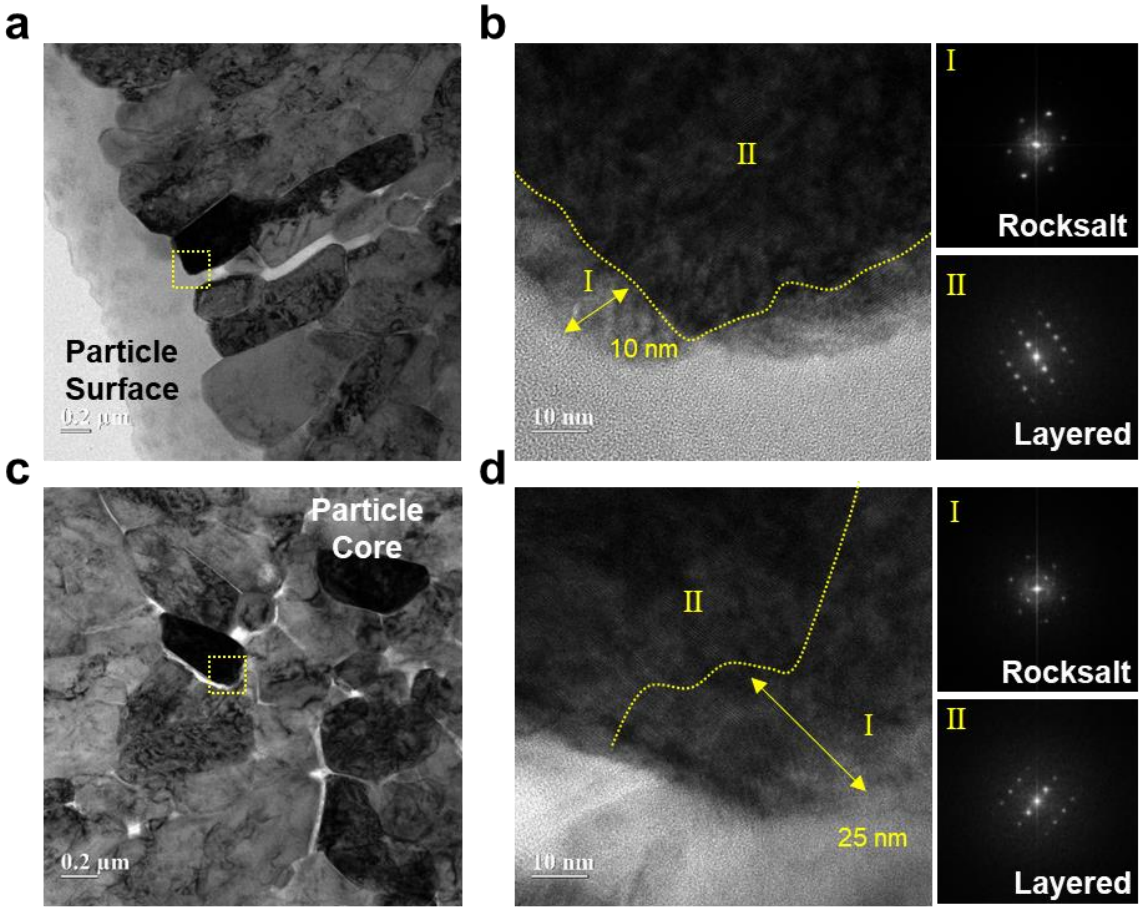

Figure S7. TEM images of cycled NCM90 cathode after 100 cycles. (a) low-magnification TEM image of surface primary particles with the corresponding (b) high-magnification TEM image of the region marked by the yellow box in (a), and Fourier transforms of the regions marked by numerals, (c) low-magnification TEM image of core primary particles with the corresponding (d) high-magnification TEM image of the region marked by the yellow box in (c), and Fourier transforms of the regions marked by numerals.

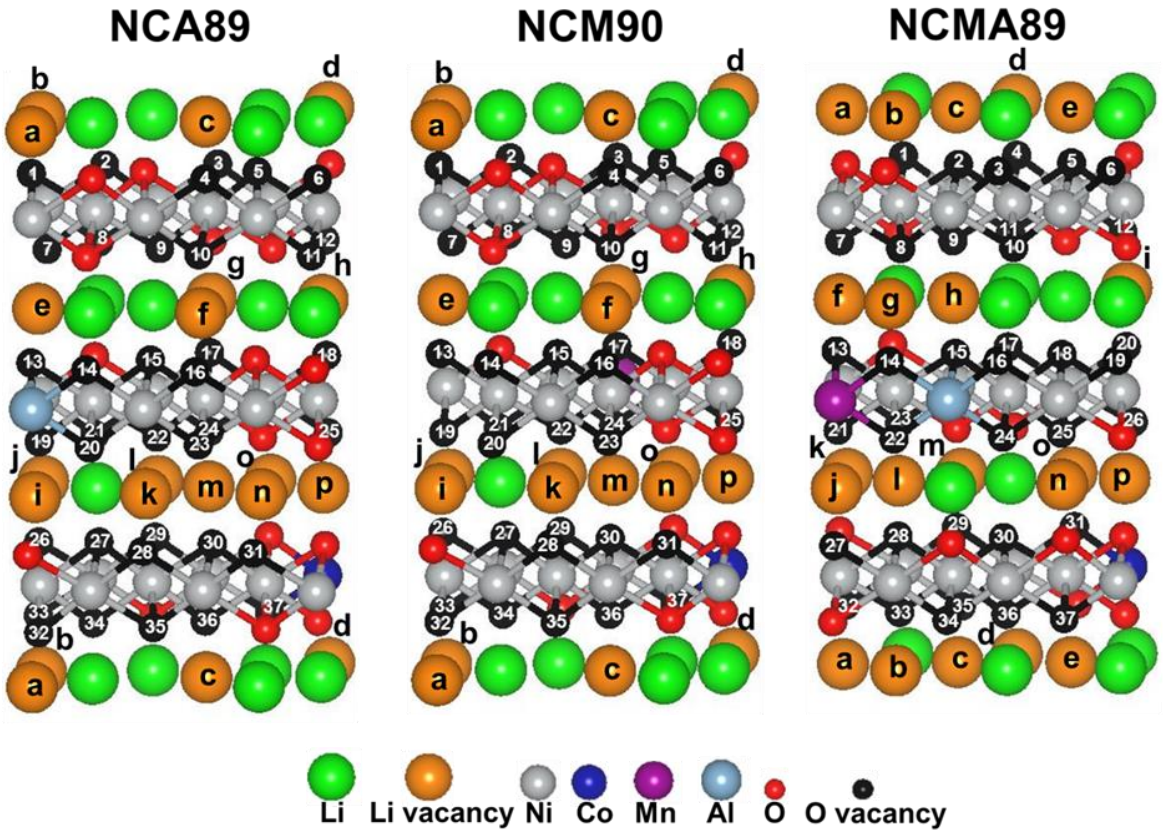

Figure S8. Side views of atomic structures of the NCA89, NCM90, and NCMA89 cathodes showing different Li vacancy sites for which Li formation energy was calculated.

Table S1. Structural parameters determined by Rietveld refinement of the X-ray diffraction data of $Li[TM]O_2$ powder. TM: Transition metal

Cathode	a_{hex} (Å)	c_{hex} (Å)	V (Å^3)	$^{a}z_{ox}$	$^{b}S_{(TMO2)}$ (Å)	$^{c}I_{(LiO2)}$ (Å)	R_p	R_{wp}	χ^2
NCA89	2.86938(1)	14.18238(8)	101.125(1)	0.24065(7)	2.0985	2.6289	12.1	14.5	4.87
NCM90	2.87385(4)	14.19793(19)	101.551(2)	0.24112(9)	2.1142	2.6185	13.1	16.0	4.78
NCMA89	2.87239(3)	14.20136(16)	101.472(2)	0.24145(7)	2.1241	2.6097	12.5	15.3	4.98

[a] Z_{ox}: atomic coordinate for oxygen ions

[b] Slab thickness: $S(MO_2) = (c_{hex}/3) - I(LiO_2)$

[c] Interslab space thickness: $I(LiO_2) = 2[(1/3) - z_{ox}]c_{hex}$

NCA89: $Li[Ni_{0.885}Co_{0.10}Al_{0.015}]O_2$

NCM90: $Li[Ni_{0.90}Co_{0.05}Mn_{0.05}]O_2$

NCMA89: $Li[Ni_{0.89}Co_{0.05}Mn_{0.05}Al_{0.01}]O_2$

Table S2. Calculated E_V^{Li} and $\bar{E}_V^{Li}$ values for the NCA89, NCM90, and NCMA89 cathodes. The labels for Li vacant sites are shown in Figure S8.

NCA89	$\boldsymbol{E_V^{Li}(eV)}$		$\boldsymbol{E_V^{Li}(eV)}$
a	4.13	i	3.78
b	3.76	j	3.83
c	4.45	k	3.78
d	3.91	l	4.39
e	3.98	m	3.90
f	3.81	n	4.44
g	3.82	o	3.71
h	3.86	p	3.75
$\boldsymbol{\bar{E}_V^{Li}(eV) = 3.96\ eV}$			
NCM90	$\boldsymbol{E_V^{Li}(eV)}$		$\boldsymbol{E_V^{Li}(eV)}$
a	3.77	i	4.12
b	4.06	j	3.78
c	3.62	k	4.19
d	3.82	l	3.80
e	3.96	m	4.18
f	3.75	n	3.81
g	3.74	o	3.64
h	4.94	p	3.88
$\boldsymbol{\bar{E}_V^{Li}(eV) = 3.94\ eV}$			
NCMA89	$\boldsymbol{E_V^{Li}(eV)}$		$\boldsymbol{E_V^{Li}(eV)}$

a	3.83	i	3.83
b	3.92	j	4.48
c	3.85	k	3.77
d	3.86	l	3.77
e	3.82	m	3.81
f	4.50	n	4.01
g	3.86	o	3.79
h	4.49	p	3.98
$\bar{E}_{\mathbf{V}}^{\mathbf{Li}}(\mathbf{eV}) = \mathbf{3.97\ eV}$			

4.4 Publication M4

"Unraveling the Role of Earth-Abundant Fe in the Suppression of Jahn–Teller Distortion of P'2-Type $Na_{2/3}MnO_2$: Experimental and Theoretical Studies"

J. U. Choi, Y. J. Park, J. H. Jo, L.-Y. Kuo, P. Kaghazchi and S.-T. Myung

ACS Appl. Mater. Interfaces, **48**, 40978 (2018)

DOI: 10.1021/acsami.8b16522

URL: https://doi.org/10.1021/acsami.8b16522

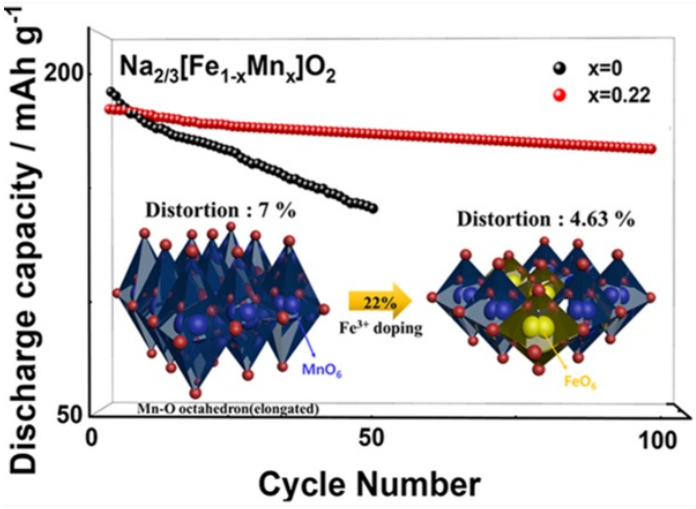

Figure 4.4: Graphical Abstract [143].

Author contributions

The fourth publication (**M4**) was a combination of experiment and theory. It was a joint project between Dr. Payam Kaghazchi at Freie Universität Berlin and Prof.Seung-Taek Myung in Sejong University Seoul. The experimental results in the manuscript were analyzed and written by Prof. Seung-Taek Myung's group. I performed the DFT calculations and prepared the figures for computational section. Dr. Payam Kaghazchi and I analyzed the

data and he wrote the theoretical part of the manuscript. All co-authors discussed the final results and finished the manuscript.

ACS APPLIED MATERIALS & INTERFACES

Letter

Cite This: ACS Appl. Mater. Interfaces 2018, 10, 40978−40984

www.acsami.org

Unraveling the Role of Earth-Abundant Fe in the Suppression of Jahn−Teller Distortion of P′2-Type $Na_{2/3}MnO_2$: Experimental and Theoretical Studies

Ji Ung Choi,[†] Yun Ji Park,[†] Jae Hyeon Jo,[†] Liang-Yin Kuo,[‡,§] Payam Kaghazchi,*[,‡,§] and Seung-Taek Myung*[,†]

[†]Department of Nanotechnology and Advanced Materials Engineering, Sejong University, Seoul 05006, South Korea

[‡]Institut für Chemie und Biochemie, Freie Universität Berlin, Takustraße 3, Berlin 14195, Germany

[§]Forschungszentrum Jülich GmbH, Institute of Energy and Climate Research (IEK-1), Materials Synthesis and Processing, Wilhelm-Johnen-Straße, Jülich 52425, Germany

Supporting Information

ABSTRACT: Layered $Na_{2/3}MnO_2$ suffers from capacity loss due to Jahn−Teller (J−T) distortion by Mn^{3+} ions. Herein, density functional theory calculations suggest $Na_{2/3}[Fe_xMn_{1-x}]O_2$ suppresses the J−T effect. The Fe substitution results in a decreased oxygen−metal−oxygen length, leading to decreases in the *b* and *c* lattice parameters but an increase in the *a* lattice constant. As a result, the capacity retention and rate capability are enhanced with an additional redox pair associated with $Fe^{4+/3+}$. Finally, the thermal properties are improved, with the Fe substitution delaying the exothermic reaction and reducing exothermic heat.

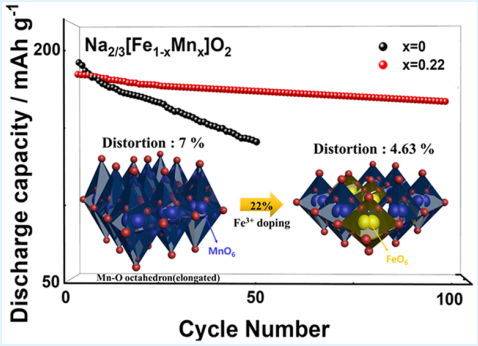

KEYWORDS: *Fe substitution, layered structure, cathode, sodium, battery, Jahn−Teller distortion*

After the success of lithium-ion batteries (LIBs), widely used in applications ranging from portable electronics to stationary power sources, significant attention has been directed to sodium-ion batteries (SIBs) because of the abundance of sodium resources. The successful launch of SIBs is expected to reduce costs to at least 80% of those for LIBs.[1] The recent introduction of earth-abundant elements such as Mn and Fe in SIBs by Yabuuchi and Komaba[2] has triggered the development of high-energy-density, low-cost, and safe cathode materials. To date, many works have focused on layered cathode materials such as Na_xMeO_2,[1−27] where Me denotes Ni, Co, Mn, Fe, Mg, or a mixture of 2 or 3 elements, including $Na_{2/3}MnO_2$,[13−15] Na_xFeO_2,[16] Na_xCoO_2,[17] Na_xCrO_2,[18] Na_xVO_2,[19,20] $Na_{2/3}[Ni_xMn_{1-x}]O_2$,[21,22] $Na_{2/3}[Fe_xMn_{1-x}]O_2$,[2,23,24] and $Na_{2/3}[Mg_xMn_{1-x}]O_2$.[25] These compounds can be classified as P-type or O-type structures and can be prepared by high-temperature solid-state chemistry routes because of the weakness of the Na−O bonds and the tendency of sodium to stabilize the high-oxidation states of transition elements.[26] At higher Na content, α-$NaMnO_2$ (space group: *C2/m*, O′3 structure) and β-$NaMnO_2$ (space group: *Pmnm*) are stable depending on the temperature; for example, the α phase is stable at low temperatures, and the β phase is stable at high temperatures.[26] At lower Na content, P3−Na_xMnO_2 (space group: *R3m*), P2−Na_xMnO_2 (space group: $P6_3/mmc$), and P′2-Na_xMnO_2 (space group: *Cmcm*) are stable depending on the temperature; low temperature < P3 < P2 < P′2 < high temperature.[4] Again, the P′2 phase is stable above 1000 °C, as reported by Stoyanova et al.[26] in 2010, and was further confirmed by Komaba et al.[15] However, P2-type $Na_{2/3}MnO_2$ shows capacity fading for this structure is rationalized by two effects. First, the Jahn−Teller (J−T) distortion coupled to Na ordering for Mn^{3+} induces a large volume change when the Na^+ concentration increases. Layered $Na_{2/3}MnO_2$, stabilized in the hexagonal P2 structure and orthorhombic P′2 structure, contains J−T Mn^{3+} ions, $Na_{2/3}[Mn^{3+}{}_{2/3}Mn^{4+}{}_{1/3}]O_2$, where the Na deficiency creates Mn^{4+} in the crystal structure.[15] Prime symbol means the distorted version (that is, P′2-Na_xMnO_2) is defined from P2−Na_xMnO_2 with distorted hexagonal lattice. The degree of distortion can be calculated using the longer *b* and the shorter *a* axes, using the relation of $b/a = \sqrt{3}$ for the hexagonal lattice.[15] Second, disproportionation of $2Mn^{3+}$ to Mn^{2+} and Mn^{4+} may cause dissolution active materials in the acidic electrolyte.[27] Recently, Kumakura et al.[15] suggested J−T distortion is less prominent in P′2-type $Na_{2/3}MnO_2$ than in

Received: September 21, 2018
Accepted: November 15, 2018
Published: November 15, 2018

DOI: 10.1021/acsami.8b16522
ACS Appl. Mater. Interfaces 2018, 10, 40978−40984

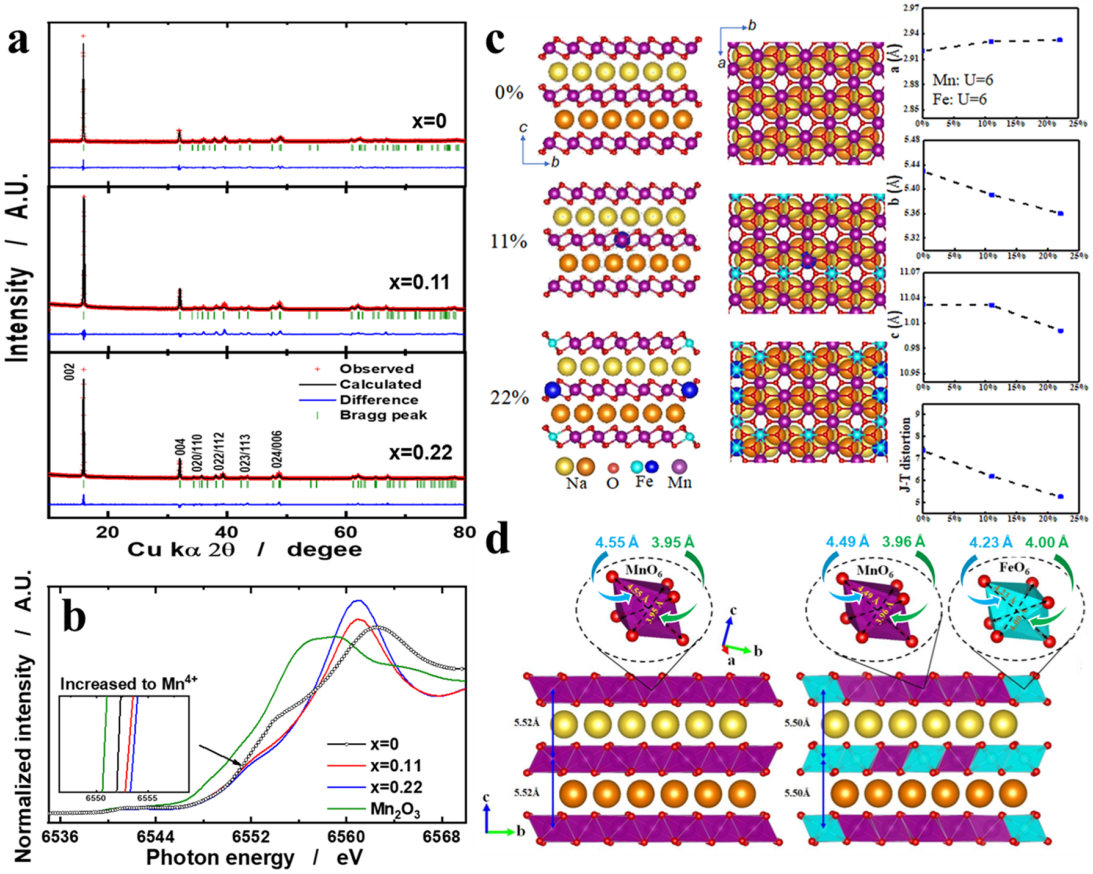

Figure 1. (a) Rietveld refinement of XRD results. (b) XANES spectra at the OCV state. (c) Calculated atomic structures (left, side views; middle, top views; right, lattice parameters) and J−T distortions of $Na_{2/3}[Fe_xMn_{1-x}]O_2$; and (d) calculated axial and averaged equatorial O−Mn−O and O−Fe−O bond lengths for the most-favorable structures of $Na_{2/3}[Fe_xMn_{1-x}]O_2$ (x equal to 0 for left and 0.22 for right sides).

P2-type $Na_{2/3}MnO_2$,[15] although multistep phase transitions occurred on discharge, OP4−P′2−P′′2. In particular, the P′′2 phase was formed in the deeply discharged state, in which the J−T Mn^{3+} ions appeared as the majority species, Na_xMnO_2 ($x \approx 1$). Nonetheless, the high capacity of P′2-type $Na_{2/3}MnO_2$ was retained with good electrode performance for 20 cycles; however, the capacity at a rate of 2C (524 mA g^{-1}) dropped to approximately 55 mAh g^{-1}.

Iron and manganese are ideal candidates for use in SIBs because they are abundant and inexpensive. Recently, Komaba et al.[2] and Delmas et al.[24] introduced P2-type layered $Na_{2/3}[Fe_{0.5}Mn_{0.5}]O_2$ (hexagonal, space group: $P6_3/mmc$), which delivers a reversible capacity of approximately 190 mAh g^{-1} activated by $Mn^{3+/4+}$ and $Fe^{3+/4+}$ redox couples with a reversible-phase transitions, as follows; P2 $Na_{2/3}[Fe_{0.5}Mn_{0.5}]O_2$ to the OP4 phase[2] and electrochemically induced P′2 $Na_{0.97}[Fe_{0.5}Mn_{0.5}]O_2$ (orthorhombic, space group: $Cmcm$) → P2 → Z phase [showing only one peak at 17.5° (2θ)][24] on charge, respectively. The success of using Fe is particularly notable because O3-type layered $NaFeO_2$ suffers from poor capacity retention resulting from the migration of Fe^{4+} in the crystal structure within a few cycles.[16]

To develop low-cost and high-energy-density cathode materials for SIBs, we used an earth-abundant element, specifically Fe, to replace Mn in P′2-type $Na_{2/3}MnO_2$. The $Fe^{3+/4+}$ redox couple is known to be available in layered compounds such as O3-type $NaFeO_2$ and P2-type $Na_{0.67}[Mn_{0.5}Fe_{0.5}]O_2$ cells. Recently, Ceder et al.[28] suggested a new mechanism of J−T effect on $Fe^{4+}O_6$ octahedra that provide the buckling capability to lower the Na migration barrier thus facilitates the Na^+ diffusion. Also, partial substitution by Ti^{4+} was resulted in the minimizing of the Jahn−Teller effect, leading to suppression of Mn dissolution and increased electrochemical properties.[6,7] In this study, we report that Fe replacement in orthorhombic P′2-type $Na_{2/3}[Mn_{1-x}Fe_x]O_2$ (x to 0.22) minimizes the effect of J−T distortion in the crystal structure, thereby improving the electrode performance. We predict the crystal structure using density functional theory (DFT) calculations to understand how the crystal structure is altered by the Fe content. We further unveil the electrode performance and reaction mechanism driving the reversible electrochemical behavior achieved by Fe replacement through X-ray absorption spectroscopy and operando synchrotron X-ray diffraction studies. We observe the reaction is activated by the $Fe^{3+/4+}$ and $Mn^{3+/4+}$ redox couple, and the added Fe results in suppression of the multistep phase transitions, caused by the J−T effect, which shows a simple phase transition, P′2 → OP4, leading to improved capacity retention for prolonged cycling. For the first time, we propose the substantial capability of P′2-$Na_{2/3}[Mn_{1-x}Fe_x]O_2$ as a high-capacity cathode material for SIBs, with the use of earth-abundant elements highlighted.

The X-ray diffraction (XRD) patterns were indexed to the P′2 structure with $Cmcm$ space group for x = 0, 0.11, and 0.22

DOI: 10.1021/acsami.8b16522
ACS Appl. Mater. Interfaces 2018, 10, 40978−40984

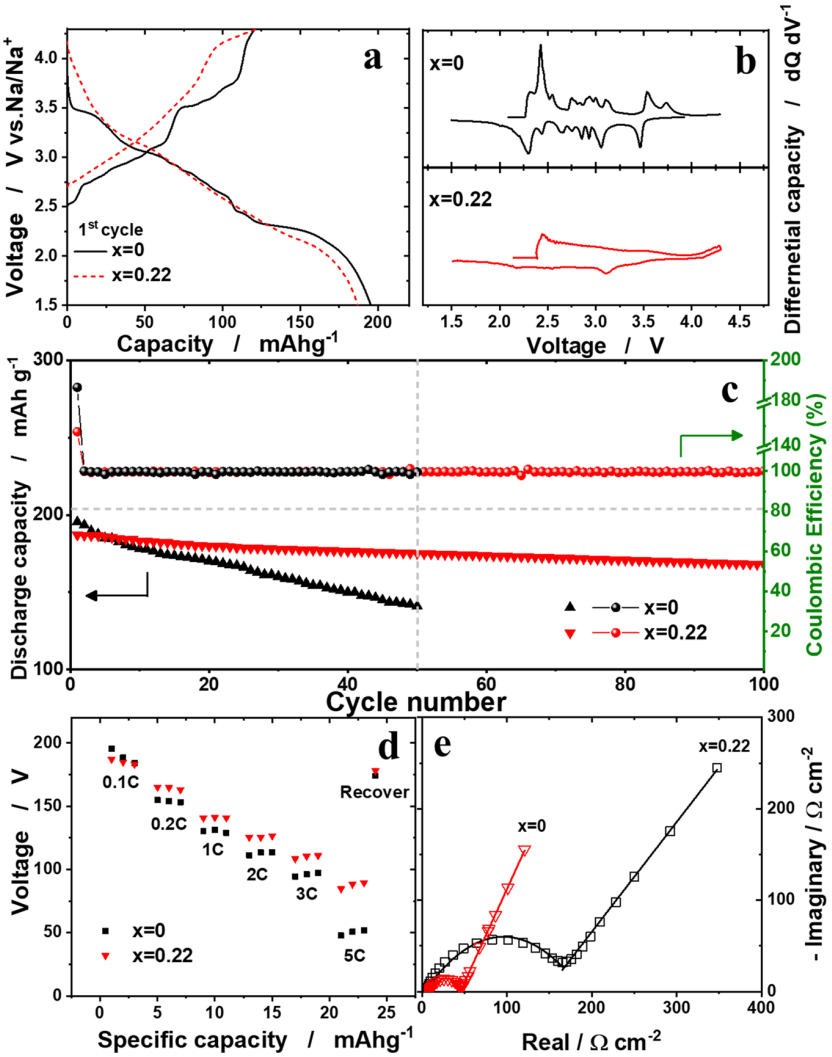

Figure 2. (a) Galvanostatic charge−discharge voltage profiles, (b) dQ/dV profiles, (c) cycling performance at 0.1C (26 mA g^{-1}), (d) resulting rate capability with recovery capacity measured at a rate of 0.1 C after the rate test, and (e) Cole−Cole plots of $Na_{2/3}[Fe_xMn_{1-x}]O_2$ (x equal to 0 and 0.22) electrodes.

in $Na_{2/3}[Fe_xMn_{1-x}]O_2$ (Figure 1a). Rietveld refinement of the XRD data was performed assuming the *Cmcm* space group.[13,14] The Na/Fe/Mn ratio was determined to be 0.669:1 for $Na_{2/3}MnO_2$, 0.659/0.109/0.891 for $Na_{2/3}[Fe_{0.11}Mn_{0.89}]O_2$, and 0.655/0.219/0.781 for $Na_{2/3}[Fe_{0.22}Mn_{0.78}]O_2$ (Table S-1). When the Fe content was higher than x = 0.22 in $Na_{2/3}[Fe_xMn_{1-x}]O_2$, unwanted $MnFe_2O_4$ impurity was formed (Figure S-1). Because of the high-temperature calcination at 1200 °C, the resulting primary particles were able to grow to approximately 3 μm in diameter (Figure S-2). P′2 $Na_{2/3}MnO_2$ has an oxidation state of $Mn^{3.33+}$ in theory, expressed as $Na_{2/3}[Mn^{3+}_{0.67}Mn^{4+}_{0.33}]O_2$.[15] In this work, we observed with increasing Fe content, stabilized as Fe^{3+}, the resulting oxidation state of Mn became higher (Figure 1b). This result indicates Fe^{3+} preferentially occupies the Mn^{3+} sites because of the similarity of the ionic radii of Mn^{3+} (0.645 Å) and Fe^{3+} (0.65 Å); it is reasonable to thus conclude the average oxidation state of Mn increases as Fe^{3+} replaces Mn^{3+}. Note that there was no change in the total oxidation state of the transition metals for these compounds because of the charge compensation of Mn^{3+} by Fe^{3+}. In this case, no structural variation is expected because of the similarity of the ionic radius of the substituent. Nevertheless, the resulting lattice parameters varied with Fe substitution (Table S-1). The only thing to consider in this case is Mn^{3+} is a J−T ion with abnormal elongation of the Mn−O distance along one direction in the MnO_6 octahedron, whereas this abnormal lengthening is not observed in the FeO_6 octahedron.

The most-favorable structure calculated using DFT was the same as that determined using the Coulomb-energy calculation (Figures S-3−S-5). The Na ions in both Na layers had a 2D hexagonal honeycomb-like arrangement (Figure 1c). The theoretical lattice parameters of a = 2.92 Å (exp: 2.8301 Å), b = 5.43 Å (exp: 5.2752 Å), and c = 11.03 Å (exp: 11.1971 Å) differed by a maximum of 2.9% from our experimental values. The calculated J−T distortion of $\frac{b}{\sqrt{3}a}$ = 7.4% was only slightly larger than the experimental value of 7.0%. Afterward, we studied the atomic structure of $Na_{2/3}[Mn_{1-x}Fe_x]O_2$. Because the ionic charge of Fe is the same as that of Mn, the Coulomb energy calculations could not guide us in determining the minimum energy structure for the Fe-doped case. We,

DOI: 10.1021/acsami.8b16522
ACS Appl. Mater. Interfaces 2018, 10, 40978−40984

therefore, applied the DFT-PBE + U calculation to explore several possible configurations in which different Mn cations at different MnO_2 layers were replaced by Fe dopants. Because the P′2 type $Na_{2/3}MnO_2$ structure has two different MO_2 layers (AB BA oxygen layer stacking), we have considered Fe → Mn replacement at each or both of the MO_2 layers. A total of 20 and 42 structures were considered for the 11% and 22% Fe dopants, respectively. The most favorable structures for Fe-doped $Na_{2/3}MnO_2$ are shown in Figure 1c. Consistent with our experimental measurements, the DFT calculations indicated the *a* lattice parameter increased, while the *b* and *c* lattice parameters and J−T distortion decreased. Our analysis of the O−Mn−O and O−Fe−O bond lengths for 22% Fe doping (Figure 1d) explains this behavior. Fe dopants suppress the J−T distortion in $Na_{2/3}[Fe_{0.22}Mn_{0.78}]O_2$ by increasing the equatorial O−Me−O (Me: Mn and Fe) distances and decreasing the axial O−Me−O ones. The equatorial O−Me−O length is located precisely along the lattice vector *a*, which is perpendicular to the *b* and *c* lattice vectors. Therefore, the Fe-doping-induced increase in the equatorial O−Me−O distances causes the lattice parameter *a* to expand. However, the axial O−Me−O bond is parallel to the *bc* plane. Thus, the Fe-doping-induced decrease in the axial O−Me−O length leads to decreases in the lattice parameters *b* and *c*.

Figure 2a compares the galvanostatic electrochemical properties of the $Na_{2/3}[Fe_xMn_{1-x}]O_2$ (x = 0 and 0.22) electrodes at C/10 (26 mA g^{-1}) between 1.5 and 4.3 V. The delivered discharge capacities were 195, 192, and 187 mAh g^{-1} for the $Na_{2/3}[Fe_xMn_{1-x}]O_2$ (x = 0, 0.1 (Figure S-6), and 0.22) electrodes, respectively. The corresponding voltage profile of the $Na_{2/3}[Fe_xMn_{1-x}]O_2$ electrodes clearly contains several voltage plateaus can be attributed to the structural change; in addition, the smooth curve at higher voltage must be associated with the suppression of such phase transitions (Figure 2b). This tendency is more evident on discharge, at which point a smooth voltage decay is observed for $Na_{2/3}[Fe_{0.22}Mn_{0.78}]O_2$. The capacity slightly decreased from 195 to 187 mAh g^{-1} with the substitution; however, the resulting energy density was improved for $Na_{2/3}[Fe_{0.22}Mn_{0.78}]O_2$ because of the appearance of capacity approximately 20 mAh g^{-1}, corresponding to 75 Wh g^{-1}, in the 4.3−3.5 V range on discharge (Figure 2a). Because this increased capacity is absent in $Na_{2/3}MnO_2$, the observed activity is likely due to the $Fe^{4+/3+}$ reaction. More importantly, the Fe substitution in $Na_{2/3}[Fe_xMn_{1-x}]O_2$ leads to improvement of the capacity retention. The first Coulombic efficiencies (CE) for both compounds are higher than 1, which is typically observed in sodium deficiency cathode materials (Figure 2c). The CEs becomes almost 1, after the first cycle. Significant enhancement of the rate capability is seen at different discharge rates (Figure 2d). After the test at a 5 C rate, the capacity was recovered to 174 mAh g^{-1} for P′2-$Na_{2/3}MnO_2$ and 178 mAh g^{-1} for the P′2-$Na_{0.67}[Fe_{0.22}Mn_{0.78}]O_2$. The improved rate capability of the $Na_{2/3}[Fe_{0.22}Mn_{0.78}]O_2$ electrode is associated with the enhanced electrical conductivity, 1.11 × 10^{-4} S cm^{-1} (Table S-1), and simple structural variation achieved by the Fe substitution. The electrical conductivity by the introduction of Fe can affect improvement in the Na^+ diffusion (Figure S-7). Specifically, the calculated coefficients ranged 10^{-13}−10^{-17} cm^{-2} s^{-1} for the P′2 $Na_{2/3}MnO_2$, while the coefficients were calculated to be 10^{-11}−10^{-15} cm^{-2} s^{-1} for the P′2 $Na_{2/3}[Fe_{0.22}Mn_{0.78}]O_2$. The electrical resistance of the active material is reflected in the AC impedance spectra, which show decreased contact resistance at the interface between the cathode and electrolyte for $Na_{2/3}[Fe_{0.22}Mn_{0.78}]O_2$ (Figure 2e).

To examine the electrochemical behavior in further detail, operando SXRD measurements were performed on the $Na_{2/3}[Fe_{0.22}Mn_{0.78}]O_2$ electrode. According to the results of the current work, the phase transformed toward the OP4 phase at the end of charge via a multistep first-order phase transition caused by the Na^+ ordering in the structure for both P′2-$Na_{2/3}MnO_2$[15] and P′2-$Na_{2/3}[Fe_{0.22}Mn_{0.78}]O_2$ (Figure 3). On discharge, the OP4 phase was recovered to the original P′2 phase, and the phase was further evolved to the P″2 phase, related to the J−T distortion of Mn^{3+} ions, because of the occurrence of a biphasic reaction when deeply discharged to 1.5 V for P′2-$Na_{2/3}MnO_2$.[15] However, the phase transformation from P′2 to P″2 is not favored because the elongation of the Mn−O distance in one direction in the octahedron generates stress in the crystal structure. This is one of the main reasons for the gradual capacity fading for P′2-$Na_{2/3}MnO_2$ (Figure 2c). The crystal structure can be gradually degraded by the effect of J−T distortion, with abnormal

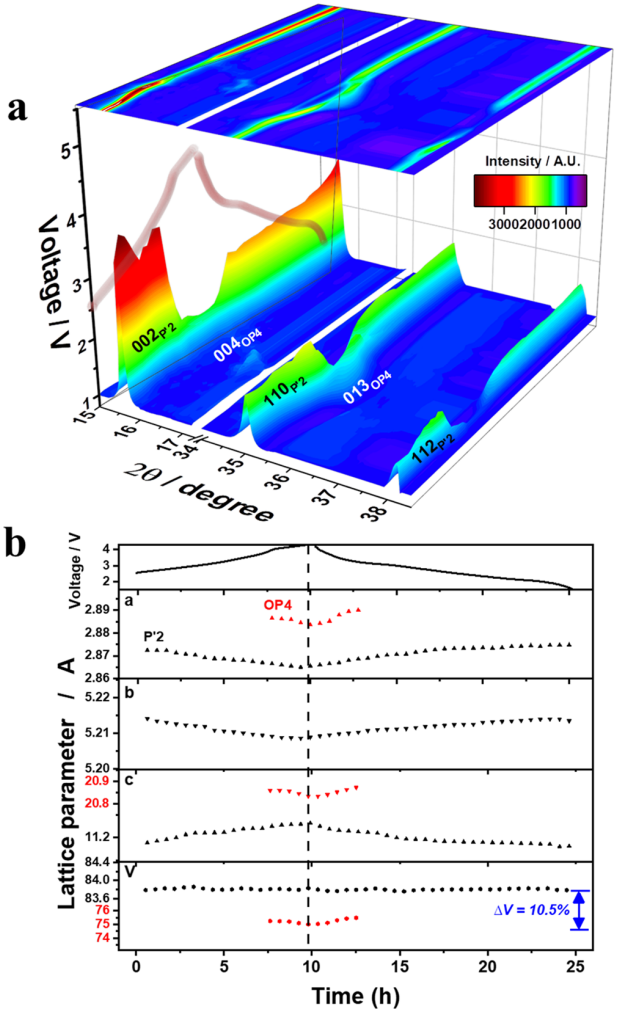

Figure 3. (a) Operando SXRD patterns and (b) change of lattice parameters of the $Na_{2/3}[Fe_{0.22}Mn_{0.78}]O_2$ electrode during the sodium intercalation process.

DOI: 10.1021/acsami.8b16522
ACS Appl. Mater. Interfaces 2018, 10, 40978−40984

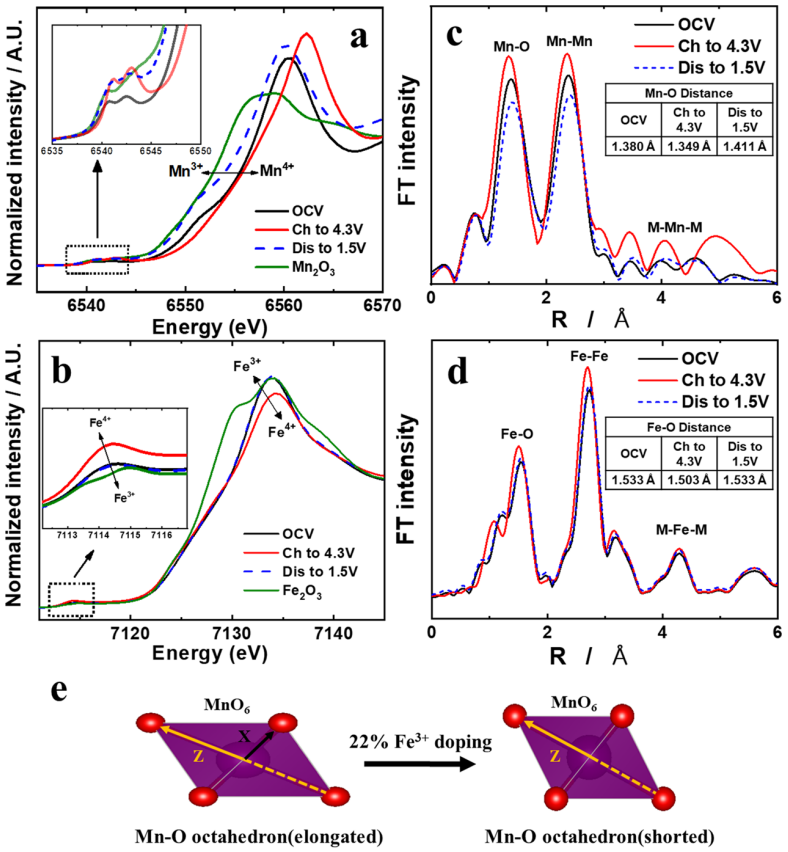

Figure 4. XANES spectra at the (a) Mn, (b) Fe K-edge, and the K^3-weighted Fourier transform magnitudes of the (c) Mn and (d) Fe K-edge EXAFS spectra for $Na_{2/3}[Fe_{0.22}Mn_{0.78}]O_2$ electrode during the sodium intercalation process. (e) Suppression of Mn−O bond length in the *Z* axis by Fe substitution.

broadening of major peaks after prolonged cycling and particle deformation (Figure S-8).

For P′2-$Na_{2/3}[Fe_{0.22}Mn_{0.78}]O_2$, such a complicated phase transition was not observed (Figure 3a). $Na_{2/3}[Fe_{0.22}Mn_{0.78}]O_2$ also underwent a structural change from the P′2 to OP4 phase on charge, although the relative intensity of the OP4 phase was very weak compared to that of P′2-$Na_{2/3}MnO_2$, with half of the intensity of the (002) peak.[15] In addition, one of the main peaks of the OP4 phase at approximately 36° (2θ) was not observed, indicating that the original P′2 phase remained predominant in the structure although with a reduced relative intensity with slight change in lattice parameters (Figure 3b). Similar to the observations for the desodiated P′2 $Na_{2/3}MnO_2$,[15] sodiation facilitated the recovery of the phase from OP4 to P′2. Note that there was no peak split of the P′2 phase or formation of the P′′2 phase at the end of discharge. Although the biphasic reaction was dominant in the voltage range of 2.3−1.5 V on discharge for the P′2-$Na_{2/3}MnO_2$ forming the P′′2 phase, such a plateau was not observed for P′2-$Na_{2/3}[Fe_{0.22}Mn_{0.78}]O_2$; instead, a simple slope was observed in the voltage range. These phase transitions are different from the earlier works of hexagonal P2−$Na_{2/3}[Fe_{0.5}Mn_{0.5}]O_2$[2] and electrochemical-induced orthorhombic P′2-$Na_{0.97}[Fe_{0.5}Mn_{0.5}]O_2$.[24] These compounds delivered high discharge over 190 mAh g^{-1} assisted by $Mn^{3+/4+}$ and $Fe^{3+/4+}$ redox couples. The electrochemical-induced orthorhombic P′2-$Na_{0.97}[Fe_{0.5}Mn_{0.5}]O_2$ underwent a phase transition to Z phase, P′2 → P2 → Z phase [showing only one peak at 17.5° (2θ)] on charge.[24] Meanwhile, the hexagonal P2−$Na_{2/3}[Fe_{0.5}Mn_{0.5}]O_2$ exhibited a simple and reversible phase transformation from P2 to OP4 phase. Our P′2-$Na_{2/3}[Fe_{0.22}Mn_{0.78}]O_2$ underwent a reversible phase transition from P′2 to OP4. Different from the Z phase, the OP4 phase clearly shows other reflections in the XRD pattern (Figure S-9). It is worth mentioning that even the same orthorhombic P′2 structure, the present P′2-$Na_{2/3}[Fe_{0.22}Mn_{0.78}]O_2$ and electrochemical-induced P′2-$Na_{0.97}[Fe_{0.5}Mn_{0.5}]O_2$ resulted in different tendency in phase transition behavior. Therefore, it is thought that this simplicity in the structural change is likely to affect the cyclability that the present P′2-$Na_{2/3}[Fe_{0.22}Mn_{0.78}]O_2$ was able to show stable cycling performance.

The X-ray absorption near-edge structure (XANES) spectra provide additional information on the structural change of $Na_{2/3}[Fe_{0.22}Mn_{0.78}]O_2$ during (de)sodiation. Compared with the reference spectra of $Mn^{3+}{}_2O_3$ and $Fe^{3+}{}_2O_3$, (de)sodiation induced a shift of the Mn and Fe K-edge spectra toward more-oxidized or -reduced states, suggesting that both Mn and Fe ions are involved in the electrochemical reaction. The Mn K-edge spectrum for the discharged electrode including pre-edge was similar to that of the Mn_2O_3 reference (Figure 4a), indicating the occurrence of the $Mn^{3+/4+}$ redox reaction. The shape of the pre-edge related to 1s to 3d transition is somehow different from that of the charged electrode due to presence of Mn^{3+} as a major portion in the discharged electrode. Similar behavior was observed for the Fe-free $Na_{2/3}MnO_2$ (Figure S-10a). An important feature is the appearance of additional

DOI: 10.1021/acsami.8b16522
ACS Appl. Mater. Interfaces 2018, 10, 40978−40984

capacity in the range of 4.3−3.5 V on discharge for $Na_{2/3}[Fe_{0.22}Mn_{0.78}]O_2$. From the Fe K-edge spectra (Figure 4b), it is apparent that the capacity delivered in this voltage range resulted from the reduction of Fe^{4+} to Fe^{3+}. The active redox pair of $Fe^{4+/3+}$ at high voltage (3.8−4.3 V) was also observed for P2-type $Na_{2/3}[Mn_{0.5}Fe_{0.5}]O_2$.[2] These results suggest that the $Fe^{4+/3+}$ redox pair is responsible for the high voltage and that the $Mn^{4+/3+}$ redox couple covers the region below 3.8 V for $Na_{2/3}[Fe_{0.22}Mn_{0.78}]O_2$. The Fourier transform (FT) magnitudes of the EXAFS spectra for $Na_{2/3}[Fe_{0.22}Mn_{0.78}]O_2$ are shown in Figure 4c,d. In general, the first peak observed in the range of 1−2 Å is related to oxygen surrounding the transition metals (Me−O bonds), and the second peak in the range of 2−3 Å is related to the bonds between transition metals. The amplitudes and intensities of the Mn−O and Mn−Mn bonds in $Na_{2/3}[Fe_{0.2}Mn_{0.8}]O_2$ varied less than those of $Na_{2/3}MnO_2$ (Figures 4c and S-10b). These variations are related to the movements of both MnO_6 and $(Fe_{0.22}Mn_{0.78})O_6$ octahedra in the crystal structure, and less movement indicates suppression of J−T distortion resulting from $Mn^{3+}O_6$ octahedra that lengthen the Mn−O distance along the z axis in the orbital. In this case, the O−Fe^{3+}−O−Mn^{3+}−O bond is formed in the octahedral environment for the deeply discharged $Na_{2/3}[Fe_{0.22}Mn_{0.78}]O_2$; however, the $Mn^{3+}O_6$ octahedron shares oxygen with the $Fe^{3+}O_6$ octahedron, such the abnormal movement of the Mn−O bond can be governed by the Fe−O bond. Indeed, the average oxidation state of Mn is 3.33+ for the P′2 $Na_{2/3}MnO_2$ ($Na_{2/3}[Mn^{3+}_{0.67}Mn^{4+}_{0.33}]O_2$). As can be seen in the XANES (Figure 4a), the Mn is oxidized toward Mn^{4+} on charge and returns to Mn^{3+} at the end of discharge, in which the J−T effect is dominant at fully sodiated state. For the P′2-$Na_{2/3}[Fe_{0.22}Mn_{0.78}]O_2$, as Fe^{3+} substituted Mn^{3+}, the total amount of Mn^{3+} decreases in $Na_{2/3}[Fe^{3+}_{0.22}(Mn^{3+}_{0.45}Mn^{4+}_{0.33})]O_2$ with average oxidation state of $Mn^{3.42+}$. This gives slight increase in the oxidation state of Mn, compared to that of $Na_{2/3}MnO_2$ (Figure 1b). The resulting electrochemical oxidation leads to oxidation of Mn close to Mn^{4+} from $Mn^{3.42+}$. The oxidation of Fe higher than 3+ is seen but it does not completely oxidize to Fe^{4+}, while it reduces to Fe^{3+} on discharge. Given that the active $Fe^{3+/4+}$ redox pair in Figure 2a that shows appearance of the new voltage plateau above 3.5 V, the estimated capacities are approximately 27 mAh g^{-1} on charge and 20 mAh g^{-1} on discharge, so that the $Fe^{3+/4+}$ redox pair contributes to roughly 50% of its redox in consideration of its full contribution theoretically, 57 mAh g^{-1}, expressed as from Fe^{3+} to $Fe^{3.5+}$ on charge in the high voltage range. That may result in the slight change in the Fe−O and Fe−Fe distance in the EXAFS spectra (Figure 4d). Recent work by Ceder et al.[28] suggests a new mechanism of Jahn−Teller effect on $Fe^{4+}O_6$ octahedra that provide the buckling capability to lower the Na^+ migration barrier, thus facilitating the Na^+ diffusion in several layered sodium transition metal oxides. These synergistic effect led to better capacity retention for the P′2-$Na_{2/3}[Fe_{0.22}Mn_{0.78}]O_2$ during cycling and suppressed the movement of Mn−O along the z-axis (Figure 4e). Such a structural change observed in $Na_{2/3}MnO_2$ can be mitigated, and overall structural distortion can effectively be reduced from 7.0% to 4.63% by the introduction of Fe^{3+} in $Na_{2/3}[Fe_{0.22}Mn_{0.78}]O_2$.

Extensively cycled P′2-$Na_{2/3}MnO_2$ and P′2-$Na_{2/3}[Fe_{0.22}Mn_{0.78}]O_2$ electrodes were examined by XRD and transmission electron spectroscopy(Figure S-8). Compared to that of P′2-$Na_{2/3}MnO_2$ (Figure S-8a), the P′2-$Na_{2/3}[Fe_{0.22}Mn_{0.78}]O_2$ was less varied even after prolonged cycles (Figure S-8c). The sharp feature of the (002) and (004) peaks still remained (Figure S-8c), and the particle was not much damaged even after 100 cycles (Figure S-8d), while particle rupture was observed for the cycled P′2-$Na_{2/3}MnO_2$ (Figure S-8b). Table S-2 shows that there is almost no change in the lattice parameters for the cycled P′2-$Na_{2/3}[Fe_{0.22}Mn_{0.78}]$-$O_2$, compared to the cycled P′2-$Na_{2/3}MnO_2$. It was assumed that the structural change and particle degradation were related to the dissolution of active materials, such that we performed the inductively coupled plasma-atomic absorption spectrometry (ICP-AAS) analysis for the post-cycled cells. The dissolved Mn contents in the electrolyte were 92 and 36 ppm for P′2-$Na_{2/3}MnO_2$ and P′2-$Na_{2/3}[Fe_{0.22}Mn_{0.78}]O_2$, respectively (Table S-3). This suggests that the structural transformation is more likely related to the capacity retention and particle degradation rather than Mn dissolution from the active materials. This finding indicates that the biphasic reaction at deeply discharged state was suppressed by the introduction of Fe in $Na_{2/3}[Fe_{0.22}Mn_{0.78}]O_2$. Therefore, the improvement in the capacity retention of $Na_{2/3}[Fe_{0.22}Mn_{0.78}]O_2$ is associated with the simple phase transition from P′2 to OP4 with suppressed J−T distortion in the presence of Mn^{3+} in the discharged state.

In summary, Fe substitution in P′2-$Na_{2/3}[Fe_xMn_{1-x}]O_2$ improved the structural stability, long-term capacity, and thermal properties in charged states (Figure S-11). More importantly, J−T distortion in the transition metal layers was significantly suppressed by the sharing of the oxygen provided by the Fe−O octahedral. This suppression of the J−T effect weakened the unwanted elongation of the Mn^{3+}−O distance in $Mn^{3+}O_6$ octahedra, which prevented the formation of P′′2 at the end of discharge. The simple phase transition from OP4 to P was responsible for the improved capacity retention of P′2-$Na_{2/3}[Fe_xMn_{1-x}]O_2$. An unexpected finding concerning the role of Fe was its redox activity in the high-voltage region contributed by the $Fe^{4+/3+}$ pair, which led to improvement in the capacity retention and rate capability. These findings demonstrate the potential of Fe-substituted $Na_{2/3}[Fe_{0.22}Mn_{0.78}]O_2$ as a cathode material for high-energy-density SIBs.

■ ASSOCIATED CONTENT

Supporting Information

The Supporting Information is available free of charge on the ACS Publications website at DOI: 10.1021/acsami.8b16522.

Experimental details; figures showing XRD patterns, SEM images, Coulomb energies, DFT-PBE+U-calculated lattice parameters, J−T distortion, charge−discharge voltage profiles, cycling performances, resulting rate capabilities, GITT results, HRTEM results, XANES spectra, and DSC curves; tables showing a summary of crystallographic parameters, degree of distortion, electric conductivity, lattice parameters, and ICP-AAS results (PDF)

■ AUTHOR INFORMATION

Corresponding Authors

*E-mail: payamk@zedat.fu-berlin.de.

*E-mail: smyung@sejong.ac.kr.

DOI: 10.1021/acsami.8b16522
ACS Appl. Mater. Interfaces 2018, 10, 40978−40984

ORCID

Seung-Taek Myung: 0000-0001-6888-5376

Notes

The authors declare no competing financial interest.

■ ACKNOWLEDGMENTS

This research was supported by the Basic Science Research Program through the National Research Foundation of funded by the Ministry of Science and ICT of Korea (grant nos. NRF-2015M3D1A1069713, NRF-2017R1A2A2A05069634, and NRF-2018K2A9A2A12000230). P.K. gratefully acknowledges financial support from the "Bundesministerium für Bildung und Forschung" (BMBF) as well as the North-German Supercomputing Alliance (HLRN) for providing HPC resources.

■ REFERENCES

(1) Vaalma, C.; Buchholz, D.; Weil, M.; Passerini, S. A Cost and Resource Analysis of Sodium-Ion Batteries. *Nature Reviews Materials* **2018**, *3*, 18013.

(2) Yabuuchi, N.; Kajiyama, M.; Iwatate, J.; Nishikawa, H.; Hitomi, S.; Okuyama, R.; Usui, R.; Yamada, Y.; Komaba, S. P2-type $Na_x[Fe_{1/x}Mn_{1/2}]O_2$ Made from Earth-Abundant Elements for Rechargeable Na Batteries. *Nat. Mater.* **2012**, *11*, 512−517.

(3) Wang, P.-F.; Xin, H.; Zuo, T.-T.; Li, Q.; Yang, X.; Yin, Y.-X.; Gao, X.; Yu, X.; Guo, Y.-G. An Abnormal 3.7-V O3-Type Na-Ion Battery Cathode. *Angew. Chem., Int. Ed.* **2018**, *57*, 8178−8183.

(4) Wang, P.-F.; You, Y.; Yin, Y.-X.; Guo, Y.-G. Layered Oxide Cathodes for Sodium-Ion Batteries: Phase Transition, Air Stability, and Performance. *Adv. Energy Mater.* **2018**, *8*, 1701912.

(5) Wang, P.-F.; Guo, Y.-J.; Duan, H.; Zuo, T.-T.; Hu, E.; Attenkofer, K.; Li, H.; Zhao, X. S.; Yin, Y.-X.; Yu, X.; Guo, Y.-G. Honeycomb-Ordered $Na_3Ni_{1.5}M_{0.5}BiO_6$ (M = Ni, Cu, Mg, Zn) as High Voltage Layered Cathodes for Sodium-Ion Batteries. *ACS Energy Lett.* **2017**, *2*, 2715−2722.

(6) Fang, T.; Guo, S.; Jiang, K.; Zhang, X.; Wang, D.; Feng, Y.; Zhang, X.; Wang, P.; He, P.; Zhou, H. Revealing the Critical Role of Titanium in Layered Manganese-Based Oxides toward Advanced Sodium-Ion Batteries via a Combined Experimental and Theoretical Study. *Small Methods* **2018**, 1800183.

(7) Guo, S.; Li, Q.; Liu, P.; Chen, M.; Zhou, H. Environmentally Stable Interface of Layered Oxide Cathodes for Sodium-Ion Batteries. *Nat. Commun.* **2017**, *8*, 135.

(8) Li, J.-Y.; Lü, H.-Y.; Zhang, X.-H.; Xing, Y.-M.; Wang, G.; Guan, H.-Y.; Wu, X.-L. P2-type $Na_{0.53}MnO_2$ Nanorods with Superior Rate Capabilities as Advanced Cathode Material for Sodium Ion Batteries. *Chem. Eng. J.* **2017**, *316*, 499−505.

(9) Zhang, X.-H.; Pang, W.-L.; Wan, F.; Guo, J.-Z.; Lü, H.-Y.; Li, J.-Y.; Xing, Y.-M.; Zhang, J.-P.; Wu, X.-L. P2-$Na_{2/3}Ni_{1/3}Mn_{5/9}Al_{1/9}O_2$ Microparticles as Superior Cathode Material for Sodium-Ion Batteries: Enhanced Properties and Mechanism via Graphene Connection. *ACS Appl. Mater. Interfaces* **2016**, *8*, 20650−20659.

(10) Wang, P.-F.; Yao, H.-R.; Liu, X.-Y.; Yin, Y.-X.; Zhang, J.-N.; Wen, Y.; Yu, X.; Gu, X.; Guo, Y.-G. Na^+/vacancy Disordering Promises High-Rate Na-Ion Batteries. *Sci. Adv.* **2018**, *4*, No. eaar6018.

(11) Wang, P.-F.; Yao, H.-R.; Liu, X.-Y.; Zhang, J.-N.; Gu, L.; Yu, X.-Q.; Yin, Y.-X.; Guo, Y.-G. Ti-Substituted $NaNi_{0.5}Mn_{0.5-x}Ti_xO_2$ Cathodes with Reversible O3-P3 Phase Transition for High-Performance Sodium-Ion Batteries. *Adv. Mater.* **2017**, *29*, 1700210.

(12) Kaliyappan, K.; Liu, J.; Xiao, B.; Lushington, A.; Li, R.; Sham, T.-K.; Sun, X. Enhanced Performance of P2-$Na_{0.66}(Mn_{0.54}Co_{0.13}Ni_{0.13})O_2$ Cathode for Sodium-Ion Batteries by Ultrathin Metal Oxide Coatings via Atomic Layer Deposition. *Adv. Funct. Mater.* **2017**, *27*, 1701870.

(13) Bordet-Le Guenne, L.; Deniard, P.; Biensan, P.; Siret, C.; Brec, R. Structural Study of Two Layered Phases in the Na_xMnO System. Electrochemical Behavior of Their Lithium Substituted Derivatives. *J. Mater. Chem.* **2000**, *10*, 2201−2206.

(14) Stoyanova, R.; Carlier, D.; Sendova-Vassileva, M.; Yoncheva, M.; Zhecheva, E.; Nihtianova, D.; Delmas, C. Stabilization of Over-Stoichiometric Mn^{4+} in Layered $Na_{2/3}MnO_2$. *J. Solid State Chem.* **2010**, *183*, 1372−1379.

(15) Kumakura, S.; Tahara, Y.; Kubota, K.; Chihara, K.; Komaba, S. Sodium and Manganese Stoichiometry of P2-Type $Na_{2/3}MnO_2$. *Angew. Chem., Int. Ed.* **2016**, *55*, 12760−12763.

(16) Yabuuchi, N.; Yoshida, H.; Komaba, S. Crystal Structures and Electrode Performance of Alpha-$NaFeO_2$ for Rechargeable Sodium Batteries. *Electrochemistry* **2012**, *80*, 716−719.

(17) Berthelot, R.; Carlier, D.; Delmas, C. Electrochemical Investigation of the P2-Na_xCoO_2 Phase Diagram. *Nat. Mater.* **2011**, *10*, 74−80.

(18) Yu, C.-Y.; Park, J.-S.; Jung, H.-G.; Chung, K.-Y.; Aurbach, D.; Sun, Y.-K.; Myung, S.-T. $NaCrO_2$ Cathode for High-Rate Sodium-Ion Batteries. *Energy Environ. Sci.* **2015**, *8*, 2019−2026.

(19) Guignard, M.; Didier, C.; Darriet, J.; Bordet, P.; Elkaïm, E.; Delmas, C. P2- Na_xVO_2 System as Electrodes for Batteries and Electron-Correlated Materials. *Nat. Mater.* **2013**, *12*, 74−80.

(20) Guignard, M.; Carlier, D.; Didier, C.; Suchomel, M. R.; Elkaïm, E.; Bordet, P.; Decourt, R.; Darriet, J.; Delmas, C. Vanadium Clustering/Declustering in P2-$Na_{1/2}VO_2$ Layered Oxide. *Chem. Mater.* **2014**, *26*, 1538−1548.

(21) Jo, J. H.; Choi, J. U.; Konarov, A.; Yashiro, H.; Yuan, S.; Shi, L.; Sun, Y.-K.; Myung, S.-T. Sodium-Ion Batteries: Building Effective Layered Cathode Materials with Long-Term Cycling by Modifying the Surface via Sodium Phosphate. *Adv. Funct. Mater.* **2018**, *28*, 1705968.

(22) Konarov, A.; Choi, J. U.; Bakenov, Z.; Myung, S.-T. Revisit of Layered Sodium Manganese Oxides: Achievements of High Energy by Ni Incorporation. *J. Mater. Chem. A* **2018**, *6*, 8558−8567.

(23) Yoncheva, M.; Stoyanova, R.; Zhecheva, E.; Kuzmanova, E.; Sendova-Vassileva, M.; Nihtianova, D.; Carlier, D.; Guignard, M.; Delmas, C. Structure and Reversible Lithium Intercalation in a New P'3-phase: $Na_{2/3}Mn_{1-y}Fe_yO_2$ (y = 0, 1/3, 2/3). *J. Mater. Chem.* **2012**, *22*, 23418−23427.

(24) Mortemard de Boisse, B.; Carlier, D.; Guignard, M.; Bourgeois, L.; Delmas, C. P2-$Na_xMn_{1/2}Fe_{1/2}O_2$ Phase Used as Positive Electrode in Na Batteries: Structural Changes Induced by the Electrochemical (De)intercalation Process. *Inorg. Chem.* **2014**, *53*, 11197−11205.

(25) Yabuuchi, N.; Hara, R.; Kubota, K.; Paulsen, J.; Kumakura, S.; Komaba, S. A New Electrode Material for Rechargeable Sodium Batteries: P2-type $Na_{2/3}[Mg_{0.28}Mn_{0.72}]O_2$ with Anomalously High Reversible Capacity. *J. Mater. Chem. A* **2014**, *2*, 16851−16855.

(26) Hwang, J.-Y.; Myung, S.-T.; Sun, Y.-K. Sodium-Ion Batteries: Present and Future. *Chem. Soc. Rev.* **2017**, *46*, 3529−3614.

(27) Ma, X.; Chen, H.; Ceder, G. Electrochemical Properties of Monoclinic $NaMnO_2$. *J. Electrochem. Soc.* **2011**, *158*, A1307−A1312.

(28) Li, X.; Wang, Y.; Wu, D.; Liu, L.; Bo, S.-H.; Ceder, G. Jahn-Teller Assisted Na Diffusion for High Performance Na Ion Batteries. *Chem. Mater.* **2016**, *28*, 6575−6583.

DOI: 10.1021/acsami.8b16522
ACS Appl. Mater. Interfaces 2018, 10, 40978−40984

Supporting Information

Unraveling the Role of Earth-abundant Fe in Suppression of Jahn–Teller Distortion of P'2-type $Na_{2/3}MnO_2$: Experimental and Theoretical Studies

Ji Ung Choi[†], *Yun Ji Park*[†], *Jae Hyeon Jo*[†], *Liang-Yin Kuo*[‡], *Payam Kaghazchi**,[‡] *and Seung-Taek Myung**,[†]

[†]*Department of Nanotechnology and Advanced Materials Engineering, Sejong University, Seoul 05006, South Korea*

[‡] *Institut für Chemie und Biochemie, Freie Universität Berlin, Takustr. 3, Berlin 14195, Germany* & *Forschungszentrum Jülich GmbH, Institute of Energy and Climate Research (IEK-1), Materials Synthesis and Processing, Wilhelm-Johnen-Straße, 52425, Jülich, Germany*

*Corresponding author. E-mail: payamk@zedat.fu-berlin.de (Payam Kaghazchi); smyung@sejong.ac.kr (S.-T. Myung)

EXPERIMENTAL

Material synthesis

$Na_{2/3}[Fe_xMn_{1-x}]O_2$ [x=0, 0.11, 0.22] compounds were prepared using a simple combustion method. An aqueous solution was stoichiometrically prepared by dissolving $Mn(NO_3)_26H_2O$, $NaNO_3$, $Fe(NO_3)9H_2O$, citric acid, and sucrose in distilled water and continuously adding an aqueous citric acid solution and sucrose to achieve a nitrates:citric acid:sucrose weight ratio of 1:0.5:0.02. The solution was heated on a hot plate at 120 °C overnight under constant stirring to evaporate the solvent. The dried powders were then further heated to 200 °C to induce auto-combustion. The obtained powders were pelletized and calcined in a furnace at 1200 °C for 10 h in air and then slowly cooled to room temperature. The synthesized samples were analyzed using X-ray diffraction (XRD; PANalytical X'Pert, Empyrean), and the chemical compositions were determined using inductively coupled plasma-optical emission spectroscopy (ICP-OES; OPTIMA 8300 PerkinElmer). The crystal structures were analyzed using the Rietveld refinement program Fullprof.[1] The particle morphologies and sizes were evaluated using scanning electron microscopy (SEM; JXA-8100, JEOL) and high-resolution transmission electron microscopy (HR-TEM, JEM-3010, JEOL). To measure the direct current (DC) electrical conductivity, we used the direct volt–ampere method (CMT-SR1000, IT), where disc samples were contacted with a four-point probe.

Electrochemical characterization

The electrochemical properties of the samples were determined using R2032-type coin cells. Electrodes were fabricated from a mixture of the active powder (85 wt.%), KS-6 and Super-P (7.5 wt.%), and polyvinylidene fluoride (PVDF) in *N*-methyl-2-pyrrolidone (7.5 wt.%).

The prepared slurry was cast on aluminum foil and dried overnight at 110°C in a vacuum oven. The electrolyte was 0.5 M $NaPF_6$ in a mixture of propylene carbonate (PC) and fluoroethylene carbonate (FEC) in a 98:2 volume ratio.[2] The fabricated cells were tested in the voltage range of 1.5–4.3 V at a rate of C/10 (26 mA g^{-1}) at 25 °C. AC impedance measurements were performed in the 1 MHz–1 mHz frequency range with an AC amplitude of 10 mV.

Density Functional theory (DFT) calculations

The atomic structures of various possible configurations of $Na_{2/3}MnO_2$ and their Coulomb energies (calculated using the Ewald summation algorithm) were determined using the so-called *supercell* code.[3] DFT calculations were performed using the projector-augmented plane-wave (PAW) method as implemented in the Vienna *Ab Initio* Simulation Package (VASP).[4] The Perdew–Burke–Ernzerhof (PBE) functional[5] with the on-site Coulomb interaction correction introduced by Dudarev *et al.*[6] was utilized. To model the bare and Fe-doped $Na_{2/3}MnO_2$, we used a 3×3×1 unit cell with a Monkhorst–Pack *k*-point mesh of 2×1×2 and energy cut-off of 500 eV. To compute the total energies of possible favorable structures of $Na_{2/3}MnO_2$ that were determined based on the Coulomb energy values, we performed DFT-PBE+U calculations with a U–J value of 4.0 for Mn. To determine appropriate values of U–J for Mn and Fe that give reasonable results for the doping-induced lattice parameter change, we studied the effect of the U–J value on the *a*, *b*, and *c* lattice sizes as well as the J–T distortion for bare as well as 11% and 22% Fe-doped $Na_{2/3}MnO_2$ (**Figures S3 and S4**). A U–J value of 6.0 for both Mn and Fe provided reasonable results compared with our experimental XRD data.

Structural study

The structures of the samples during cycling were examined using *ex situ* and *operando* synchrotron XRD (SXRD) and *ex situ* X-ray absorption spectroscopy (XAS). *Operando* SXRD and *ex situ* XAS measurements were performed at beamlines 9B (Source = synchrotron light, λ = 0.8265 Å) and 8C, respectively, of the Pohang Accelerator Laboratory (PAL), Pohang, South Korea. The SXRD data were converted to Cu wavelength (λ = 1.5406 Å) for convenience. The raw XAS data were corrected for pre-edge and post-edge background and normalized to unit step height. The X-ray absorption near-edge structure (XANES) data were analyzed using the Athena software package.[7] The effects of the phase stability and redox behaviors during cycling are discussed based on these results.

Thermal property

For differential scanning calorimetry (DSC) analysis, the R2032 coin-type cells were fully charged to 4.3 V and disassembled in a glove box, and the electrodes were rinsed in salt-free dimethyl carbonate for 1 day. After the remaining electrolyte was carefully removed from the electrode surface, the cathode materials were recovered from the current collector. A stainless-steel sealed pan with a gold-plated copper seal was used to collect 3–5 mg samples. These measurements were performed in a Pyris 1 calorimeter (Perkin-Elmer) at a temperature ramp rate of 1 °C min^{-1}. The weight was constant in all cases, indicating that no leaks occurred during the experiments.

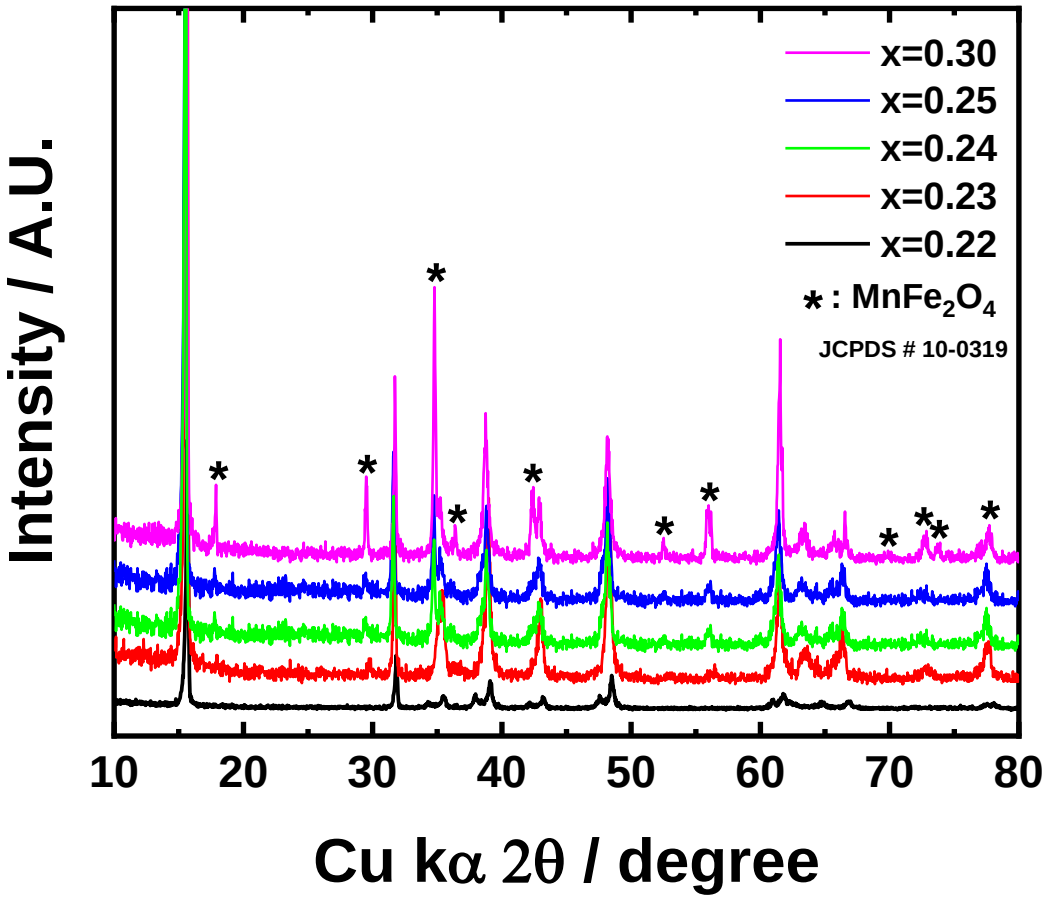

Figure S-1. XRD patterns of the $Na_{2/3}[Fe_xMn_{1-x}]O_2$ ($0.22 \leq x \leq 0.3$) compounds with different Fe-substitution ratio with $MnFe_2O_4$ reference.

To confirm the soluble range of Fe in P'2-type $Na_{2/3}[Mn_{1-x}Fe_x]O_2$, the addition of Fe was increased to 30% of the Mn content (**Figure S-1**). The $MnFe_2O_4$ phase appeared for Fe contents greater than 22%, indicating that a solid solution is formed up to x = 0.22 in $Na_{2/3}[Mn_{1-x}Fe_x]O_2$.

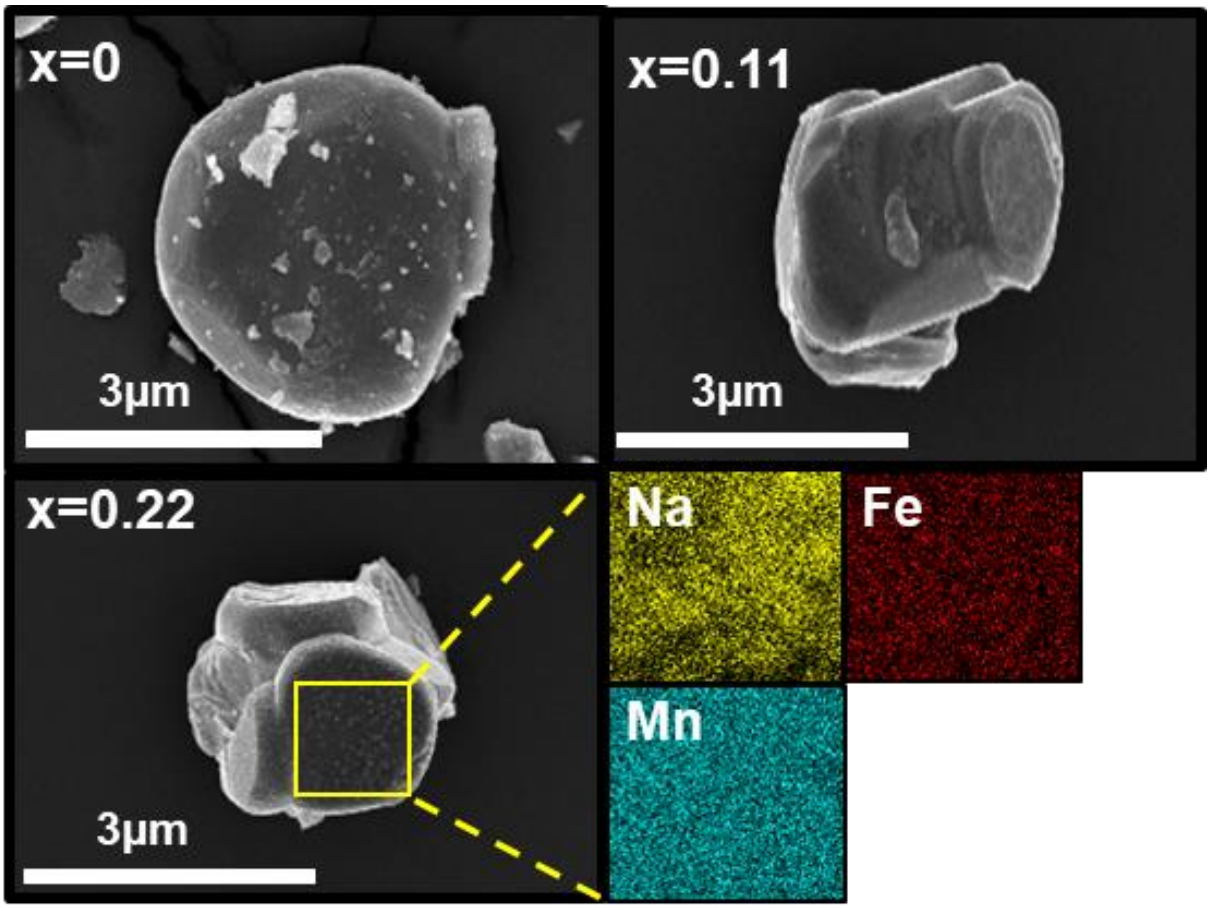

Figure S-2. SEM image with EDX maps of Na, Fe, Mn of $Na_{2/3}[Fe_xMn_{1-x}]O_2$ (x=0, 0.11, and 0.22) samples.

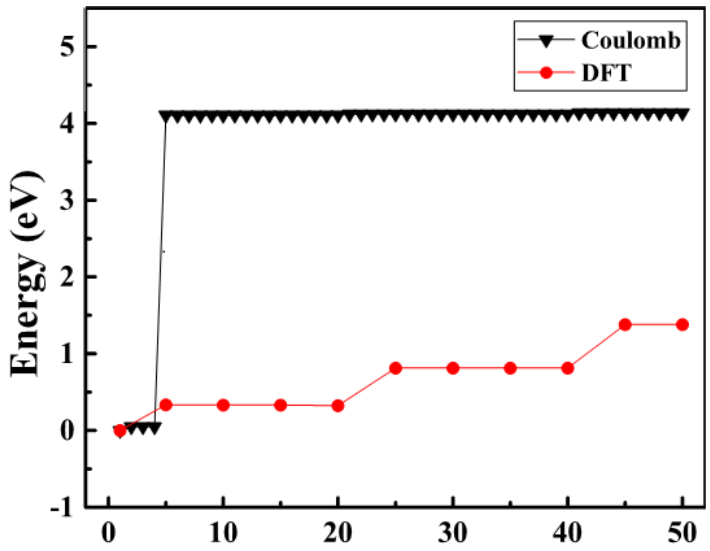

Figure S-3. Coulomb energies of the top 50 low-energy structures of $Na_{2/3}MnO_2$ as well as DFT-PBE+U total energies of several low-energy structures. Both the Coulomb and DFT energies are referenced to their lowest values.

To find the minimum-energy structure of bare $Na_{2/3}MnO_2$, we determined the arrangement of Na ions in Na sites. We focused on a 3×3×1 unit cell, for which 24 of the 36 prismatic sites should be occupied by Na ions. To reduce the number of possible configurations, the positions of 4 Na ions were fixed at 4 homogenously separated prismatic sites. The Coulomb energies of all the possible arrangements of the remaining 20 Na ions in the remaining unoccupied 32 prismatic sites ($\frac{32!}{20!12!}$=225792840) were then calculated. To maintain charge neutrality, we considered the following charges for the ions: Na: +1.5, Mn: +3, O: –2. In fact, Na cations should have a charge value of +1, and Mn cations should have either a charge value of +3 or +4 depending on the arrangement of nearest neighbor Na cations and vacancies (V_{Na}^{-}). Finding the minimum-energy structure of $Na_{2/3}MnO_2$ with a favorable arrangement of Mn^{+3}/Mn^{+4} and $Na^{+}/V_{Na}^{-}$is a formidable task since we have to explore a huge number of possible structures of more than 10^8, which is beyond the capability of the Supercell program by which we created different configurations. We, therefore, had to choose a charge of +1.5 for Na and +3.0 for Mn. Since the determined structure of $Na_{2/3}MnO_2$ from the Coulomb energy analysis is in agreement with that from DFT calculation, we believe that this charge assignment is reasonable. The Coulomb energies of the first 50 favorable configurations and the corresponding total energies (determined using the DFT-PBE+U calculations) of 11 structures from the 50 configurations are shown in **Figure S-3**.

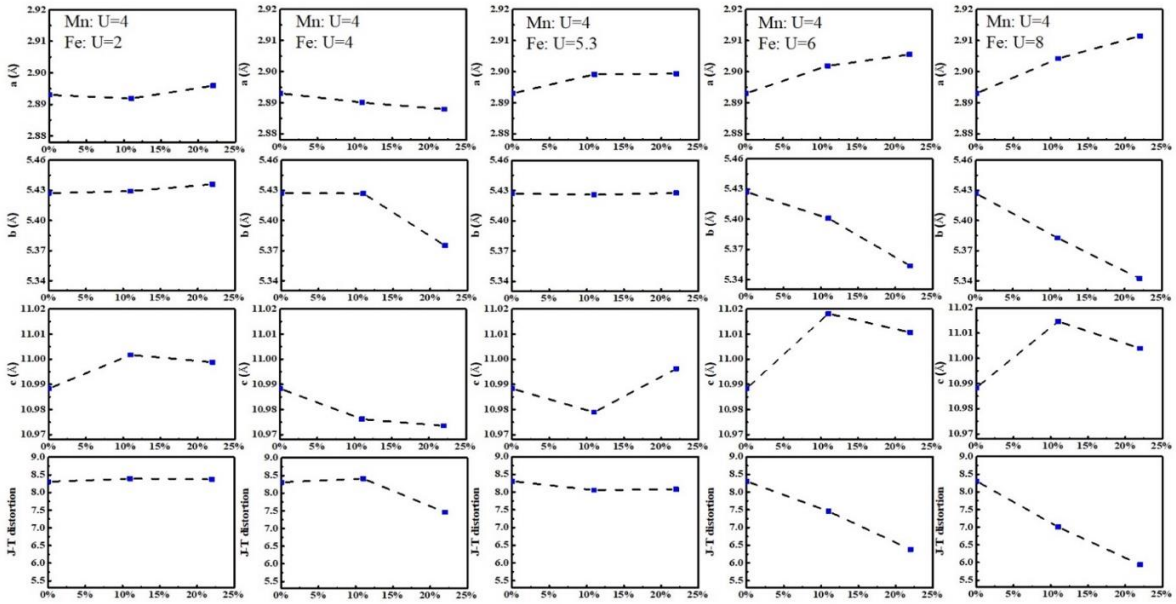

Figure S-4. DFT-PBE+U-calculated lattice parameters and J-T distortion in $Na_{2/3}MnO_2$ as function of level of Fe doping with different U-J values of Fe. The U-J value of Mn was fixed to 4.0.

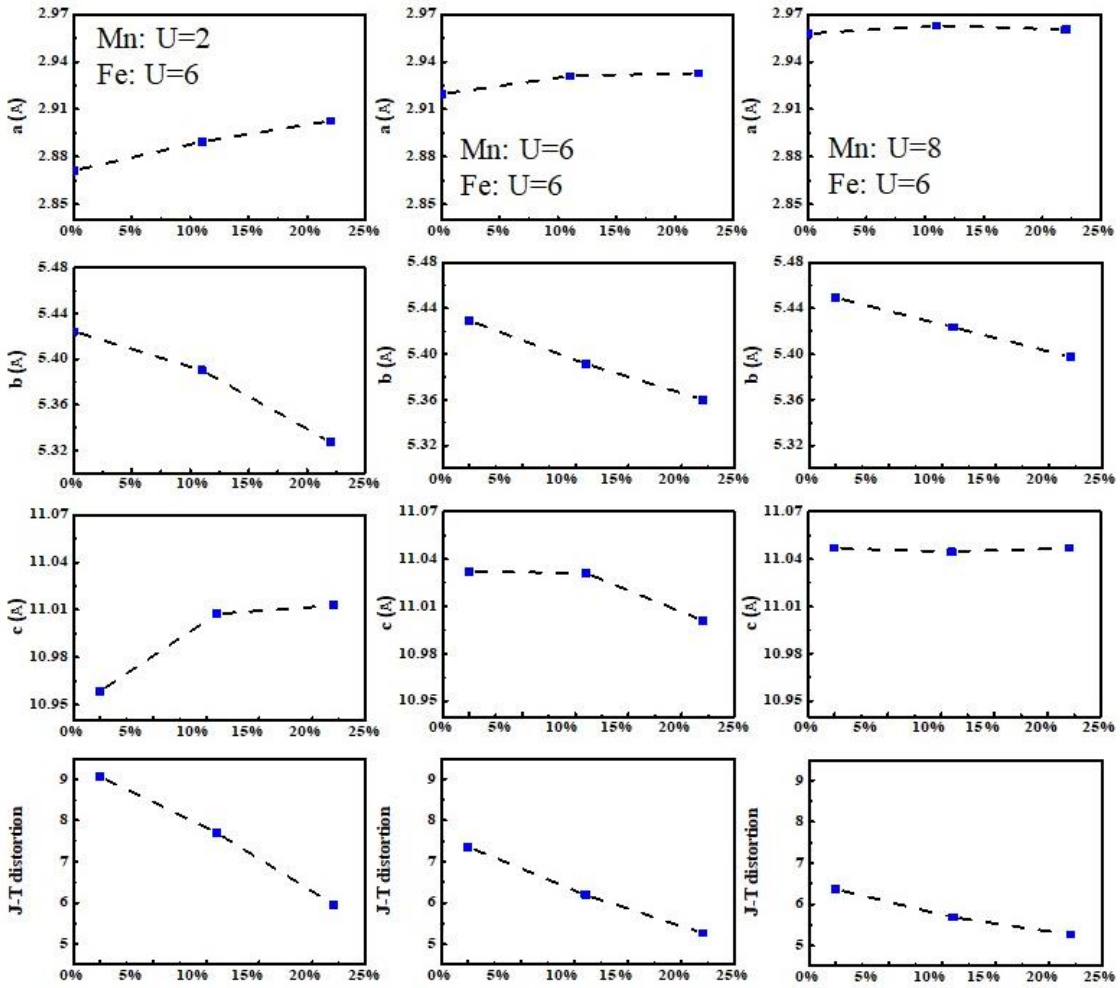

Figure S-5. DFT-PBE+U-calculated lattice parameters and J-T distortion in $Na_{2/3}MnO_2$ as function of level of Fe doping with different U-J values of Mn. The U-J value of Fe was fixed to 6.0 based on the results of **Figure S-4**.

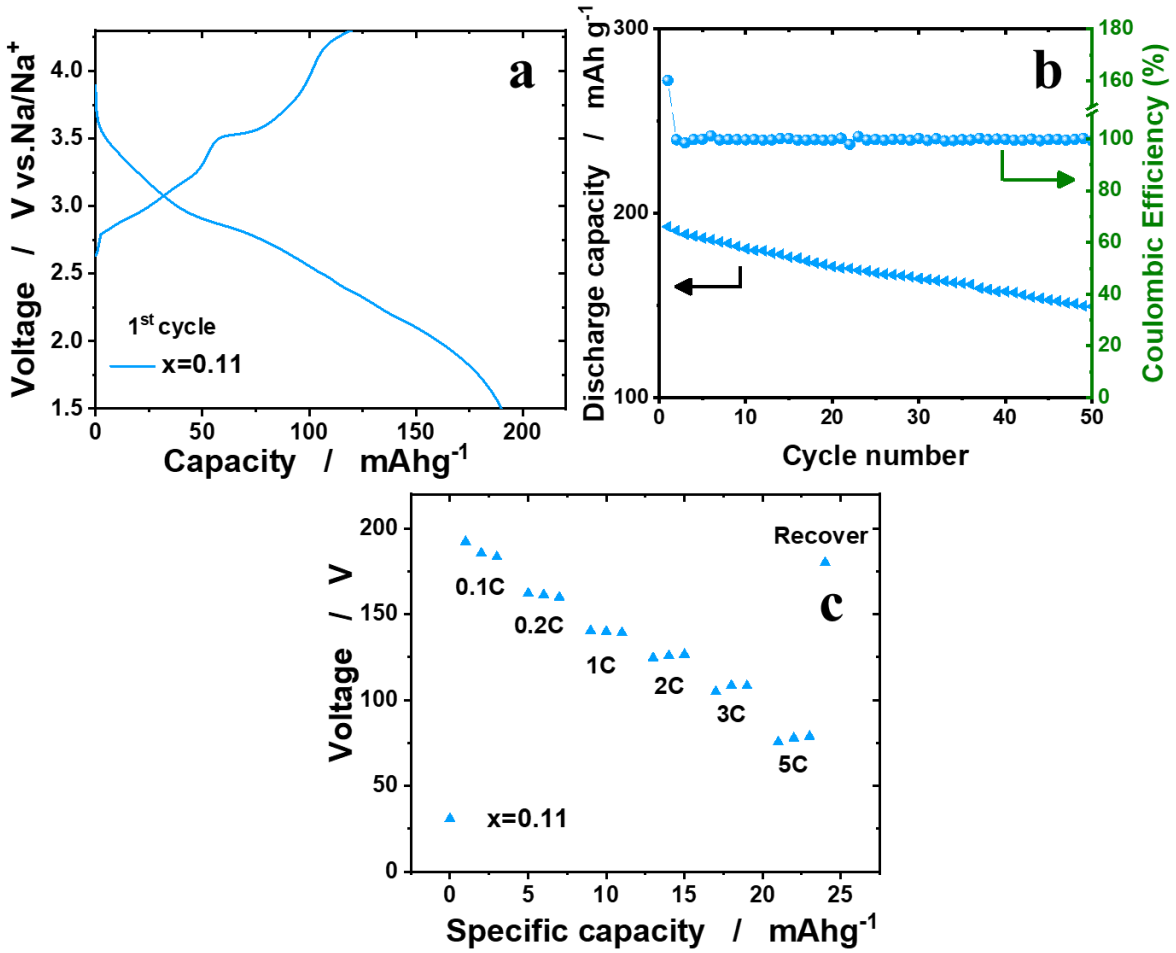

Figure S-6. (a) Galvanostatic charge/discharge voltage profiles, (b) cycling performance at 0.1C (26 mA g^{-1}) and (c) resulting rate capability of $Na_{2/3}[Fe_{0.11}Mn_{0.89}]O_2$ electrode.

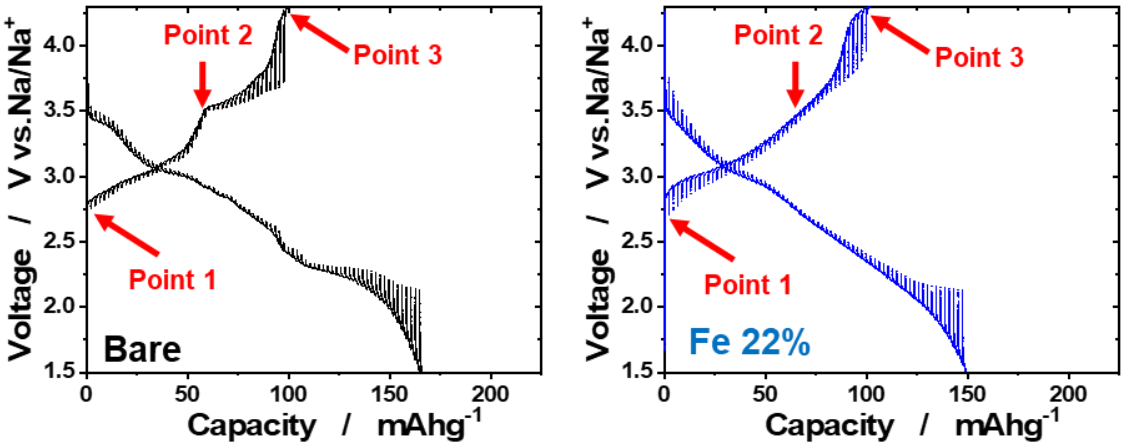

D_{na}^{+} ($cm^2\ s^{-1}$)	Point 1 (δ=0.043)	Point 2 (δ=0.427)	Point 3 (δ=0.666)
Bare	1.23×10^{-13}	1.31×10^{-14}	2.13×10^{-17}
Fe 22%	5.37×10^{-11}	2.09×10^{-12}	4.39×10^{-15}

Figure S-7. GITT results of $Na_{2/3}[Fe_{0.22}Mn_{0.78}]O_2$ (x=0, 0.22) electrodes.

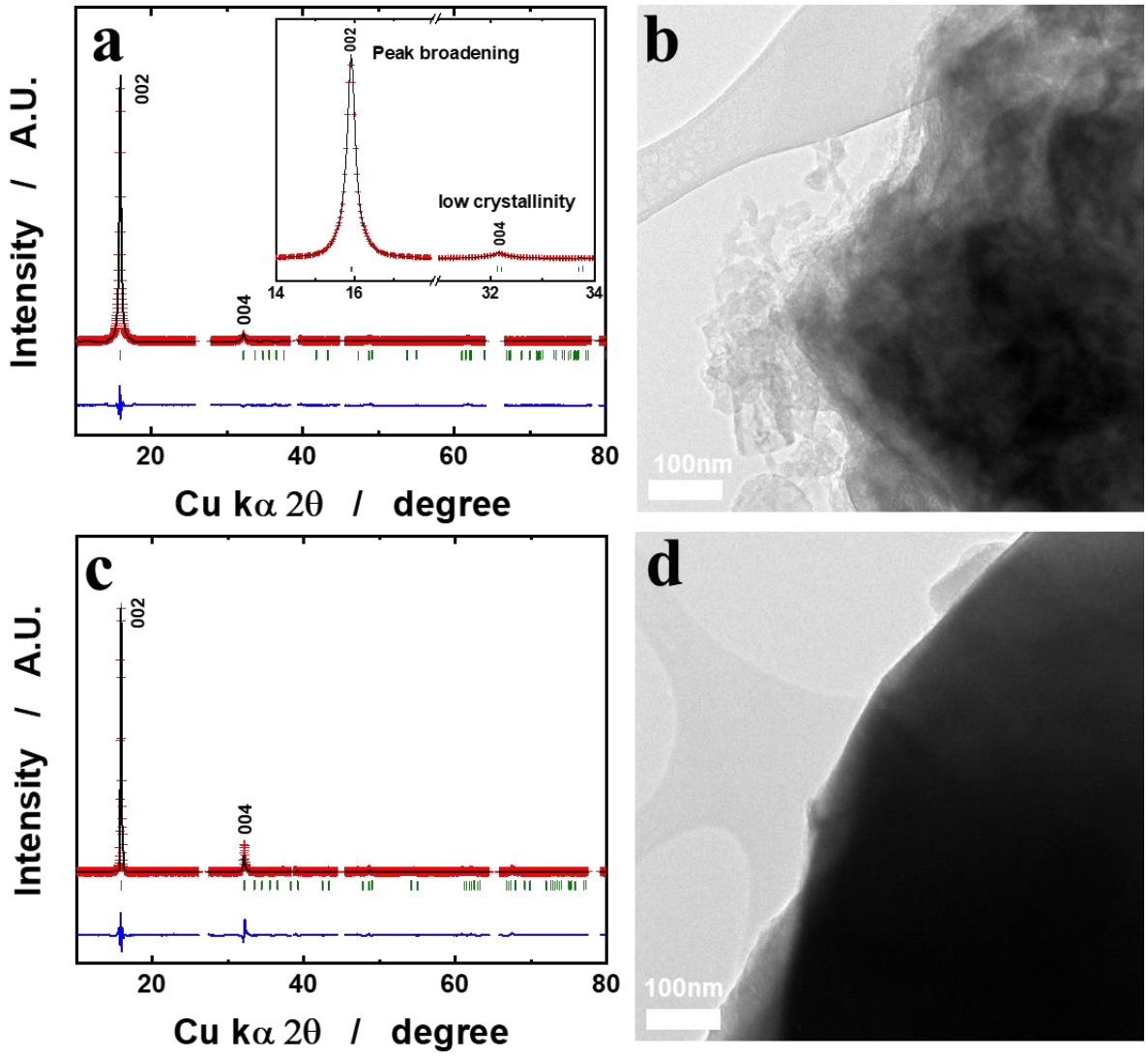

Figure S-8. *ex-situ* XRD and HRTEM images of (a,b) after 50 cycled $Na_{2/3}MnO_2$ and (c,d) after 100 cycled $Na_{2/3}[Fe_{0.22}Mn_{0.78}]O_2$ electrodes.

The sharp feature of the (002) and (004) peaks still remained (**Figure S-8c**), and the particle was not greatly damaged even after 100 cycles (**Figure S-8d**). It is also interesting that compared with that of P'2-$Na_{2/3}MnO_2$, the lattice was less varied even after prolonged cycling (**Figure S-8a and S-8b**). This finding indicates that the biphasic reaction was suppressed by the introduction of Fe in $Na_{2/3}[Fe_{0.22}Mn_{0.78}]O_2$.

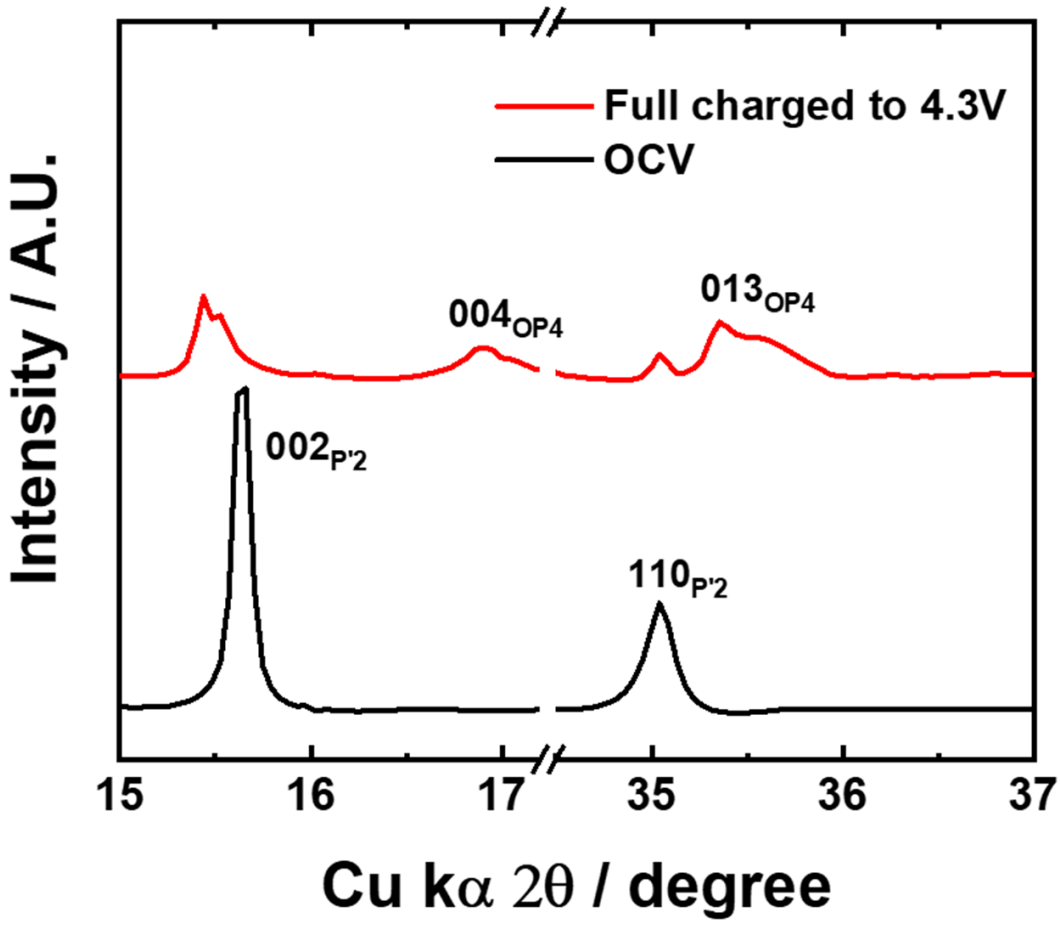

Figure S-9. XRD patterns of $Na_{2/3}[Fe_{0.22}Mn_{0.78}]O_2$ electrodes for OCV (Black) and Full charged to 4.3 V (Red) from *Operando* SXRD patterns.

In the case of the $Na_{2/3}[Fe_{0.22}Mn_{0.78}]O_2$ electrode, the P'2 is transformed to OP4 on charge (desodiation), and it moves like OP4 → P'2 → P''2 for the P'2 $Na_{2/3}MnO2$ but a simpler transition is seen for the P'2 $Na_{2/3}[Fe_{0.22}Mn_{0.78}]O_2$ followed by OP4 → P'2 on discharge (sodiation). As shown in **Figure S-9**, such OP4 phase is clearly observed in the in situ XRD pattern.

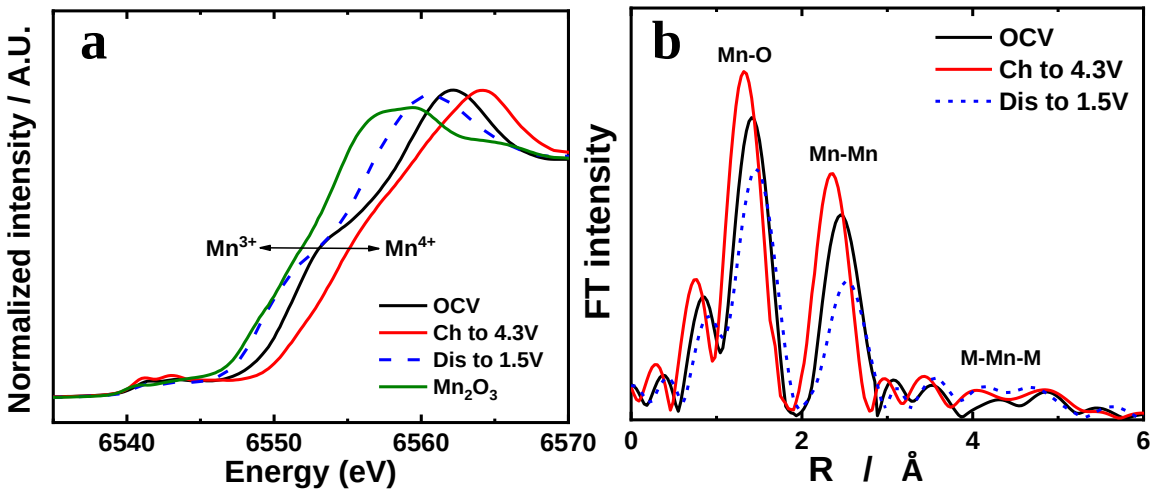

Figure S-10. XANES spectra at the (a) the Mn and the K^3-weighted Fourier transform magnitudes of the (b) the Mn for $Na_{2/3}MnO_2$ electrode during the sodium intercalation process.

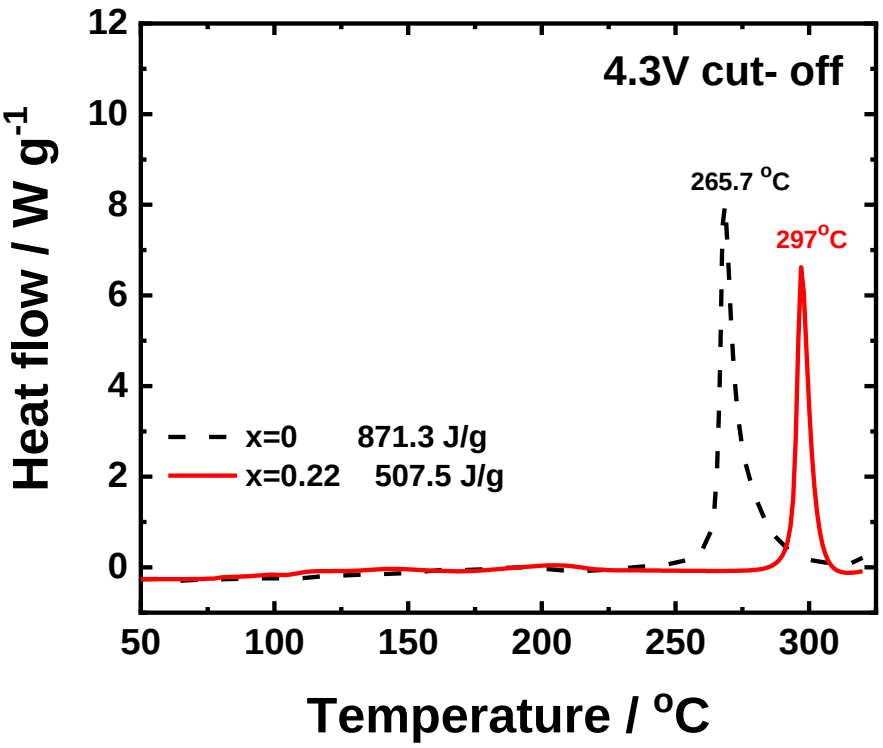

Figure S-11. DSC curves of $Na_{2/3}[Fe_xMn_{1-x}]O_2$ (x=0 and 0.22) electrodes charged to 4.3V.

Figure S-11 presents the DSC curves for desodiated $Na_{0.18}MnO_2$ and $Na_{0.18}[Fe_{0.22}Mn_{0.78}]O_2$ electrodes obtained after charging to 4.3 V. The onset temperature of the exothermic reaction shifted from 238 °C to 281 °C with the introduction of Fe in the crystal structure, which further raised the main reaction temperature from 265 °C to 297 °C. Hence, the Fe substitution delays the destructive exothermic reaction with substantially reduced heat generation.

Table S-1. Summary of refined crystallographic parameters, degree of distortion and electric conductivity of $Na_{2/3}[Fe_xMn_{1-x}]O_2$ (x=0, 0.11, and 0.22) compounds.

Compound	Atom	x	y	z	B	occ	R_{wp} / %	Electric conductivity (Scm^{-1})
x=0	Na	0	0.068	0.25	3.16	0.215	13.4%	6.09×10^{-6} S cm^{-1}
	Na	0	0.312	0.25	1.5	0.455		
	Mn	0	0	0	0.273	1.0		
	O	0	0.651	0.097	0.728	1.0		
	a(Å)	2.8301(5)	b(Å)	5.2752(1)	c(Å)	11.1971(1)	Distortion	7.0%
x=0.11	Na	0	0.081	0.25	3.5	0.213	14.7%	2.09×10^{-5} S cm^{-1}
	Na	0	0.330	0.25	2.217	0.452		
	Mn	0	0	0	0.42	0.89		
	Fe	0	0	0	0.42	0.11		
	O	0	0.668	0.089	0.85	1.0		
	a(Å)	2.8405(9)	b(Å)	5.2602(9)	c(Å)	11.1801(2)	Distortion	6.46%
x=0.22	Na	0	0.084	0.25	3.5	0.205	10.5%	1.11×10^{-4} S cm^{-1}
	Na	0	0.335	0.25	2.2	0.447		
	Mn	0	0	0	0.4	0.78		
	Fe	0	0	0	0.4	0.22		
	O	0	0.654	0.090	0.85	1.0		
	a(Å)	2.8708(1)	b(Å)	5.2141(1)	c(Å)	11.1719(5)	Distortion	4.63%

Table S-2. Lattice parameters obtained from Rietveld refinement after extensively cycled electrodes.

After extensive cycled $Na_{2/3}[Fe_xMn_{1-x}]O_2$ electrodes	Atom	x	y	z	B	Occ	R_{wp} / %
x=0	Na	0	-0.066	0.25	3.154	0.179	11.2%
	Na	0	0.3321	0.25	1.383	0.358	
	Mn	0	0.0	0.0	0.27	1.0	
	O	0	0.6878	0.9040	0.73	1.0	
	a(Å)	2.8728(2)	b(Å)	5.3156(1)	c(Å)	11.1312(8)	
x=0.22	Na	0.0	-0.084	0.25	3.5	0.203	14.1%
	Na	0.0	0.335	0.25	2.2	0.407	
	Mn	0.0	0.0	0.0	0.4	0.78	
	Fe	0.0	0.0	0.0	0.4	0.22	
	O	0.0	0.6694	0.8931	1.0	1.0	
	a(Å)	2.8907(1)	b(Å)	5.2297(3)	c(Å)	11.1709(7)	

Table S-3. ICP-AAS results of Mn dissolution obtained from extensively cycled cells.

After extensive cycled $Na_{2/3}[Fe_xMn_{1-x}]O_2$ electrodes	**Mn concentration in electrolyte (ppm)**
x=0	92 ppm
x=0.22	36 ppm

REFERENCES

(1) Roisnel, T.; R Rodriguez-Carjaval, J; Fullprof Manual, Institut Laue-Langevin, Grenoble, France, **2002**.

(2) Komaba, S.; Ishikawa, T.; Yabuuchi, N.; Murata, W.; Ito, A.; Ohsawa, Y. Fluorinated Ethylene Carbonate as Electrolyte Additive for Rechargeable Na Batteries. *ACS Appl. Mater. Interfaces* **2011**, *3*, 4165-4168.

(3) Okhotnikov, K.; Charpentier, T.; Cadars, Supercell program: a combinatorial structure-generation approach for the local-level modeling of atomic substitutions and partial occupancies in crystals. S. *Journal of Cheminformatics* **2016**, *8*, 17

(4) Kresse, G.; Furthmuller, Efficient iterative schemes for ab initio total-energy calculations using a plane-wave basis set. J. *Phys. Rev. B: Condens. Matter. Mater. Phys.* **1996**, *54*, 11169.

(5) Perdew, J. P.; Burke, K.; Ernzerhof, Generalized Gradient Approximation Made Simple. M. *Phys. Rev. Lett.* **1996**, *77*, 3865.

(6) Dudarev, S. L.; Botton, G. A.; Savrasov, S. Y.; Humphreys, C. J.; Sutton, A. P. Electron-energy-loss spectra and the structural stability of nickel oxide: An LSDA1U study. *Phys. Rev.B: Condens. Matter Mater. Phys.* **1998**, *57*, 1505.

(7) Ravel, B.; Newville, M.; Athena, Artemis, Hephaestus, J. Synchrotron Radiat. **2005**, 12, 537.

Chapter 5

SUMMARY

In this dissertation, we simulated and studied the structural changes in three types of NCM materials for LIBs and one NMO material for SIBs. The effect of increasing amount of Ni contents (substitution) on the structural changes (*i.e.* mechanical stability) in NCM and lattice doping on chemical and mechanical stability of NCM and NMO were studied. We showed that the arrangements of Li and Na ions in Li and Na sites can be determined by performing an extensive set of electrostatic (Coulomb energy) and DFT calculations. By analyzing the crystal, atomic and electronic structures, we explained the reason behind the lattice parameters change and phase transitions in NCM111 and NCM811 during delithiation. The Li and O vacancy formation energies (*i.e.* chemical stability) of Al-doped NCM90505 were computed and analyzed to understand the reason for its relative high structural stability compared to the undoped one. Moreover, we modelled and explained the influence of various amount of Fe dopant on the structural stability (*i.e.* mechanical stability) of $Na_{0.67}MnO_2$. The results of these studies are summarized in the following.

In the first work of this dissertation, we modelled the non-monotonic variation of lattice parameters in Li*x*NCM111 with various amount of Li contents *x*. The most favorable arrangements of Li ions in Li sites at different levels of charging (delithiation) were obtained by combining an extensive set of Coulomb energy and DFT calculations. Among PBE, PBE+*U*, and SCAN functionals, we found that the SCAN functional can compute the lattice parameters (*a*, *b*, and *c*) in better agreement with experimental data (see Fig.5.1) [140].

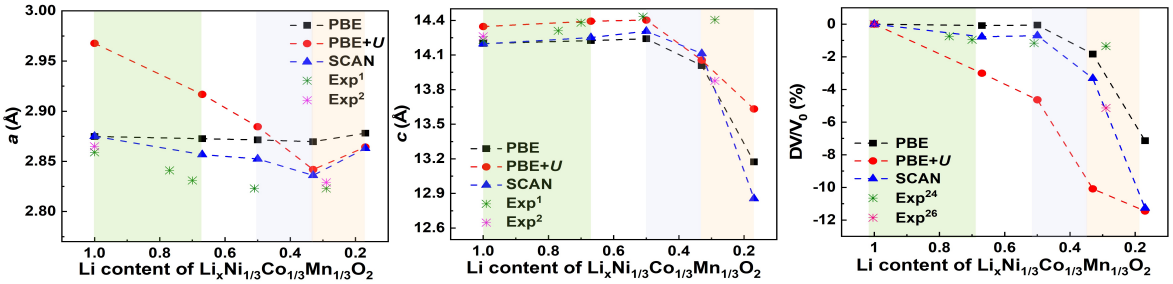

Figure 5.1: Calculated variation of lattice parameters and unit cell volume of Li_xNCM111 with delithiation using different XC functionals [140].

Our detailed analysis of the number of unpaired spins N↑ −N↓ (NUS), spin density difference (SDD), density of state (DOS) and Bader charges (BCs) helped us to explain the reason behind the lattice parameters change and the O-stacking-induced phase transition. It was found that the lattice parameter *a* decreases upon charging (delithiation), however it increases at very low Li contents. The contraction of *a* is due to the oxidation of Ni cations (*i.e.* charge changes on Ni) upon delithiation leading to the decrease in their ionic radii. Moreover, the lattice parameter *a* is related to the projection of equatorial Ni−O bond lengths, thus the decrease in these bond lengths (due to the J−T distortion) causes the value of *a* to decrease. However, the expansion of *a* at very low Li contents is due to the oxidation of Co cations (*i.e.* charge changes on Co). Since the radius of Co do not reduce much, the increase in the electrostatic repulsion between TMs controls the expansion of *a*. The lattice parameter *c* increases at the low delithiated structure, however, it decreases at the half delithiated structure, and being significant at very low Li contents. The increase in the lattice parameter *c* is due to the removal of Li ions (*i.e.* the number of Li ions decreases) leading to the weakening of the O−Li−O attraction. However, the value of *c* decreases at the half delithiated structure is because of the oxidation of O anions (*i.e.* charge changes on O). The sharp decrease in the lattice parameter *c* at very low Li contents is due to the sliding of O−TM−O layers with respect to each other (which is related to the electrostatic interactions) packing in the *c* direction. At the full delithiated structure, we found that O anions are oxidized more strongly than those at high Li concentration and thus the O stacking is changed, leading to the structural

phase transition. Our total Coulomb energy calculation indicates that the O-stacking-induced phase transition is driven by increased strength of ionic bonds and electrostatic interaction.

In the second work of this dissertation, we studied the lattice parameters change and phase transitions in LixNCM811 at various delithiated states (charging) by using a similar approach to the first work. The SCAN functional was used for all DFT calculations. By analyzing the NUS, SDD, DOS and BCs, we investigated the variation of a, b, and c, and, in particular the phase transitions during charge/discharge processes. It was found that (i) number of Li ions, (ii) charges on TMs and O, (iii) TM sites, (iv) J−T distortion, and (v) electrostatic interactions are the main factors controlling lattice parameters and symmetry. The decrease in the lattice parameter a upon charging (delithitaion) is controlled by the factors (ii) and (iv), while the increase in the value of a at very low Li contents is due to the factors (ii) and (v). However, the increase in the lattice parameter c at the low delithiated structure is controlled by the factor (i). The decrease in the value of c at the half delithiated structure is driven by the factors (ii) and (iv), and the large decrease in the parameter c at very low Li contents is induced by the factors (ii) and (v). The H−M phase transition at half Li concentration relies on the factors (iii) and (iv). Since every third layer consists of only Ni cations, the ordering of J−T active Ni^{3+} and J−T inactive Ni^{4+} at the Ni/Ni layer controls the H−M phase transition. This is because the length of axial axis in Ni^{3+}−O octahedra is larger than that in Ni^{4+}−O and the length of equatorial axis in Ni^{3+}−O and Ni^{4+}−O octahedra (see Fig. 5.2) [141].

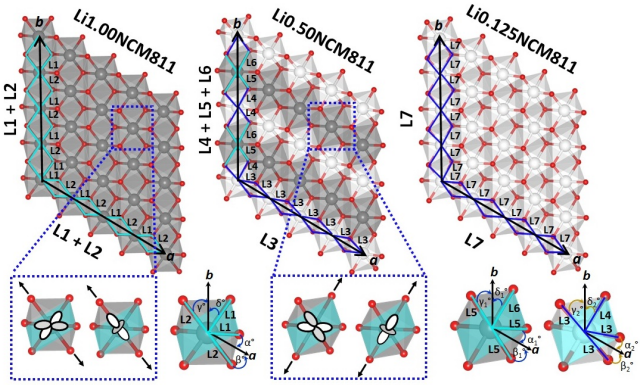

Figure 5.2: Top views of the Ni/Ni layer of NCM811 for different Li concentrations [141].

The third work of this dissertation was study of the effect of Al doping on Li and O va-

cancy formation energies (*i.e.* chemical stability) in NCM90505. By combining the experimental (experimental works from the group of prof. Yang-Kook Sun in Hanyang University Seoul) and theoretical results, we explained the reason for the improved structural stability of Al-doped NCM90505 (*i.e.* NCMA89) material. The formation energies of Li vacancy at high Li concentration and O vacancy at low Li concentration for NCM90505 (NCM90), NCMA89, and NCA89 were simulated by using DFT-PBE+U calculation (see Fig.5.3) [142]. It was found that the average value of Li vacancy energy for NCMA89 is nearly the same as that for NCM90 and NCA89 at high Li concentration. This indicates that the driving force of Li ions extraction/insertion with high Li contents is almost equal for them. Thus, they delivered almost the same initial discharge capacity in experiments. However, the average O vacancy energy for NCMA89 is between the value for NCM90 and NCA89 at low Li concentration. Among them, NCA89 shows the highest average formation energy of O vacancy, indicating that the reales of O from NCA89 is less likely compared to NCM90 and NCMA89. The high structural stability of NCA89 is due to strong binding energy of Al−O bonds. Our DFT calculation indicates that Al doping in NCMA89 is beneficial for improving its structural stability.

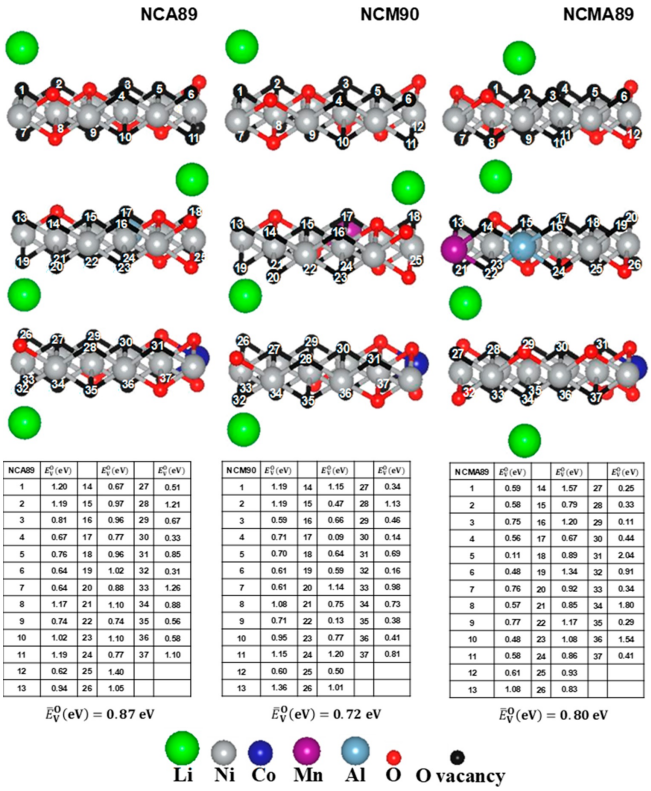

Figure 5.3: Side views of atomic structures and calculated oxygen vacancy formation energy for the cathodes [142].

In the fourth work of this dissertation, we studied the structural changes in $Na_{0.67}MnO_2$

with various amount of Fe contents in SIBs by combining experiment (experimental works from the group of prof. Seung-Taek Myung in Sejong University Seoul) and theory. A similar approach ((by combing extensive Coulomb energy and DFT calculations)) to the study of NCM systems was used to determine the most favorable arrangements of Na ions in $Na_{0.67}MnO_2$. Different *U*–*J* values for Mn and Fe were examined to find appropriate values for computing lattice parameters change and J−T distortion with Fe doping. The computing results indicate that the lattice parameter *a* increases, while the lattice parameter *b* and *c* decrease with increasing amount of Fe dopant, which are fair agreement with experimental results. The changes in *a*, *b* and *c* are due to the J−T distortion on Mn^{3+} cations. The elongation of equatorial Mn−O bond lengths cause the expansion of *a*, while the contraction of axial Mn−O bond lengths lead to the decrease in the lattice parameter *b* and *c* (see Fig.5.4) [143]. Thus, Fe doping in $Na_{0.67}MnO_2$ results in the suppression of J−T distortion on Mn cations. These findings show the benefits of improved structural stability of $Na_{0.67}MnO_2$ with Fe dopant in its lattice.

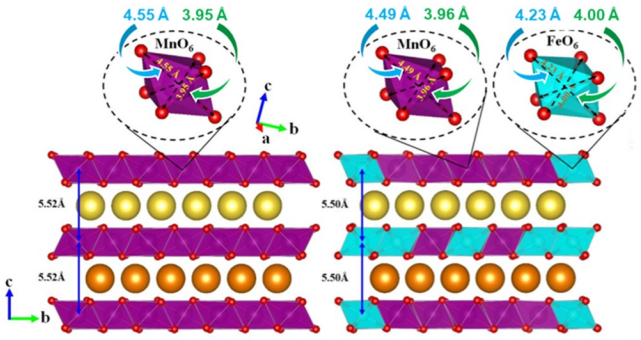

Figure 5.4: Calculated axial and averaged equatorial bond lengths for the most favorable structures of $Na_{0.67}Fe_xMn_{1-x}O_2$ [143].

In this dissertation, we used an approach to model and simulate the non-monotonic lattice parameters change, structural phase transitions and voltage profiles in cathode materials at different levels of delithiation in fair agreement with the experimental results. A detailed analysis of unpaired electrons on ions, spin density difference, density of state and Bader charges was applied to explain the variation of lattice parameters, symmetry, inter(intra)layer distances and mechanism of redox reactions during charging/discharging in cathode materials. Our results show that choosing the exchange-correlation (XC) functional is important in

modelling and understanding the structural changes in cathode materials. The simulations of this dissertation help to study the variation of crystal, atomic and electronic structures as function of the state of charge, and predict a promising way to improve the mechanical and chemical stability of cathode materials. Similar approaches to what have been used here can be applied in the future to predict the electrochemical properties of new types of cathodes for Li-, Na-, K-, and Mg-based batteries.

Acknowledgements

First of all, I would like to express my deep gratitude to my supervisor Dr. Payam Kaghazchi for giving me the chance to study on these interesting topics. His guidance and support were very important for me to finish the dissertation.

I would also like to express my sincere gratitude to Prof. Dr. Beate Paulus for her wiliness to be my second supervisor, supporting me during my Ph. D. studies, and her valuable and insightful comments for the dissertation.

A special thanks goes to Prof. Dr. Olivier Guillon for giving me the opportunity to work with him and finishing my dissertation in IEK-1 Forschungszentrum Jülich.

For comments and suggestions on writing the dissertation, I appreciate for the help from Sara Panahian Jand, Thomas Grohmann and Tu Lan. I am grateful to my office mate Kai Wilkner in IEK-1 at Forschungszentrum Jülich for giving me a nice atmosphere to work. Even though we work from home now, he is always helpful to give me suggestions and advice on my research. I would also like to thank my office mate Qian Zhang at Freie Universität Berlin for giving me a nice atmosphere to work. I am also grateful to Kangli Wang and Chunmei Liu for their help and encouragment, especially when I prepared to move to Jülich.

Having a nice time at Freie Universität Berlin, I would also like to thank Ashkan Moradabadi and Pouya Partovi-Azar for their scientific help on my research. I am grateful to Prof. Dr. Christina Roth and her research group for their experimental knowledge. My sincere thanks goes to Öznur Delikaya, Maike Schnucklake, Tintula Kottakkat and Michael Labza, who vivid my working life. I also appreciate Mrs. Julija Djordjevic for all her administrative works during my Ph. D. studies. Thanks for all the colleagues at Freie Universität Berlin. I also thank all my colleagues in IEK-1 at Forschungszentrum Jülich, especially the members in modelling team.

I acknowledge the financial support by the Bundesministerium für Bildung und Forschung (BMBF) as well as the computing time through Hochleistungsrechenzentrum Nord (HLRN) and JARA-HPC on the supercomputer JURECA at Forschungszentrum Jülich.

Additionally, I would like to thank my friends in Berlin and Jülich, who always give me

energies and fulfill my life in Germany. I would also appreciate my friends in Taiwan for supporting me and sharing my happiness and sadness with them.

Finally, I would like to express my great appreciation to my family and parents for their love and encouragement, without their support I would never have enjoyed so many opportunities.

Bibliography

[1] Ogumi, Z. *Energy Systems for a Green Community: The Role of Energy Conversion and Storage*, 1–6 (Springer New York, New York, NY, 2014).

[2] Tobias, P., Richard, K., Simon, D. & Martin, W. Lithium ion, lithium metal, and alternative rechargeable battery technologies: the odyssey for high energy density. *Journal of Solid State Electrochemistry* **21**, 1939–1964 (2017).

[3] Julien, C. *Design Considerations for Lithium Batteries*, 1–20 (Springer Netherlands, Dordrecht, 2000).

[4] Winter, M. & Besenhard, J. O. Wiederaufladbare batterien. *Chemie in unserer Zeit* **33**, 320–332 (1999).

[5] Armand, M. B. *Intercalation Electrodes*, 145–161 (Springer US, Boston, MA, 1980).

[6] Mizushima, K., Jones, P., Wiseman, P. & Goodenough, J. Li_xCoO_2 ($0<x<-1$): A new cathode material for batteries of high energy density. *Materials Research Bulletin* **15**, 783–789 (1980).

[7] Nishi, Y. The dawn of lithium-ion batteries. *Interface magazine* **25**, 71–74 (2016).

[8] Dixit, M. *et al.* Thermodynamic and kinetic studies of $LiNi_{0.5}Co_{0.2}Mn_{0.3}O_2$ as a positive electrode material for Li-ion batteries using first principles. *Physical Chemistry Chemical Physics* **18**, 6799–6812 (2016).

[9] Spinner, N., Zhang, L. & Mustain, W. E. Investigation of metal oxide anode degradation in lithium-ion batteries *via* identical-location TEM. *Journal of Materials Chemistry A* **2**, 1627–1630 (2014).

[10] Liu, C., Neale, Z. G. & Cao, G. Understanding electrochemical potentials of cathode materials in rechargeable batteries. *Materials Today* **19**, 109–123 (2016).

[11] Dreizler, A. M. *et al.* Investigation of the influence of nanostructured $LiNi_{0.33}Co_{0.33}Mn_{0.33}O_2$ lithium-ion battery electrodes on performance and aging. *Journal of The Electrochemical Society* **165**, A273–A282 (2018).

[12] Kondrakov, A. O. *et al.* Charge-transfer-induced lattice collapse in Ni-rich NCM cathode materials during delithiation. *The Journal of Physical Chemistry C* **121**, 24381–24388 (2017).

[13] Noh, H.-J., Youn, S., Yoon, C. S. & Sun, Y.-K. Comparison of the structural and electrochemical properties of layered $Li[Ni_xCo_yMn_z]O_2$ (x = 1/3, 0.5, 0.6, 0.7, 0.8 and 0.85) cathode material for lithium-ion batteries. *Journal of Power Sources* **233**, 121–130 (2013).

[14] Koyama, Y., Makimura, Y., Tanaka, I., Adachi, H. & Ohzuku, T. Systematic research on insertion materials based on superlattice models in a phase triangle of $LiCoO_2$-$LiNiO_2$-$LiMnO_2$. I. First-principles calculation on electronic and crystal structures, phase stability and new $LiNi_{1/2}Mn_{1/2}O_2$ material. *Journal of The Electrochemical Society* **151**, A1499 (2004).

[15] Dixit, M., Markovsky, B., Schipper, F., Aurbach, D. & Major, D. T. Origin of structural degradation during cycling and low thermal stability of Ni-rich layered transition metal-based electrode materials. *The Journal of Physical Chemistry C* **121**, 22628–22636 (2017).

[16] Chang, K., Hallstedt, B. & Music, D. Thermodynamic description of the $LiNiO_2$–NiO_2 pseudo-binary system and extrapolation to the $Li(Co,Ni)O_2$–$(Co,Ni)O_2$ system. *Calphad* **37**, 100–107 (2012).

[17] Märker, K., Reeves, P. J., Xu, C., Griffith, K. J. & Grey, C. P. Evolution of structure and lithium dynamics in $LiNi_{0.8}Mn_{0.1}Co_{0.1}O_2$ (NMC811) cathodes during electrochemical cycling. *Chemistry of Materials* **31**, 2545–2554 (2019).

[18] Zhu, Z. *et al.* Gradient-morph $LiCoO_2$ single crystals with stabilized energy density above 3400 W h L-1. *Energy & Environmental Science* **13**, 1865–1878 (2020).

[19] Myung, S.-T. *et al.* Nickel-rich layered cathode materials for automotive lithium-ion batteries: Achievements and perspectives. *ACS Energy Letters* **2**, 196–223 (2017).

[20] M., Y. & H., N. *A Review of Positive Electrode Materials for Lithium-Ion Batteries*, 9–48 (Springer New York, New York, NY, 2009).

[21] Shao-Horn, Y., Hackney, S., Kahaian, A. & Thackeray, M. Structural stability of $LiCoO_2$ at 400°c. *Journal of Solid State Chemistry* **168**, 60–68 (2002).

[22] Dahéron, L. *et al.* Electron transfer mechanisms upon lithium deintercalation from $LiCoO_2$ to CoO_2 investigated by XPS. *Chemistry of Materials* **20**, 583–590 (2008).

[23] Antolini, E. $LiCoO_2$: formation, structure, lithium and oxygen nonstoichiometry, electrochemical behaviour and transport properties. *Solid State Ionics* **170**, 159–171 (2004).

[24] Ménétrier, M., Saadoune, I., Levasseur, S. & Delmas, C. The insulator-metal transition upon lithium deintercalation from $LiCoO_2$: electronic properties and 7Li NMR study. *Journal of Materials Chemistry* **9**, 1135–1140 (1999).

[25] Amatucci, G. G., Tarascon, J. M. & Klein, L. C. CoO_2, the end member of the Li_xCoO_2 solid solution. *Journal of The Electrochemical Society* **143**, 1114–1123 (1996).

[26] Laubach, S. *et al.* Changes in the crystal and electronic structure of $LiCoO_2$ and $LiNiO_2$ upon Li intercalation and de-intercalation. *Physical Chemistry Chemical Physics* **11**, 3278–3289 (2009).

[27] Reimers, J. N. & Dahn, J. R. Electrochemical and *in situ* X-Ray diffraction studies of lithium intercalation in Li_xCoO_2. *Journal of The Electrochemical Society* **139**, 2091–2097 (1992).

[28] Chen, Z. & Dahn, J. Methods to obtain excellent capacity retention in $LiCoO_2$ cycled to 4.5 V. *Electrochimica Acta* **49**, 1079–1090 (2004).

[29] Van der Ven, A., Aydinol, M. K., Ceder, G., Kresse, G. & Hafner, J. First-principles investigation of phase stability in $LiCoO_2$. *Physical Review B* **58**, 2975–2987 (1998).

[30] Maugeri, L. *et al.* Local structure of $LiCoO_2$ nanoparticles studied by Co K-edge x-ray absorption spectroscopy. *Journal of Physics: Condensed Matter* **24**, 335305 (2012).

[31] Koyama, Y., Yabuuchi, N., Tanaka, I., Adachi, H. & Ohzuku, T. Solid-state chemistry and electrochemistry of $LiCo_{1/3}Ni_{1/3}Mn_{1/3}O_2$ for advanced lithium-ion batteries I. First-principles calculation on the crystal and electronic structures. *Journal of the Electrochemical Society* **151**, A1545–A1551 (2004).

[32] Kohn, W. & Sham, L. J. Self-consistent equations including exchange and correlation effects. *Physical Review* **140**, A1133–A1138 (1965).

[33] Arup, C., Dixit, M., Doron, A. & T, M. D. Predicting accurate cathode properties of layered oxide materials using the SCAN meta-GGA density functional. *npj Computational Materials* **4** (2018).

[34] Perdew, J. P., Burke, K. & Ernzerhof, M. Generalized gradient approximation made simple. *Physical Review Letters* **77**, 3865–3868 (1996).

[35] Dudarev, S. L., Botton, G. A., Savrasov, S. Y., Humphreys, C. J. & Sutton, A. P. Electron-energy-loss spectra and the structural stability of nickel oxide: An LSDA+U study. *Physical Review B* **57**, 1505–1509 (1998).

[36] Grimme, S. Semiempirical GGA-type density functional constructed with a long-range dispersion correction. *Journal of Computational Chemistry* **27**, 1787–1799 (2006).

[37] Arai, H., Okada, S., Sakurai, Y. & ichi Yamaki, J. Reversibility of $LiNiO_2$ cathode. *Solid State Ionics* **95**, 275–282 (1997).

[38] Nitta, N., Wu, F., Lee, J. T. & Yushin, G. Li-ion battery materials: present and future. *Materials Today* **18**, 252–264 (2015).

[39] Radin, M. D. *et al.* Narrowing the gap between theoretical and practical capacities in Li-ion layered oxide cathode materials. *Advanced Energy Materials* **7**, 1602888 (2017).

[40] Delmas, C. *et al.* On the behavior of the Li_xNiO_2 system: an electrochemical and structural overview. *Journal of Power Sources* **68**, 120–125 (1997).

[41] Arai, H., Okada, S., Sakurai, Y. & ichi Yamaki, J. Electrochemical and thermal behavior of $LiNi_{1-z}M_zO_2$ (M = Co, Mn, Ti). *Journal of The Electrochemical Society* **144**, 3117–3125 (1997).

[42] Liu, W. *et al.* Nickel-rich layered lithium transition-metal oxide for high-energy lithium-ion batteries. *Angewandte Chemie International Edition* **54**, 4440–4457 (2015).

[43] Ohzuku, T., Ueda, A. & Kouguchi, M. Synthesis and characterization of $LiAl_{1/4}Ni_{3/4}O_2$ for Lithium-ion (shuttlecock) batteries. *Journal of The Electrochemical Society* **142**, 4033–4039 (1995).

[44] Cho, J., Kim, T.-J., Kim, Y. J. & Park, B. High-performance ZrO_2-coated $LiNiO_2$ cathode material. *Electrochemical and Solid-State Letters* **4**, A159 (2001).

[45] Li, H., Zhang, N., Li, J. & Dahn, J. R. Updating the structure and electrochemistry of Li_xNiO_2 for $0 \leq x \leq 1$. *Journal of The Electrochemical Society* **165**, A2985–A2993 (2018).

[46] Nakai, I., Takahashi, K., Shiraishi, Y., Nakagome, T. & Nishikawa, F. Study of the Jahn–Teller distortion in $LiNiO_2$, a cathode material in a rechargeable lithium battery,

by *in situ* X-Ray absorption fine structure analysis. *Journal of Solid State Chemistry* **140**, 145–148 (1998).

[47] Rougier, A., Delmas, C. & Chadwick, A. Non-cooperative Jahn-Teller effect in $LiNiO_2$: An EXAFS study. *Solid State Communications* **94**, 123–127 (1995).

[48] Radin, M. D. & Van der Ven, A. Simulating charge, spin, and orbital ordering: Application to Jahn–Teller distortions in layered transition-metal oxides. *Chemistry of Materials* **30**, 607–618 (2018).

[49] Bianchini, M., Roca-Ayats, M., Hartmann, P., Brezesinski, T. & Janek, J. There and back again-the journey of $LiNiO_2$ as a cathode active material. *Angewandte Chemie International Edition* **58**, 10434–10458 (2019).

[50] He, P., Yu, H., Li, D. & Zhou, H. Layered lithium transition metal oxide cathodes towards high energy lithium-ion batteries. *Journal of Materials Chemistry* **22**, 3680–3695 (2012).

[51] Hwang, S.-J., Park, H.-S., Choy, J.-H. & Campet, G. Evolution of local structure around manganese in layered $LiMnO_2$ upon chemical and electrochemical delithiation/relithiation. *Chemistry of Materials* **12**, 1818–1826 (2000).

[52] Wang, D. *et al.* β-MnO_2 as a cathode material for lithium ion batteries from first principles calculations. *Physical Chemistry Chemical Physics* **15**, 9075–9083 (2013).

[53] Shao-Horn, Y. *et al.* Structural characterization of layered $LiMnO_2$ electrodes by electron diffraction and lattice imaging. *Journal of The Electrochemical Society* **146**, 2404–2412 (1999).

[54] Choi, W. & Manthiram, A. Comparison of metal ion dissolutions from lithium ion battery cathodes. *Journal of The Electrochemical Society* **153**, A1760 (2006).

[55] Robert Armstrong, A. & Gitzendanner, R. The intercalation compound $Li(Mn_{0.9}Co_{0.1})O_2$ as a positive electrode for rechargeable lithium batteries. *Chemical Communications* 1833–1834 (1998).

[56] Belharouak, I., Sun, Y.-K., Liu, J. & Amine, K. $Li(Ni_{1/3}Co_{1/3}Mn_{1/3})O_2$ as a suitable cathode for high power applications. *Journal of Power Sources* **123**, 247–252 (2003).

[57] de Biasi, L. *et al.* Between scylla and charybdis: Balancing among structural stability and energy density of layered NCM cathode materials for advanced lithium-ion batteries. *The Journal of Physical Chemistry C* **121**, 26163–26171 (2017).

[58] Ohzuku, T. & Makimura, Y. Layered lithium insertion material of $LiCo_{1/3}Ni_{1/3}Mn_{1/3}O_2$ for lithium-ion batteries. *Chemistry Letters* **30**, 642–643 (2001).

[59] Li, Z. *et al.* Comparative study of the capacity and rate capability of $LiNi_yMn_yCo_{1-2y}O_2$ (y = 0.5, 0.45, 0.4, 0.33). *Journal of The Electrochemical Society* **158**, A516 (2011).

[60] Choi, J. & Manthiram, A. Role of chemical and structural stabilities on the electrochemical properties of layered $LiNi_{1/3}Mn_{1/3}Co_{1/3}O_2$ cathodes. *Journal of The Electrochemical Society* **152**, A1714 (2005).

[61] Koerver, R. *et al.* Chemo-mechanical expansion of lithium electrode materials - on the route to mechanically optimized all-solid-state batteries. *Energy & Environmental Science* **11**, 2142–2158 (2018).

[62] Hua, W. *et al.* (De)Lithiation mechanism of hierarchically layered $LiNi_{1/3}Co_{1/3}Mn_{1/3}O_2$ cathodes during high-voltage cycling. *Journal of The Electrochemical Society* **166**, A5025–A5032 (2018).

[63] Buchberger, I. *et al.* Aging analysis of graphite/$LiNi_{1/3}Mn_{1/3}Co_{1/3}O_2$ cells using XRD, PGAA, and AC impedance. *Journal of The Electrochemical Society* **162**, A2737–A2746 (2015).

[64] Hwang, B. J., Tsai, Y. W., Carlier, D. & Ceder, G. A combined computational/experimental study on $LiNi_{1/3}Co_{1/3}Mn_{1/3}O_2$. *Chemistry of Materials* **15**, 3676–3682 (2003).

[65] Min, K. *et al.* A comparative study of structural changes in lithium nickel cobalt manganese oxide as a function of Ni content during delithiation process. *Journal of Power Sources* **315**, 111–119 (2016).

[66] Hoang, K. & Johannes, M. Defect physics and chemistry in layered mixed transition metal oxide cathode materials: (Ni,Co,Mn) vs (Ni,Co,Al). *Chemistry of Materials* **28**, 1325–1334 (2016).

[67] Schipper, F. *et al.* Review-recent advances and remaining challenges for lithium ion battery cathodes. *Journal of The Electrochemical Society* **164**, A6220–A6228 (2016).

[68] Kim, J.-H., Park, K.-J., Kim, S. J., Yoon, C. S. & Sun, Y.-K. A method of increasing the energy density of layered Ni-rich $Li[Ni_{1-2x}Co_xMn_x]O_2$ cathodes (x = 0.05, 0.1, 0.2). *Journal of Materials Chemistry A* **7**, 2694–2701 (2019).

[69] Liang, C. *et al.* Obstacles toward unity efficiency of $LiNi_{1-2x}Co_xMn_xO_2$ (x = 0 $\sim$ 1/3) (NCM) cathode materials: Insights from *ab initio* calculations. *Journal of Power Sources* **340**, 217–228 (2017).

[70] Hashem, A. M. *et al.* Doped nanoscale NMC333 as cathode materials for Li-ion batteries. *Materials* **12**, 2899 (2019).

[71] Chen, C. *et al.* Aluminum-doped lithium nickel cobalt oxide electrodes for high-power lithium-ion batteries. *Journal of Power Sources* **128**, 278–285 (2004).

[72] Susai, F. A. *et al.* Improving performance of $LiNi_{0.8}Co_{0.1}Mn_{0.1}O_2$ cathode materials for lithium-ion batteries by doping with molybdenum-ions: Theoretical and experimental studies. *ACS Applied Energy Materials* **2**, 4521–4534 (2019).

[73] Kim, U. *et al.* Pushing the limit of layered transition metal oxide cathodes for high-energy density rechargeable Li ion batteries. *Energy and Environmental Science* **11**, 1271–1279 (2018).

[74] Schipper, F. *et al.* Stabilizing nickel-rich layered cathode materials by a high-charge cation doping strategy: zirconium-doped $LiNi_{0.6}Co_{0.2}Mn_{0.2}O_2$. *Journal of Materials Chemistry A* **4**, 16073–16084 (2016).

[75] Liu, L., Sun, K., Zhang, N. & Yang, T. Improvement of high-voltage cycling behavior of $Li(Ni_{1/3}Co_{1/3}Mn_{1/3})O_2$ cathodes by Mg, Cr, and Al substitution. *Journal of Solid State Electrochemistry* **13**, 1381–1386 (2009).

[76] Wang, L. Q. *et al.* Synthesis and electrochemical properties of Mo-doped $Li[Ni_{1/3}Mn_{1/3}Co_{1/3}]O_2$ cathode materials for Li-ion battery. *Journal of Power Sources* **162**, 1367–1372 (2006).

[77] Billaud, J. *et al.* β-$NaMnO_2$: A high-performance cathode for sodium-ion batteries. *Journal of the American Chemical Society* **136**, 17243–17248 (2014).

[78] Sathiya, M., Hemalatha, K., Ramesha, K., Tarascon, J.-M. & Prakash, A. S. Synthesis, structure, and electrochemical properties of the layered sodium insertion cathode material: $NaNi_{1/3}Mn_{1/3}Co_{1/3}O_2$. *Chemistry of Materials* **24**, 1846–1853 (2012).

[79] Wang, P.-F., You, Y., Yin, Y.-X. & Guo, Y.-G. Layered oxide cathodes for sodium-ion batteries: Phase transition, air stability, and performance. *Advanced Energy Materials* **8**, 1701912 (2018).

[80] Delmas, C., Braconnier, J.-J., Fouassier, C. & Hagenmuller, P. Electrochemical intercalation of sodium in Na_xCoO_2 bronzes. *Solid State Ionics* **3-4**, 165–169 (1981).

[81] Shacklette, L. W., Jow, T. R. & Townsend, L. Rechargeable electrodes from sodium cobalt bronzes. *Journal of The Electrochemical Society* **135**, 2669–2674 (1988).

[82] Rami Reddy, B. V., Ravikumar, R., Nithya, C. & Gopukumar, S. High performance Na_xCoO_2 as a cathode material for rechargeable sodium batteries. *Journal of Materials Chemistry A* **3**, 18059–18063 (2015).

[83] Han, M. H., Gonzalo, E., Casas-Cabanas, M. & Rojo, T. Structural evolution and electrochemistry of monoclinic $NaNiO_2$ upon the first cycling process. *Journal of Power Sources* **258**, 266–271 (2014).

[84] Ma, X., Chen, H. & Ceder, G. Electrochemical properties of monoclinic $NaMnO_2$. *Journal of The Electrochemical Society* **158**, A1307 (2011).

[85] Velikokhatnyi, O. I., Chang, C.-C. & Kumta, P. N. Phase stability and electronic structure of $NaMnO_2$. *Journal of The Electrochemical Society* **150**, A1262 (2003).

[86] Mendiboure, A., Delmas, C. & Hagenmuller, P. Electrochemical intercalation and deintercalation of Na_xMnO_2 bronzes. *Journal of Solid State Chemistry* **57**, 323–331 (1985).

[87] Caballero, A. *et al.* Synthesis and characterization of high-temperature hexagonal P2-$Na_{0.6}MnO_2$ and its electrochemical behaviour as cathode in sodium cells. *Journal of Materials Chemistry* **12**, 1142–1147 (2002).

[88] Kumakura, S., Tahara, Y., Kubota, K., Chihara, K. & Komaba, S. Sodium and manganese stoichiometry of P2-type $Na_{2/3}MnO_2$. *Angewandte Chemie International Edition* **55**, 12760–12763 (2016).

[89] Su, D., Wang, C., Ahn, H.-j. & Wang, G. Single crystalline $Na_{0.7}MnO_2$ nanoplates as cathode materials for sodium-ion batteries with enhanced performance. *Chemistry – A European Journal* **19**, 10884–10889 (2013).

[90] Dai, Z., Mani, U., Tan, H. T. & Yan, Q. Advanced cathode materials for sodium-ion batteries: What determines our choices? *Small Methods* **1**, 1700098 (2017).

[91] Kim, H. *et al.* Ab initio study of the sodium intercalation and intermediate phases in $Na_{0.44}MnO_2$ for sodium-ion battery. *Chemistry of Materials* **24**, 1205–1211 (2012).

[92] Billaud, J. *et al.* $Na_{0.67}Mn_{1-x}Mg_xO_2$ ($0 \leq x \leq 0.2$): a high capacity cathode for sodium-ion batteries. *Energy & Environmental Science* **7**, 1387–1391 (2014).

[93] de la Llave, E. *et al.* Improving energy density and structural stability of manganese oxide cathodes for Na-ion batteries by structural lithium substitution. *Chemistry of Materials* **28**, 9064–9076 (2016).

[94] Yang, L. *et al.* Lithium-doping stabilized high-performance P2-$Na_{0.66}Li_{0.18}Fe_{0.12}Mn_{0.7}O_2$ cathode for sodium ion batteries. *Journal of the American Chemical Society* **141**, 6680–6689 (2019).

[95] Tang, W., Sanville, E. & Henkelman, G. A grid-based bader analysis algorithm without lattice bias. *Journal of Physics: Condensed Matter* **21**, 084204 (2009).

[96] Born, M. & Oppenheimer, R. Zur quantentheorie der molekeln. *Annalen der Physik* **389**, 457–484 (1927).

[97] Hartree, D. R. The wave mechanics of an atom with a non-coulomb central field. Part I. Theory and methods. *Mathematical Proceedings of the Cambridge Philosophical Society* **24**, 89–110 (1928).

[98] Fock, V. V. Näherungsmethode zur Lösung des quantenmechanischen Mehrkörperproblems. *Zeitschrift für Physik* **61**, 126–148 (1930).

[99] Slater, J. C. The theory of complex spectra. *Physical Review* **34**, 1293–1322 (1929).

[100] Møller, C. & Plesset, M. S. Note on an approximation treatment for many-electron systems. *Physical Review* **46**, 618–622 (1934).

[101] Sherrill, C. D. & Schaefer, H. F. The configuration interaction method: Advances in highly correlated approaches. *Advances in Quantum Chemistry* **34**, 143–269 (1999).

[102] Bartlett, R. J. Coupled-cluster approach to molecular structure and spectra: a step toward predictive quantum chemistry. *The Journal of Physical Chemistry* **93**, 1697–1708 (1989).

[103] Thomas, L. H. The calculation of atomic fields. *Mathematical Proceedings of the Cambridge Philosophical Society* **23**, 542—-548 (1927).

[104] Fermi, E. Eine statistische Methode zur Bestimmung einiger Eigenschaften des Atoms und ihre Anwendung auf die Theorie des periodischen Systems der Elemente. *Zeitschrift für Physik* **48**, 73–79 (1928).

[105] Dirac, P. A. M. Note on exchange phenomena in the thomas atom. *Mathematical Proceedings of the Cambridge Philosophical Society* **26**, 376–385 (1930).

[106] Hohenberg, P. & Kohn, W. Inhomogeneous electron gas. *Physical Review* **136**, B864–B871 (1964).

[107] Perdew, J. P., Schmidt, K., Van Doren, V., Van Alsenoy, C. & Geerlings, P. Jacob's ladder of density functional approximations for the exchange-correlation energy. *AIP Conference Proceedings* **577**, 1–20 (2001).

[108] Ceperley, D. M. & Alder, B. J. Ground state of the electron gas by a stochastic method. *Physical Review Letters* **45**, 566–569 (1980).

[109] Vosko, S. H., Wilk, L. & Nusair, M. Accurate spin-dependent electron liquid correlation energies for local spin density calculations: a critical analysis. *Canadian Journal of Physics* **58**, 1200–1211 (1980).

[110] Perdew, J. P. & Zunger, A. Self-interaction correction to density-functional approximations for many-electron systems. *Physical Review B* **23**, 5048–5079 (1981).

[111] Perdew, J. P. & Wang, Y. Accurate and simple analytic representation of the electron-gas correlation energy. *Physical Review B* **45**, 13244–13249 (1992).

[112] Sham, L. J. & Kohn, W. One-particle properties of an inhomogeneous interacting electron gas. *Physical Review* **145**, 561–567 (1966).

[113] Gunnarsson, O. & Lundqvist, B. I. Exchange and correlation in atoms, molecules, and solids by the spin-density-functional formalism. *Physical Review B* **13**, 4274–4298 (1976).

[114] Perdew, J. P. & Yue, W. Accurate and simple density functional for the electronic exchange energy: Generalized gradient approximation. *Physical Review B* **33**, 8800–8802 (1986).

[115] Becke, A. D. Density-functional exchange-energy approximation with correct asymptotic behavior. *Physical Review A* **38**, 3098–3100 (1988).

[116] Lee, C., Yang, W. & Parr, R. G. Development of the colle-salvetti correlation-energy formula into a functional of the electron density. *Physical Review B* **37**, 785–789 (1988).

[117] Perdew, J. P. Unified theory of exchange and correlation beyond the local density approximation. In Ziesche, P. & Eschrig, H. (eds.) *Electronic Structure of Solids '91*, vol. 17 of *Physical Research*, 11–20 (Akademie Verlag, Berlin, 1991).

[118] Hammer, B., Hansen, L. B. & Nørskov, J. K. Improved adsorption energetics within density-functional theory using revised Perdew-Burke-Ernzerhof functionals. *Physical Review B* **59**, 7413–7421 (1999).

[119] Becke, A. D. A new inhomogeneity parameter in density-functional theory. *The Journal of Chemical Physics* **109**, 2092–2098 (1998).

[120] Perdew, J. P., Kurth, S., Zupan, A. c. v. & Blaha, P. Accurate density functional with correct formal properties: A step beyond the generalized gradient approximation. *Physical Review Letters* **82**, 2544–2547 (1999).

[121] Tao, J., Perdew, J. P., Staroverov, V. N. & Scuseria, G. E. Climbing the density functional ladder: Nonempirical meta-generalized gradient approximation designed for molecules and solids. *Physical Review Letters* **91**, 146401 (2003).

[122] Sun, J., Ruzsinszky, A. & Perdew, J. P. Strongly constrained and appropriately normed semilocal density functional. *Physical Review Letters* **115**, 036402 (2015).

[123] Himmetoglu, B., Floris, A., de Gironcoli, S. & Cococcioni, M. Hubbard-corrected DFT energy functionals: The LDA+U description of correlated systems. *International Journal of Quantum Chemistry* **114**, 14–49 (2014).

[124] Mott, N. F. The basis of the electron theory of metals, with special reference to the transition metals. *Proceedings of the Physical Society. Section A* **62**, 416–422 (1949).

[125] Hubbard, J. & Flowers, B. H. Electron correlations in narrow energy bands. *Proceedings of the Royal Society of London. Series A. Mathematical and Physical Sciences* **276**, 238–257 (1963).

[126] Hubbard, J. Electron correlations in narrow energy bands. II. The degenerate band case. *Proceedings of the Royal Society of London. Series A, Mathematical and Physical Sciences* **277**, 237–259 (1964).

[127] Liechtenstein, A. I., Anisimov, V. I. & Zaanen, J. Density-functional theory and strong interactions: Orbital ordering in Mott-Hubbard insulators. *Physical Review B* **52**, R5467–R5470 (1995).

[128] Tao, J., Perdew, J. P. & Ruzsinszky, A. Accurate van der Waals coefficients from density functional theory. *Proceedings of the National Academy of Sciences* **109**, 18–21 (2012).

[129] Grimme, S. Density functional theory with London dispersion corrections. *WIREs Computational Molecular Science* **1**, 211–228 (2011).

[130] Grimme, S. Accurate description of van der Waals complexes by density functional theory including empirical corrections. *Journal of Computational Chemistry* **25**, 1463–1473 (2004).

[131] Grimme, S., Antony, J., Ehrlich, S. & Krieg, H. A consistent and accurate *ab initio* parametrization of density functional dispersion correction (DFT-D) for the 94 elements H-Pu. *The Journal of Chemical Physics* **132**, 154104 (2010).

[132] Wannier, G. H. Quantum theory of solids. C. Kittel. Wiley, New York, 1963. xii + 435 pp. Illus. 13.50. *Science* **143**, 672 (1964).

[133] Ashcroft, N. W., Mermin, N. D. & Rodriguez, S. Solid state physics (1998).

[134] Payne, M. C., Teter, M. P., Allan, D. C., Arias, T. A. & Joannopoulos, J. D. Iterative minimization techniques for ab initio total-energy calculations: molecular dynamics and conjugate gradients. *Reviews of Modern Physics* **64**, 1045–1097 (1992).

[135] Hamann, D. R., Schlüter, M. & Chiang, C. Norm-conserving pseudopotentials. *Physical Review Letters* **43**, 1494–1497 (1979).

[136] Vanderbilt, D. Soft self-consistent pseudopotentials in a generalized eigenvalue formalism. *Physical Review B* **41**, 7892–7895 (1990).

[137] Blöchl, P. E. Projector augmented-wave method. *Physical Review B* **50**, 17953–17979 (1994).

[138] Ewald, P. P. Die Berechnung optischer und elektrostatischer Gitterpotentiale. *Annalen der Physik* **369**, 253–287 (1921).

[139] de Leeuw, S. W., Perram, J. W., Smith, E. R. & Rowlinson, J. S. Simulation of electrostatic systems in periodic boundary conditions. II. Equivalence of boundary conditions. *Proceedings of the Royal Society of London. A. Mathematical and Physical Sciences* **373**, 57–66 (1980).

[140] Kuo, L.-Y., Guillon, O. & Kaghazchi, P. On the origin of non-monotonic variation of the lattice parameters of $LiNi_{1/3}Co_{1/3}Mn_{1/3}O_2$ with lithiation/delithiation: a first-principles study. *Journal of Materials Chemistry A* **8**, 13832–13841 (2020).

[141] Kuo, L.-Y., Guillon, O. & Kaghazchi, P. Origin of structural phase transitions in Ni-rich $Li_xNi_{0.8}Co_{0.1}Mn_{0.1}O_2$ with lithiation/delithiation: A first-principles study. *ACS Sustainable Chemistry & Engineering* **9**, 7437–7446 (2021).

[142] Kim, U.-H., Kuo, L.-Y., Kaghazchi, P., Yoon, C. S. & Sun, Y.-K. Quaternary layered Ni-rich NCMA cathode for lithium-ion batteries. *ACS Energy Letters* **4**, 576–582 (2019).

[143] Choi, J. U. *et al.* Unraveling the role of earth-abundant Fe in the suppression of Jahn–Teller distortion of P'2-type $Na_{2/3}MnO_2$: Experimental and theoretical studies. *ACS Applied Materials & Interfaces* **10**, 40978–40984 (2018).